UNIVERSITY OF SOUTHAMPTON

FACULTY OF ENGINEERING AND PHYSICAL SCIENCES

SCHOOL OF CHEMISTRY

The Effects of Model Membrane Complexity for the *E.coli* Cell Envelope

by

Jonathan Shearer

Thesis for the degree of Doctor of Philosophy

January 2020

UNIVERSITY OF SOUTHAMPTON

ABSTRACT

FACULTY OF ENGINEERING AND PHYSICAL SCIENCES
SCHOOL OF CHEMISTRY

Thesis for the degree of Doctor of Philosophy

THE EFFECTS OF MODEL MEMBRANE COMPLEXITY FOR THE *E.COLI* CELL ENVELOPE

by Jonathan Shearer

To overcome resistance to antibiotics in bacteria, such as *Escherichia coli*, further understanding of the nature of the cell envelope is required. Molecular dynamics has provided a powerful tool into investigations of the dynamics and structure of biological systems of varying complexity. In this thesis, coarse-grained simulations were used to probe the behaviour of the outer membrane and the proteins within, relative to typical phospholipid membranes. In the first chapter, nanopores of varying sizes, shapes and chemistry were studied in the context of symmetric and asymmetric bacterial membranes. It was found that communication between leaflets played a significant role in lipid sorting of larger lipids. Following this, a broad study of the protein-lipid interactions between a range of different proteins and outer membrane models was carried out. The interactions between a protein and any given outer membrane model were found to have a unique fingerprint. The stability of the lipids in outer and inner membranes were then investigated by measuring the free energy of lipid extraction. The results concluded that there was little similarity between the extraction of different lipopolysaccharide lipids, as well as repeats of the same lipid. A further study on the effects of a membrane protein on the stability of local and bulk lipids was carried out for the inner membrane. In the final chapter, the use of sparse lipopolysaccharide densities and Hamiltonian Replica Exchange Molecular Dynamics were investigated to enhance lipopolysaccharide mixing.

Contents

List of Figures

List of Tables

Research Thesis: Declaration of Authorship

Print name: JONATHAN ROY WILLIAM SHEARER

Title of thesis: The Effects of Model Membrane Complexity for the *E.coli* Cell Envelope

I declare that this thesis and the work presented in it are my own and has been generated by me as the result of my own original research.
I confirm that:

1. This work was done wholly or mainly while in candidature for a research degree at this University;
2. Where any part of this thesis has previously been submitted for a degree or any other qualification at this University or any other institution, this has been clearly stated;
3. Where I have consulted the published work of others, this is always clearly attributed;
4. Where I have quoted from the work of others, the source is always given. With the exception of such quotations, this thesis is entirely my own work;
5. I have acknowledged all main sources of help;
6. Where the thesis is based on work done by myself jointly with others, I have made clear exactly what was done by others and what I have contributed myself;
7. Parts of this work have been published as:
    - P.-C. Hsu, F. Samsudin, J. Shearer and S. Khalid, *Journal of Physical Chemistry Letters*, 2017, **8**, 5513-5518.
    - J. Shearer and S. Khalid, *Scientific Reports*, 2018, **8**, 1805.
    - J. Shearer, D. Jefferies and S. Khalid, *Journal of Chemical Theory and Computation*, 2019, **15**, 2608-2619.

Signature: Date: 02 / 10 / 2019

Acknowledgements

I would like to thank my supervisor, Professor Syma Khalid, who has provided an endless well of support, discussions and knowledge during the course of my PhD. I really appreciate the amount of effort that Syma put into checking that the PhD gears were always turning smoothly.

I would also like to thank the Khalid group, old and new, for all the help they provided, from useful discussions, to enabling the occasional pub trip. In particular, thanks are due to Conrado Pebedos for his tireless proofreading of an entire chapter of my thesis.

One of the advantages of the TMCS CDT has been friendships and scientific camaraderie born across a range of topics that I would have otherwise been ignorant of. In particular, I would like to thank Lee Steinberg and our talks of science and life on the long journey home, that often formed the spark for new ideas.

Outside of science, three years in Southampton has been a lively experience that has been enriched through old and new friendships alike. In this vein, my thanks go out to the Berkeley boys, the Bristol crew and friends from home who made these three years so enjoyable.

And last but not least a special thanks goes out to my family. Their support and encouragement over the years has been invaluable in getting to this stage in the first place! In addition, my panicked corrections at the end of thesis writing process would not have been possible without their help with proof-reading.

Definitions and Abbreviations

AA	All-atom
ACF	Autocorrelation function
APL	area per lipid
AqpZ	Aquaporin Z
BBCOM	Bootstrapped Block Covariance Overlap Analysis Method
BCOM	Block Covariance Overlap Analysis Method
BtuB	Outer membrane cobalamin transporter
CDL	cardiolipin
CDL2	dianionic cardiolipin
CG	Coarse-grained
CNT	carbon nanotube
CNP	carbon nanoparticles
CV	Collective variable
DBSCAN	Density-based spatial clustering of applications with noise
DPPC	16:0 phosphocholine
EAI	Exchange attempt interval
EstA	Esterase A
FhuA	Ferric hydroxamate receptor A
HREX	Hamiltonian Replica Exchange
HREMD	Hamiltonian Replica Exchange Molecular Dynamics
IACT	Integrated correlation time
IM	Inner membrane
LJ	Lennard-Jones
LPS	lipopolysaccharides
MBAR	Multistate Bennett Acceptance Ratio
MD	Molecular Dynamics
MM	Molecular mechanics
OM	Outer membrane
Omp	Outer membrane protein
OmpA	Outer membrane protein A
OmpF	Outer membrane protein F
OmpX	Outer membrane protein X

PBC	periodic boundary conditions
PCA	Principal component analysis
PGN	Petidoglycan
PE	Phosphoethanolamine
PES	Potential energy surface
PG	Phosphatidylglycerol
PGP	Phosphatidylglycerol phosphate
PME	Particle mesh Ewald
PMF	Potential mean force
POPE	16:0,18:1 phosphoethanolamine
POPG	16:0,18:1 phosphatidylglycerol
PS	Phosphatidylserine
QM	Quantum mechanics
RMSD	Root mean squared deviation
RMSF	Root mean squared fluctuation
UA	United Atom
US	Umbrella Sampling
VMD	Visual molecular dynamics
WHAM	Weighted histogram analysis method

Chapter 1

Introduction

1.1 The Cell

Prokaryotes are unicellular organisms that lack any form of membrane bound organelles. An organelle describes any specialised sub unit of a cell that performs a certain function e.g. nucleus, mitochondria etc. Prokaryotes can be divided into two subdomains, archaea and bacteria, of which this work will focus on the latter. Conversely, Eukaryotes describe unicellular organisms that do have membrane bound organelles, such as animal and plant cells. There are numerous morphologies (i.e. shapes) that bacteria can take, two common ones are coccus or baccilus (see Figure 1.1).

This thesis will focus on the the rod shaped (baccilus) bacteria Escherichia coli (*E. coli*)[1]. *E. coli* is a Gram-negative bacteria that is responsible for a range of bacterial infections [2–5]. In recent years many strains of *E. coli* have become resistant to antibiotics [6] and so have become one of key bacteria of interest in understanding drug resistance. However, beating bacterial resistance is far from trivial and studies have struggled with understanding how the cell adapts to different stimuli [7–9].

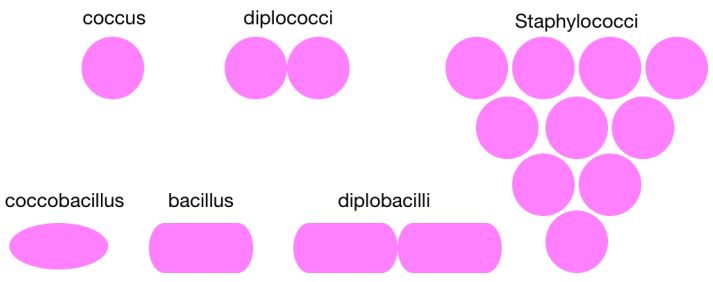

FIGURE 1.1: Examples of shapes bacteria can take.

The cell membrane acts as the gateway into the cell and so is of great importance in understanding a range of biological processes. Membranes are composed of a variety of lipids that form a film around the cell in the form of a bilayer. Biological processes such as the regulation of salt and water concentration, cell division or the activity of antimicrobials all depend on the cell membrane and the proteins that lie within them.

1.2 The Bacterial Cell Envelope

Bacteria can be divided into Gram-negative and Gram-positive bacteria, based on the structure of their respective cell envelopes. The nomenclature of these two bacterial subtypes was derived from the Gram staining method developed by Christian Gram [10]. Gram staining involves the staining of the cell with some form of dye that is retained by the 3D biopolymer mesh, peptidogylcan, that both bacterial subtypes have (Figure 1.2). For Gram-positive bacteria the peptidoglycan mesh is thick enough ($\sim 40 - 80$ nm) for the dye to be retained; while the peptidoglycan mesh for Gram-negative bacteria is too thin to retain the dye and can be washed out. Thus Gram-negative bacteria are defined by the the absence of the dye, upon visual observation of the cells.

The Gram-positive bacterial cell membrane contains one lipid bilayer, which is comprised of a variety of phospholipids and lipidated aminoacids[11, 12]. In the extracellular region

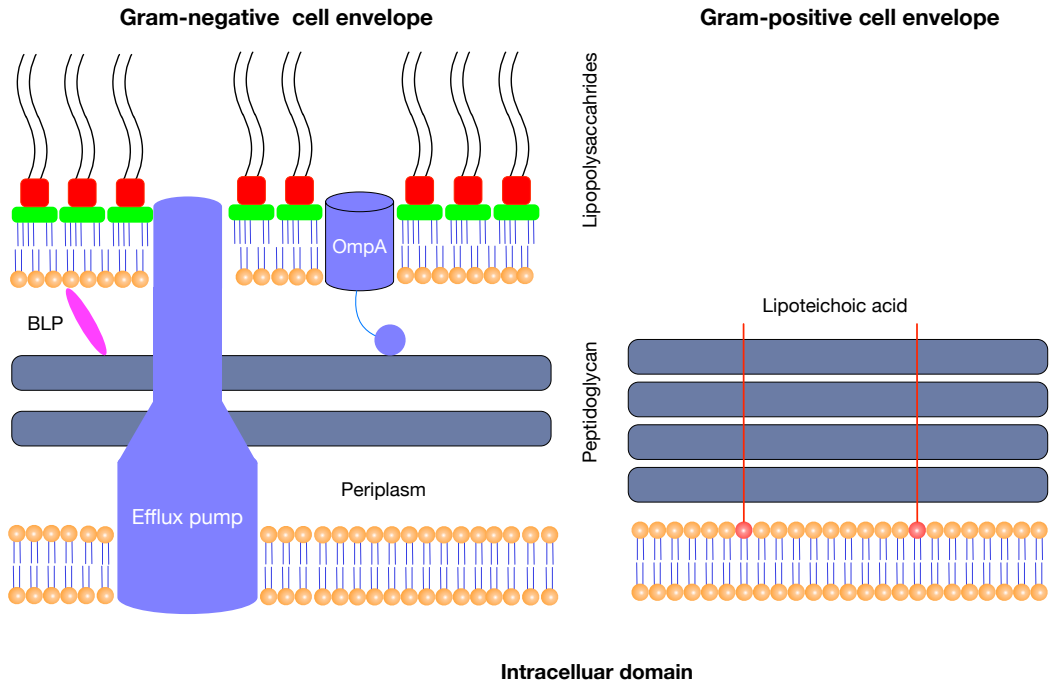

FIGURE 1.2: Diagrams of the Gram-positive and Gram-negative bacterial cell envelopes. Phospholipids are coloured in orange, BLP is braun's lipoprotein, membrane proteins are coloured in blue, green and red blocks are the lipid A headgroup and lipopolysaccharide core sugars, respectively.

of the cell there is a thick layer (up to 80 nm) of peptidoglycan (PGN) (Figure 1.2)[13], which is connected to the membrane by mainly glycolipids (e.g. Lipoteichoic acid) that pass through the PGN mesh (Figure 1.2).

Gram-negative bacteria, such as *E. Coli* have two membranes, the outer and inner membranes (OM and IM, respectively) and sandwiched between these layers is $1-2$ layers of PGN ($7-8$ nm, see Figure 1.2)[14].

1.3 The Outer Membrane

The OM is an asymmetric membrane that has an upper leaflet where 75% surface area is covered with lipopolysaccharides (LPS)[15], while the lower leaflet is mainly mixture of phosphoethanolamine (PE), phosphoglycerol (PG) and cardiolipin (CDL) lipids (see Figure 1.3 for chemical structures)[11, 14]. It is believed that the upper leaflet of some Gram-negative bacteria may contain contain significant amounts of phospholipids[16].

LPS is chemically diverse lipid and provides a chemical and physical barrier to entry into a bacterium. LPS can have up to three sections Lipid A, the core oligosacchardies and O-Antigen. Any LPS that has all three sections is termed 'smooth LPS', while LPS lipids without the O-Antigen chain are called 'Rough LPS' (Figure 1.3). The lipid A headgroup is composed of two glucosamine units that are chemically modified with two $R-PO_4^{-2}$ groups. The lipid A headgroup is a well conversed part of LPS and that not change greatly across a wide variety of bacterial strains. The number lipid tails ranges from $\sim 5-8$, depending on the strain of the bacteria[17, 18]. The Core sugar region is solely composed of sugars, such as 3-Deoxy-D-manno-oct-2-ulosonic acid (KdO) or heptose, which are often chemically modified with negatively charged groups[19]. The core sugars can be further divided into the inner (e.g. 2 KdO units) and outer core sugars (usually heptose). RaLPS and ReLPS are variants of LPS that have either the core sugars, or just the inner sugars, respectively. The O-Antigen chain is comprised from $0-50$ sugars and the composition and length varies across different bacteria[19]. One of the important functions of LPS is to provide a chemical and physical barrier to permeation into the cell of large, polar or anionic molecules[20, 21]. Recent studies also suggest that LPS plays a vital role in the elasticity of the cell envelope [22, 23]]. LPS lipids are known to non-covalently bind to each other via interactions between phosphate groups and divalent cations, such as calcium or magnesium [24]. Replacement of these divalent cation with monovalent cations has been found to lead to increased water permeation through the membrane[25].

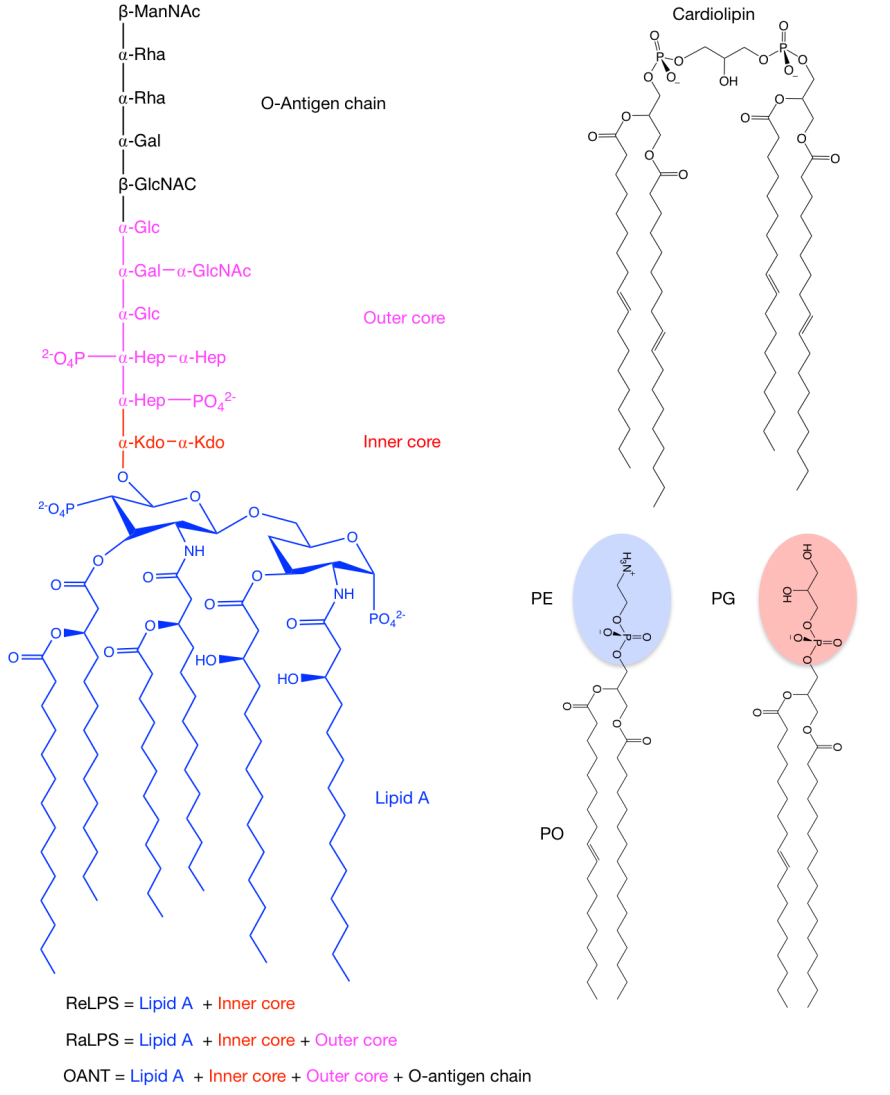

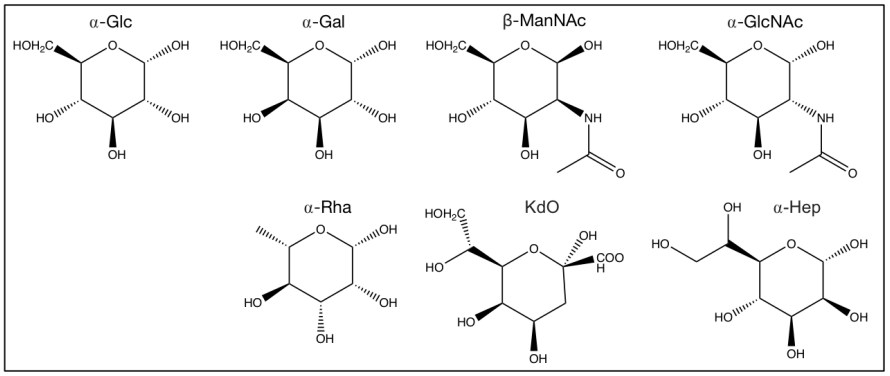

FIGURE 1.3: Chemical structures of the lipids used in the outer membrane model. Rough Mutant lipopolysaccharides (ReLPS and RaLPS), Smooth LPS with five sugar units (OANT), 16:0,18:1 phosphoethanolamine (POPE), 16:0,18:1 Phosphatidylglycerol (POPG) and 18:1,18:1 / 18:1,18:1 cardiolipin. Sugar abbreviation key: Glc, glucose, Gal, Galactose, ManNAc, N-Acetylmannosamine, GlcNAc, N-Acetylglucosamine, Rha, Rhamnose, Hep, L-Glycero-D-Manno-Heptose and KdO, 3-Deoxy-D-manno-oct-2-ulosonic acid.

1.4 Peptidoglycan and the Inner Membrane

The most abundant lipoprotein in the outer membrane is Braun's lipoprotein (BLP) and is covalently linked to the PGN layer (Figure 1.2)[26]. There are believed to be further non-covalent interactions between outer membrane proteins (Omps), such as OmpA and PGN [27]. The PGN layer is often of importance when considering diffusion of small molecules and proteins in the periplasmic region of the cell envelope.

The last barrier of the Gram-negative cell envelope is the IM (also called the plasma membrane), consists of a mixture of phospholipids. The major components of the membrane are usually PE, PG and CDL lipids (Figure 1.3). Other lipids that can be present in the membrane include Phosphatidylserine (PS) and Phosphatidylglycerol phosphate (PGP)[14].

1.5 Escherichia Coli: Membrane Model Composition

The focus of this work is the IM and OM of *E.coli*. In computational work the composition of each membrane model must remain fixed, unlike their *in vivo* counterparts. Thus an important question to ask is what the composition each model membrane should be. The flux of membrane compositions in a bacterium depends on a number of factors such as: temperature, pH and the life cycle of the cell[28]. The metabolic pathway of important phospholipids in *E.coli* is shown in Figure 1.4, where the lipids which tend to be present in amounts $> 1\%$ [14] are highlighted in red. Extensive knockout studies conclude that the absence of either PE[29, 30] or CDL[31] does not result in cell death, only if both are absent will the cell die[30]. Cell envelopes that are lacking in CDL tend to have increased amounts of PG, which is the most similar lipid in the metabolic pathway [32]. When both PE and CDL are removed it is thought that the lack of inverted-cone shaped lipids leads to cell death[14]. Thus the requirement of certain lipids often have biophysical motivations. Different temperatures during cell growth can also encourage different levels of lipid unsaturation, which can affect the fluidity of the cell [33].

Given the complexity of variations in composition *in vivo*, it is difficult to justify any one model membrane composition. Thus the ethos of going from an *in vivo* membrane to a computational model is one of simplification. Therefore any phospholipid that made up less than $< 1\%$ of a leaflet or membrane was ignored. The upper leaflet of the OM was modelled as an LPS monolayer LPS, while the lower leaflet and inner membrane were a mixture of PE, PG and CDL. The model of LPS used in this work was comprised of lipid A with 6 lipid tails and R3 core sugars, as this was the most

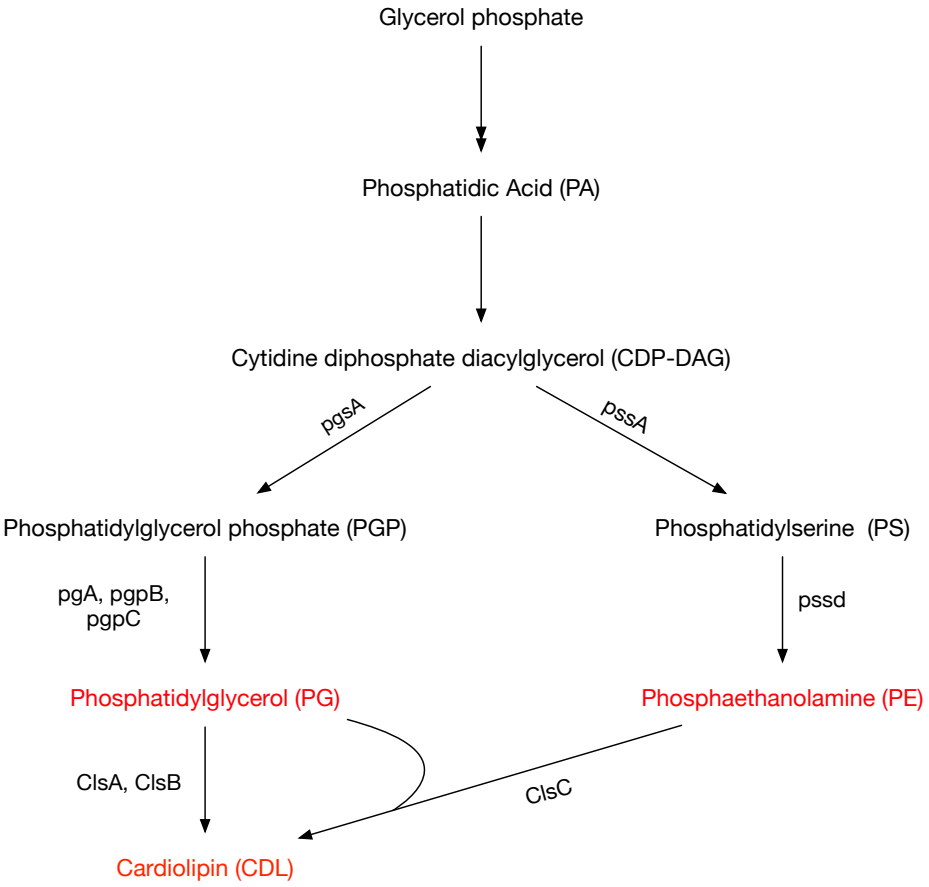

FIGURE 1.4: Figure showing the metabolic pathways of lipids in *E. coli*. The lipids with the most abundance in the cell envelope are highlighted in red; for chemical structures of these lipids see Figure 1.3. Abbreviations are as follows: cardiolipin synthasase (Cls), phosphatidylglycerol phosphate synthase (pgs), phosphatidylglycerol phosphate phosphatase (pgp), phosphatidylserine decarboxylase (psd) and phosphatidylserine synthase (pss). Note that this figure was adapted from a previous paper[14].

common LPS structure in virulent extraintestinal *E.coli* [34]. The composition of the inner leaflet of the model outer membrane was 90 % 6:0,18:1 phosphoethanolamine (POPE), 5 % 16:0,18:1 Phosphatidylglycerol (POPG) and 5 % 18:1,18:1 / 18:1,18:1 cardiolipin (see Figure 1.3 for chemical structure). The membrane composition and levels of tail unsaturation were based on previous computational and experimental studies of *E.coli* [7, 35]. The composition of the inner membrane was based on previously carried out atomistic simulations[36]: 75% POPE, 20% POPG and 5% CDL.

1.6 Membrane Proteins and the Membrane

Membrane proteins can be broadly divided in two categories, integral and peripheral proteins. Peripheral proteins do not interact with the hydrophobic core of the membrane and lie on the polar/charged surface of the membrane. Whereas integral proteins

have at least one section that is embedded into the hydrophobic core of the membrane. Integral proteins can be further defined by how deeply they penetrate the membrane, and if they span the entire membrane they are referred to as transmembrane proteins (Figure 1.5). Although the OM and IM contain peripheral and intrinsic proteins, transmembrane proteins will be the focus of this work.

In the last 50 years our understanding of the cell envelope has advanced greatly. A popular model for the cell envelope 40 year ago was the fluid mosaic model[37]. In the fluid mosaic model the proteins are in low concentration and randomly distributed in the membrane. It was believed that these proteins were largely responsible for cell function, while the lipids were not important. Protein-lipid interactions were hypothesised to be a factor this model, but were labelled as a minor component of interactions. In more recent years it has been found that proteins make up to 25 % of the surface area of bacterial membranes[38]; this is far larger than the sparse concentrations that were previously predicted. Thus it can be inferred that protein-lipid interactions should be play a significant role in the cell envelope.

Lipids can be defined by their strength of interactions with a transmembrane protein (Figure 1.5). Lipids with no significant interactions with a protein are termed termed bulk lipids. Lipids that form a ring around a protein are termed annular lipids and have non-specific interactions with the protein[39]. Bound lipids form strong interactions with specific site/sites of a protein[40]. It has been reported experimentally that the dynamics of annular and bound lipids is significantly reduced compared to bulk lipids[41, 42]. Extensive molecular dynamics studies show that thee effects of a protein on the structure and dynamics of the membrane are usually restricted to a 3 nm and 6 nm radius around the protein, respectively. [40, 43, 44]. The 3 nm radius around a protein will be referred to as the annular region during this work.

Before going into any more depth on the breadth of different protein-lipid interactions, first the nature of transmembrane protein interactions should be discussed in more detail. Transmembrane proteins span the membrane as both ends have lots of polar and charged residues, while the core of the protein is largely nonpolar. At the interfaces between the polar and hydrophobic domains of α-helical and β-barrel membrane proteins, two rings of aromatic residues have been observed in experimental and computational studies[45–47]. It is widely believed that these aromatic residues form preferential interactions with the lipid headgroups and are thus key in determining the orientation of the protein in the membrane[48, 49]. Trp and Tyr are the residues thought to be the most important residues for the anchoring of a transmembrane protein[49, 50] at the lipid-water interface. The effects of aromatic residues on the orientation of transmembrane proteins has been explored in both experimental[46, 51] and computational studies[52].

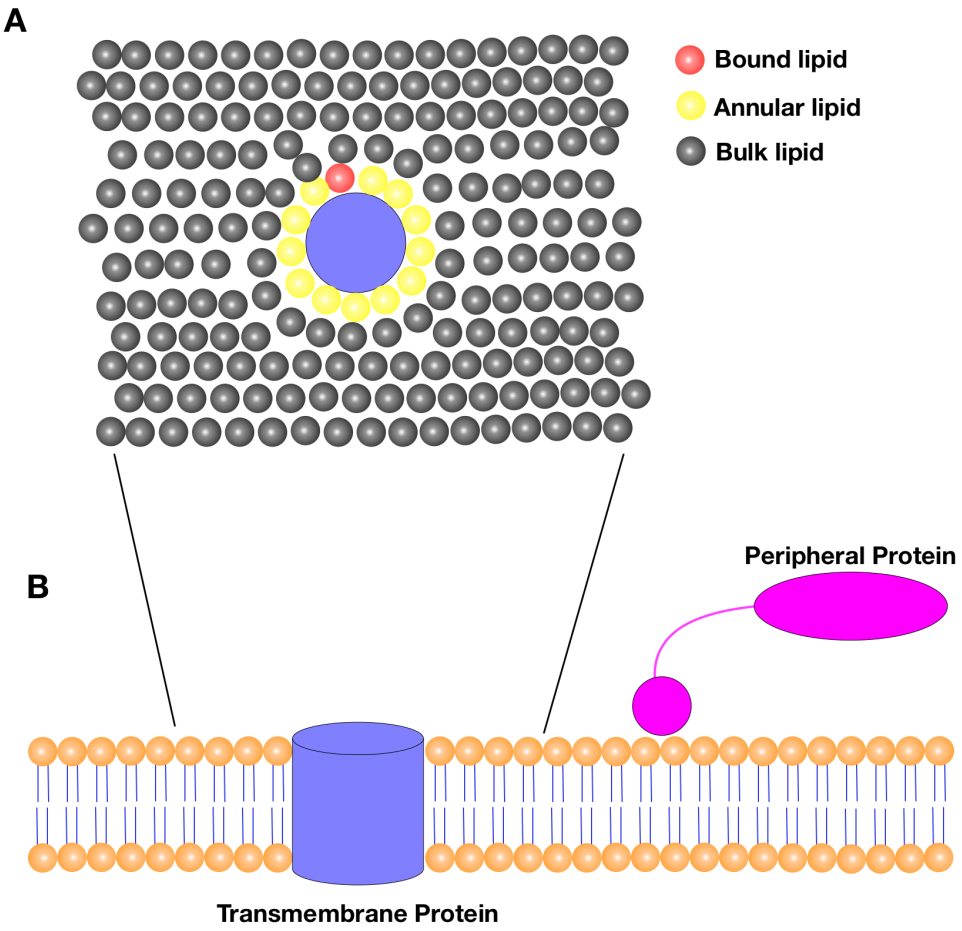

FIGURE 1.5: A) Diagram of bound (red), annular (yellow) and bulk (gray) lipids around a transmembrane protein (blue) from a top-down view. B) Diagram of a phospholipid (orange) membrane and the positions of a membrane protein (blue) and peripheral protein (purple) relative to the membrane.

When the hydrophobic core of a transmembrane protein and a membrane are different lengths, this is termed hydrophobic mismatch. There is no singular response to hydrophobic mismatch[54]. In some systems the lipids around the protein will adjust their structure in order to change the local membrane thickness and in turn minimise hydrophobic mismatch[55, 56]. In membranes with multiple lipids, the hydrophobic mismatch can be minimized through the formation of lipid domains that gives the ideal membrane thickness or curvature[57, 58]. The formation of local lipid domains, with compositions different to that of the bulk membrane, is often referred to as 'lipid sorting'. Protein meditated membrane thicknesses and curvatures are well documented in the literature[56, 59, 60]. If two membrane proteins get close to each other the overlap of their local effects on curvature and thickness has been found to drive oligmerisation of proteins[55, 56].

Hydrophobic mismatch can also cause changes in protein structure and orientation to

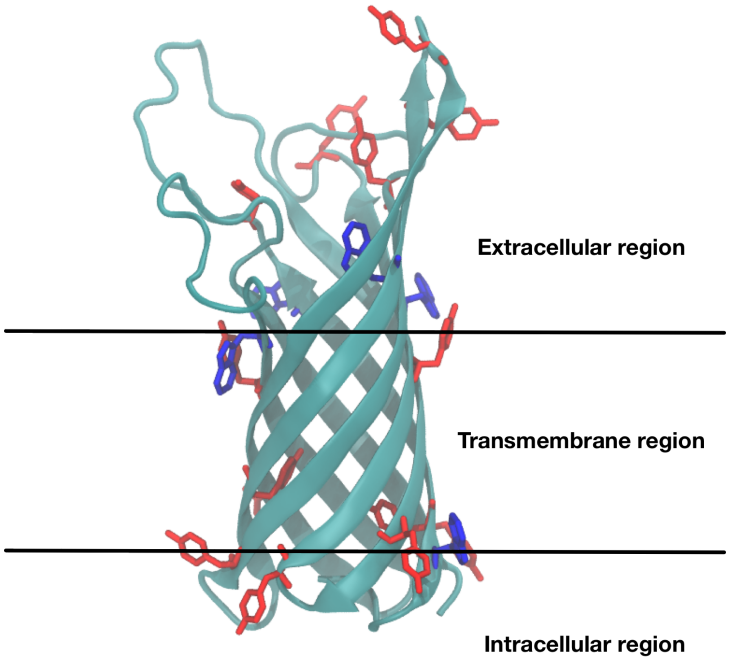

FIGURE 1.6: Diagram of OmpA (pdb code 1QJP [53]) with aromatic residues tyrosine (blue) and tryptophan (red) highlighted. Horizontal dividing lines are drawn to show the transmembrane region of this protein.

occur. In the case of smaller membrane proteins, hydrophobic mismatch usually causes the protein to tilt with respect to the membrane. Protein tilt is a frequently measured parameter in membrane protein studies[54, 60, 61]. For mechanosensitive ion channels such as MscL, tilting can trigger conformational changes in the protein to active or inactive states[60, 62–64]. For larger proteins, tilting can be thermodynamically unfavorable [65] and so the lateral sorting of lipids or proteins to minimise hydrophobic mismatch is preferred[66]. Certain proteins are also responsible for the regulation of asymmetric membrane compositions[67–69].

While proteins can affect lipid organisation, lipids can also modulate protein function. Often only certain lipids can modulate a protein's function. One such example is aquaporin (AqpZ), a water efflux pump in the inner membrane of *E. coli*[70], which preferentially binds to cardiolipin. When the membrane is cardiolipin deficient the water flux through AqpZ has been found to be significantly reduced[71]. This example is far from an isolated case and there are numerous other examples where it is believed that a particular lipid modulates the function of a protein [72–75] or specifically binds to a particular protein[75–78].

1.7 Outer Membrane Proteins

The class of proteins focused on in this work are outer membrane proteins (Omps). Interestingly, all transmembrane Omps are beta barrels, while inner membrane proteins are generally alpha helices[79]. The sizes of Omp monomers range from $8 - 22$ beta strands and some Omps are known to oligomerize, giving a wide range of protein sizes in the OM[79]. Omps perform a variety of roles in the OM from allowing small molecules across the OM to modifying lipids or signaling. Some integral proteins function as efflux channels that expel certain molecules (e.g. drug molecules) from the cell. One such example is the multi-drug efflux pump AcrABZ-Tol, that spans the OM and IM (Figure 1.2)[80]. It is thought that Omps are synthesised in the cytoplasm and are then translocated in an unfolded state across the IM, and into the periplasm[81]. The proteins then diffuse through the periplasm to the OM where it they inserted into the OM with the beta-barrel assembly complex (BAM). The BAM complex is also involved in the optimisation of Omp folding. Further details on the biogenesis of Omps and the workings of the BAM complex have been discussed at length elsewhere[82].

One of the most abundant transmembrane proteins in the OM is OmpA. OmpA is an 8 stranded beta-barrel that has a number of functions in the outer membrane. OmpA has two domains, the membrane domain (170 residues, N-terminal domain Figure 1.6) and the periplasmic domain (155 residues, C-termal domain)[79]. OmpA has been found to improve the structural stability of the outer membrane[53, 83]. Furthermore, the intracellular domain is widely believed to provide non-covalent binding to the PGN layer[84]. There has also been a lot of debate in the literature on whether OmpA is a pore or not[85–87]. Most experimental and computational studies show OmpA as a monomer beta barrel, but recent experimental work suggested the existence of a dimer form that may further stabilise OmpA[88].

1.8 Outer Membrane Simulations: A Brief Review

Molecular dynamics (MD) simulations have been shown to provide insights into the structure and dynamics of biomolecular systems. LPS is a complicated biomolecule that can have up to three sections, and is many times larger than most lipids. Moreover, the parameterisation of polysaccharides is a difficult problem within the MD community. Thus the development and validation of LPS models has proved challenging. The first asymmetric OM was simulated by R.Lins *et.al*[89] and was of a RaLPS all-atom membrane of *Pseudomonas aeruginosa*. Subsequently, a range of all-atom and united atom models have been developed for Re[35, 90], Ra[91] and smooth LPS[92]. The majority of studies of LPS have focused on LPS models of *Pseudomonas aeruginosa* and *E.coli*[35,

90–93]. Coarse-grained models for LPS in *Pseudomonas aeruginosa*[94] and *E.coli*[95] have been developed to extend the time and length scales available to computational studies of the outer membrane. In more recent years, the generation of OM membranes at the all-atom and coarse-grained levels has been trivialised by the CHARMM-GUI web interface[96–99], which allows the initial coordinates and the forcefield files to be generated within a few minutes.

Initial models of the lower leaflet of the OM were comprised of solely PE lipids[89, 91]. Studies of IM systems have demonstrated the importance of the heterogeneity of membrane compositions, in particular, for identifying protein induced lipid sorting[100, 101]. Thus in more recent simulations of the OM, the lower leaflet has been comprised of a mixture of PE, PG and CDL[90, 102, 103].

Simulation studies have confirmed experimentally known properties of LPS, such as a preference for divalent cations and slow diffusion compared to phospholipids[35]. This is not surprising as LPS models are fitted to reproduce the available structural data from experiments[91]. MD simulations have also been used to provide new insights into the importance of the asymmetry of the OM. Umbrella sampling simulations of the permeation of small molecules across an RaLPS OM (*E. coli*), found that the free energy profile was asymmetric across the OM[90]. LPS provided a substantial barrier to organic compounds (up to $\sim$ 6 $kcal^{-1}mol^{-1}$), however there was no barrier to entry from the intracellular side of the membrane.

It is widely known that protein function can be modulated by the surrounding lipids. Thus it was of interest to study protein-lipid interactions, in the environment of OM models. One example that highlighted the importance of LPS, when considering *in vivo* Omp interactions, was shown by simulations of FecA in an *E. coli* OM model[103]. Comparison of simulations of FecA in the OM and a simple phospholipid membrane, showed that the conformational dynamics of the loops in FecA were greatly affected by the presence of LPS. The permeability of porins, such as OmpF, have also been shown to be inversely proportional to the size of LPS in the extracellular domain[93]. In summary, the consideration of the lipid environment of an Omp is key in elucidating the correct protein structure and dynamics *in vivo*.

1.9 Aims

The long terms goals of this project are to further the understanding of the Gram-negative envelope, with the eventual goal of putting this knowledge into the fight against

superbugs. This is a rather nebulous and broad goal, for which the level of understanding required is not known. Previous simulations have studied Omps, but usually in symmetric membrane models that are not close to the *in vivo* environment[43, 104]. Work within and outside the Khalid group has shown the large differences in membrane and protein behaviour in OM models, compared to symmetric membranes[35, 103, 105, 106]. This thesis focused on furthering the understanding of complexity in the Gram-Negative bacterial cell envelope, both in terms of the membrane model and inclusion of a variety of proteins and nanopores. The time required for convergence of OM properties is often much larger than phospholipid systems[91]. Thus coarse-grained models of the OM will be used to access the time and length scales relevant to answering the questions posed in the coming chapters. The following chapters can be summarised as follows:

- Chapter 2: To give an overview of the theory of molecular dynamics and other important facets of simulation techniques and analysis methods.
- Chapter 3: To ascertain how nanopore chemistry, shape and size affect the local structure and dynamics in symmetric and OM membrane models.
- Chapter 4: Building on the previous chapter, the effects of OM model complexity and LPS type were to be investigated across proteins of a variety of sizes and functions.
- Chapter 5: The ease of lipid extraction from the OM and crowded IMs was to be explored.
- Chapter 6: The use of spare LPS concentrations and Hamiltonian Replica Exhange were to be applied to increase the speed LPS dynamics within the membrane.

Chapter 2

Methods

2.1 Molecular Dynamics

There is so much that is not known about biological systems and a lot of these issues stem from the fact that experimental techniques often have difficulty analysing processes on the molecular level at small timescales (< ns). Simulations can patch this blind spot through the use of molecular dynamics (MD). In MD simulations an atom or groups of atoms are represented by a point. For each particle its position in the potential energy surface (PES) of a system and thus the force, $\boldsymbol{F}_i$, that it experiences can be determined (this will be discussed later),

$$\boldsymbol{F}_i = -\frac{dV(\boldsymbol{r}^N)}{d\boldsymbol{r}_i} \tag{2.1}$$

where $V(\boldsymbol{r}^N)$ is the PES of N particles and $\boldsymbol{r}_i$ is the position of a single particle. The positions of each particle can be evolved with respect to time, t, using Newtonian dynamics (Equation (2.2)),

$$\boldsymbol{F}_i = m_i \frac{d^2\boldsymbol{r_i}}{dt^2} \tag{2.2}$$

where m_i is the mass of a particle. Ideally these equations should be solved analytically, however for a system larger than two particles Newton's equations of motion become unsolvable. Instead these equations can be numerically integrated using the finite difference method, which involves discretised differential equations. Thus the system can be evolved through time using discrete intervals, dt, referred to as the timestep of the simulation. The general workings of an MD program are outlined in Figure 2.1 and will be explained in detail later in this chapter.

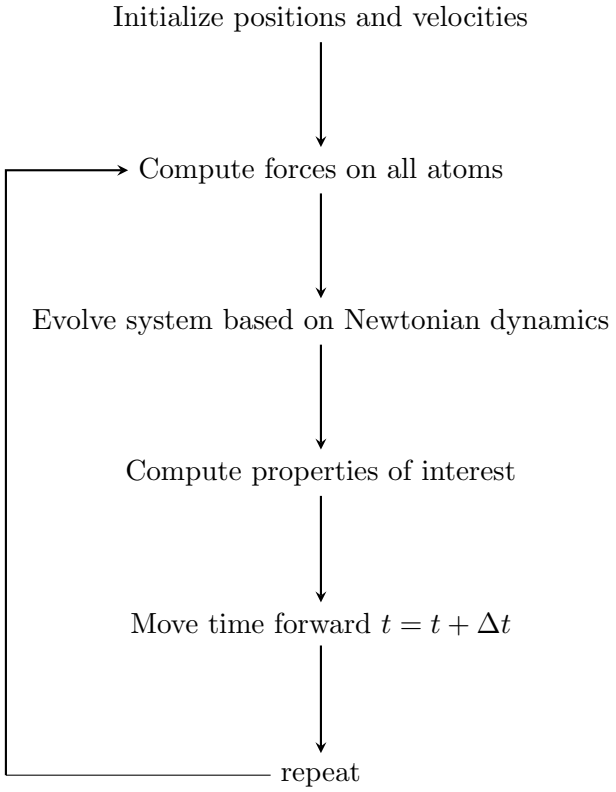

FIGURE 2.1: A scheme of a simplified Molecular Dynamics algorithm, where Δt is the timestep of the simulation

2.2 Integrators

As discussed in the previous section, Newton's equation of motion must be solved numerically to evolve a system through time. The method used to integrate these equations of motions is termed the *integrator*. In MD we can gain the average for a property of an ensemble via an average across an MD simulation, as stated by the Ergodic hypothesis: an average across time of an ergodic system is equivalent to the ensemble average. The integrator does not need to exactly reproduce the true trajectory, it only needs to reproduce the correct statistical properties of the ensemble. There are a few conditions that an integrator must fulfill given that they are true for Newton's equations of motion: 1) An integrator should approximately conserve energy (1st law of thermodynamics) and 2) should be time reversible. In the case of MD time reversibility mean that moving forward two timesteps and then back two timesteps should result in the original positions. Time reversibility does not hold true in the limit of long simulations for any integrator, due to numerical errors inherent to computational methods.

The integrator used in this work is the leap frog integrator[107]. The leap frog integrator is based on the Verlet integrator[108], which can be derived through a Taylor expansion of Newton's equations of motion,

$$\boldsymbol{r}_i(t+\delta t) = \boldsymbol{r}_i(t) + \frac{\boldsymbol{r}_i(t)}{\delta t}\delta t + \frac{1}{2}\frac{\delta^2 \boldsymbol{r}_i(t)}{\delta t^2}\delta t^2 + \frac{1}{6}\frac{\delta^3 \boldsymbol{r}_i(t)}{\delta t^3}\delta t^3 + O(\delta t^4) \tag{2.3}$$

If we substitute in equations 2.1 and 2.2, we get

$$\boldsymbol{r}_i(t+\delta t) = \boldsymbol{r}_i(t) + \boldsymbol{v}_i(t)\delta t + \frac{\boldsymbol{f}_i(t)}{2m_i}\delta t^2 + \frac{1}{6}\frac{\delta^3 \boldsymbol{r}_i(t)}{\delta t^3}\delta t^3 + O(\delta t^4) \tag{2.4}$$

and then moving back two intervals of δt.

$$\boldsymbol{r}_i(t-\delta t) = \boldsymbol{r}_i(t) - \boldsymbol{v}_i(t)\delta t + \frac{\boldsymbol{f}_i(t)}{2m_i}\delta t^2 - \frac{1}{6}\frac{\delta^3 \boldsymbol{r}_i(t)}{\delta t^3}\delta t^3 + O(\delta t^4) \tag{2.5}$$

Following this Equations (2.4) and (2.5) can be added together to give,

$$\boldsymbol{r}_i(t+\delta t) = 2\boldsymbol{r}_i(t) - \boldsymbol{r}_i(t-\delta t) + \frac{f_i(t)}{m_i}\delta t^2 + O(\delta t^4) \tag{2.6}$$

which is the Verlet scheme and the positions are accurate to $O(\delta t^3)$. Equation (2.6) does not include the velocities, which are important for the calculation of the kinetic energy and temperature. The velocities can be obtained by subtracting Equation (2.5) from Equation (2.4) to give Equation (2.7).

$$\boldsymbol{v}_i(t) = \frac{1}{2\delta t}\left[\boldsymbol{r}_i(t+\delta t) - \boldsymbol{r}_i(t-\delta t)\right] + O(\delta t^2) \tag{2.7}$$

Now the Leapfrog algorithm can be derived from the Verlet scheme by defining the velocities at half steps of δt

$$\boldsymbol{v}_i(t-\frac{\delta t}{2}) = \frac{\boldsymbol{r}_i(t) - \boldsymbol{r}_i(t-\delta t)}{\delta t} \tag{2.8}$$

and

$$\boldsymbol{v}_i(t+\frac{\delta t}{2}) = \frac{\boldsymbol{r}_i(t+\delta t) - \boldsymbol{r}_i(t)}{\delta t} \tag{2.9}$$

By rearranging equation 2.9 an expression can be obtained for the new positions, as a function of the old positions and velocities:

$$\boldsymbol{r}_i(t+\delta t) = \boldsymbol{r}_i(t) + \boldsymbol{v}_i(t+\frac{\delta t}{2})\delta t \tag{2.10}$$

We then subtract Equation (2.8) from Equation (2.9) and substitute in Equation (2.6) to get:

$$\boldsymbol{v}_i(t+\frac{\delta t}{2}) = \boldsymbol{v}_i(t-\frac{\delta t}{2}) + \frac{\boldsymbol{f}_i(t)}{m_i}\delta t \tag{2.11}$$

The velocities are calculated half a step after the positions and thus the positions 'leap frog' over the velocities. The value of the timestep, δt, is essential to produce plausible dynamics for a given system. If the timestep is too large this will result in energetically unfavourable collisions and eventually the system will explode. Conversely, if the

timestep is too small this would be a waste of computational resources. As a rule of thumb the timestep should be set to be at least an order of magnitude smaller than the fastest motion expected in the system.

2.3 Force Fields

When determining the force on any atom there are a few levels of detail molecular system can be modelled with: quantum mechanics (QM), atomistic and coarse grained. At the QM level of theory an atom is represented by a nucleus and its surrounding electrons. To determine the force on any atom the Schrodinger equation must be solved, which can be very computationally expensive. QM MD gives chemically accurate energies, but cannot be applied to systems larger than 20,000 atoms for more than a few picoseconds. To access larger length and timescales a system can be modelled using a classical molecular mechanics (MM) force field.

An MM force field describes a collection of potential energy functions that are used to determine the potential energy of a particle at a given point in space and is dependent on the positions of every particle $\boldsymbol{r}^N$. Here a particle could be either a single atom or a collection of atoms. The total potential energy of a particle i, $V_i(\boldsymbol{r})$, is made up of the summation all non-bonded and bonded terms. The bonded potential energy includes

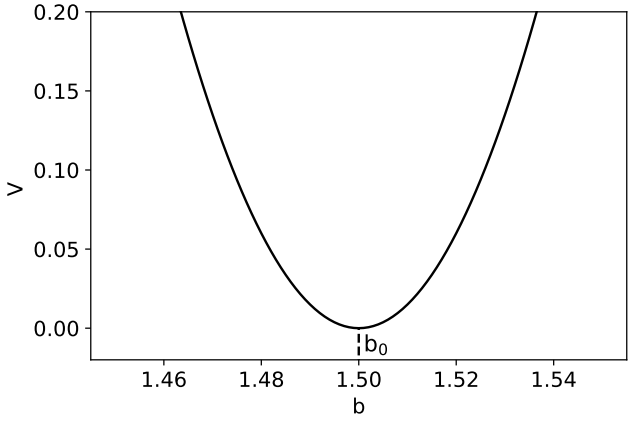

FIGURE 2.2: Plot of the form of a harmonic oscillator (see Equation (2.13)) which represents the potential, V, of a bond of length b

terms for bonds, angles and dihedrals,

$$V_{bonded} = V_{bonds} + V_{angles} + V_{dihedrals} + V_{impropers} \tag{2.12}$$

which force restraints on bonds etc within molecules. The bonds and angles are modelled as harmonic oscillators, centred on equilibrium values of b_0 and θ_0, respectively

$$V_{bonds} = \sum_{bonds} \frac{1}{2} k_b (b - b_0)^2 \tag{2.13}$$

$$V_{angles} = \sum_{angles} \frac{1}{2} k_\theta (\theta - \theta_0)^2 \tag{2.14}$$

where k_b and k_θ are spring constants. These spring constants determine the strength of the bonded terms.

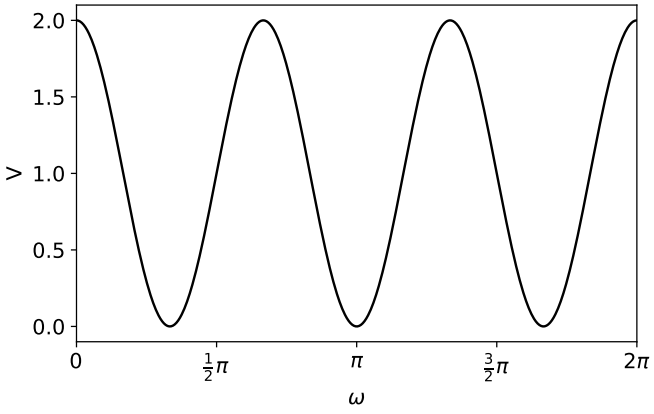

FIGURE 2.3: Plot of the form of the dihedral term (Equation (2.15)) where $n = 3$.

The dihedral term describes the rotation of two groups around a covalent bond. Unlike bond and angle terms, there are multiple minima for dihedral potentials and they are usually modelled as a sum of cosine functions

$$V_{dihedrals} = \sum_{dihedrals} k_\omega (1 + cos(n\omega - \omega_0)) \tag{2.15}$$

where k_ω is the dihedral force constant, n is the periodicity of the term and ω_0 the phase shift. Improper dihedrals are used to enforce the planarity of functional groups such as carbonyls. Improper dihedrals are represented using a harmonic potential,

$$V_{impropers} = \sum_{impropers} \frac{1}{2} k_\gamma (\gamma - \gamma_0)^2 \tag{2.16}$$

where k_γ is the out of plane force force constant and γ is the out of plane torsional angle.

The non-bonded term for the ith particle is comprised of the Van der Waals (VdW) and electrostatics terms, which are represented by the Lennard-Jones (LJ) and Coulombic

potentials, respectively, and are summed over all N atoms,

$$V_{i,nonbonded} = V_{i,elec} + V_{i,vdw} = \sum_{j}^{N} \frac{q_i q_j}{4\pi\epsilon_0 r_{ij}} + 4\epsilon \sum_{j}^{N} \left(\left(\frac{\sigma}{r_{ij}} \right)^{12} - \left(\frac{\sigma}{r_{ij}} \right)^{6} \right) \tag{2.17}$$

where q is a particles charge, ϵ_0 is the permittivity of free space, r_{ij} is the distance between two atoms, ϵ and σ are constants. In terms of physical relevance ϵ is the well depth of the function and sets the strength of the interaction, while σ corresponds to the pair wise distance r_{ij} where $V_{i,vdw}(r_{ij}) = 0$. The r^{-12} term describes short range repulsion between atoms, while the r^{-6} terms models the attractive dispersion interactions (Figure 2.4). It is important to note that $i \neq j$ during the summation of the non-bonded potential energy.

How a force field is parametrised depends on the level of resolution of the model. Atomistic models are usually parametrised through comparison to properties obtained from QM or experimental calculations e.g. bond lengths, frequencies and free energies of partition.

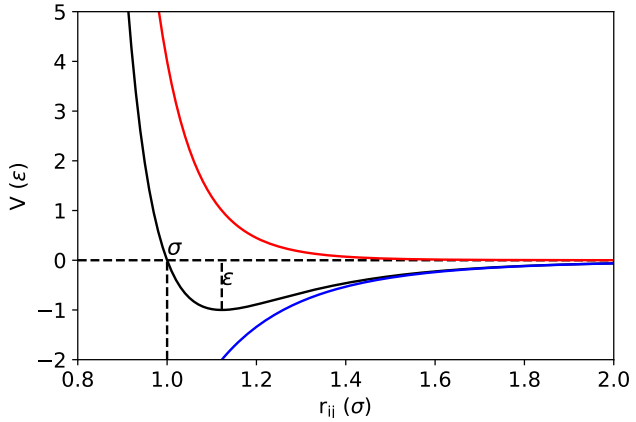

FIGURE 2.4: Form of the Lennard Jones potential, where the black line is the total potential (Equation (2.17)) while the red and blue lines are the attractive and repulsive terms, respectively.

2.3.1 Coarse-grained Molecular Dynamics

There are multiple levels of detail with which a molecule can be modelled using classical forcefields. In the fully atomistic model (AA) each atom is represented by a point and in the united atom (UA) model the aliphatic hydrogens are ignored. To further reduce the resolution of the model multiple atoms can be grouped into a single particle, this is referred to as a coarse grained (CG) model. The number of atoms to map to a CG particle is not fixed; in some CG force fields a particle only represents a few atoms, while

in others it may represent a tertiary domain of a protein.

By coarse-graining a system the speed of the subsequent MD simulation can be increased by a few orders of magnitude. The speed up for a given system depends on a number of factors: 1) There are fewer particles so calculating changes in position for each timestep is faster. 2) The coarse-graining of molecules simplifies the energy landscape, resulting in faster sampling of a system's phase space. The simplification of the PES also allows a larger timestep (20 fs) to be used, compared to AA/UA simulations (2 fs), without any unrealistic collisions occurring.

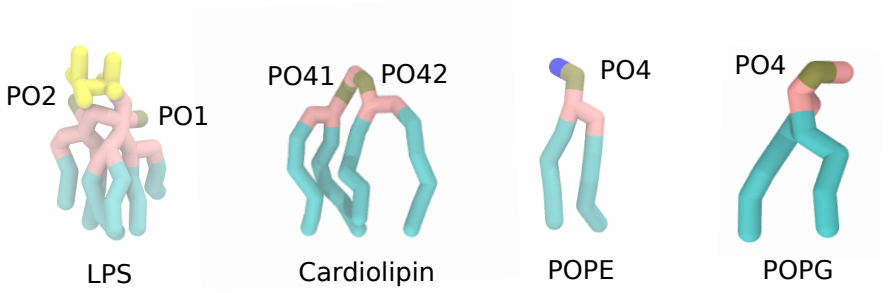

FIGURE 2.5: Diagrams of the martini model representations of some of the lipids studied in this report. The phosphate beads are a golden colour and are labelled as they are in the Martini model. See Figure 1.3 for the chemical structures of all of these lipids.

In this thesis the CG force field used was called Martini (version 2.2)[109–112]. The Martini model maps four heavy atoms to one CG particle or 2:1 mapping for special type beads (e.g. rings). The model includes four types of interaction sites: polar, non polar, apolar and charged. The difference between apolar and nonpolar types is that the latter is miscible in organic solvents and water. In total there are 18 subtypes: hydrogen-bond capabilities are indicated by a letter (d=donor, a=acceptor, da=both and 0=none) and polarity of each interaction site is defined on a scale of 1(low) to 5(high). The interaction strength between two particle subtypes is set by an interaction matrix that can be found in the original paper[109] (see Table 2.1), that outputs an interaction level of O-IX. The interaction level defines the well depth ϵ used for the corresponding LJ term. The interaction size for all LJ terms was $\sigma = 0.47$ nm, except for the IX interaction level and special type beads. The LJ terms for each particle type were parameterised by matching to thermodynamic data, such as oil/water partition coefficients.

A lot of other coarse-grained models will use iterative boltzmann inversion[113, 114] or force matching [115] to determine the parameters for both the non-bonded and bonded terms. This results in a lack of transferability of any coarse-grained beads as a butane fragment in one molecule will not necessarily have the same non-bonded terms as in another very different chemical environment. Therefore a new CG model would need

TABLE 2.1: Level of interaction indicates the well depth in the LJ potential: O, $\epsilon = 5.6$ kJ/mol; I, $\epsilon = 5.0$ kJ/mol; II, $\epsilon = 4.5$ kJ/mol; III, $\epsilon = 4.0$ kJ/mol; IV, $\epsilon = 3.5$ kJ/mol; V, $\epsilon = 3.1$ kJ/mol; VI, $\epsilon = 2.7$ kJ/mol; VII, $\epsilon = 2.3$ kJ/mol; VIII, $\epsilon = 2.0$ kJ/mol; IX, $\epsilon = 2.0$ kJ/mol. The LJ parameter $\sigma = 0.47$ nm for all interaction levels except level IX for which $\sigma = 0.62$ nm. Four different CG sites are considered: charged (Q), polar (P), nonpolar (N), and apolar (C). Subscripts are used to further distinguish groups with different chemical nature: 0, no hydrogen-bonding capabilities are present; d, groups acting as hydrogen bond donor; a, groups acting as hydrogen bond acceptor; da, groups with both donor and acceptor options; 1-5, indicating increasing polar affinity. Reprinted with permission from S.J Marrinck, *J. Phys. Chem. B*, 2007, 111, 27, 7812-7824. Copyright 2007 American Chemical Society (Figure A.1).

		Q				P					N				C				
	sub	da	d	a	0	5	4	3	2	1	da	d	a	0	5	4	3	2	1
Q	da	O	O	O	II	O	O	O	I	I	I	I	I	IV	V	VI	VII	IX	IX
	d	O	I	O	II	O	O	O	I	I	I	III	I	IV	V	VI	VII	IX	IX
	a	O	O	I	II	O	O	O	I	I	I	I	III	IV	V	VI	VII	IX	IX
	0	II	II	II	IV	I	O	I	II	III	III	III	III	IV	V	VI	VII	IX	IX
P	5	O	O	O	I	O	O	O	O	O	I	I	I	IV	V	VI	VI	VII	VIII
	4	O	O	O	O	O	I	I	II	II	III	III	III	IV	V	VI	VI	VII	VIII
	3	O	O	O	I	O	I	I	II	II	II	II	II	IV	IV	V	V	VI	VII
	2	I	I	I	II	O	II	II	II	II	II	II	II	III	IV	IV	V	VI	VII
	1	I	I	I	III	O	II	II	II	II	II	II	II	III	IV	IV	IV	V	VI
N	da	I	I	I	III	I	III	II	II	II	II	II	II	IV	IV	V	VI	VI	VI
	d	I	III	I	III	I	III	II	II	II	II	III	II	IV	IV	V	VI	VI	VI
	a	I	I	III	III	I	III	II	II	II	II	II	III	IV	IV	V	VI	VI	VI
	0	IV	IV	IV	IV	IV	IV	IV	III	III	IV	IV	IV	IV	IV	IV	IV	V	VI
C	5	V	V	V	V	V	V	IV	IV	IV	IV	IV	IV	IV	IV	IV	IV	V	V
	4	VI	VI	VI	VI	VI	VI	V	IV	IV	V	V	V	IV	IV	IV	IV	V	V
	3	VII	VII	VII	VII	VI	VI	V	V	IV	VI	VI	VI	IV	IV	IV	IV	IV	IV
	2	IX	IX	IX	IX	VII	VII	VI	VI	V	VI	VI	VI	V	V	V	IV	IV	IV
	1	IX	IX	IX	IX	VIII	VIII	VII	VII	VI	VI	VI	VI	VI	V	V	IV	IV	IV

to be developed for every new molecular system studied, which can make setting up a CG system quite laborious. One of the great advantages of the Martini force field is the transferability of particle types that allow for the simplified construction of a wide variety of organic molecules, in solvents of varying properties. In particular Martini has been used a lot to simulate membrane systems and can reproduce a variety of physical properties from atomistic models and experimental data[43, 44, 116–119].

Martini is not without its own limitations, of which a few key ones are[109, 120]:

1. Martini performs poorly for solid or gas phase simulations.
2. The beads were parameterised with free energies that are themselves dependant on temperature. Thus the use of this forcefield outside the range of $270 - 330$ K has been discouraged by the developers.
3. The electrostatics are poor (will be discussed in Section 2.4.1).
4. Martini has no directional hydrogen bonding and therefore protein secondary structure cannot be maintained.

The issues with the secondary structure of Martini proteins was of particular importance to the work outlined here. There are two methods which are often used to maintain

the secondary structure of Martini proteins: elastic networks (ENs) and the ElNeDyn model[120]. In both cases an EN is used to restrain the protein structure, relative to a reference structure. The reference structure could be an experimental structure or a structure from atomistic simulations. In the first method harmonic restraints between backbone beads are added, up to a user set cutoff. The ElNeDyn model is quite similar to the first approach, but in this model the backbone beads are centred at the C-α position, instead of the centre of mass of the backbone of an amino acid. Harmonic restraints are then added between backbone beads within set cutoff of each other, only if they are separated by more than one position in the protein sequence. This approach has been found to lead to models that have been shown to be able to reproduce local and global deformation of proteins[120]. The parameters of the ElNeDyn model have been studied across a range of proteins and optimised to 500 $kJmol^{-1}nm^{-2}$ and 0.9 nm [120]. The ElNeDyn model was used for the majority of proteins studied in this work.

2.4 Periodic Boundary Conditions

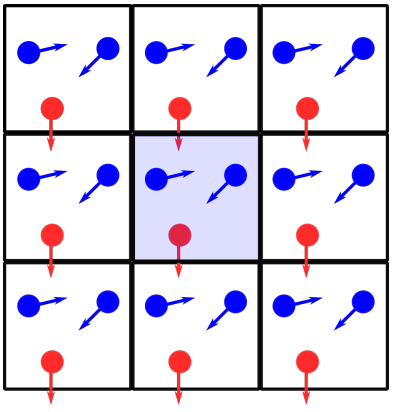

FIGURE 2.6: Diagram of the concept behind periodic boundary conditions in 2D. Note as the red sphere leaves one side of the box in enters on the other side. The shaded box is the primary simulation cell.

For MD, simulating a macroscopic system would be ideal. However, this is not computationally feasible and instead a much smaller number of particles is used. Periodic boundary conditions (PBC) can be used to allow a smaller system to mimic a macroscopic system. PBC involves treating the simulation cell as the primary unit in a lattice of infinitely replicated simulation cells, termed 'periodic images' (Figure 2.6). When a particle moves from the primary simulation cell into a periodic image, simultaneously the same particle re-enters the simulation cell from a different periodic image.

2.4.1 Cutoffs

Earlier it was mentioned that the non-bonded terms for a given particle are summed across all pairs in the system. This would be extremely expensive for larger systems and so the non-bonded interactions are ignored at longer distances (e.g. > 1.2 nm). The magnitude of VdW interactions scale as function of $\frac{1}{r^6}$, meaning that they have a negligible effect at longer distances. Electrostatic interactions scale as a function of $\frac{1}{r}$, and so are much larger at long distances. The long range electrostatics can be calculated much faster in reciprocal space, by using the Particle Mesh Ewald's (PME) method. Therefore most atomistic force fields use the PME method[121, 122] to model long range electrostatics.

In CG systems the use of the computationally expensive PME method is usually avoided, as CG electrostatics are known to be poor. In simulations with the Martini forcefield, the lack of solvent dipoles leads to unrealistic shielding of charge[123]. The lack of long-range electrostatics in CG simulations can result in artifacts in the force and potential energy at the cutoff distance. To remove the artifacts in force and energy, the reaction field method can be used[124]. The reaction field method models the long range electrostatics with the analytical solution of the PoissonBoltzmann equation and assumes a uniform dielectric constant. The advantage of this method is that it requires minimal computational cost to calculate and the resulting electrostatic energy function is continuous across the short-range cutoff. The reaction field method has been found to give better results for the CG model Martini, compared to ignoring the long range electrostatics, with a minimal increase in computational cost [125]. All of the simulations detailed here use the reaction field method, unless stated otherwise.

2.4.2 Neighbour lists

As discussed in Section 2.4.1, it is impractical to calculate pair-wise non-bonded interactions across the entire simulation cell and instead this is only done within a short range cutoff. However, whether an atom i is within the cutoff of atom j still has to be determined. To reduce this cost a Neighbour List[108] is constructed for each atom with a cutoff that is equal to or larger than the non-bonded cutoff; this neighbour list is then updated every n steps. If the update frequency is too low then the atoms in the neighbour list will move out of the cutoff range before the next update, which could result in unfavourable clashes; whereas if it is too high this will significantly slow down the simulation. In the simulations in this work, an update frequency of every 10 steps was used, unless stated otherwise.

2.5 Thermostats and Barostats

Biomolecular simulations involving membranes are carried out using Isobaric-Isothermal conditions, i.e constant number of particles, pressure and temperature, otherwise known as the NPT ensemble. The temperature for a given MD timestep can be obtained from the velocities of the particles

$$T = \frac{1}{3k_B N} \sum_{i}^{N} m_i v_i^2 \tag{2.18}$$

where k_B is the Boltzmann constant. Similarly the instantaneous pressure of the system can be determined from the pairwise forces

$$P = \rho k_B + \frac{1}{3V} \left\langle \sum_{i<j} f(r_{ij}).r_{ij} \right\rangle \tag{2.19}$$

where ρ is the density of the system and V is the volume of the simulation cell. To maintain the conditions of the NPT ensemble, thermostats and barostats are used to control temperature and pressure, respectively, to defined reference values.

To understand what properties a good barostat or thermostat should have, the exact definition of an ensemble must be explored. In statistical mechanics the ensemble is defined as a collection of a large number of virtual systems that replicate the macroscopic properties of the system of interest. A virtual state can be thought of as a configuration of the system i.e the state of one timestep of an MD simulation (positions, velocities, pressure etc). In fact in the NPT ensemble P and T are not constant, but their ensemble averages are constant. From the ergodic hypothesis it is known that the ensemble average of a property is the same as the average of that same property over a long period of time. Thus for an ideal barostat or thermostat:

1. The ensemble or time average should equal the reference value.
2. The distribution of values match the expected ensemble density of states.
3. Changes done by the thermostats do not disrupt system dynamics.

Three common thermostats are the Berendsen, stochastic velocity rescale and the Nose-Hoover thermostats. The Berendsen thermostat scales velocities proportional to the displacement of the instantaneous temperature from the reference value[126]. While the Berendsen thermostat allows for rapid corrections of temperature drifts, it does not maintain the ensemble, and thus is usually only used for the initial equilibration step. The stochastic velocity rescale thermostat builds on the Berendsen method and adds an additional stochastic term that scales the velocities using a kinetic energy drawn from the Maxwell-Boltzmann distribution[127]. This method does maintain the ensemble, but

the random drawing of kinetic energies can result in unrealistic jumps in the dynamics. The Nose-Hoover thermostat adds an extra term to the equations of motion, which acts as a friction term[128–130]. By definition this thermostat samples the ensemble and does not result in any unrealistic dynamics. However, such accuracy comes at the cost of expensive computation and very slow equilibration to the ensemble average.

Barostats work by altering the volume of the simulation box to control the pressure. The Berendsen and Nose-Hoover barostats work in a similar manner to their thermostat counterparts and thus have the same advantages and disadvantages as described previously. A barostat that scales all box lengths by the same amount is referred to as a isotropic barostat. In systems with lipid bilayers the stress parallel and perpendicular to the membrane surface are very different. Thus it is common to use a semi-isotropic barostat to control the pressure in a system with a lipid bilayer. For a semi-isotropic barostat the changes of box length in the x and y dimensions (the plane of the membrane) are the same, but independent to box changes in the z dimension. The Parinello-Raham barostat is an extension of the Nose-Hoover barostat that allows pressure coupling to be applied separately to each dimension of the simulation cell.

2.6 Enhanced Sampling

In an MD simulation the length scales and timescales of simulations are limited by the available computational power. MD simulations sample the phase space of the PES of the system and thus in theory the entire PES could be sampled, if given enough time. The PES of a system often contain a lot of barriers that are difficult to traverse on the timescales of an unbiased simulation. To overcome such issues many enhanced sampling techniques have been developed to allow the accelerated sampling of phase space.

2.6.1 Umbrella Sampling

One popular enhanced sampling method is umbrella sampling (US)[131, 132]. Umbrella sampling involves the simulation of a number of "windows", N_w, in which the molecule of interest is restrained by an additional bias along a reaction coordinate ξ. Typically each window, i, is restrained by a harmonic bias,

$$U_i(\xi) = \frac{k_i}{2}(\xi - \xi_i) \tag{2.20}$$

of strength k_i at ξ_i and then the system is sampled perpendicular to the reaction coordinate. The probability distribution along the reaction coordinate with respect to the biased simulations, p_{bias}, can be determined. However, what we really want to obtain is the probability of finding the molecule at any point of the reaction coordinate in the

unbiased simulation. The unbiased probability distribution $P(\xi)$ can be obtained using the Weighted Histogram Analysis Method (WHAM)[133, 134]. WHAM is defined in the following manner[134, 135]:

$$P(\xi) = \frac{\sum_{i=1}^{N_w} g_i^{-1} h_i(\xi)}{\sum_{j=1}^{N_w} n_j g_j^{-1} exp[-\beta(U_j(\xi) - f_j)]} \tag{2.21}$$

and

$$exp(-\beta f_j) = \int d\xi exp[-\beta U_j(\xi)] P(\xi) \tag{2.22}$$

Here, $h_i(\xi)$ denotes the histogram of the biased simulation, n_j the number of data points in each window and β is $1/k_B T$, where k_B is the Boltzmann constant and T is temperature. The statistical inefficiency of a window, g_i, can be determined from the autocorrelation time τ_i, $g_i = 1 + 2\tau_i$. The autocorrelation time is often approximated by taking the integral of the autocorrelation function $ACF(\Delta t)$ with lag time Δt

$$\tau = \sum_{\Delta t} ACF(\Delta t) \tag{2.23}$$

while $ACF(\Delta t) > 0$. A lower weight is given to windows with greater integrated autocorrelation times (IACT) in Equation (2.21). There are two unknown variables in Equation (2.21), the free energy constants of each window f_j and $P(\xi)$. These equations are solved iteratively, using initial guesses for f_j which are put into Equation (2.21) to get $P(\xi)$. Then the initial value of $P(\xi)$ is used to get another set of f_j and this process is repeated until a set convergence threshold is reached.

The potential mean force (PMF) profile is the free energy profile along ξ. The PMF can be defined as $W(\xi) = k_B T ln[P(\xi)/P(\xi_0)]$, where xi_0 is a reference point which is set to have zero free energy. Thus the free energies of a PMF are always relative free energies.

The error in the PMF can be found through a variety of bootstrapping methods. Bootstrapping techniques work by taking a data set, d, with n values and generating a number of new data sets, each of size n. The probability a given value, d_i, is put into a new data set is $1/n$. In the context of umbrella sampling, a data set is a trajectory of ξ values. For each new trajectory generated via bootstrapping a PMF can be calculated. The average and standard deviation along ξ for all generated PMFs results in an average profile along with an uncertainty as a function of ξ. However, the probability of each value being selected does not have to be equal and this is the core of the Bayesian bootstrap method. In the Bayesian method, each value in a data set has a random probability (instead of $1/n$) of being selected for a new data set. The IACT of each umbrella window can also be used to generate a bootstrapped trajectories that account for autocorrelation between values.

2.6.2 Multistate Bennett Acceptance Ratio

The multistate bennett acceptance ratio (MBAR) is a free energy estimator that is equivalent to WHAM in the limit of infinitely small bin size and is thus terms a 'binless' free energy estimator[136]. One of the advantages of MBAR over WHAM is that it provides a direct estimation of uncertainties. MBAR allows for the determination of the free energy difference between multiple thermodynamic states and is equivalent to its predecessor, BAR, when there are only two sampled states. To derive MBAR, there must be a total of N_i uncorrelated states, which span a total of K states within the same ensemble (e.g. NPT). The reduced potential energy of a state i, $u_i(\mathbf{x})$, can be defined as[136],

$$u_i(\mathbf{x}) = \beta(U_i(\mathbf{x}) + p_i V(\mathbf{x}) + \mu_i^T \mathbf{n}(\mathbf{x})) \tag{2.24}$$

where $\mathbf{x}$ is a point in configurational space, $V(\mathbf{x})$ is the fixed volume (for NPT) and $\mathbf{n}(\mathbf{x})$ the number of molecules in each component of the system (for Grand canonical ensemble). For every state i there is an inverse temperature, β_i, an external pressure, p_i and a vector of chemical potential energies μ_i^T for each component of the system.

The reduced free energy difference between two states i and j takes the form,

$$\Delta f_{ij} = f_j - f_i = -\ ln\left(\frac{Q_j}{Q_i}\right) \tag{2.25}$$

where Q_i is the partition function of state i. The estimate for the dimensionless free energy, according to MBAR is,

$$\hat{f}_i = -ln \sum_{j=1}^{K} \sum_{n=1}^{N_j} \frac{exp(-u_i(\mathbf{x}_{jn}))}{\sum_{k=1}^{K} N_k exp(\hat{f}_k - u_k(\mathbf{x}_{jn}))}\ , \tag{2.26}$$

which can be solved self-consistently to calculate $\hat{f}_i$ (guess $\hat{f}_i$ to get all f_k). The free energy is then compared to a reference state to calculate the reduced free energy difference $\hat{f}_{ij} = \hat{f}_j - \hat{f}_j$. The uncertainty in the free energy difference can be determined from a covariance matrix,

$$\delta^2 \Delta \hat{f}_{ij} \equiv cov\left(-ln\frac{\hat{Q}_j}{\hat{Q}_i}, -ln\frac{\hat{Q}_j}{\hat{Q}_i}\right) = \hat{\Theta}_{ii} - 2\hat{\Theta}_{ij} + \hat{\Theta}_{jj} \tag{2.27}$$

where $\hat{\Theta}_{ij} = cov(ln\ Q_i, ln\ Q_j)$. Further details on the estimation of the uncertainty can be found in the original MBAR paper[136].

To calculate the PMF of an US simulation using MBAR, there are a few steps that must be followed. Each state k, corresponds to an umbrella window and so the reduced potential of a state can be simplified to,

$$u_k(\mathbf{x}) = \beta_k(U_0(\mathbf{x}) + U_k^{bias}(\mathbf{x})) \tag{2.28}$$

, where $U_0(\mathbf{x})$ and $U_k^{bias}(\mathbf{x})$ are the potential energies of the original system and the bias, respectively. The unknown term $U_0(\mathbf{x})$ cancels out when determining the free energy difference $\hat{f}_{ij}$ and so can be ignored. The probability of finding the system in PMF bin i can be written as

$$p_i = \langle \chi_i(\mathbf{x}) \rangle \tag{2.29}$$

, where $\chi_i(\mathbf{x})$ is a step function that equals 1 if $\mathbf{x}$ is in bin i and 0 in all other cases. The probability can then be written as,

$$p_i = \sum_{n=1}^{N} \hat{Q}_a^{-1} \frac{exp(-u_n(\mathbf{x}_n))}{\sum_{k=1}^{K} N_k exp(\hat{f}_k - u_k(\mathbf{x}_n))} \chi_n(\mathbf{x}_n) \ , \tag{2.30}$$

where Q_a is the partition function of all K umbrella windows. One powerful element to MBAR is that p_i can be calculated directly from the solutions to Equation (2.26), with no need for addition iterative solving of self-consistent equations. In fact MBAR can be used to calculate any mechanistic observable, that only depends on $\mathbf{x}$. It then follows that the reduced free energy of a bin is,

$$f_i = ln(p_i) \tag{2.31}$$

, if all bins are the same size. This equation can be trivially generalised to take into account bins of different sizes.

Chapter 3

The Flow of Proteins and Idealized Pores Within the Membranes of Gram-Negative Bacteria

3.1 Introduction

In recent years attempts have been made to mimic the function of membrane proteins using artificial nanostructures such as carbon nanotubes (CNTs). The use of CNTs in biomedicence has been of great interest for potential use as imaging agents [137, 138], in drug delivery [139] and as artificial ion channels. Experimental [140] and computational studies [141, 142] have observed that functionalized CNTs can spontaneously insert into or translocate across a bilayer. Furthermore the toxicity of a CNT is low if the CNT length and diameter is comparable to the membrane thickness [143].

Protein-lipid interactions occur through multiple modes that combine to carry out complex biological processes in the membrane. A number of computational studies have probed the effect of membrane proteins on local dynamics and structure of the membrane[42, 43, 144–146]. The influence of a protein on the dynamics of the surrounding lipids can extend up to 6 nm into the bulk of the membrane[43, 44, 144, 146]. Often the effects of protein-lipid interactions on the membrane are different for each leaflet of a symmetric bilayer. In one coarse grain study this was attributed to the asymmetry in the electrostatic environment near the head groups in each leaflet[43]. While the electrostatics certainly play an important role, it seems plausible that the shape of the protein may play an equally large role in the observed trends. Many computational

studies of protein-lipid interactions have been carried out for symmetric membranes[40, 43, 44, 146, 147], but there are a lack of comparable studies for asymmetric membranes. One asymmetric membrane of particular interest is the outer membrane (OM) of *E. coli*.

Coarse-grained simulations provide an ideal platform to study protein and lipid diffusion and structure over biologically relevant time- and length-scales, [43, 44, 116, 117]. Computational methods have the advantage of being able to study model systems that allow the effects of size and chemistry to be isolated in a way that is not possible with experimental methods. Here a number of coarse-grained simulation systems were constructed in which a single nanopore was embedded in either a mixed phospholipid or Gram-negative outer membrane. The natural nanopores studied here included two Omps, OmpA and OmpF. OmpA is an 8 stranded beta barrel, which is one of the most abundant proteins in the outer membrane and is believed to be necessary for the structural integrity of the membrane[53, 83]. OmpF is a beta barrel trimer which is a cation selective ion channel[148]; each barrel contains 16 beta strands.

Simple models of OmpA and OmpF were made with functionalised CNTs to probe the difference between nanopores with similar sizes, but with different chemistry and shapes. The effects of changes to the shape of a CNT were also investigated through the construction of a carbon nanoparticle (CNP) hourglass and cone.

Some of the work described in this chapter has been published in previous papers[105, 149] (Figures A.3 and A.4).

3.2 Methods

3.2.1 Nanopore Model Details

Simulations were carried out using the Martini v2.2 forcefield[109–112] and the GROMACS (version 5.1.4) MD package [150]. The structures for the Omps were obtained from X-ray diffraction data from the Protein Data Bank for OmpA (1QJP, 0.165 nm resolution) and OmpF (2OMF, 0.240 nm resolution). Any missing residues or broken loops were then completed with the MODELLER program[151]. The resulting structure was then coarse-grained to the ElNeDyn model[120] with the 'martinize.py' script[152]. The secondary structure was restrained with a 500 kJ mol^{-1} nm^2 elastic network with a 0.9 nm cutoff.

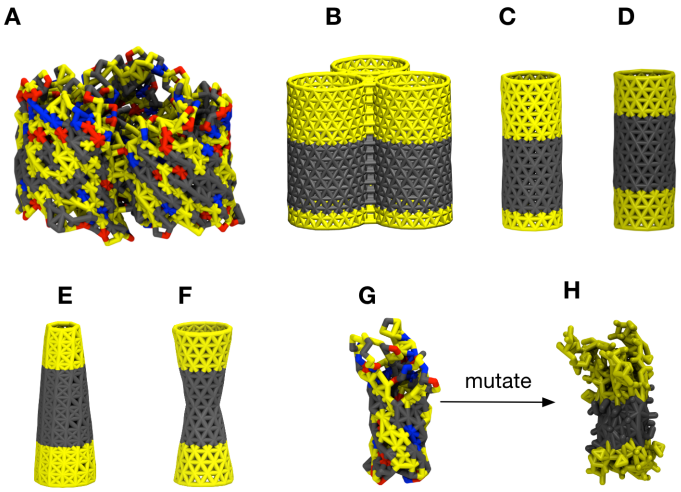

FIGURE 3.1: Some of the nanopores involved in this study A) OmpF B) carbon nanotube (CNT trimer) C) CNT D) CNT symmetric (CNT sym) E) carbon nanoparticle (CNP) cone F) CNP hourglass G) OmpA H) mutated OmpA. key: gray = non polar, yellow = polar, red = positively charged and blue = negatively charged.

The CNT model and bead types used here was based on a previous CNT model[142, 153]. All CNTs had polar ends composed of SNda beads, which is analogous to the partial hydroxylation of the nanotube surface. CNTs were $\sim$ 5.6 nm (14 layers) long with a 2.4 nm hydrophobic core, as these values were comparable to the proteins investigated in this study. The CNT monomer had a diameter of 2.2 nm to best mimic the transmembrane radius of OmpA. Neighbouring particles within each CNT ring and every 4th ring were connected by harmonic bonds with a strength of 20000 kJ mol^{-1} nm^2. Angular restraints of 1000 kJ mol^{-1} nm^2 were used with equilibrium values of 154 within rings and 90 and 180 between rings.

A simple model of OmpF was composed with a trimer of CNTs, each with a diameter of 30 nm to best match the transmembrane radius of OmpF (CNT trimer). For the each CNT monomer an elastic network with a bond strength of 5000 kJ $mol^{-1}nm^2$ and a cutoff of 1.5 nm was applied within each monomer to maintain the rigidity of the CNT. To keep the CNTs in a trimer a further elastic network (bond strength 5000 kJ mol^{-1} nm^2, cutoff 0.6 nm) was applied between all pairs of monomers. The carbon nanoparticle hourglass and cone had minimum and maximum diameters of 1.2 and 2.2 nm, respectively. To maintain the rigidity of each nano-structure a 10000 kJ mol^{-1} nm^2 elastic network was used with a cutoff of 1.5 nm.

The hydrophobic core of the CNT and CNT trimer were positioned such that the CNT to match the size of the intracellular domains of their protein counter parts. To assess the effect of the position of the hydrophobic core, an alternate set of CNTs were made with the hydrophobic core centered in the middle of the tube (CNT sym and CNT trimer

sym, Figure 3.1).

A mutant OmpA and OmpF (OmpA mut and OmpF mut, respectively) were generated to match the chemistry of the CNTs. The procedure for mutating each protein was to first identify the hydrophobic core between the two rings of aromatic residues. Following this the CG beads in the hydrophobic region had their type altered to C4 or CNP for ring type beads. The rest of the beads in the protein were then changed to the Nda or SNda bead types(Figure 3.1).

3.2.2 Simulation Details

For the nonbonded interactions and the electrostatics a short range cutoff of 1.2 nm was used, with the potential shift Verlet cutoff scheme. The verlet buffer tolerance was 0.005 kJ mol^{-1} ps^{-1}. The electrostatics were modelled with the reaction-field method [154] with dielectric constants of 15 and infinity for the short range and long range regimes, respectively. The temperature of simulations was 313 K and was controlled with the velocity rescale thermostat (1.0 ps coupling constant). Minimisations used the steepest descent algorithm and were always followed with a short period of equilibriation with a semi-isotropic Berendsen barostat (4.0 ps coupling constant). For all production runs the Parrinello-Rahman semi-isotropic barostat, with a coupling constant of 12.0 ps, was used. The neighbour list was updated every 10 steps.

All membranes were generated with the CHARMM GUI web interface[96, 98, 155] to have dimensions of approximately 23 $\times$ 23 nm in the xy plane (Figure A.5). The outer membrane composition was based on previous experimental and computational studies[7, 8, 35]. The upper leaflet was solely comprised of ReLPS and the lower leaflet was made up of 90% 16:018:1 phosphoethanolamine (POPE), 5% 16:018:1 phosphoglycerol (POPG) and 5% cardiolipin. A symmetric mixed phospholipid membrane (Mixed) with the same composition as the lower leaflet of the outer membrane model was also generated. LPS was neutralized with calcium ions and then any remaining charge imbalanced was removed through the addition of sodium or chlorine ions. To prevent any localized freezing in solution 2% anti-freezing particles were added. Then each membrane was minimized and equilibrated for up to 6 μs, until membrane properties converged, using a 20 fs timestep.

Each nanopore was then inserted into the membrane in a transmembrane position and any overlapping residues were removed. An overlapping residue was defined by whether it lay within the concave hull of the protein. Each nanopore was inserted stochastically within a 2D disk in the xy plane with a radius of 3 nm. Insertion of the nanopore was

accepted when the composition change of the membrane upon deletion of overlapping lipids was less than 0.2%. Additional water was then added to simulation such that the height of each simulation box was ~ 15 nm. Following this, each system was minimised, the backbone of the protein restrained and a short equilibriation of 50 ns carried out. For each system a production run of 8 μs was then generated using a 10 fs timestep. Further details of all of the simulations in this chapter are described in Table 3.1.

Outer membrane systems are known to have slow dynamics compared to most phospholipid membranes[35]. To check the convergence of membrane properties after protein insertion simulations were extended by 6 μs for OmpA and OmpF in a ReLPS OM. All measured membrane properties had converged within 2 μs (fig. 3.2).

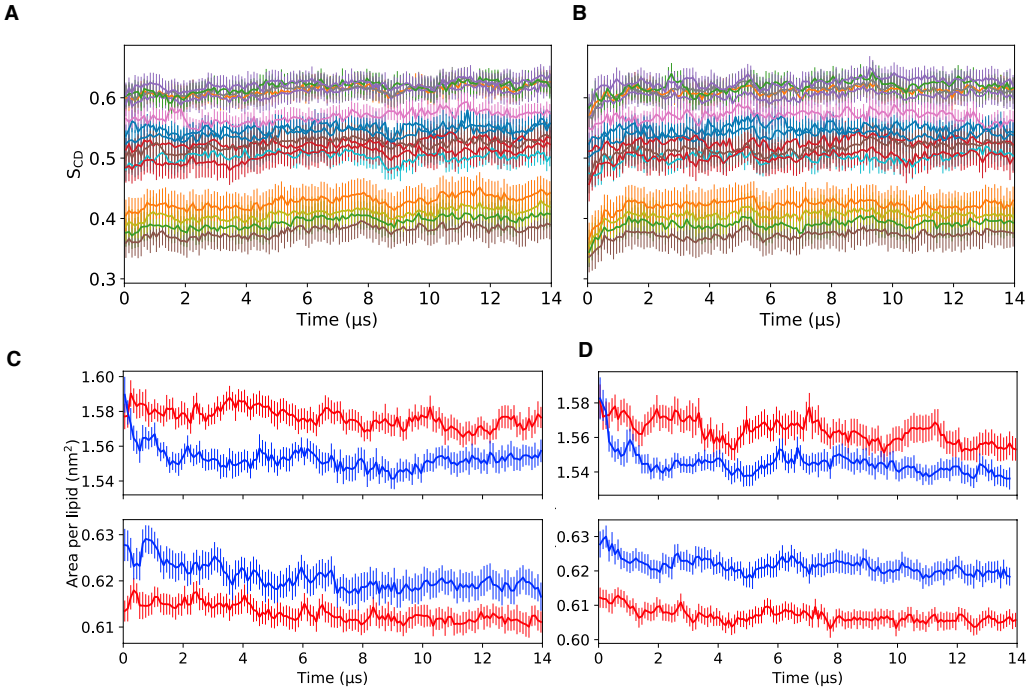

FIGURE 3.2: The lipid tails orders (Equation (3.1)) with respect to time for A) OmpA and B) OmpF in an ReLPS outer membrane. C) The area per lipid for ReLPS (top) and POPE (bottom) as a function of time in an outer membrane containing either OmpF (blue) or OmpA (red). D) The area per lipid for repeat simulations of those analysed in C). The averages and errors above were generated from the block average across 100 ns windows of each trajectory.

TABLE 3.1: This table contains descriptions of the simulations carried out in this chapter that contained a nanopore. The OM membrane was an asymmetric membrane with an upper leaflet of 100% LPS and lower leaflet of 90% POPE, 5% POPG and 5% cardiolipin. The Mixed membrane was a symmetric membrane with the composition of the lower leaflet of the OM membrane. The OM and Mixed membranes were generated with CHARMM-GUI to have the following dimensions $23.9 \times 23.9 \times 12.0$ and $23.2 \times 23.2 \times 9.4$, respectively. The nanopores were then inserted into these two systems and additional water added such that the height of simulation box was roughly 14 nm.

System	Membrane	Nanopore	Solvent beads	Time (μs)
1	Mixed	OmpA	41857	2×8
2	Mixed	OmpF	42031	2×8
3	Mixed	CNT	41872	2×8
4	Mixed	CNT sym	41872	2×8
5	Mixed	CNT trimer	43864	2×8
6	Mixed	CNT trimer sym	43864	1×8
7	Mixed	CNP hourglass	41875	2×8
8	Mixed	CNT cone	41799	2×8
9	Mixed	OmpA mut	41857	2×8
10	Mixed	OmpF mut	42031	2×8
11	OM	OmpA	40340	2×14
12	OM	OmpF	40722	2×14
13	OM	CNT	40203	2×8
14	OM	CNT sym	40203	2×8
15	OM	CNT trimer	40195	2×8
16	OM	CNP hourglass	40969	2×8
17	OM	CNT cone	41012	2×8
18	OM	OmpA mut	40340	2×8
19	OM	OmpF mut	40722	2×8

3.2.3 Analysis Methods

3.2.3.1 Structural and diffusion analysis

Structural analysis was carried out on the last 4 μs of each production run, unless stated otherwise. The 2D density, lipid tail order and thickness maps of membrane systems were generated using tools developed by N. Castillo et al[156]. The contact analysis maps were calculated with an in-house tcl script and visualized with VMD[157]. The partial density map of a patch of the membrane was calculated using an in house script, which utilized the python module MDAnalysis[158, 159]. The script was written to mimic the functionality of the GROMACS 'gmx density' tool, but could also analyse subsets of a system that changed size over time. The partial density analysis was carried out on the last 1 μs of each 8 μs production run.

The lipid tail order, S, is dependant on the angle between each CG bond in lipid tails relative to the z axis, θ, averaged over all lipids and simulation time,

$$S = \left\langle 3cos^2\theta - 1 \right\rangle /2. \tag{3.1}$$

If $S = 1$ then the lipid tails are aligned with the z axis, but if $S = 0$ then the lipid tails are aligned perpendicular to the z axis.

The membrane thickness can be approximated by measuring the distance between the phosphate beads in opposing leaflets. The phosphates bead are often used as the reference beads for membrane thickness, as water rarely permeates past the phosphate beads. There are many ways to calculate the membrane thickness, but here a grid based method was used. First the reference beads (i.e the phosphates) in a given membrane leaflet are projected onto a grid in the xy plane. The size of each voxel in the grid must be tuned to the model resolution and the density of reference beads in each leaflet ($\sim 4 - 9$ $\mathring{A}^2$). Note that the grid for each leaflet (G_u and G_l) must have the same resolution. Then an average height can be calculated for each voxel in the grid. The thickness is then the difference between the average heights of the ij th voxel of the grid for each leaflet. An average thickness can be obtained by averaging across the grid and/or with respect to time.

The lipid depletion-enrichment index (D-E index) is a measure of the number of lipids in a local region of a membrane that was originally used by Corradi *et.al*[160]. The first step of determining the D-E index was to calculate the number of lipids within a certain cutoff of the protein in each system, where the reference point of each lipid was the molecular centre of geometry. Then the local fraction ($c_{local,l}$ of each lipid type, l, within the previously defined cutoff was determined,

$$c_{local,l} = \frac{n_{local,l}}{n_{local,T}} \tag{3.2}$$

where $n_{local,l}$ was the number of local lipids of type l and $n_{local,T}$ was the total number of lipids within the local region. The local fraction of each lipid can then be compared to what would be expected if the membrane density was homogeneous.

$$\text{D-E index} = \frac{c_{local,l}}{c_{global,l}} \tag{3.3}$$

Here $c_{global,l}$ was the fraction of each lipid present in the entire membrane. Thus a D-E index of > 1 indicates enrichment, while an index < 1 indicated depletion.

The lateral diffusion coefficient, D, of lipids (in the xy plane) was determined by fitting the probability density of a 2D random walk to,

$$P(r, \Delta t) = \frac{r}{2D\Delta t} \exp\left(\frac{r^2}{4D\Delta t}\right) \tag{3.4}$$

where $P(r, \Delta t)$ is the probability that a lipid centre of geometry moved r nm within a period of time Δt. The displacement of each lipid was determined across all intervals of Δt in an analysed trajectory, to generate the final probability distribution $P(r, \Delta t)$. The probability distribution was fitted to Equation (3.4) to obtain the lateral diffusion coefficient. The centre of geometry of each lipid was used as the reference point for all displacement vectors, as this was found to give the fastest convergence of D to bulk properties, as a function of Δt[43].

To adapt this method to determine the local lateral diffusion around a nanopore involved the addition of a single extra step. When the displacement vector over Δt was determined for a given lipid, it was then binned into 1 nm intervals, based on its distance from the nanopore's surface. This process was repeated over all intervals of Δt in a trajectory, to obtain the lateral diffusion as a function of distance from the nanopore.

The correlation between protein and lipid movement was determined in a similar manner to the lateral diffusion. Over a given time interval the displacement of the centre of geometry of every protein and lipid in the system was measured. The correlation between a pair of protein ($\mathbf{d}_p$) and lipid ($\mathbf{d}_l$) displacement vectors can be determined,

$$c_{pl} = \cos\theta = \frac{\mathbf{d}_p.\mathbf{d}_l}{|\mathbf{d}_p||\mathbf{d}_l|}. \tag{3.5}$$

This process was repeated for all protein lipid pairs across all time intervals and to obtain an average correlation value and the standard error. This analysis method can be applied in an equivalent manner to determine the correlation in motions between lipids by using a single lipid as a reference. The correlation values were binned based on their distance in the xy plane from the reference lipid. To increase the accuracy of the average correlation values, this process was repeated for 20 randomly chosen lipids of the same type.

3.2.3.2 Lipid Clustering Analysis

Lipid Clustering was analysed using a python implementation [161] of Density-based spatial clustering of applications with noise (DBSCAN)[162, 163]. DBSCAN is a clustering technique that is designed to detect unevenly shaped clusters, which have similar densities; in both cases lipid clustering satisfies these conditions. In DBSCAN first a

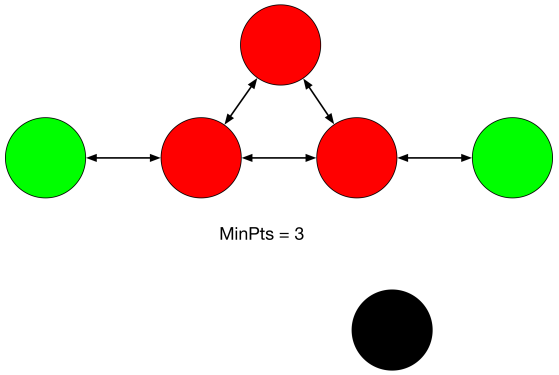

FIGURE 3.3: Diagram of a DBSCAN cluster, with a point classified as noise (black). Core points are red and are within a certain cutoff distance of at least $minPts$ points including the point itself. Border points (green) are within the cutoff of less than $minPts$ core points.

distance matrix of the target system to be clustered is required. There is a lot of flexibility on what this distance matrix can be of, but in this instance it was the 2D distance matrix of the centres of geometry all lipids of interest. Like most clustering algorithms, DBSCAN has parameters that must be set based on user intuition, the distance between two points for them to be connected (ϵ) and the minimum number of points in a cluster ($minPts$). A core point is defined as being within ϵ of at least $minPts$ and these points form a cluster. A point is said to be 'directly density reachable' if it is a core point and within ϵ of another core point. Any points that are within ϵ of core point, but are not necessarily core points themselves are termed 'density reachable'(Figure 3.3); non-core points are called 'border points'. Thus a DBCAN cluster is composed points that are *density reachable* from at least a single point in the cluster. Any points that are not part of any cluster are defined as 'noise'. The choice of these parameters will be further assessed in the following results section.

3.3 Results and Discussion

3.3.1 Choice of Diffusion Observation Time Period

First the bulk diffusion properties of the Mixed and OM membranes, without any proteins present, will be discussed as a function of Δt. For the Mixed system, at small time intervals the diffusion values were elevated by particle vibration, but as Δt increased the measured diffusion values converged (Figure 3.4). To determine the value of the lateral diffusion as a function of distance from the nanopore a suitable Δt must be chosen, under the constraint that Δt should not be so large that the lipids move too far from their original positions. The plot of lateral diffusion as a function of Δt showed that the diffusion converged when $\Delta t \geq 20$ ns. As Δt increases the lipids are more likely to have greater displacements (Figure 3.4 B) and this will lead to a loss of locality of the

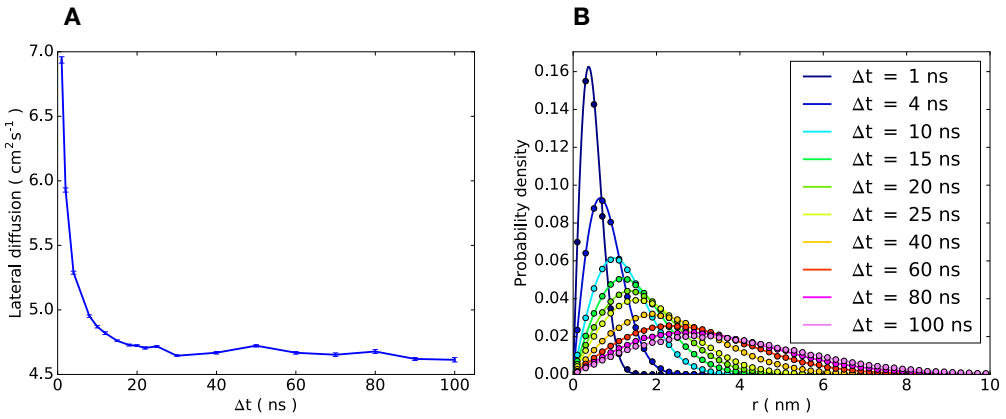

FIGURE 3.4: A) Lateral diffusion of a mixed phospholipid system with respect to the time interval (Δt) sampled across B) Probability density that a lipid is displaced by r for a given time interval Δt for a mixed phospholipid membrane (Equation (3.4)). Analysis was carried out on the last 4 μs of the production run.

diffusion coefficient. Therefore Δt was set to 20 ns, as this was the smallest Δt that gave bulk diffusive behaviour. This process was repeated for LPS as it has much slower dynamics compared to most phospholipids (Figure 3.5). The $P(r, \Delta t)$ distributions of LPS confirmed their slow diffusion compared to phospholipids; even at large Δt LPS was unlikely to have moved over 1 nm. For the same reasons as before, it was found that the optimal Δt was 20 ns. Interestingly, as Δt increased the fit of $P(r, \Delta t)$ to Equation (3.4) became much worse. In fact, when $\Delta t = 100$ ns the probability distribution had become bimodal, suggesting that the motion of LPS at longer timescales (> 25 ns) cannot be modelled by the random walk model.

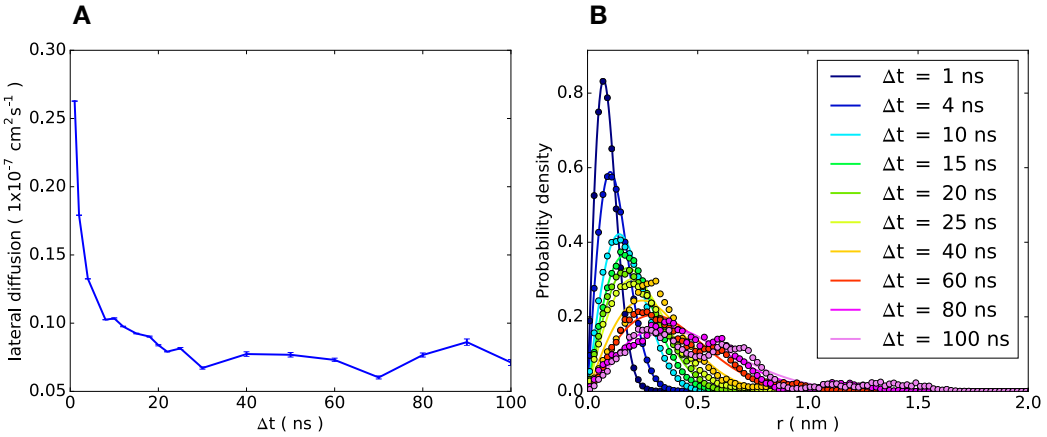

FIGURE 3.5: A) Probability density that a lipid is displaced by r for a given time interval Δt for LPS in the outer membrane B) Probability density that a lipid is displaced by r for a given time interval Δt for LPS. Analysis was carried out on the last 4 μs of the production run.

3.3.2 Macromolecule Size

Here the effect of nanopore size on the local membrane environment was investigated. In both membranes, the lateral diffusion of phospholipids closest to the larger nanopores was slower than for lipids closest to the smaller nanopores. The lateral diffusion was measured across the last 6×1 μs of each production run to get the standard deviation in D values. In both membranes, the bulk diffusive properties are reached at distance > 5 nm. Interestingly, the rates of diffusion were split into two groups (based protein size) for the Mixed membranes, but not for the outer membrane (Figure 3.6). This definitive split in diffusion values seen in Figure 3.6 matched groups of nanopores of similar sizes. The larger the nanopore the greater the perturbation of diffusion within the local vicinity (< 1 nm) and the further this effect extended into the bulk region. This matched previous work [43] on protein crowding within coarse-grained membranes that found that lipid dynamics was reduced as protein size increased. It is possible that the concave regions of the OmpF and the CNT trimer also played a role in the reduced diffusion by trapping phospholipids. A diffusion value of $4.5 \times 10-7$ cm^2 s^{-1} was obtained for the bulk of the mixed phospholipid system, which was comparable to previous values from coarse-grained simulations[43] and experiment[164]. No dependency on nanopore size was observed for the outer membrane, an observation which will be discussed in detail later in this chapter.

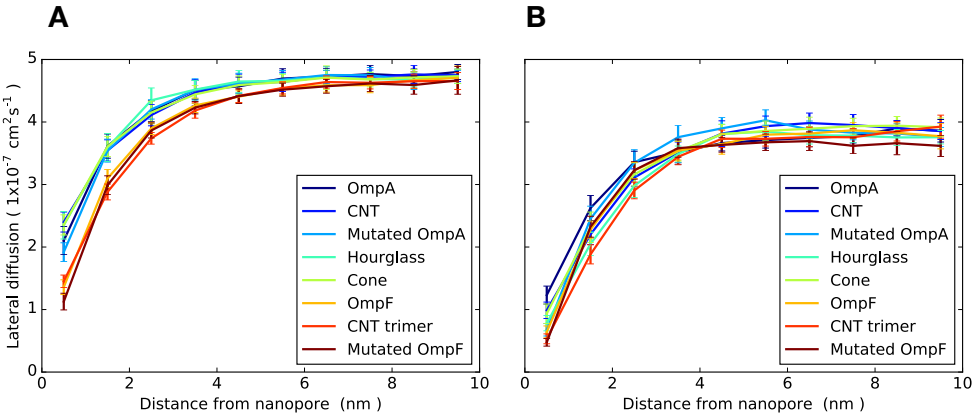

FIGURE 3.6: Lateral diffusion of lipids as a function of distance for a series of nanopores for A) the mixed phospholipid system and B) the inner leaflet of the outer membrane. Each point is the midpoint of 1 nm bins for lipid diffusion. The diffusion was measured across the last 6 μs of a single production run and the errors taken from the standard deviation of the diffusion across 6×1 μs intervals.

3.3.3 Macromolecule Shape

To explore the response of the symmetric membrane to the nanopores in more detail, the structure and dynamics of each leaflet was studied. Diffusion ratios between the

upper and lower leaflet and lipid head group-protein contacts were monitored for the mixed phospholipid membrane. The diffusion ratios between the upper and lower leaflets were determined as a function of distance from the nanopore for 6×1 μs time intervals to obtain the standard deviation in each value. Comparison of OmpA and the CNT showed that the diffusion in the upper leaflet was found to be slower than that of the lower leaflet at a distance of less than 2 nm (Figure 3.7). The asymmetry in diffusion was explained by the greater number of contacts between the upper leaflet and the nanopore, compared to the lower leaflet. The contacts for the CNT were ordered in rings of homogenous contact numbers, where all regions with contacts were with the polar particles on the carbon nanotube. For OmpA the patterns in the contact maps are far from ordered, as a result of the rough nature of the protein surface. A number of potential binding sites were observed across the surface of OmpA.

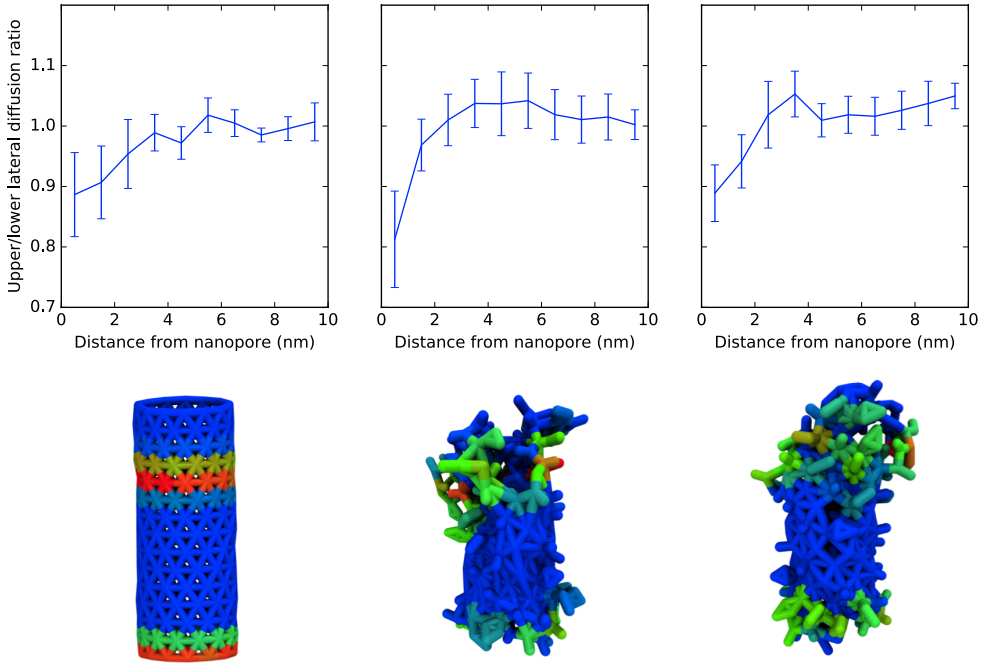

FIGURE 3.7: Upper row: The ratio of lateral diffusion between leaflets of a mixed phospholipid membrane (18:2:2 POPE:POPG:cardiolipin) with respect to the distance from an embedded nanopore left) carbon nanotube (CNT) middle) OmpA and right) OmpA mutated with bead types present in CNT. The center of geometry of each lipid was used as the reference point for diffusion calculations. The distances are the midpoints of each bin. Lower row: contact analysis (cutoff 0.6 nm) between each nanopore and all phosphate groups in the membrane. Blue and red regions depict regions with low and high contact numbers, respectively.

The diffusion asymmetry profiles for OmpA and CNT were identical, to within the observed errors, which was interesting given their vastly different topologies and chemistry. The same trend was observed for OmpF and its CNT equivalent, the CNT trimer (Figure A.6). The diffusion ratio was approximately one at all distance for the CNT sym and CNT trimer sym nanopore systems, and so the diffusion asymmetry of CNTs could be

controlled by the position of the hydrophobic core (Figures 3.7 and A.6). The nanotube with the shifted core (CNT) had a larger polar surface in the upper leaflet, which caused the observed diffusion asymmetry. For OmpA the determination of the contributions of chemical asymmetry and the shape of the molecule was not as simple. To decouple the effects of nanopore shape and chemistry the OmpA particle types were mutated to match the chemistry of the CNT. OmpA was mutated (OmpA mut) such that the thickness of the hydrophobic core was comparable to that of OmpA (2.1 nm), but with completely polar caps (see Section 3.2). The diffusion ratio profile of OmpA mut was identical, to within error bars, as the profiles of the OmpA and the CNT systems. A comparison of OmpA, the mutant OmpA and the CNT suggested that the asymmetry of diffusion was not strongly dependent on the shape of the molecule. The same process was repeated for OmpF, however in this case there were larger differences between the diffusion asymmetry profiles for OmpF and OmpF mut (Figure A.6).

Previous work linked the diffusion asymmetry of a variety of beta barrels to the number of charged groups in contact with the phosphate groups in the lower and upper leaflet of the membrane[43]. However, although this may have an effect on diffusion asymmetry, the similarity of the diffusion ratio plots of the CNT and OmpA suggested that in many cases this was not the dominating factor. It was hypothesized that the difference in the surface area of polar and charged groups between the upper and lower leaflets was correlated to the diffusion ratio. To probe the validity of this hypothesis, the diffusion ratio less than 1 nm from the nanopore was plotted against the contact ratio between leaflets to polar and charged CG beads in each nanopore. The Spearman rank-order correlation test was carried out, which determined whether two variables were monotonically increasing or decreasing based on maximum coefficients of +1 or -1, respectively. The two tailed p-value was also obtained, which tested the validity of the null hypothesis that the two variables were uncorrelated. If the p-value was less than 0.05 the null hypothesis was rejected. For diffusion ratio vs the phosphate contact ratio a p-value of 4.64×10^{-3} and a Spearman coefficient of -0.63 were obtained. Thus there was a reasonable monotonically decreasing correlation between the diffusion asymmetry and available surface area of polar and charged CG beads on a nanopore surface.

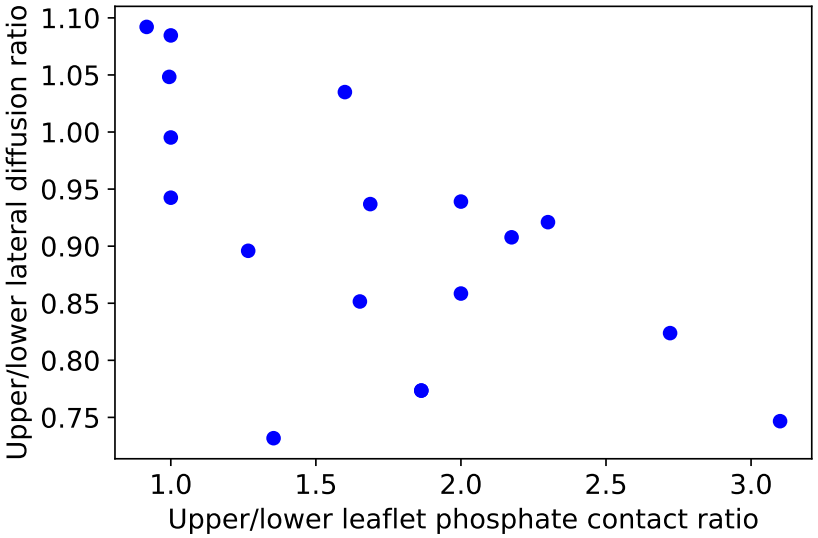

FIGURE 3.8: Upper/lower leaflet diffusion ratio less than 1 nm from the nanopore surface against the upper/lower leaflet phosphate contacts to the polar/charged particles in each nanopore. The contact ratio and diffusion values were determined across the last 4 μs of each production run. Analysis was carried out for all repeat calculations that, involved the mixed phospholipid membrane.

If the surface area of polar and charged residues on the nanopore was the most important factor in determining the diffusion asymmetry of the bilayer then the shape and ratio of charge groups between layers will have a part to play. For example, two nanopores may have the same number of polar particles, but a rough surface would affect the packing of lipid head groups around the nanopore, and thus the strength of binding of nearby lipids to the nanopore. Moreover, it would be expected that a charged particle would contribute more to perturbing diffusion of local lipids than a similarly sized polar residue. Further work could attempt to quantify the effect of nanopore charge by mutating varying amounts of the charged residues of the natural nanopores into polar particles to assess the effect of the electrostatics on diffusion asymmetry. The poor treatment of charges in CG models may also downplay the effects of charge that have been observed here.

While nanopore shape was often not the dominating factor for diffusion asymmetry, it was when determining the effect of a nanopore on the local structure of the membrane. A rough nanopore surface led to a reduction in the local lipid tail order and membrane thickness (Figures 3.9 and 3.10), while the opposite was true for the smooth CNT surface. These observations matched those of a previous atomistic MD study, which investigated the effects of a variety of artificial nanopores on membrane properties [40]. Membrane proteins are known to affect the structural properties of the membrane within a $\sim$ 3 nm radius. However, from the 2D membrane thickness maps of OmpA and OmpF in a mixed phospholipid leaflet it can be seen that thickness of the bulk membrane slightly

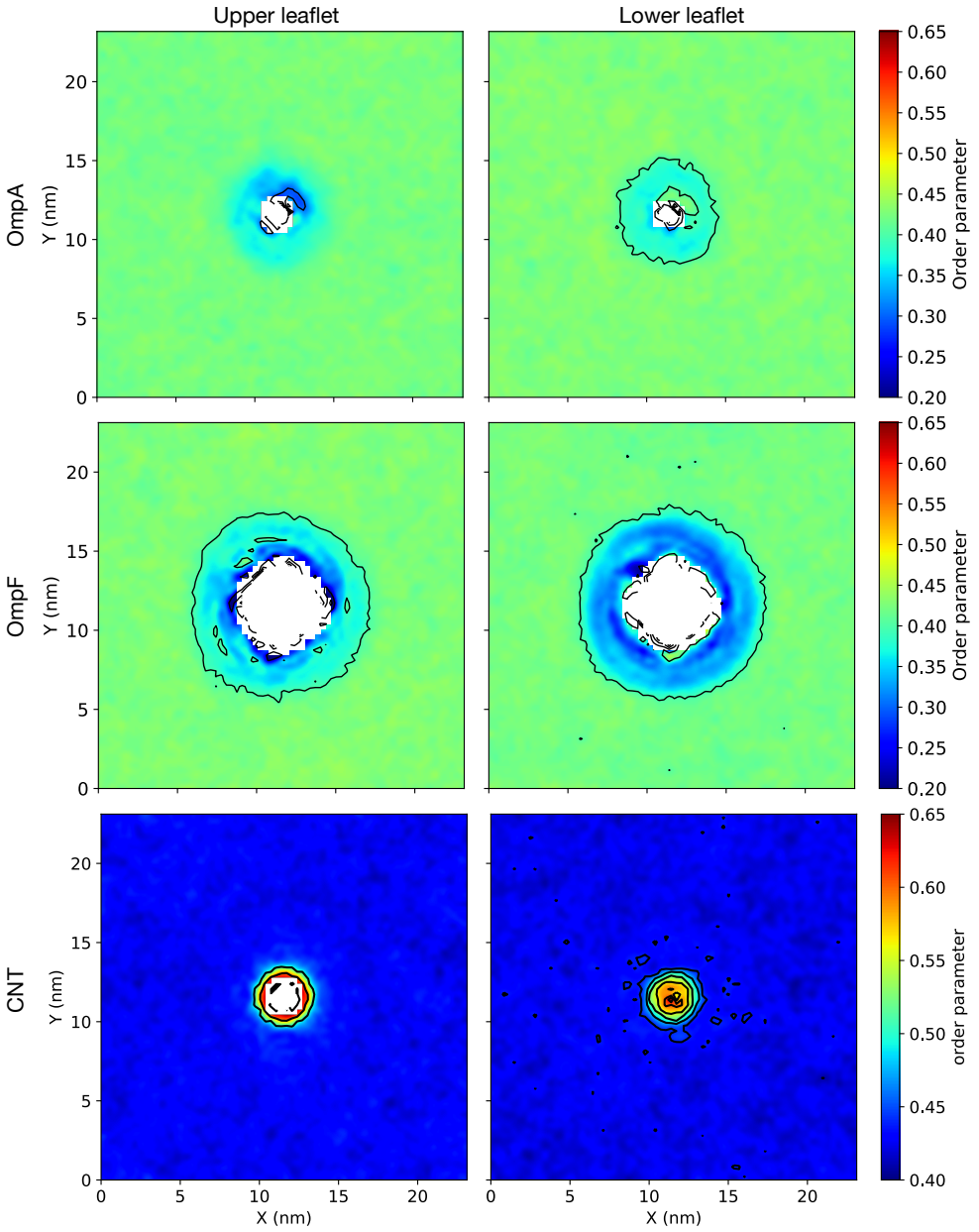

FIGURE 3.9: Order analysis map of the lipid tails of POPE (Equation (3.1)) in a mixed phospholipid membrane centred on an embedded nanopore.

differed between nanopores (Figure 3.10). Such observations are likely to be a product of varying membrane curvatures as a function of nanopore size.

It was observed that the structural effects on the annular region of the membrane were not the same in each leaflet (Figures 3.1 and A.7). Asymmetry in shape, size and chemistry will play a role in the differing trends between leaflets. Structural asymmetry within each leaflet was also observed for the CNT and CNP cone systems, which had similar chemistry, but disparate shapes. The effect of the CNP cone on the local membrane thickness was greater than that of the CNT. Given that both CNT and CNP cone

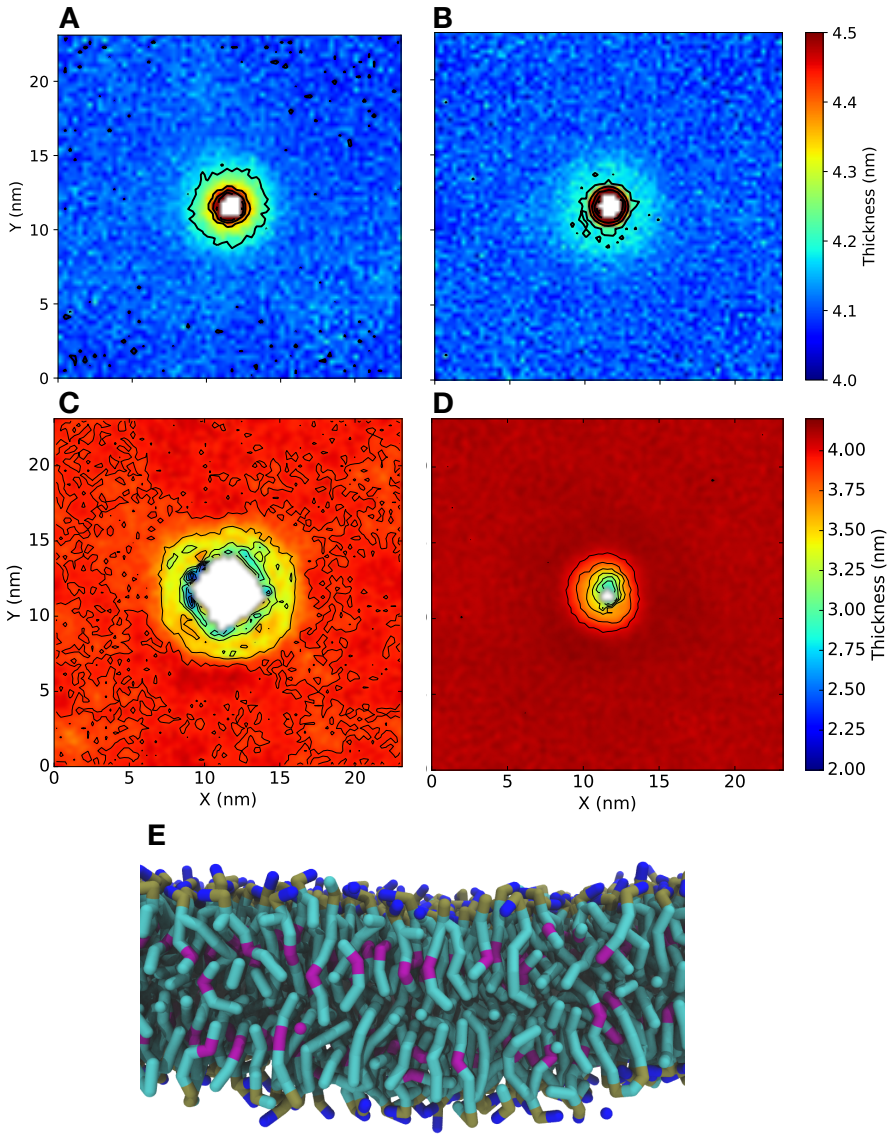

FIGURE 3.10: Membrane thickness map of a mixed phospholipid membrane centred on an embedded A) CNP cone B) CNT C) OmpF or D) OmpA. The thickness was measured using the phosphate beads (PO4, PO41 and PO42). E) Side on view of the mixed phospholipid system with a membrane OmpA, key: green=saturated chains, purple=unsaturated chains, golden=phosphate beads and blue=amine beads

had a similar hydrophobic core thickness, this suggested that their shape resulted in the observed differences. Therefore it seemed possible that nanopores could be designed to manipulate membrane properties through simple changes to nanopore shape.

The consideration of lipid sorting in multi-component bilayers can have important consequences on membrane structure and the nanopores within. One method to quantify lipid sorting near a nanopore is the D-E index, which signifies the local depletion or enrichment of a lipid type within a cutoff (1.4 nm) of the nanopore. This method was originally used by Corradi et.al [160] and is further described in section 3.2.3. If the

D-E index was greater 1 this suggested enrichment of said lipid type, while less than 1 suggested depletion. Here D-E indices were calculated for all lipids, for each leaflet of the mixed phospholipid systems (Figure 3.11). Each D-E index was calculated from $2-8$ μs, in 1.5 μs blocks for both repeats of a single system to get a total of twelve values for each system; these twelve values were then averaged, and the error determined from their standard deviation.

The D-E indices of POPE were ~ 1 for all systems, which indicated that there was not much difference between the POPE density near and away from the nanopores. This did not mean that there were no specific POPE binding sites present, as localised enrichment and depletion could have averaged out. Local depletion and enrichment around proteins has been demonstrated by 2D lipid density plots (A.7) in this work and previous work by Corradi *et al.*[160]. For POPG there was greater variation in D-E indices, although most values lay within a range of $\sim 0.8 - 1.1$. The largest variation from normality was seen for the upper leaflet region of OmpF, where caridolipin was depleted. It may be the case that there are specific binding sites for PG in the upper region of OmpF. Further analysis showed that the phospholipid headgroups preferred to be in contact with positively charged lysine. However this was a biologically irrelevant point, as *in vivo* the upper region of OmpF should be surrounded by mainly LPS lipids.

The cardiolipin enrichment varied greatly and brought to light some interesting trends. One area of focus was to investigate how changes in nanopore shape, chemistry and size affected lipid enrichment. A comparison of OmpA and OmpA mut showed little difference between the enrichment indices for both leaflets. This was indicative of the importance of the shape of the protein. To see if nanopore shape was the dominating factor for lipid sorting, the OmpF and OmpF mut systems were also compared. In both the upper and lower leaflet there were differences in the enrichment indices for OmpF and OmpF mut. The upper leaflet in particular exhibited a large (~ 0.4) drop in the D-E index of POPG, upon the mutation of the protein. These trends are in direct contrast with those observed for OmpA and thus it seems their significance requires further consideration. One possibility was that the effect of charge versus shape on the D-E index was proportional to the size of the nanopore. Therefore as the size of the nanopore increases the importance of shape versus chemistry may be reduced. Given the complexity of lipid sorting, the consequences of mutating a protein will vary greatly as a function of the size, chemistry and shape of the protein mutated and the composition of the membrane itself.

Now the results of simple changes of shape was probed across a range of CNP models. There were no significant differences between the D-E indices of the CNT and CNT sym systems. Thus the position of the hydrophobic core in a CNT had little effect on the lipids sorting, but did on the dynamics of the lipids. For all of the CNT and CNP

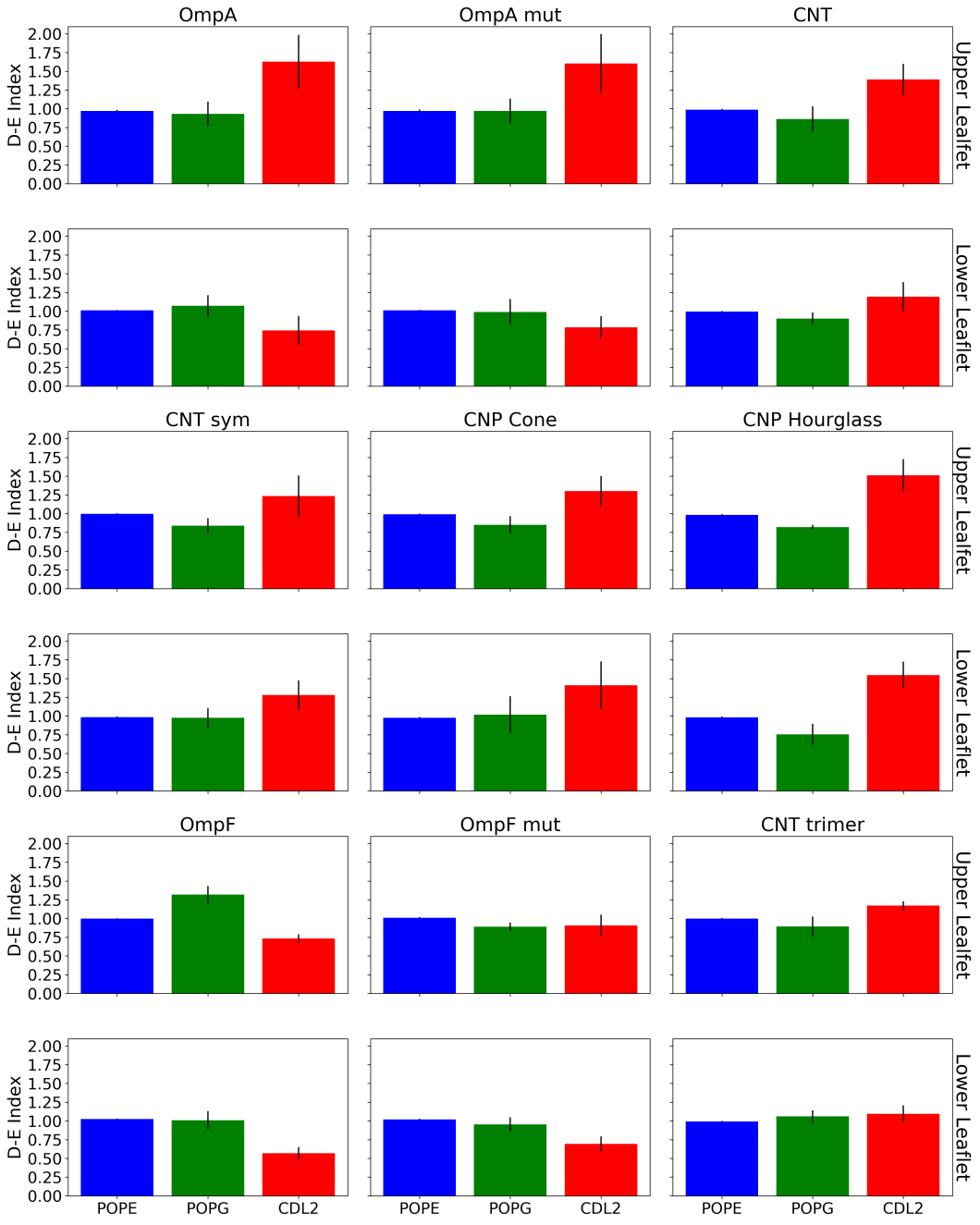

FIGURE 3.11: Depletion-enrichment (D-E) indices for POPE, POPG, and cardiolipin (CDL2) for each protein in the ReLPS membranes. The D-E index was obtained by dividing the lipid composition of the 1.4 nm shell around the protein by the bulk membrane composition; therefore, a D-E index > 1 indicates enrichment, while a D-E index < 1 indicates depletion. Each D-E index was calculated from $2 - 8$ μs, in 1.5 μs blocks for both repeats of a single system to get a total of twelve values for each system; these twelve values were then averaged, and the error determined from their standard deviation.

systems cardiolipin was enriched, even though these nanopores had no charge. The D-E index of cardiolipin within the mixed phospholipid system (no nanopores) with respect to other cardiolipin lipids was also found to be ~ 1.5. Thus the previously observed cardiolipin enrichment could have been related to lipid-lipid clustering, as opposed to nanopore mediated lipid sorting. There was little difference between the D-E indices around the CNT sym and the CNP cone. Whereas there was a small increase in the enrichment of cardiolipin from the CNT sym to the CNP hourglass; this could indicate a small preference of lipids with lower head to tail volume ratios (e.g. cardiolipin) to cluster around the CNP hourglass.

3.3.4 Communication Between Outer Membrane Leaflets

This section will discuss the structural and dynamics differences between the outer membrane and the mixed phospholipid systems. It was expected that the large differences lipid diffusion between the leaflets in the outer membrane would also lead to differences in the effect of a nanopore on its local environment.

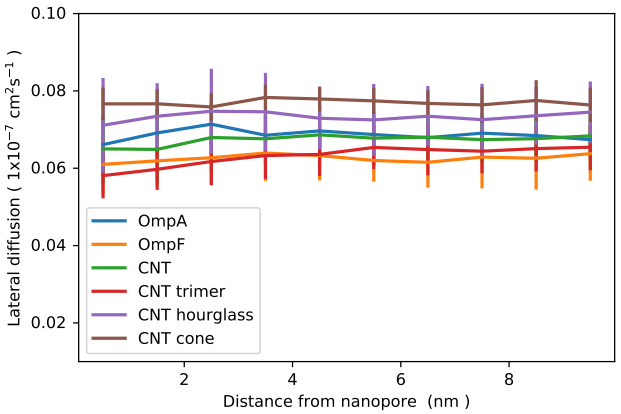

FIGURE 3.12: Lateral diffusion of LPS as a function of distance for a series of nanopores in the outer membrane. Each point was the midpoint of 1 nm bins for lipid diffusion. The diffusion was measured across the last 6 μs of the production run and the errors taken from the standard deviation of the diffusion across 6×1 μs intervals.

The diffusion of phospholipids in the OM was $1-3$ cm^2 s^{-1} slower than that of the equivalent mixed phospholipid system (Figure 3.6). This reduction of phospholipid diffusion in the OM was a result of intercalculation of lipid tails with the slow LPS layer. Surprisingly, LPS showed changes in diffusion as a function of distance from any nanopore (Figure 3.12). The size or type of nanopore also did not appear to have a significant effect on the diffusion of LPS.

The correlation between protein and lipid displacement vectors was determined using Equation (3.5) across 20 ns intervals for OM systems containing a single nanopore (Figure 3.13A and B). The correlation between nanopore and LPS motion was greater than 0.7, even up to 10 nm from the nanopore's surface. A flow diagram of LPS and nanopore displacement over 100 ns (for OmpA and OmpF) showed that LPS moved in the same direction as the nanopore (Figure 3.13C and D). These observations are a result of inter LPS non-covalent binding by calcium ions, which restrict LPS movement on the timescales available to CG simulations.

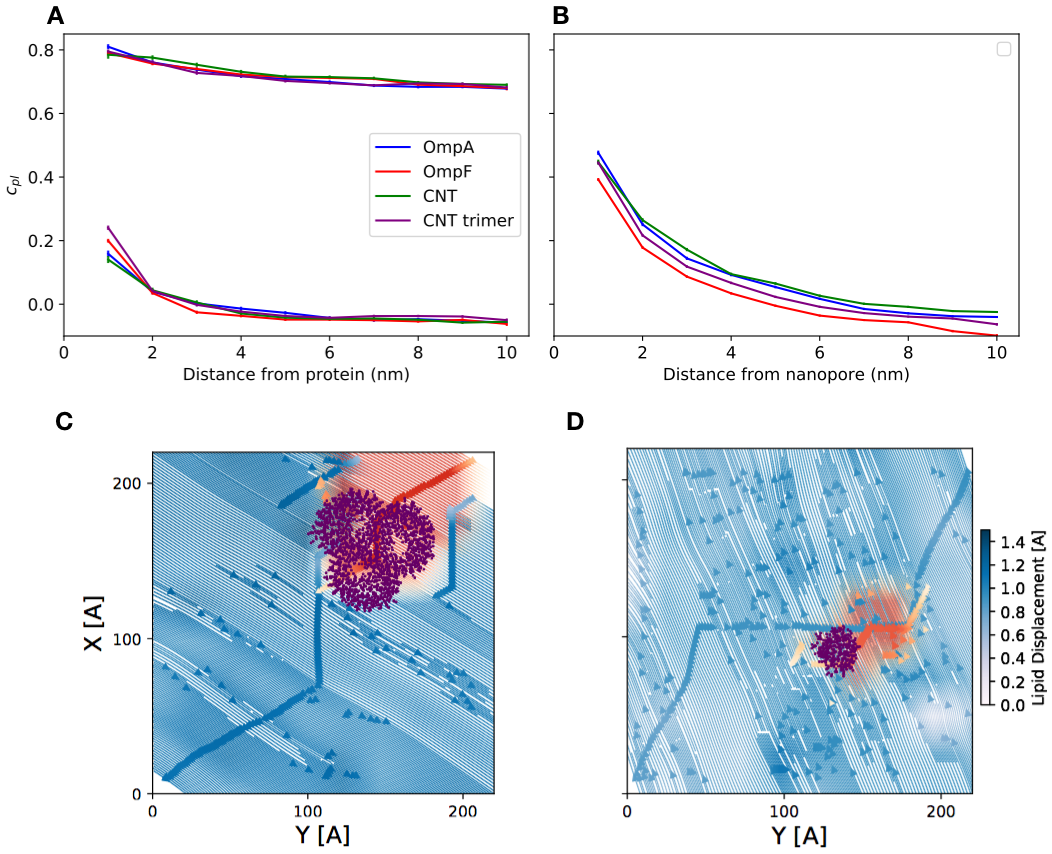

FIGURE 3.13: Correlation between nanopore and lipids motion (c_{pl}, see Equation (3.5)) as a function of distance from the embedded nanopore for the a) outer membrane, where PL was phospholipids in the inner leaflet, and for the b) lower leaflet of the mixed phospholipid membrane. The correlation was measured across the last 6 μs of each simulation across a series of 1 nm intervals every 20 ns. Flow diagram of lipid (blue) and protein displacement vectors (red) over a 100 ns interval. In all cases the displacement vector was determined using the centre of geometry as the reference point. Adapted with permission from Hsu et al.[96]. Copyright 2017 American Chemical Society.

At short distances ($<$ 1 nm) the inner leaflet of the OM exhibited smaller correlation to nanopore movement ($\sim$ 0.2) compared to LPS. The correlation between phospholipid and nanopore movement quickly decayed to 0 within 3 nm, which was a lot faster than previously observed for symmetric membrane systems[44]. The correlation between nanopore and lipid movement was also determined for the lower leaflet of the

mixed phospholipid systems, to offer a comparison to the inner leaflet of the outer membrane. The correlation between nanopore and phospholipid movement (Figure 3.13B) was ~ 0.2 higher than seen in the inner leaflet of OM and extended 6 nm into the bulk of the membrane, as seen in a previous study of proteins in vesicles [44]. The observed differences in correlation between the mixed phospholipid and outer membrane may have been the result of differences in the correlation of lipid motion between leaflets. A more likely explanation was that the protein motion was very different in the OM, due to the pinning of the surrounding LPS lipids. Thus the reduced correlation between nanopore-lipid motion in the lower leaflet was a reflection of the effect of LPS on nanopore movement.

Now the correlation between the motion of different lipids will be discussed for membrane only systems. The correlation between lipid in each leaflet was measured for the OM and the mixed phospholipid system (Figure 3.14). Further details of the analysis method are provided in section 3.2.3. From Figure 3.14B it was clear that LPS showed no correlation with phospholipid movement; this was not surprising given the difference in diffusion rates between the two leaflets. The inter-leaflet correlation in the the mixed phospholipid system was ~ 0.1 at short distances (< 1 nm) (Figure 3.14A). Therefore, when leaflets have similar dynamics the motion between them is slightly correlated and this in turn strengthens the correlation of motion within leaflets. Therefore the observed correlation between protein and lipid movement could be influenced by the correlation of lipid motion within and between leaflets.

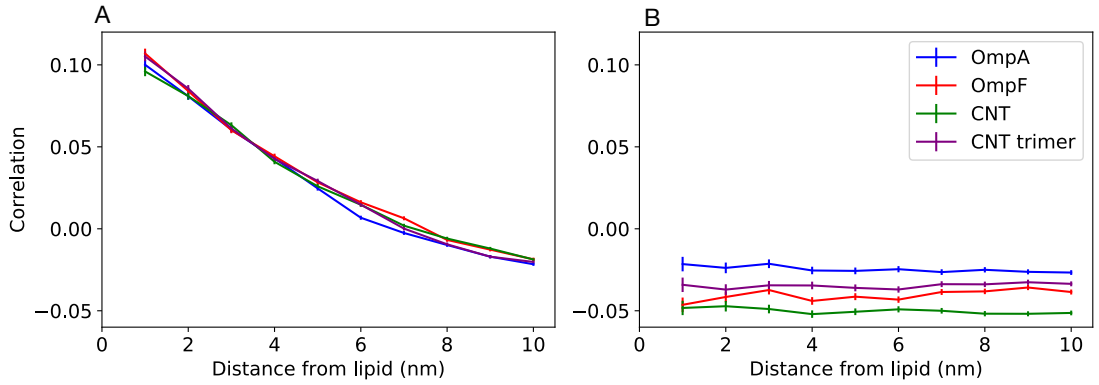

FIGURE 3.14: Correlation of lipid motion as a function of distance from the a chosen lipid for a) POPE between leaflets in the mixed phospholipid membrane and b) LPS and POPE in the outer membrane. The correlation was measured across the last 6 μs of each simulation every 20 ns.

The intra leaflet correlation was also determined for all lipids in the OM and mixed phospholipid membranes (Figures 3.15 and 3.16). The correlation between lipids motion is intrinsically related to the time interval, Δt, used for the analysis method and

so a range of Δt were used (2, 10, 20, 100 and 200 ns). For the smallest Δt (Δt = 2 ns), there was significant correlation (0.4) between LPS motion at distances over 6 nm. As Δt increased the LPS-LPS correlation increased, until it tended towards 1.00 (when Δt = 100 ns). For a lipid moving under the 2D random walk model it would be expected that the correlation in motion between lipids would be uncorrelated at large distances; this was further proof that LPS motion could not be modelled with the random walk model. The correlation of motion between lipids of the same type in the outer membrane was found to be greater for cardiolipin, compared to POPE and POPG, for most values of Δt(Figure 3.15); the same trend was not observed for the mixed phospholipid system (Figure 3.16). These observations may be indicative of cardiolipin clustering.

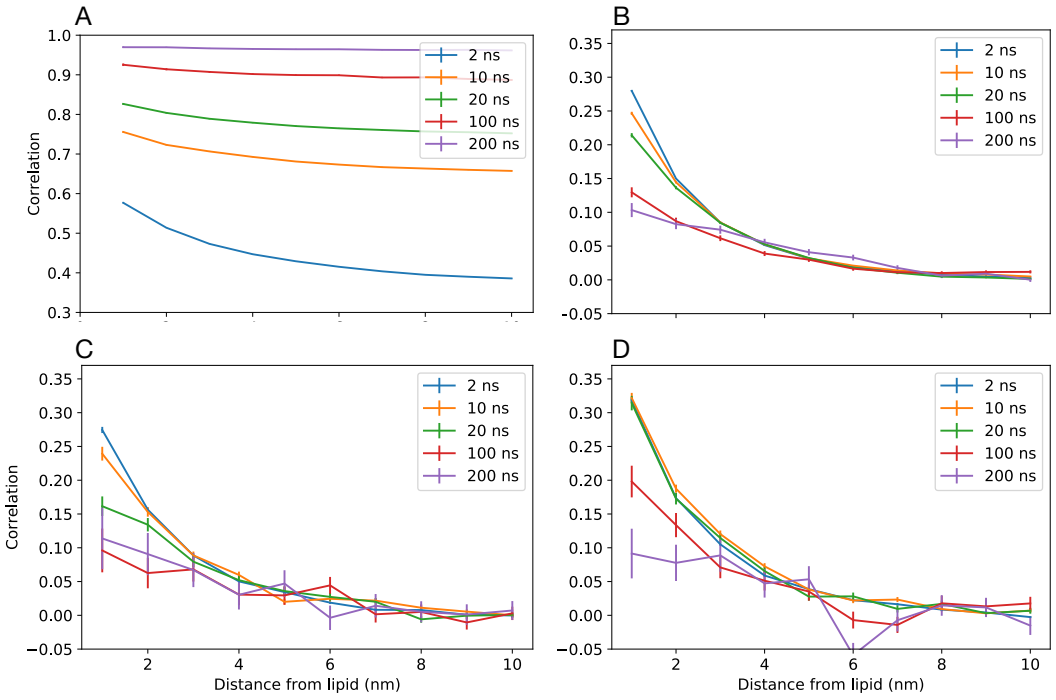

FIGURE 3.15: Correlation of lipid motion (see Equation (3.5)) in the outer membrane as a function of distance from a lipid of interest for a) LPS b) POPE c) POPG. The correlation was measured across the last 4 μs of each simulation every Δt, where Δt = 2, 10, 20, 100 or 200 ns.

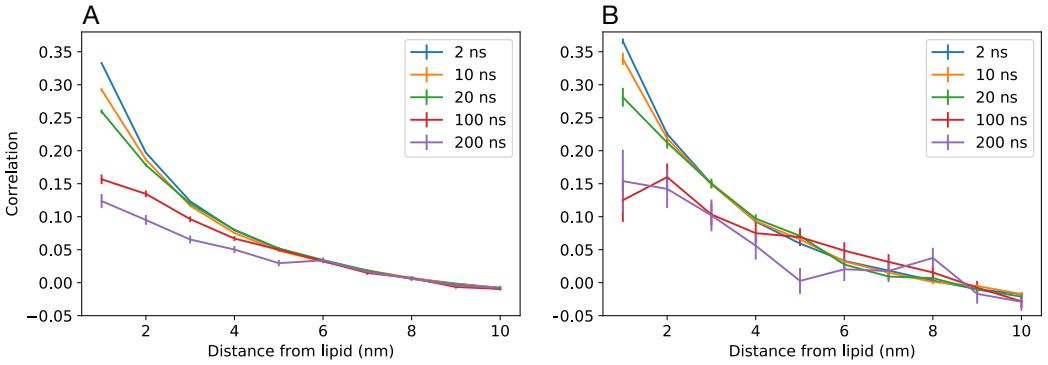

FIGURE 3.16: Correlation between lipids motion as a function of distance (see Equation (3.5)) from the chosen lipid for a) POPE and b) cardiolipin in the upper leaflet of the mixed phospholipid membrane. The correlation was measured across the last 5 μs of each simulation every Δt, where $\Delta t = 2, 10, 20, 100$ or 200 ns.

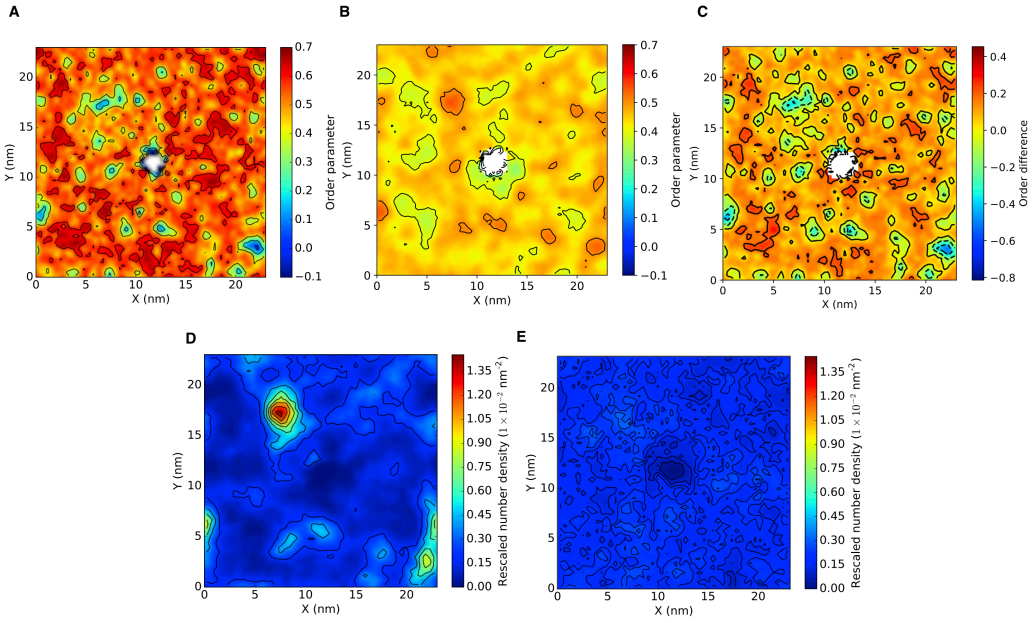

FIGURE 3.17: Order analysis of the lipid tails (Equation (3.1)) of (A) lipopolysaccharide, (B) POPE and the (C) diference between lipopolysaccharide and POPE order parameters (Equation (3.1)) in the outer membrane. (D,E) Density maps of cardiolipin in the outer and mixed phospholipid membrane, respectively. Te density was measured using one phosphate particle per lipid and all values normalised by the number of lipids in a given leaflet. Each system was centered around a transmembrane OmpA. Reused with permission from Shearer et al.[149]

Now focus will be shifted to the structural trends observed in the outer membrane system that contained an OmpA. The order and density analysis for the equivalent mixed phospholipid system had a ~ 3 nm region around the nanopore in which the order and density of lipid was different compared to bulk membrane properties (Figures 3.9 and A.7). The order values of LPS tails ranged from $-0.1 - 0.70$, which matched experimental values for multiple phases of LPS[165]. Similarly, tails orders of POPE varied greatly across the entire membrane and not just the local region around the protein (Figure 3.17B).

Interestingly, regions of high disorder within the LPS leaflet were directly above regions of high order within the lower leaflet. Given that LPS dynamics is much slower than the dynamics of the lower leaflet, this suggested that the order of the tails in the LPS layer determined the order in the lower leaflet.

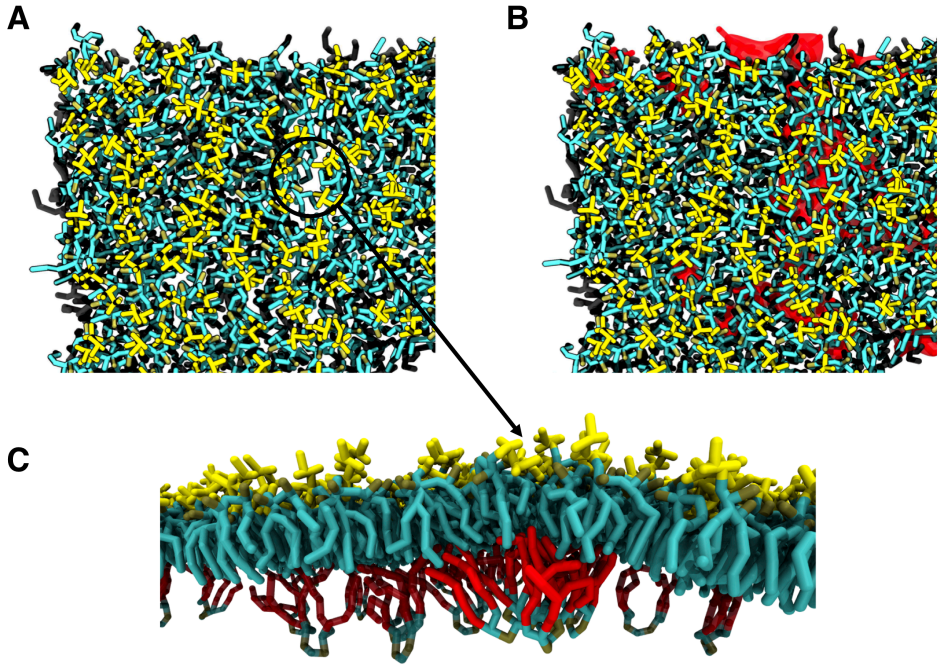

FIGURE 3.18: Top down view of the upper left quarter ($\sim 11.5 \times 11.5$ nm in the xy plane) of the outer membrane with a transmembrane OmpA (A) with and (B) without cardiolipin (highlighted in red) shown to emphasis the void in lipopolysaccharide sugar-sugar packing. (C) Side view of cardiolipin cluster (tails highlighted in red) below a void in LPS sugar-sugar packing. The system was centred on the transmembrane OmpA. Reused with permission from Shearer et al.[149]

2D density maps of each lipid type in the lower leaflet of the outer membrane, over 4 μs, showed that there was an increase in density below region of high LPS disorder (Figures 3.17 and A.8). The increase of density below region of LPS tail disorder was particularly pronounced for cardiolipin (Figure 3.17). One possible explanation for these observed structural nano-domains was related to voids in LPS packing caused by reduced conformational freedom of LPS, due to binding between LPS lipids by Ca^{2+} ions. From the correlation analysis it was known that LPS tended to move as a raft, with extremely high correlation between neighbouring LPS lipids. The conformation restriction of LPS was further highlighted by a 2D density map of LPS phosphate groups across 4 μs, where drift motion of the LPS raft was removed by centering the system on OmpA (Figure 3.19). The voids in LPS sugar packing could lead to LPS tails splaying into adjacent voids to maintain the bilayer surface, explaining the regions of high disorder in the LPS layer. Thus the phospholipids in the areas below LPS voids may extend into the regions

of high LPS disorder to maximize the hydrophobic interactions with the upper leaflet.

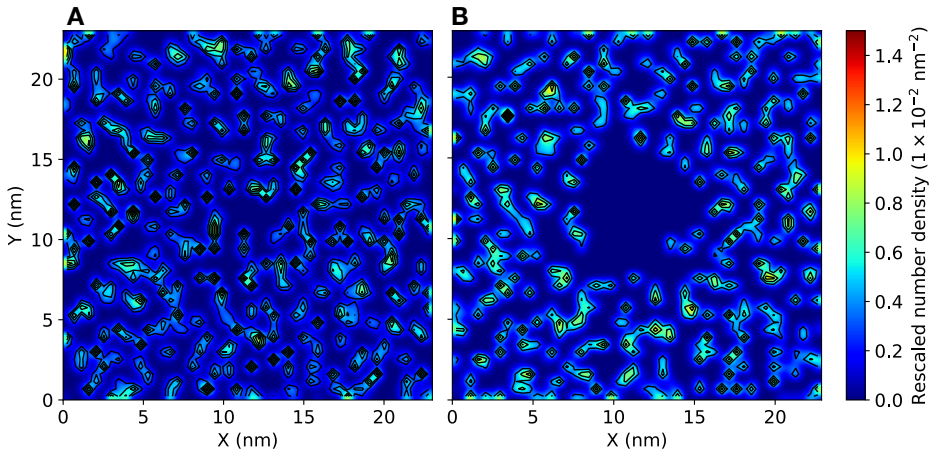

FIGURE 3.19: Density maps of LPS in the outer membrane systems containing A) OmpA and B) OmpF. The density was measured using a phosphate bead (PO1) per lipid and all values normalised by the number of lipids in a given leaflet. Trajectories were centred on the nanopore. Reused with permission from Shearer et al.[149]

Visualization of a snapshot of the upper left quarter of the outer membrane showed that the large LPS voids in sugar-sugar packing were above areas of cardiolipin clustering (Figure 3.18A and B). A side on view of the largest LPS packing void (circled in Figure 3.18) showed cardiolipin tails in the lower leaflet extended into the upper leaflet, to fill the void caused by poor LPS packing. Clustering of POPE and POPG below regions of high LPS tail disorder was also seen, but to a lesser degree than that of cardiolipin. Cardiolipin may preferentially cluster below LPS voids based on entropic arguments, as it is the largest lipid in the lower leaflet.

It seemed plausible that partial interdigitation could be occurring between leaflets. Full interdigitation would be easily observed from snapshots of a trajectory, but the same is not true of partial interdigitation. To assess the amount of interdigitation in the outer membrane a partial density profile was determined in a 3 nm square patch, centred on the LPS head group void circled in Figure 3.18. For the sake of comparison, the partial density of a 3 nm patch of the mixed phospholipid membrane with a membrane OmpA was also calculated. In the mixed phospholipid membrane the density of phospholipid tails and heads was completely symmetric, with no observable interdigitation. In the density profile of the OM (Figure 3.20.A) the tails in the lower leaflet extend closer to the phosphate heads in the upper leaflet, which suggested that partial interdigitation occurred between the lipid tails in each leaflet.

When OmpF was in the OM the same trends caused by voids in LPS packing were observed (Figure 3.21). As before, preferential clustering of cardiolipins was seen below regions of high LPS disorder. There seemed to be little similarity in the size and

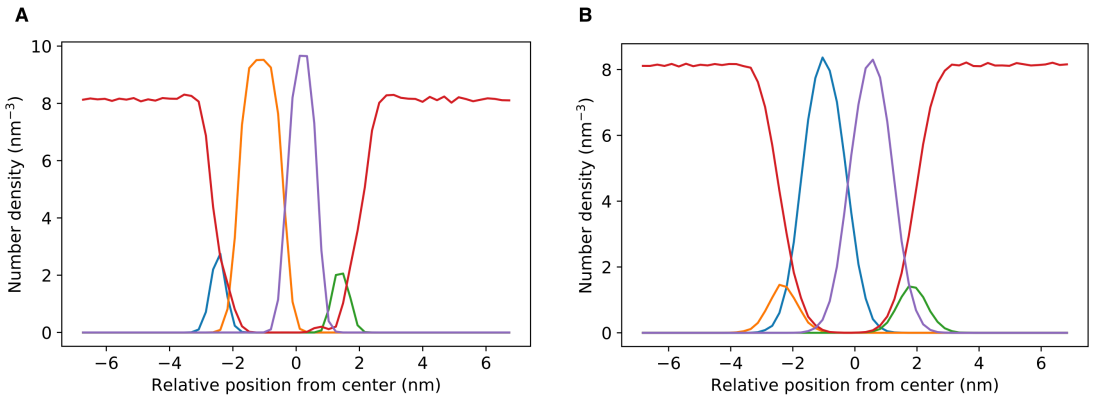

FIGURE 3.20: Partial density profile in the z direction for a 3×3 nm patch of the OmpA (A) outer membrane and the (B) mixed phospholipid systems, relative to the centre of mass of each membrane - note that in (A) LPS was the upper leaflet of the membrane. The membrane patch had the bounds in the xy plane of $6 < x < 9$ nm and $16 < y < 19$ nm relative to a trajectory centred about the membrane OmpA (refer to Figure 3.17). Key: red, water; blue, lower leaflet phosphate groups; yellow, lower leaflet tails; purple, upper leaflet tails; green, upper leaflet phosphate groups. Reused with permission from Shearer et al.[149]

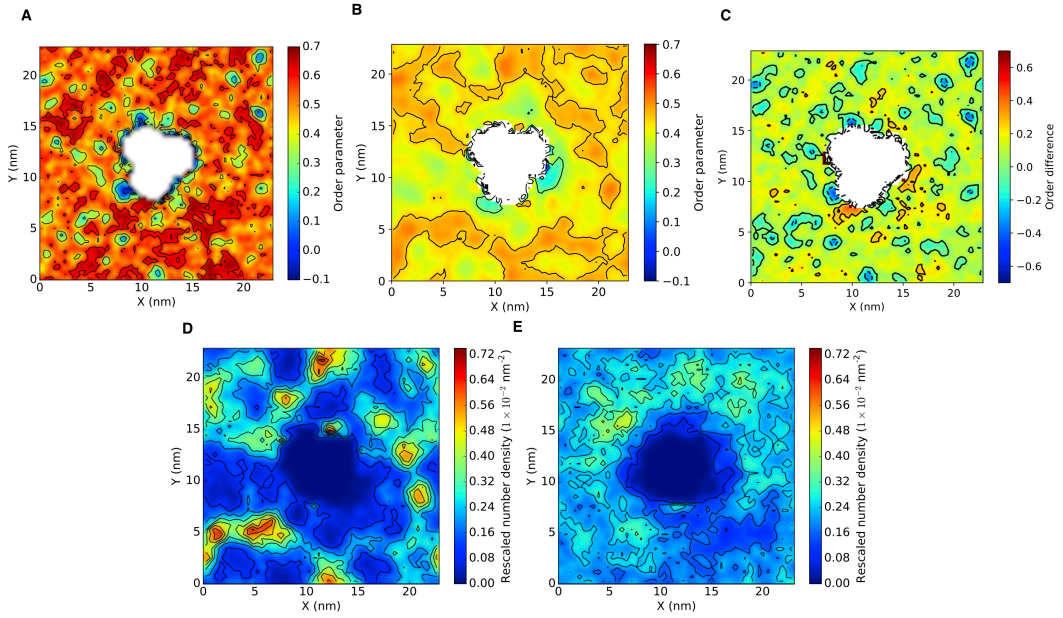

FIGURE 3.21: Order analysis of the lipid tails (Equation (3.1)) of (A) lipopolysaccharide, (B) POPE and the (C) difference between lipopolysaccharide and POPE order parameters in the outer membrane. (D,E) Density maps of cardiolipin in the outer and mixed phospholipid membrane, respectively. Te density was measured using one phosphate particle per lipid and all values normalized by the number of lipids in a given leaflet. Each system was centred around a transmembrane OmpF. Reused with permission from Shearer et al.[149]

shape of regions of cardiolipin density between the OmpA and OmpF systems, which could suggest that membrane proteins affect LPS packing. Analysis of the OM with no proteins showed that cardiolipin clustering still occurred below regions of low LPS tail disorder (Figure A.9). Thus these trends between leaflets were clearly dependant on the membrane.

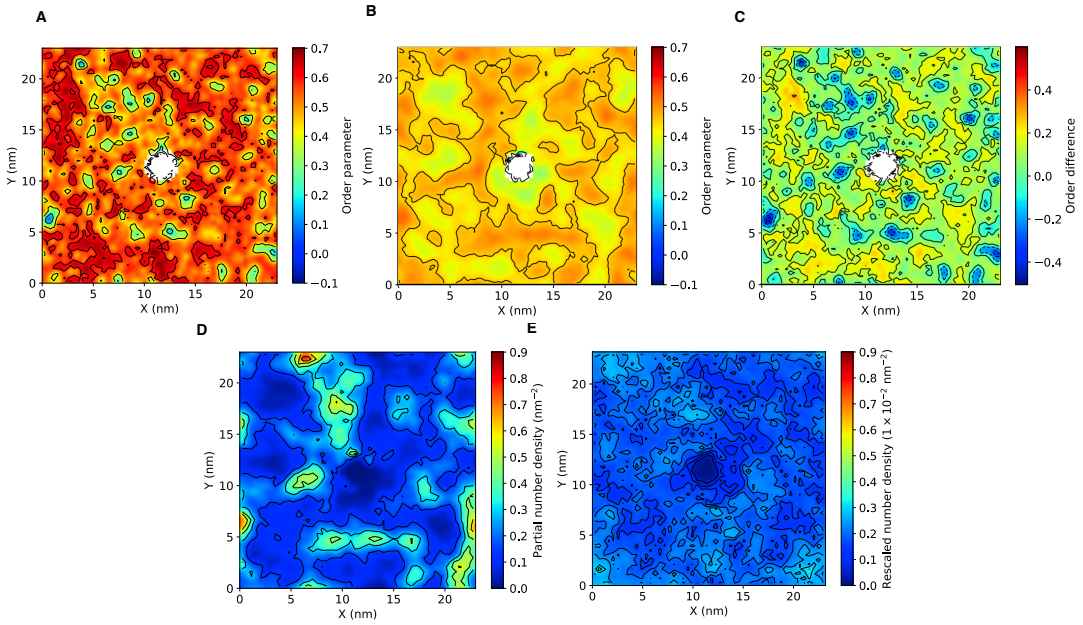

FIGURE 3.22: Order analysis of the lipid tails (Equation (3.1)) of A) lipopolysaccharide, POPE and the C) difference between lipopolysaccharide and POPE order parameters in the outer membrane. (D, E) Density maps of cardiolipin in the outer and mixed phospholipid membrane, respectively. The density was measured using one phosphate particle per lipid and all values normalised by the number of lipids. Each system was centred around a transmembrane OmpA. This is the analysis from the last 4 μs of an extended 14 μs simulation. Reused with permission from Shearer et al.[149]

Following this the production runs of OmpA and OmpF in the OM were extended to 14 μs. Analysis was then repeated for $8-14$ μs of the OmpA and OmpF production runs to see how these structural nano-domains evolved. The same trends of order and disorder between leaflets were observed (Figure 3.22). However the size, number and positions of the structural nano-domains had completely changed compared to Figure 3.17. The size of regions of high cardiolpin density also changed significantly and so it was determined that the effect of the protein on LPS packing and therefore cardiolipin clustering cannot be considered over such small timescales. Analysis of the repeat of the OmpA simulation showed the same general trends of cardiolipin clustering being associated with nano-domains of LPS disorder (Figure A.10). The size and number of domains of increased cardiolipin density was not consistent between repeats.

It was of interest to perform cluster analysis on cardiolipin to search for a parallel between protein type and cluster size frequency. To probe the clustering of lipids in the

lower leaflet of the outer membrane the current length of simulations in this chapter was not sufficient. Given that the LPS packing takes microseconds to change significantly this was expected to have an effect on the lipid clustering. The following simulations were extended to 90 μs: OM 1) with and 2) without OmpA, and the 3) Mixed membrane. These three systems were chosen to ascertain the effects of membrane asymmetry and the presence of a protein on lipid clustering. Given the computational cost of generating these trajectories only a single repeat of each system was extended. The clustering of both POPG and cardiolipin was determined to provide a comparison between two lipids of the same abundance in the membrane.

To determine which lipids were in a cluster, a python implementation of the DBSCAN method[161] was applied, which is further described in Section 3.2.3.2. There are numerous clustering techniques that can be applied and the advantages of DBSCAN lie in that it excels at identifying clusters with similar densities, but inhomogenous shapes; this description fits lipid clustering well. The main difficulty of applying DBSCAN is that it requires the user to choose two parameters that define the nature of what is considered a cluster, the minimum number of points in a cluster $minPts$ and the minimum neighbour distance ϵ. It is quite difficult to justify the use of a certain set of parameters, but a recent review provides some basic guidelines to follow[163]. The default $minPts$ for 2D data has been found to be 4 (2$\times$ number of dimensions)[166]; whereas ϵ should be as small as possible, however the range of acceptable ϵ is very much dependant on the problem at hand. Previous work investigating the clustering of two tailed phospholipids in mammalian cell membranes[167] used DBSCAN parameters of $\epsilon = 1.5$ nm and $minPts = 3$. Here these parameters are used along with some other variations to show the rigidity of these results to small changes in clustering parameters. The degree of clustering for each cluster size was measured as a fraction of the total number of clusters indentified. Clustering analyis was carried out from $10 - 90$ μs in each simulation.

There are two conditions in data science which can be used to maximise the chance of identifying interesting patterns in the data from clustering:

1. A suitable fraction of the data should be in clusters. $1 - 30\%$ of data should not be in any clusters, i.e. $1 - 30\%$ noise.

2. If $20 - 50\%$ of the lipids are in the largest cluster then a smaller ϵ should be used.

The two points above are not a measure of the quality of clustering, but instead the degeneracy of the clustering in the dataset. In this case degeneracy refers to absorption of information by larger clusters or noise. To assess the degeneracy of cardiolipin clusters the following were determined for the OM system as a function of ϵ (Figure 3.23): the fraction of 1) noise, 2) lipids in clusters, 3) lipids in the largest cluster and 4) the total number of clusters. The minimum number of points in a cluster ($minPts$) was kept

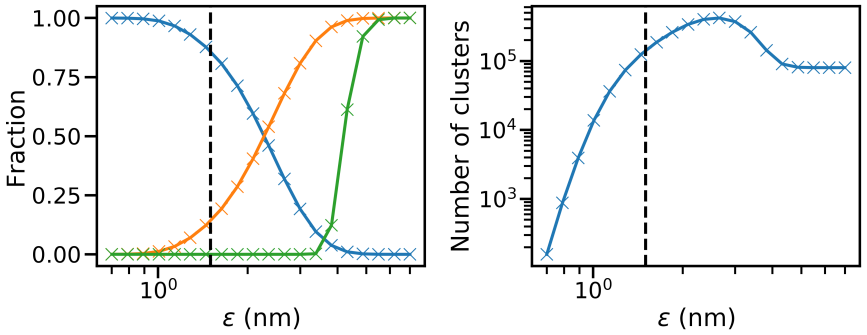

FIGURE 3.23: (left) Fraction of cardiolipin in clusters (orange), noise (blue) and in largest cluster (green) as a function of cutoff distance between neighbours (ϵ). (right) The number of clusters as a function of ϵ. All figures are for the ReLPS outer membrane system and clustering was measured between $10-90$ μs The minimum cluster size was 3 for all figures. The dotted line marks the ϵ used in the chapter (1.5 nm).

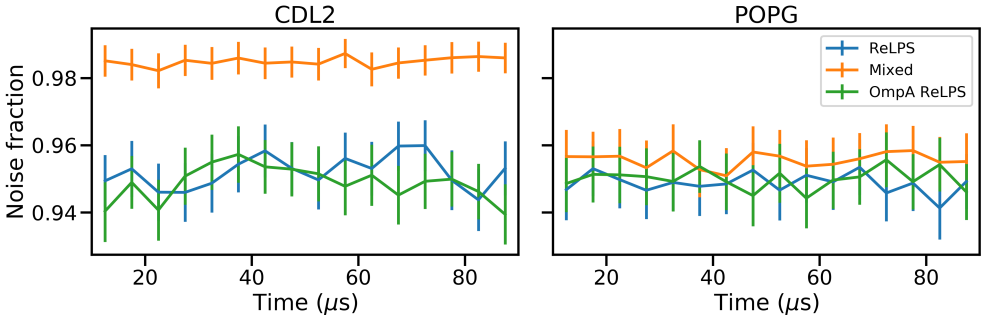

FIGURE 3.24: Fraction POPG and cardiolipin (CDL2) not within clusters, block averaged across 5 μs blocks from $10-90$ μs. Analyses were carried out for three systems, Mixed (90% POPE, 5% POPG and 5% CDL2), the ReLPS outer membrane and OmpA in a ReLPS outer membrane. The lower leaflet of each outer membrane system had the same composition as the symmetric system. The DBSCAN parameters used were $\epsilon = 1.5$ nm and $minPts = 3$.

constant at 3. The dotted line marks the ϵ used in this work (1.5 nm). The fraction of noise for the parameters used in this work was greater than 0.8, while less than 1% of the lipids were in the largest cluster; from the view of data science the degeneracy in clustering was too high. If ϵ was increased to at least 2.5 nm then noise would have been below 30% and the number of cluster would have been maximised. Another heuristic for setting ϵ, that was based on the k-th nearest neighbour of the data (where k is the value of $minPts$), gave an optimal ϵ of 3.6 nm [162]. However, the best parameters from a data science perspective are not necessarily physically reasonable when analysing a biological system. For example, the motion of lipids greater than 2 nm apart would not be very correlated and so should not be considered to be within the same cluster. Instead, an ϵ of 1.5 nm used, as this was approximately the distance between second nearest neighbours. Furthermore an ϵ of 1.5 nm and $minPts$ of 3 was used in a previous study of lipid clustering in the plasma membrane[167].

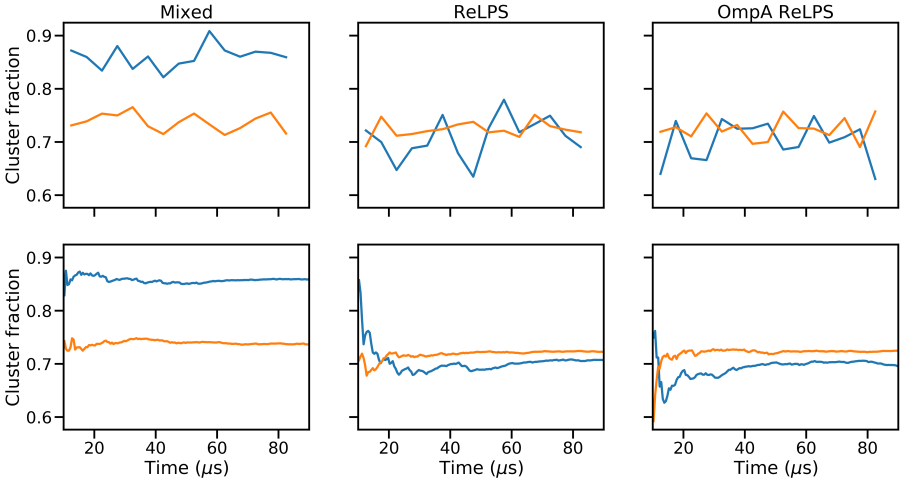

FIGURE 3.25: (top) Fraction of each clusters of each size, with respect to the total number of clusters, averaged across across 5 μs blocks from 10−90 μs for POPG (orange) and cardiolipin (blue). (bottom) Rolling average of cluster fraction, from $10 - 90\mu s$ for POPG (orange) and cardiolipin (blue). Analyses were carried out for three systems, Mixed (90% POPE, 5% POPG and 5% CDL2), the ReLPS outer membrane and OmpA in a ReLPS outer membrane. The lower leaflet of each outer membrane system had the same composition as the Symmetric system. The DBSCAN parameters used were $\epsilon = 1.5$ nm and $minPts = 3$.

First the fraction of noise was averaged across 5 μs blocks for cardiolipin and POPG in each system. (Figure 3.24). In outer membrane systems there were more cardiolipins in clusters, while for POPG the number of clusters did not change significantly between systems. In all cases, the number of lipids in clusters was less than 10% of the total number of a given lipid type. Given the previously observed localisation of cardiolipin density in OM systems, the small fraction of cardiolipin clusters identified with DBSCAN does not make sense. It could be possible that the localisation of cardiolipin density was caused by increased cardiolipin residency times below voids in LPS sugar packing, rather than the formation of large clusters.

Now the size distribution of the identified clusters will be discussed. The number of cluster of each size was presented as a fraction of the total number of clusters. First rolling and block averages of cluster sizes of three ($\epsilon = 1.5$ nm and $minPts = 3$) were used to assess convergence (Figure 3.25). For the Mixed membrane the clustering fraction oscillated around a mean of ~ 0.75 and ~ 0.85 for POPG and cardiolipin, respectively. For OM systems the POPG block average converged, whereas there were greater fluctuations in the cardiolipin cluster fractions. The rolling average of cluster fractions showed that in all cases POPG clustering fractions converged. The rolling averages of caridolipin cluster fraction converged for all systems, except for system with OmpA in ReLPS. It was noted that most of these clusters had lifetimes smaller than 1 ns, which was the time resolution of the trajectory.

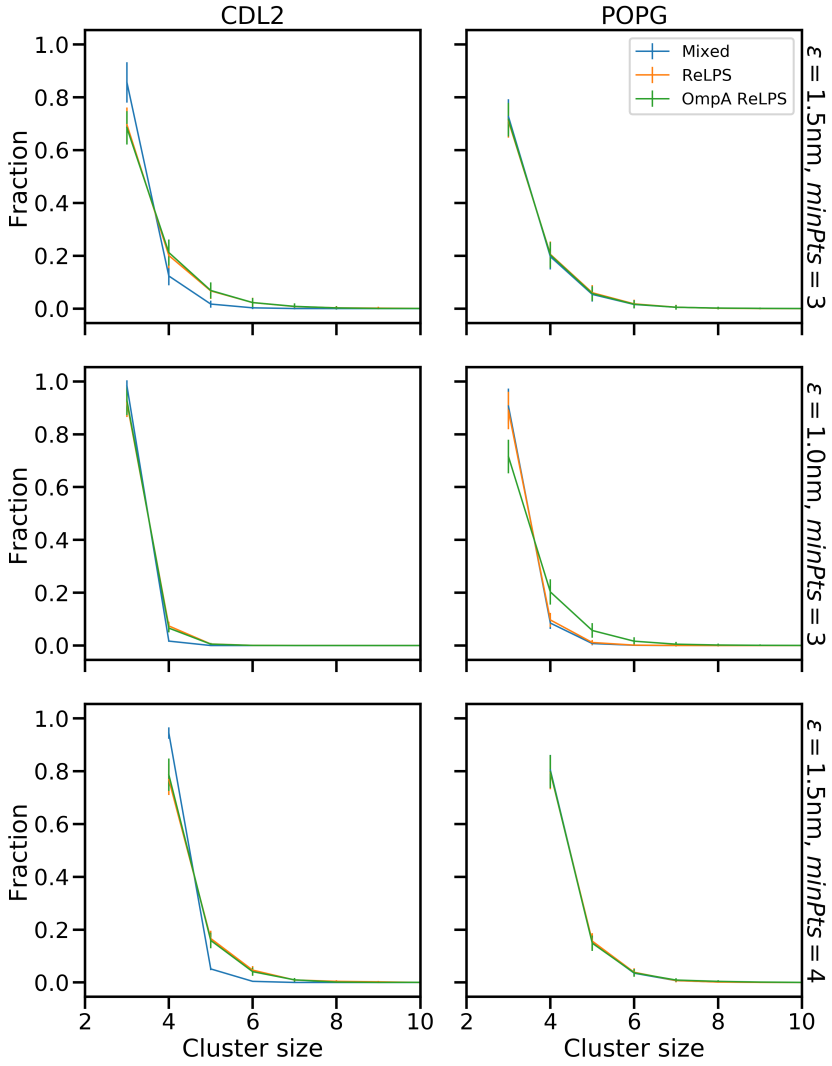

FIGURE 3.26: DBSCAN cluster analysis from $10 - 90$ μs of each trajectory utilising different parameters ϵ and $minPts$, as a function of cluster size. The standard error in each value was determined. ϵ sets the distance required between pairs of points to be in a cluster. $minPts$ was the minimum number of points within ϵ of each other for a cluster to be defined. A more in depth description of DBSCAN was provided in Section 3.2.3.2.

The cluster fraction as a function of cluster size was determined for a number of parameters (Figure 3.26). The additional two sets of parameters tested has either a reduced ϵ (1.0 nm) or an increased $minPts$ (4), compared to the original parameters ($\epsilon = 1.5$ nm and $minPts = 3$). For the original parameter set, more than 90% of clusters were smaller than 5 lipids. There was no difference in the distribution of cluster sizes between the Mixed, or both OM systems for POPG; whereas for cardiolipin clusters were larger for OM systems. What was interesting was that the clustering of cardiolipin appeared to be completely independent of the protein. While this was not definitive proof, smaller proteins may not have a large effect on clustering in the outer membrane.

For cardiolipin and POPG changing the minimum size of the cluster had little effect on the trends observed between systems, but did affect the quantitative values themselves. Changing ϵ to 1.0 nm had a larger influence on the trends observed. The increase in clustering from Mixed to OM membranes was much less than it was for the original parameter set. Whereas, for POPG the identified clusters exhibited an increase in cluster size when OmpA was in the outer membrane compared to other systems. The curve for the OmpA ReLPS system was identical to when the DBSCAN parameters were $\epsilon = 1.5$ nm and $minPts = 3$. Therefore the clustering density of POPG, for OmpA in ReLPS, was slightly larger than the other systems.

3.4 Conclusions

Coarse grained MD simulations were performed on natural and model nanopores in a mixed phospholipid (18:2:2 POPE:POPG:cardiolipin) bilayer and the Gram-negative outer membrane, to determine the contribution of the shape, size and chemistry on the structural and dynamic properties of bacterial membranes. For systems where the leaflet dynamics were similar, the protein shape, size and chemistry had a major effect on local membrane properties. The magnitude of the reduction in diffusion at short ranges increased with the size of the embedded nanopore. The diffusion of lipids in each leaflet depended on the number of contacts between lipid headgroups and the polar or charged surface of each nanopore. While the effects of the shape of a nanopore certainly played a role in the asymmetry of diffusion between leaflets, for most systems it was not the dominating factor. Further quntification of residue charge could be done by mutating only the charged residues in natural nanopores to polar beads. However, the results of such a study may be hampered by the poor representation of long range electrostatics within the Martini forcefield. A variant of Martini uses a polarisable water model to give a better charge screening in biological systems[168]. The polarisable water model can be combined with PME, to give improved electrostatics in Martini, at a cost of nearly an order of magnitude in simulation speeds. Any in depth study of the effect of mutating charged beads in a protein would benefit from the consideration of multiple CG representations of electrostatics.

For the asymmetric outer membrane the system properties were much more dependent on the structure and dynamics of the slow moving ReLPS layer. LPS motion was extremely correlated to nanopore motion, even at large distances from the nanopore ($> 8nm$). However, the movements of phospholipids in the inner leaflet of the outer membrane were less correlated to nanopore motion than in the equivalent symmetric membrane. These observations were believed to have been caused by differences in protein motion in the outer membrane system. The local structure around each nanopore was minimally affected by the nanopore in an outer membrane system. Instead, the global structure of the inner leaflet of the outer membrane was affected by the packing of ReLPS. Comparison between the structure and dynamics of outer membranes containing different nanopores and the membrane only system suggested that the nanopore may affect the packing of the ReLPS layer and thus the properties of the lower leaflet. As a general rule, if the leaflet dynamics differ greatly, then the slowest layer will likely dominate the importance of protein-lipid interactions.

Chapter 4

The Interactions Between Outer Membrane Proteins and Membrane Complexity

4.1 Introduction

In Chapter 1 it was discussed how proteins can modulate lipid properties and conversely how lipids can affect protein function. Thus it is key that we understand how protein-lipid interactions affect the biological functions of the cell envelope. Outer membrane proteins (Omps) play a larger number of roles from structural stability, to signalling. The Omps in *E.coli* are solely comprised of beta barrels that vary in size from $8 - 22$ beta strands[79].

The most comprehensive study of Omps so far has been that of Stansfield *et.al*[169] who developed a database that automatically inserts proteins into DPPC membranes and performs analysis on the resulting coarse-grained and atomistic simulations. However the behaviour of Omps are not only a function of their structure, but the membrane that they reside in. The outer membrane (OM) is asymmetric with an upper leaflet of mainly LPS and a lower leaflet containing a mixture of phospholipids. The significant differences in structure and dynamics of the outer membrane versus symmetric membrane models have been discussed in previous simulations[35, 149]. The inclusion of an *E.coli* membrane model in simulations of FecA has been shown to affect both the conformation and the loop dynamics of the protein[103]. A few Omps such as FhuA and OmpF have been known to have specific LPS binding sites[170, 171].

In recent work by Corradi *et. al*[160] a combination of lipid sorting and lipid-protein interactions were found to form a unique 'fingerprint' across a range of proteins in model

plasma membranes. As far as the author is aware there is no such study that has been carried out for a range of Omps in the OM. The length and time-scales required for such a broad study are well suited to coarse-grained models.

Here coarse-grained simulations of OmpA, OmpX, OmpF, FhuA, BtuB and EstA were carried out on a series of outer membrane models with varying LPS levels (ReLPS, RaLPS etc.). The proteins chosen represented a wide range of sizes, functions and oligomeric forms found in the outer membrane. OmpA and OmpX are small monomers, OmpF is a trimer, FhuA and BtuB are large beta barrels and EstA is a multidomain protein. Through studying a range of proteins and LPS levels the aim was to identify patterns in behaviour as a function of protein type and membrane model. A large amount of the work described in this chapter contributed to a recent paper[172].

4.2 Methods

4.2.1 Membranes

There are five outer membrane compositions that were investigated in this chapter. In all cases the lower leaflet contained 90% POPE, 5% POPG and 5% cardiolipin, the composition used in the previous chapter. Three out of five compositions of the upper leaflet were comprised of solely Re, Ra or Smooth LPS (OANT). Here smooth LPS referred to the Ra model used in this work, with an additional O-Antigen chain containing 5 monomer units(Figure 1.3). For the last two systems the upper leaflet was comprised of: 1) a mixture of smooth LPS and POPE in a 4:1 ratio (OANT_PE) and 2) smooth LPS, Ra LPS and POPE in a 2:2:1 ratio (MIXED). These LPS models were all obtained from the CHARMM-GUI 'Martini Maker' module[96, 155]. The LPS models used here were parameterized by previous members of the group[95, 172]. For the sake of comparison a symmetric DPPC system was also studied here. For snapshots of all membrane systems used in this chapter see Figure B.1.

4.2.2 GoMartini: A Flexible Protein Model

Martini force field protein model cannot reproduce the effects of directional interactions (e.g. hydrogen bonding) that are required to maintain protein secondary structure. The standard approach is to restrain the backbone close to a reference structure (usually the crystal structure) with an elastic network model constructed of pairwise harmonic restraints with a set cutoff (the ElNeDyn model) [173]. One issue with the ElNeDyn model is that it assumes the reference structure is close to the true ensemble of structures in solution, which may not be the case. A recently developed model, GoMartini [173],

utilises a Lennard-Jones (LJ) network to maintain the secondary structure of proteins, thus allowing protein folding to be studied at the CG level. The backbone pairs in the LJ network are decided by the contact map of the native protein, which leads to a smaller network compared to the ElNeDyn model. The LJ parameters were set based on the C_α-C_α distance, d, between pairs that formed contacts, such that $\sigma_{ij} = d/2^{1/6}$. Whereas epsilon, ϵ_{ij}, was set to 9.414 kJmol^{-1}, as this was found to give behaviour that compared well to atomistic simulations[173]. During this chapter the ElNeDyn model was mainly used, but the effects of the GoMartini model will be discussed.

4.2.3 Simulation Protocol

Initial structures for OmpA (1QJP)[53], OmpX (1QJ8)[174], OmpF (3POX)[175], BtuB (1NQE)[176], FhuA (1QFG)[170] and EstA (3KVN) [177] were obtained from the RCSB protein databank. Missing residues or broken loops were added with MODELLER[178] and then missing hydrogens added with PDB2PQR[179]; subsequently the protein was given a transmembrane alignment by the program MemEmbed[180]. Each protein was then fed into the CHARMM-GUI pipeline and inserted into the membranes mentioned in Section 4.2.1. Each protein was coarse-grained using the ElNeDyn model and the backbone beads within a 0.9 nm cutoff restrained with a 500 kJmol^{-1}nm^{-2} elastic network. In addition to the previously described simulations, the GoMartini protein model was also used for ReLPS systems containing OmpA and OmpX. The LPS lipids were neutralised with Ca^{2+} ions and remaining charge imbalance with NaCl ions, as needed. An additional 0.15 M NaCl was added to each system to mimic the ion concentrations found *in vivo*.

All simulations in this chapter were carried out with GROMACS 2016[150] and the Martini forcefield (version 2.2)[152]. Simulations were performed at a temperature and pressure of 323K and 1 bar, respectively and the temperature coupled to a stochastic velocity rescale thermostat with a coupling constant if 1.0 ps. Once the initial structure of each system was generated with CHARMM-GUI, minimisations and equilibration were carried out according to the protocol recommended by CHARMM-GUI[96]:

1. Steepest descent minimisation with soft core potentials
2. Steepest descent minimisation
3. A series of equilibrations with timesteps of 5 and 10 ps and restraints on the lipid headgroups in the Z direction ranging from 200 to 0 for a total of 20 ns - The protein was restrained with a 1000 kJmol^{-1}nm^{-2} harmonic restraint. In these steps a Berendsen barostat with a coupling constant of 4.0 ps was used.

Following equilibration, production runs of up to 60μs were run for each system with 2 repeats. All production runs had a timestep of 10 fs and the pressure regulated with a

semi-isotropic Parrinello-Rahman barostat, with a coupling constant of 12 ps. The full details of all simulations can be found in Table 4.1. It is worth noting that there was not enough time to get sufficient simulation data for some of the MIXED systems and thus any system that had less than 30 μs for both repeats was ignored.

The short range cutoff for non-bonded interactions was 1.2 nm and utilised the Potential-Shift-Verlet cutoff scheme. The electrostatic interactions were determined with reaction field with short and long range dielectric constants of 15 and 0 (infinite shielding), respectively. The Verlet buffer tolerance was set to 0.005 kJmol^{-1}ps^{-1}.

TABLE 4.1: Details of all simulations carried out during Chapter 4.

membrane protein	membrane	time (μs)	box dimensions (nm)
OmpA	ReLPS	2×40	$13.0 \times 13.0 \times 16.2$
	RaLPS	2×60	$13.0 \times 13.0 \times 18.7$
	OANT	2×30	$13.0 \times 13.0 \times 27.2$
	OANT_PE	2×30	$13.1 \times 13.1 \times 26.8$
	OANT_RA_PE	2×40	$13.2 \times 13.2 \times 26.8$
	DPPC	2×20	$13.5 \times 13.5 \times 15.8$
OmpX	ReLPS	2×30	$13.5 \times 13.5 \times 16.4$
	RaLPS	2×30	$13.5 \times 13.5 \times 18.7$
	OANT	2×30	$13.0 \times 13.0 \times 26.8$
	OANT_PE	2×30	$13.5 \times 13.5 \times 26.9$
	OANT_RA_PE	2×30	$13.4 \times 13.4 \times 26.8$
	DPPC	2×20	$13.5 \times 13.5 \times 16.0$
OmpF	ReLPS	2×30	$16.6 \times 16.6 \times 16.1$
	RaLPS	2×30	$16.9 \times 16.9 \times 18.4$
	OANT	2×30	$16.2 \times 16.2 \times 26.8$
	OANT_PE	2×30	$16.2 \times 16.2 \times 26.8$
	OANT_RA_PE	2×30	$16.3 \times 16.3 \times 26.5$
FhuA	ReLPS	2×30	$13.6 \times 13.6 \times 17.8$
	RaLPS	2×30	$13.1 \times 13.1 \times 18.7$
	OANT	2×30	$13.1 \times 13.0 \times 27.1$
	OANT_PE	2×30	$13.1 \times 13.0 \times 27.1$
EstA	ReLPS	2×30	$15.8 \times 15.8 \times 20.1$
	RaLPS	2×30	$15.8 \times 15.8 \times 20.1$
	OANT	2×30	$15.8 \times 15.8 \times 26.5$
	OANT_PE	2×30	$15.8 \times 15.8 \times 26.9$
BtuB	ReLPS	2×40	$13.0 \times 13.0 \times 16.7$
	RaLPS	2×40	$13.0 \times 13.0 \times 18.5$
	OANT	2×40	$13.0 \times 13.0 \times 30.6$
	OANT_PE	2×40	$13.1 \times 13.1 \times 26.7$
OmpA (GO)	ReLPS	2×30	$13.0 \times 13.0 \times 16.2$
OmpX (GO)	ReLPS	2×30	$13.5 \times 13.5 \times 16.3$

4.2.4 Analysis

In general analysis was carried out on simulations from 25-30 μs, unless stated otherwise. Analysis was carried out using a combination of GROMACS tools and in house scripts written with the python module 'MDAnalysis' as the base[158]. Any images of molecular systems in this chapter were rendered with VMD[157].

4.2.4.1 Protein Tilt

The Protein tilt was determined by first defining a transmembrane backbone region for all proteins, except OmpF;for OmpF the entire backbone of the trimer was used. The selected regions of the proteins were then used to determine the transmembrane principal axis and subsequently the protein tilt angle was defined as the angle between this principal axis and the z axis.

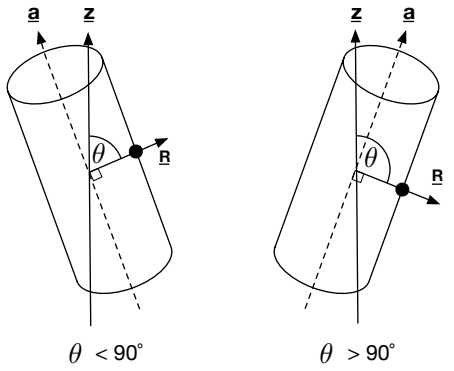

FIGURE 4.1: Diagram that outlines the calculation of the relative angle (θ). The cylinder represents a model membrane beta barrel. Where **a** is the trans membrane principal axis and **R** is the shortest distance between **a** and the reference point. Reprinted with permission from Shearer et al. [172]. Copyright 2019 American Chemical Society 2019.

The relative tilt angle was defined as the angle (θ) between **R** and the z-axis (**z**) as shown in Figure 4.1. **R** was the shortest vector between the centre of geometry of a reference residue and the transmembrane principal axis **a**. The reference residues used for θ were Thr 144, Ser 469, and Gly 232 for OmpA, EstA and OmpF, respectively; these reference residues were chosen such that they were on the surface of the protein.

4.2.4.2 Contact analysis

Contact analysis of lipids with each protein were carried out with an in-house script that defined a contact as when the two groups of interest are within 0.6 nm of each other. When there were multiple contacts between a protein residue and a lipid these

were counted as only one contact. Contact maps were generated with a combination of VMD and an in-house script.

4.2.4.3 Membrane Structure and Dynamics

For all membrane thickness methods, the thickness was defined with respect to the phosphate beads, as water does not tend to permeate past the phosphates. For symmetric membranes grid based methods[156] are often used to determine thickness. In a grid based method each membrane leaflet is discretised onto a 2D grid and the average reference bead position in each voxel determined. Therefore the thickness is the absolute difference between the 2D grids of the bilayer. However, in the case where one leaflet is a lot less dense in phosphate groups than the other, e.g. the outer membrane, this means that not many thickness values can be calculated. Here Delaunay triangulation was used for thickness calculations as done in a previous software package, APLVORO[181]. The thickness was found by finding the projected distance in the z dimension between the phosphate headgroups in one leaflet to the Delaunay triangulation of the other leaflet. Thus thickness values can be obtained with respect to the triangulation of either leaflet. In general the average thickness will not be dependant on the leaflet used for projection; however, 2D thickness maps can show large differences. The method can be adapted to give better estimations of lipid area and membrane thickness near a protein[181]. In this work the thickness was measured from the projection from the lower leaflet onto the triangulation of the LPS layer.

The lipid depletion-enrichment indices (D-E indices) and 2D enrichment maps were methods originally used by Corradi *et.al*[160]. The first step of determining the D-E index was to calculate the number of lipids within a certain cutoff of the protein, where the reference point of each lipid was the molecular centre of geometry. Then the local fraction ($c_{local,l}$ of each lipid, l, within the previously defined cutoff was determined

$$c_{local,l} = \frac{n_{local,l}}{n_{local,T}} \tag{4.1}$$

where $n_{local,l}$ was the number of local lipids of type l and $n_{local,T}$ was the total number of lipids within the local region. The local fraction of each lipid can then be compared to what would be expected if the membrane density was homogeneous.

$$D - E\ index = \frac{c_{local,l}}{c_{global,l}} \tag{4.2}$$

where $c_{global,l}$ was the fraction of each lipid present in the entire membrane. Thus a D-E index of > 1 indicates enrichment, while an index < 1 indicated depletion. For each system the D-E index was calculated between 10 to 30 μs in 5 μs blocks across both repeats and all eight values averaged to get a final D-E index and standard deviation. A 2D enrichment map for a given lipid type was determined by normalising the density of

the each voxel of a 2D grid in the xy plane with respect to the average density. Again if the Enrichment percentage is > 0 % then this indicates enrichment, while < 0 % means the voxel is depleted of lipids.

$$Enrichment\ percentage = \frac{density}{average\ density} \times 100 \tag{4.3}$$

In membrane systems Equations (4.1) and (4.2) can be applied to either the entire membrane or a single leaflet. In this chapter lipids in each leaflet were considered separately for all enrichment related calculations.

4.2.4.4 Analysis of O-Antigen Structure and Dynamics

Multiple measurements of the relative tilt of the O-Antigen chains were developed based on the normalized end to end vector of each O-Antigen chain. Calculating the angle between the end to end vector and the z axis gave the tilt relative to the plane of the membrane. The values of the tilts were presented as a probability distribution with units of $\cos(\theta)$. Two probability distributions were generated based on whether the lipid A group of each smooth LPS was within 2.5 nm of the membrane protein i.e. in the "local" or "bulk" region. The cutoff was set as 2.5 nm as this is roughly the radius of the annular region based on previous simulations[149, 160]. The relative tilt between pairs of O-Antigen chains was obtained by taking the angle (in units of $\cos(\theta)$) between their end to end vectors, if the chains were within 0.6 nm of each other. Relative tilt values were defined in the range $[-2, 0)$ and $[0, 2]$ if the chains tilted away or toward each other, respectively. Cosine probability distributions were used as they are less sensitive to random fluctuations.

4.2.4.5 Block Covariance Overlap Analysis Method

The block covariance overlap method (BCOM) was developed by Romo and Grossfield and uses a combination of block averaging, principal component analysis (PCA) and bootstrapping[182]. First PCA was carried out on subsets of the trajectory, resulting in the vectors that describes the orthogonal motions of the system and their relative importance. Following this the similarity between the PCA modes in each subset was found via computing the covariance between PCA modes. The trajectory subsets can be obtained through the use of contiguous blocks or via bootstrapping techniques (BBCOM) and computing the ratio between these two methods can estimate the relaxation times of sampling. In both cases the block sizes used were increased incrementally from 0.3 to 30 μs in 0.3 μs intervals. For the BBCOM method the number of blocks used was always 10, whereas for contiguous blocks the number of blocks was inversely proportional to the block size. Further details of the mathematical basis of these methods is described in detail in the original paper[182].

4.3 Results and Discussion

4.3.1 Protein Orientation

Protein tilt relative to the membrane can be an important measure of protein-lipid interactions, that is often decided by the oligomerisation state of the protein and hydrophobic mismatch. While the protein tilt can be determined experimentally[183, 184], MD has been shown to be a powerful tool for such measurements[185, 186]. The protein tilt was determined for all protein containing systems, for at least 20 μs of simulation time per repeat. In this next section only the results for DPPC, ReLPS, RaLPS, OANT and OANT_PE membrane systems will be discussed to simplify the discussion of trends. Note that the protein tilts were block averaged across 100 ns intervals to obtain averages and standard deviations. Overall, the trends in protein orientation seen for outer membrane systems (Figure 4.2) were very different from their phospholipid counterparts in the literature [185] and the DPPC systems in this chapter (Figure 4.6). In the DPPC systems both repeats have block averages that do not differ outside measured standard deviations at any point in these simulations. There also was no observable equilibration time at the time scale these results were shown, suggesting that the system relaxed within the first 100 ns of the simulation.

For each LPS system it can be seen that extreme changes ($\sim 10^{\circ}$) in protein orientation usually occur within the first 5 μs of the simulation and often larger fluctuations were present throughout the entire trajectory. It was reasoned that such differences in the timescale of fluctuations in protein orientation was a result of the LPS limiting the rate of change of orientation, compared to regular phospholipid systems. While the protein orientation appears to converge within, and between repeats by the end of the simulation for some systems, this was not always the case. For example, for OmpA in OANT during the early parts of both repeats the tilts were similar, but after around 10 μs the tilt values diverged from each other by around 8°. It seemed likely that the protein tilt in LPS systems can appear converged over microsecond periods, but is in fact in a metastable state; this really highlights the need for simulations on the 10s of μs scale when studying LPS.

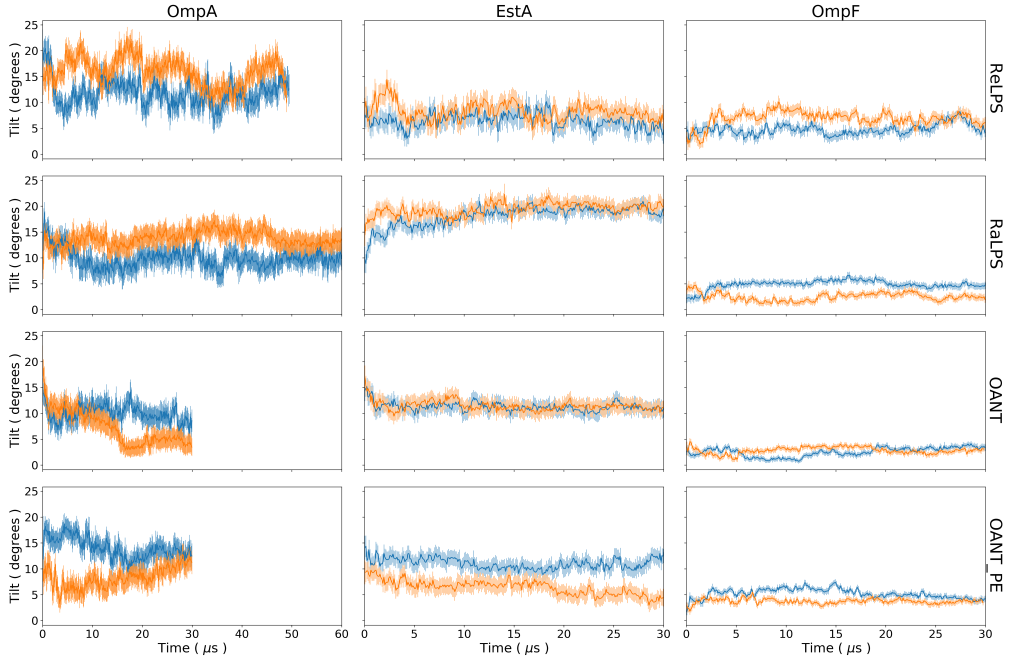

(a)

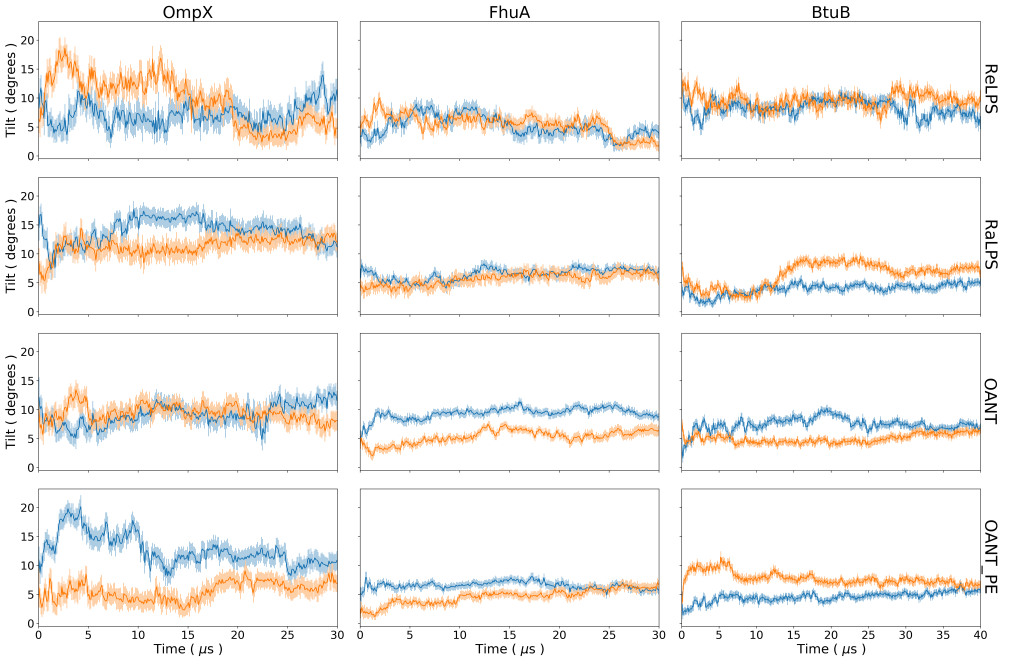

(b)

FIGURE 4.2: The protein tilt of the trans-membrane region of each protein backbone with respect to the z-axis as a function of time for each repeat. In the case of OmpF, the tilt was determined using the entire protein backbone. Further details of the protein tilt calculation can be found in the Methods section (Section 4.2). Each column corresponds to a single membrane protein, while each row contains a certain level of LPS: ReLPS, RaLPS, and OANT in descending order. The errors were generated from the standard deviation of block averages taken over 100 ns intervals. Reprinted with permission from Shearer et al. [172]. Copyright 2019 American Chemical Society 2019.

The trends observed in tilt angle as a function of LPS level are often unclear. For example, for OmpA tilts average $\sim 12°$ in ReLPS, $10-12°$ in RaLPS, around $8-10°$ in OANT and $11°$ (although it is still changing linearly) for OANT_PE - there was no obvious pattern in these observations. Similar conclusions can be drawn from four of the other proteins studied here. Some broad patterns can be noted in that the tilts for the larger proteins (FhuA, BtuB and EstA) tend to vary a lot less than the smaller ones (OmpA and OmpX). This is not a surprising observation as the energetic cost of larger proteins tilting is much larger and so will often be avoided if other alternatives such as lipid sorting and membrane distortions are more favourable.

In the case of EstA a clear pattern was observed in the trends of protein tilt as a function of LPS level. EstA tilts were $\sim 8°$ ReLPS, $\sim 20°$ RaLPS and $\sim 11°$ for OANT systems. It was initially thought that a protein with such a large extracellular domain, like EstA, would experience a general decrease in tilt with increasing LPS level as the protein becomes more and more restricted by the sugar region of LPS. Instead, the tilt increased from the ReLPS to the RaLPS system and then decreased when in the OANT system to a value even lower than that seen for ReLPS. Upon visualisation of these systems it became apparent why these initially obscure trends occurred (Figure 4.3). In the RaLPS system (Figure 4.3B) the bulb like extracellular domain can tilt to form preferential interactions with the core sugars in RaLPS, whereas the core sugar region in ReLPS was too short to form these favourable interactions - thus RaLPS had the largest tilt. Going into more detail, in the ReLPS system EstA tilt would have had to have been larger than that of RaLPS to form the same interactions, which was thermodynamically unfavorable (due

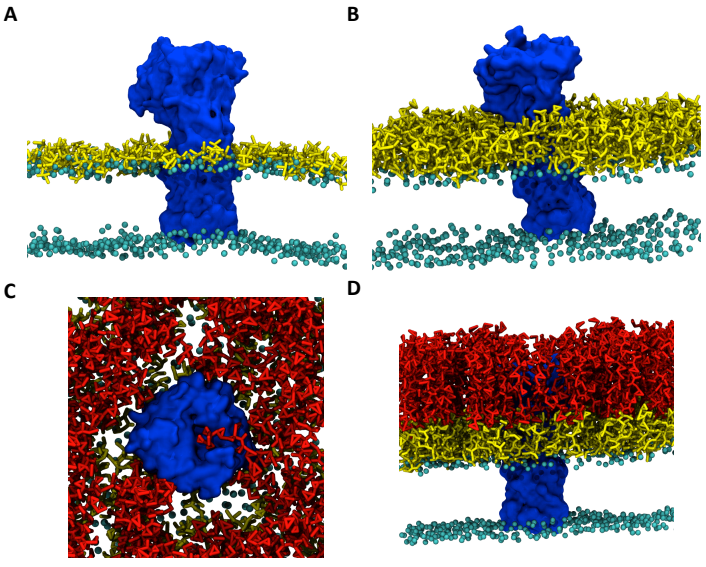

FIGURE 4.3: Snapshots taken at 30 μs of EstA in the A) ReLPS, B) RaLPS, C) OANT (top view) and D) OANT (side view) systems. Colour key: blue=protein, red=O-Antigen, yellow=core sugars and cyan=phosphates. In the RaLPS system it can be see that the extracellular bulb-like domain of EstA tilts to contact the LPS core oligosaccharides. Reprinted with permission from Shearer et al. [172]. Copyright 2019 American Chemical Society 2019.

to larger hydrophobic mismatch and the distortion of the membrane). For the OANT system the LPS had a more extensive extracellular domain than EstA (Figure 4.3C and D) and so EstA was pinned in an upright position by the surrounding O-Antigen chains. It is plausible that for any protein with a significant extracellular domain the level of LPS will have a large effect on protein orientation within the membrane.

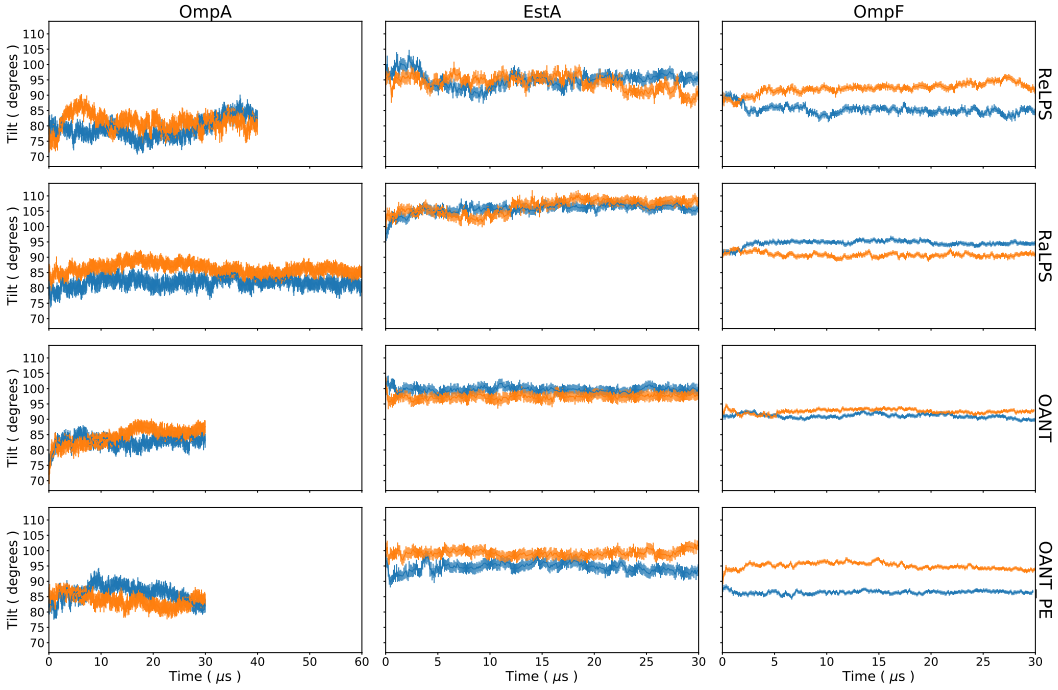

FIGURE 4.4: The relative protein tilt of the transmembrane region of each protein backbone with respect to the z axis relative to a certain residue as a function of time for each repeat. Further details of what this tilt angle means can be found in the Methods section and Figure 4.2. Each column corresponds to a single membrane protein, while each row contains a certain level of LPS: ReLPS, RaLPS, OANT and OANT_PE in descending order. The residues used for the relative angles were THR 144, SER 469 and GLY 232 for OmpA, EstA and OmpF, respectively. The errors were generated from the standard deviation of block averages taken over 100 ns intervals. Reprinted with permission from Shearer et al. [172]. Copyright 2019 American Chemical Society 2019.

So far it has been uncovered that while observed patterns are complex, LPS level can have a profound effect on protein orientation. However, do the same residues always tilt towards membrane? To answer this question the concept of a relative protein tilt was required, such that the direction of tilt towards the membrane can be quantified in a manner that it is invariant to the rotation and translation of the protein in the xy plane. A reference residue was picked on the surface of the transmembrane region of a protein. Then the relative tilt was defined as the angle between the shortest vector, $\underline{\mathbf{R}}$, between the transmembrane principal axes of a protein and the centre of geometry of the reference residue and the z-axis (see Figure 4.2 and Section 4.2 for more details). If the relative tilt was greater than 90° then $\underline{\mathbf{R}}$ points towards the membrane, otherwise $\underline{\mathbf{R}}$ points away from the membrane. The relative tilt was calculated for OmpA, EstA

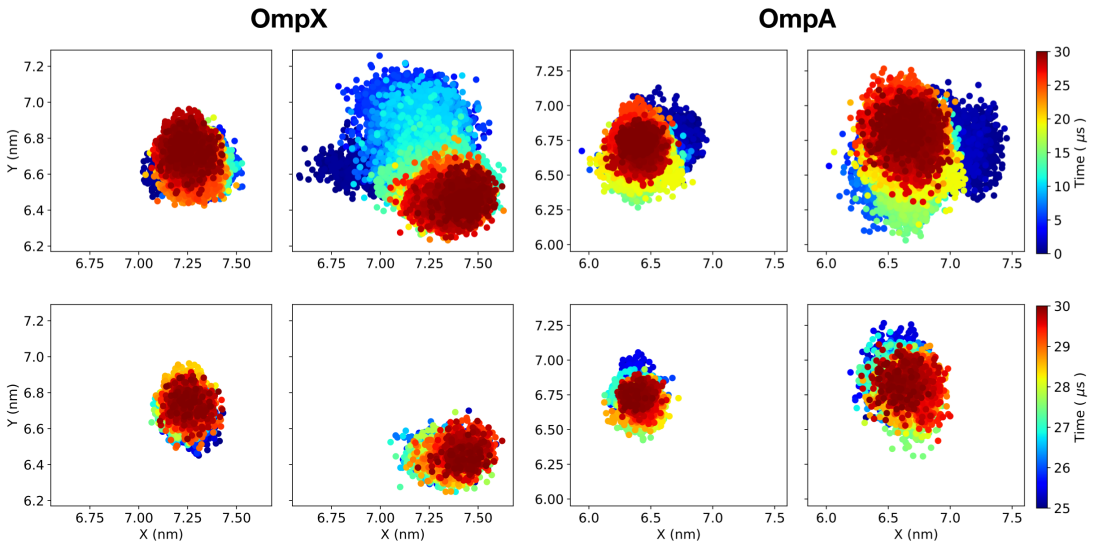

FIGURE 4.5: The barrel of each protein was divided into regions that were in either the lower or upper leaflet of the ReLPS outer membrane based on the centre of geometry of the entire transmembrane region of the protein backbone. The centre of geometry of the protein backbone of each region was then plotted as a function of time for (top) 0-30 μs and (bottom) 25-30 μs. Before this analysis was carried out each trajectory was centred on the protein's centre of mass. Reprinted with permission from Shearer et al. [172]. Copyright 2019 American Chemical Society 2019.

and OmpF using reference residues of Thr 144, Ser 469 and Gly 232, respectively (see Figure 4.4). For all OmpA and most EstA systems the relative tilt for both repeats was similar to within the measured errors. For OmpA the reference residue was always tilting away from the membrane, while for EstA the reference point generally tilted towards the membrane. Interestingly, OmpF could tilt away from or towards the membrane within the different repeats. In the OmpF trimer there was a residue in each monomer that was identical, in type and position, to the reference residue, which may explain the observed inconsistencies across repeats. Thus it can be concluded that the same monomer did not always tilt towards the membrane.

One thing neglected in previous studies of protein orientation was the potential effects of asymmetry of leaflet dynamics on the mobility of the protein in each leaflet. It has been established in this work and previous studies that LPS lipids diffuse significantly slower than most phospholipids. It seemed reasonable that this may have effect on the motion of smaller Omps, such as OmpA and OmpX. Here the mobility of OmpA and OmpX in each leaflet was shown by dividing the transmembrane region of each barrel into two parts in either the upper or the lower leaflet of the membrane. Then the centre of geometry was monitored for each section of the barrel from $0 - 30$ μs (Figure 4.5). During the first 20 μs of the OmpA and OmpX simulations the motion in the lower leaflet was significantly larger than in the LPS leaflet; this was particularly pronounced for OmpX. In the last 5 μs of each simulation the motion of the proteins in each leaflet was very similar. For the sake of comparison this analysis was also carried out for

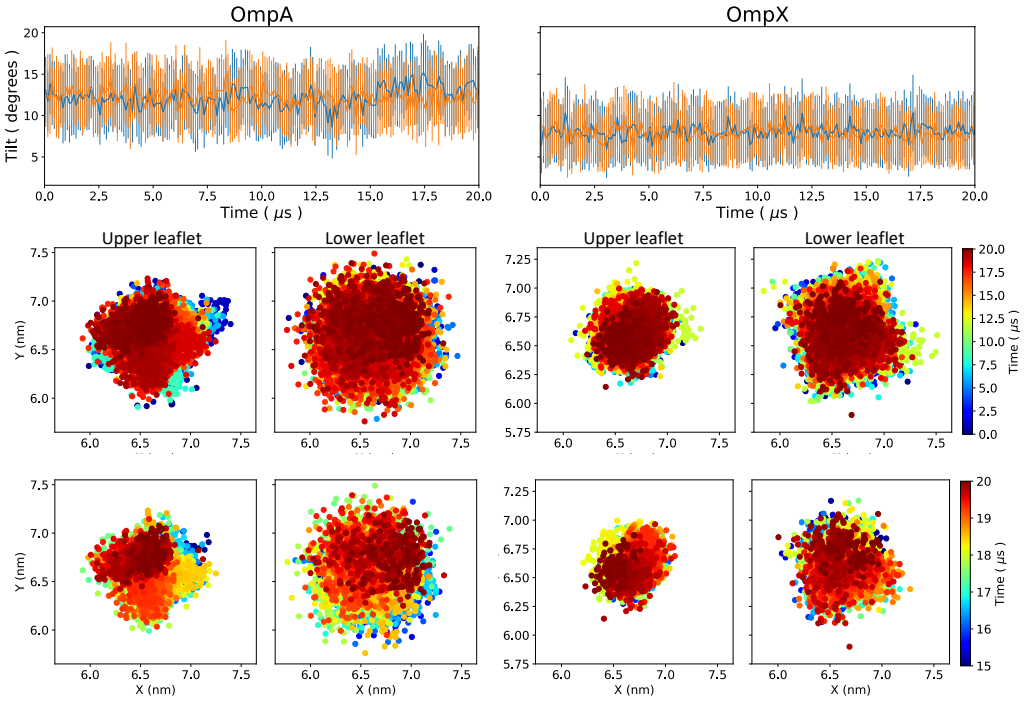

FIGURE 4.6: The protein tilt (top) and the motion of the protein in the upper and lower leaflet of the membrane as a function of time for OmpA and OmpX in a DPPC system. The protein tilt was determined with respect to the backbone of the transmembrane region of each protein. The errors were generated from the standard deviation of block averages taken over 100 ns intervals. Note that each line corresponds to a single repeat. The barrel of each protein was divided into regions that were in either the lower or upper leaflet of the ReLPS outer membrane based on the centre of geometry of the entire transmembrane region of the protein backbone. The centre of geometry of the protein backbone of each region was then plotted as a function of time for (middle) 0-30 μs and (bottom) 25-30 μs. Before this analysis was carried out each trajectory was centred on the protein's centre of mass. Reprinted with permission from Shearer et al. [172]. Copyright 2019 American Chemical Society 2019.

OmpA and OmpX in a simple DPPC bilayer (Figure 4.6). In both cases the motion of the protein in each leaflet was much more similar during the entire simulation. Thus for smaller Omps in the outer membrane, LPS pins the upper half of the protein, while the lower half moves to achieve the optimal protein orientation. In the literature it has been established that Omp orientation in the membrane is determined by the positioning of rings of aromatic residues with respect to the membrane thickness[187]. However, in the case of smaller Omps in the outer membrane this is clearly a far too simplistic conclusion.

In Figure 4.2 particularly poor mismatch between repeats was observed in many OANT and OANT_PE systems, which was likely due to poor sampling (as will be discussed later in this chapter). In an attempt to improve sampling the simulations for FhuA in OANT and OANT_PE were repeated at 360 K, for 15 μs per repeat. It was worth noting that this is quite outside the range of temperatures for which the Martini model is known to perform optimally, but was done more as a proof of principle. The protein

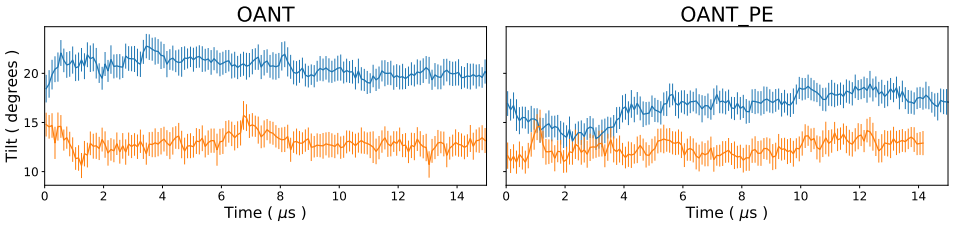

FIGURE 4.7: The protein tilt of the trans-membrane region of the FhuA backbone in OANT and OANT_PE with respect to the z-axis as a function of time for each repeat. These systems were simulated at 360 K. Further details of the protein tilt calculation can be found in the Methods section (Section 4.2). The errors were generated from the standard deviation of block averages taken over 100 ns intervals.

transmembrane tilt was measured for these simulations (Figure 4.7) and it was found that while tilt values increased, there was still no overlap between repeats. More aggressive enhanced sampling methods such as replica exchange or umbrella sampling are likely required to solve these sampling issues.

4.3.2 Protein-lipid Interactions

The protein orientation is directly a result of the specific interaction between the protein and the membrane. Thus it is pertinent to discuss how specific interactions vary across protein membrane systems. As protein orientation is often determined by interactions with the lipid headgroup the interactions with the Lipid A headgroup shall be discussed first. Only the results for ReLPS membranes will be discussed as all LPS levels have the same lipid A headgroup. Overall it was observed that Lipid A headgroups prefer to form specific interactions with either basic or aromatic residues, which fits in with the importance of aromatic residues observed for atomistic and CG simulations of symmetric membranes [43, 187] (Figure 4.8). This doesn't seem too far fetched as ReLPS has a very small core sugar region (2 KdO units) and is the LPS in this work that is most similar to regular phospholipids.

While aromatic and basic residues often take up a large proportion of the contacts this does not appear to always be the case and each protein has it's own unique fingerprint. Contact histograms between these proteins and just the ReLPS phosphates showed that they formed a large contribution to the previously seen interactions with basic residues (Figure B.2). For OmpF and FhuA most interactions with basic residues were with lysine, while for the other proteins the interactions between lysine and arginine were similar. Even when contacts between the two basic residues were similar lysine still tended to have the greater number of contacts. For all proteins but OmpA and FhuA there was a preference for interactions with tyrosine above other aromatic residues.

OmpA was the only protein where basic and aromatic residues did not dominate the contacts formed to the Lipid A headgroup; instead forming strong contacts with polar

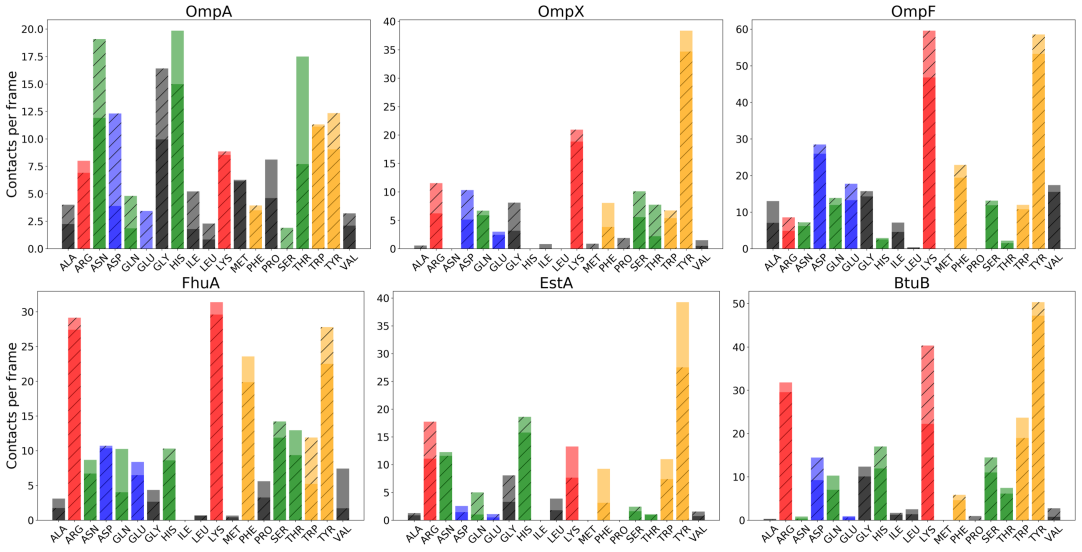

FIGURE 4.8: Average number of contacts per frame between each residue in a protein and the Lipid A headgroup for $25 - 30$ μs across repeats (one repeat has hash markings). Each bar was coloured with respect to the polarity of each residue: red=basic, blue=acidic, orange=aromatic, green=polar and black=non-polar. Reprinted with permission from Shearer et al. [172]. Copyright 2019 American Chemical Society 2019.

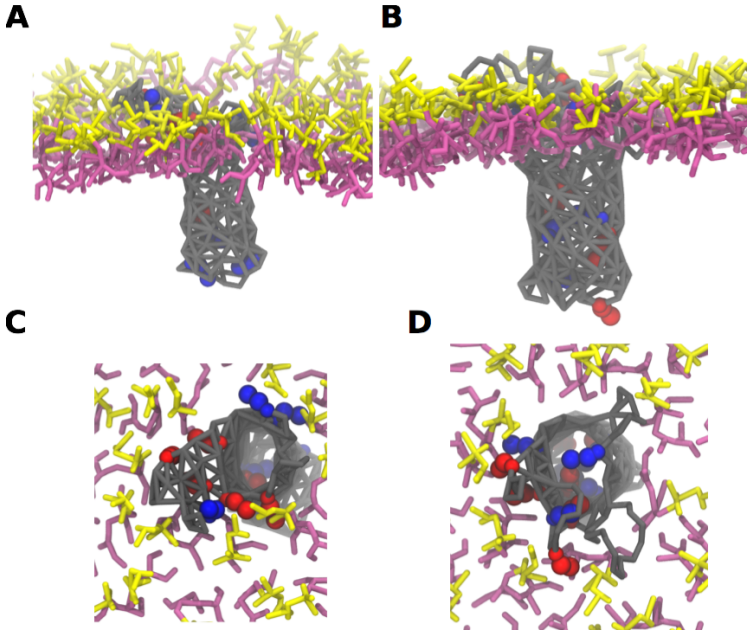

FIGURE 4.9: Snapshots of (A and C) OmpX and (B and D) OmpA in a ReLPS system, taken at 25 μs. Colour key: Lysine (red), Arginine (blue), protein backbone (grey), lipopolysaccharide (LPS) sugars (yellow) and Lipid A headgroup (purple). Reprinted with permission from Shearer et al. [172]. Copyright 2019 American Chemical Society 2019.

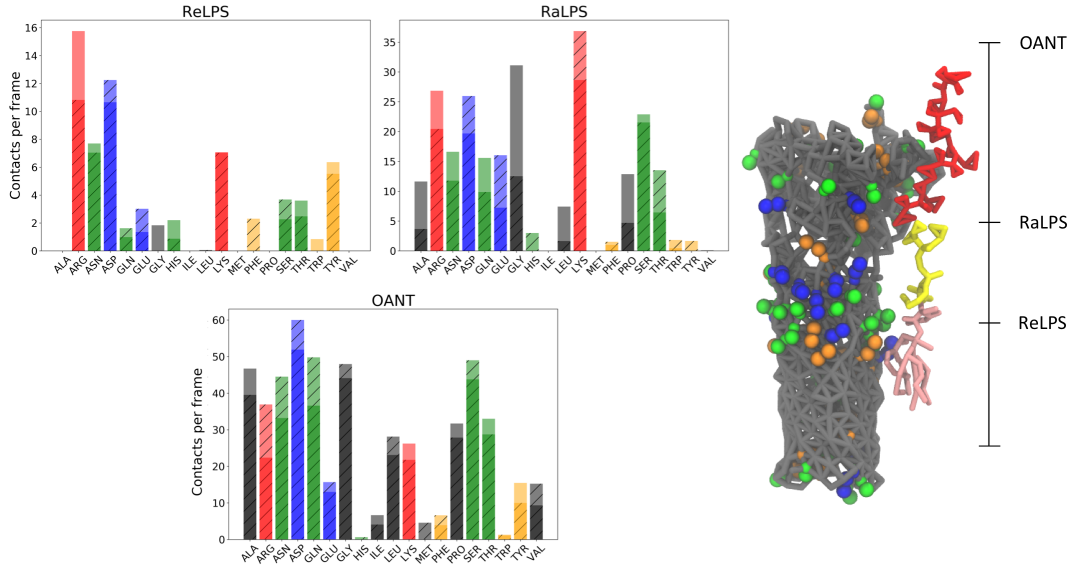

FIGURE 4.10: (left) Average number of contacts per frame between each residue in EstA and the lipopolysaccharide (LPS) core oligosaccharides and O-antigen (if present) from 25 to 30 μs across repeats (one repeat has hash markings). Every bar was coloured with respect to the polarity of each residue: red=basic, blue=acidic, orange = aromatic, green = polar, and black = nonpolar. Note that multiple contacts between a single residue and another lipid A headgroup were only counted once. (right) Model of EstA backbone (gray) with all arginine (orange), aspartate (green), and lysine (blue) residues shown next to a smooth LPS lipid. The height of LPS in ReLPS (pink), RaLPS (yellow), and OANT (red) systems is marked next to the LPS model. Reprinted with permission from Shearer et al. [172]. Copyright 2019 American Chemical Society 2019.

residues, such as asparagine and histidine. Comparing to the similarly sized OmpX (8 beta strands), polar residue contact frequencies were half that of OmpA, while contact frequencies with basic and aromatic residues are at least twice as large. Visualisation of the trajectories of each protein system showed that in both cases the extracellular loops of the proteins formed interactions with the ReLPS core sugars and lipid A headgroups (Figure 4.9). Upon further inspection of the composition of the loops it was found that OmpA had less basic residues than OmpX. Previous atomistic simulations in the literature have noted that the extracellular loops of OprH from *P.aeruginosa*, which are packed with positively charged residues, formed stabilising interactions with lipid A headgroups. One significant difference between the behaviours of OmpA and OmpX in the cell is the ability of the former to dimerise [88, 188]. The extracellular loops are known to be part of the interface involved in dimerisation [189] and thus it was likely that high concentrations of charged residues could destabilise dimerisation. The degree of dimerisation of OmpA is still a debated topic, however it is thought that OmpA is mostly present in its monomer form in the outer membrane.

Now focus was shifted to how the LPS sugars interacted with these proteins. Contact histograms were determined for the interactions between LPS sugars and the studied proteins for all levels of LPS (ReLPS, RaLPS and OANT) between $25 - 30$ μs of each

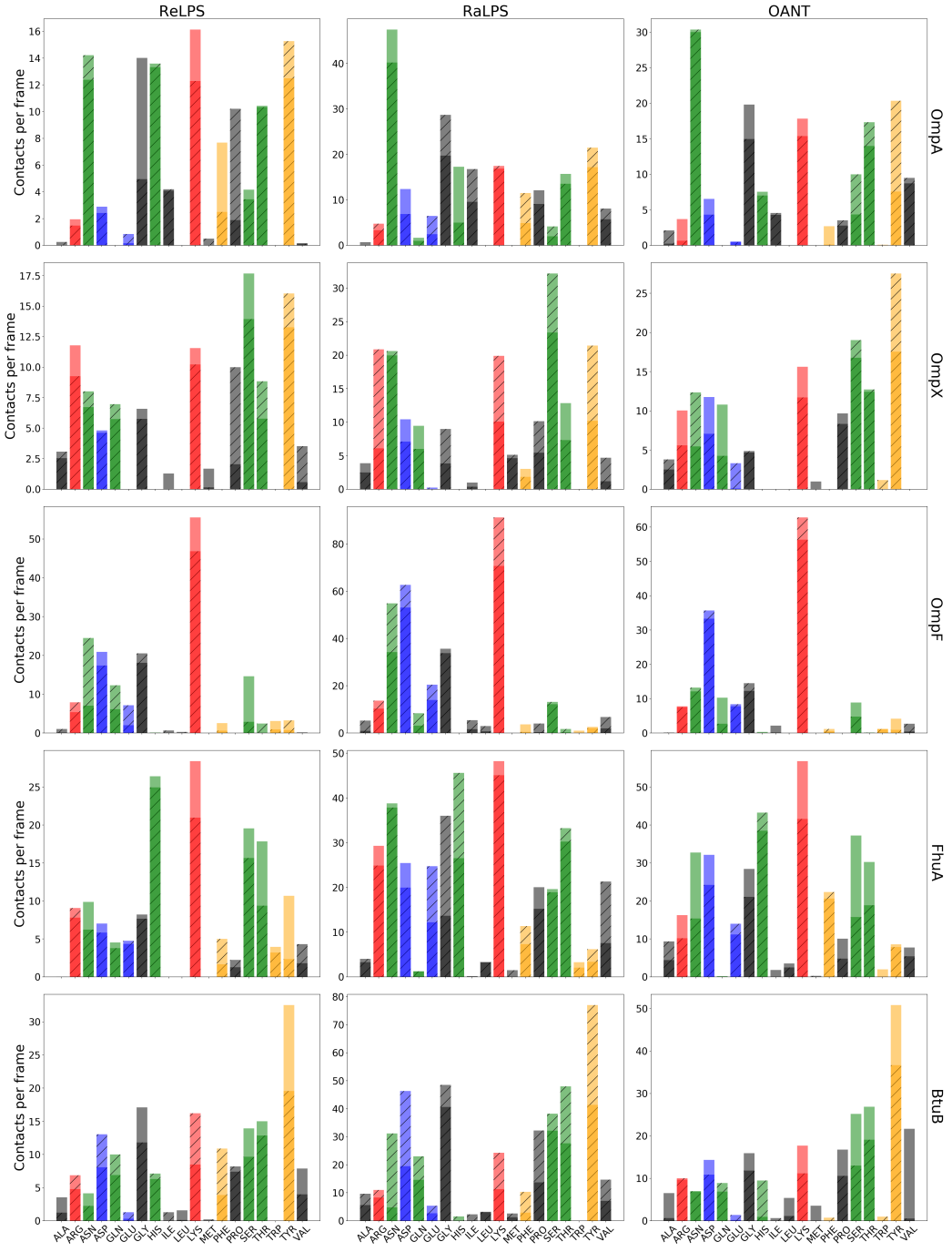

FIGURE 4.11: Average number of contacts per frame between each residue in a protein and the LPS core oligosaccharides and O-Antigen (if present) for 25 μs across repeats (one repeat has hash markings). Each row corresponds to a given protein, while each column corresponds to the LPS system the protein was embedded in (see Table 4.1). Every bar was coloured with respect to the polarity of each residue: red=basic, blue=acidic, orange=aromatic, green=polar and black=non-polar. Note that multiple contacts between a single residue and an LPS sugar group were only counted once. Reprinted with permission from Shearer et al. [172]. Copyright 2019 American Chemical Society 2019.

simulation (Figures 4.10 and 4.11). Similar to the Lipid A headgroups, for most ReLPS systems interactions between sugars and basic residues strongly contributed to the total number of contacts (for most proteins). For RaLPS or OANT systems the contact frequency of basic residues was often not as significant as seen for ReLPS. Comparing the contacts between BtuB and FhuA, which are similar in size and their function in the cell, we would expect them to form similar contacts in different levels of LPS, however this was far from true. For all levels of BtuB the highest contact frequency was with tyrosine, an aromatic residue, while for FhuA it was tyrosine for ReLPS, lysine for RaLPS and OANT. Conversely, all FhuA systems interacted preferentially with the same charged residue (lysine); whereas for BtuB the most prevalent charged residue alternated between aspartic acid and lysine for different levels of LPS. Comparing another two proteins which are very similar in size, OmpA and OmpX, there were again very different trends as a function of LPS level.

EstA showed particularly large changes in contact frequencies between different levels of LPS. For ReLPS the most prevalent contacts were for arginine and aspartate, whereas for RaLPS it was lysine followed by arginine and aspartate and then for smooth LPS (OANT), aspartate. It was interesting that the most frequently contacted residues changed in terms of polarity and charge as a function of LPS level. To understand these trends the relative abundance of arginine, lysine and aspartate residues as a function of extracellular height were studied. There was an abundance of arginine and aspartate residues in the regions which are accessible to ReLPS (Figure 4.10). Large bands of lysine residues (around 5) were present in the middle region of the extracellular domain that were not accessible to ReLPS, which explained the abundance of Lysine contacts seen for RaLPS. For OANT the relative increase in aspartate contacts matched the cluster of aspartate observed in the bulb-like region of EstA, which was only accessible to smooth LPS. While these patterns are not simple, it is clear that the nature of protein-lipid interactions can vary quite a lot based on a protein's LPS environment and the extracellular domain size.

Another point of interest was how the magnitude of average contacts changed as a function of LPS level. It would be expected that as the level of LPS increased the overall number of contacts would increase, however this was not always the case. In fact, EstA was the only system in which most contact frequencies increased with LPS level, while for other systems values were similar or decreased. In the case of OmpF and FhuA there were large decreases in sugar contacts from RaLPS to OANT systems. This may suggest that when the protein does not have a significant extracellular domain then the O-Antigen chains prefer to lean away from the protein, reducing contacts with sugars in the core region. This effect likely scales with protein size e.g. OmpF.

Across this section there were many cases when the contact frequencies changed between repeats, which again highlighted potential issues with sufficient sampling in LPS systems. It could be argued that the interval for analysis (5 μs) was not large enough and thus

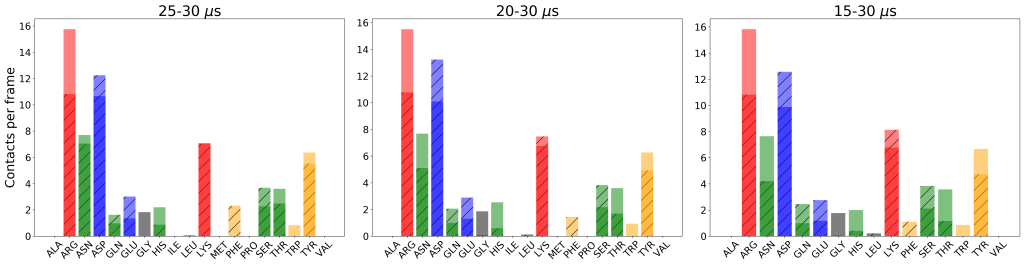

FIGURE 4.12: Average number of contacts per frame between each residue in EstA and the ReLPS core oligosaccharides across repeats (one repeat has hash markings) as a function of increasing analysis times. Each row corresponds to a given protein, while each column corresponds to the LPS system the protein was embedded in (see Table 4.1). Every bar was coloured with respect to the polarity of each residue: red=basic, blue=acidic, orange=aromatic, green=polar and black=non-polar. Note that multiple contacts between a single residue and an LPS sugar group were only counted once.

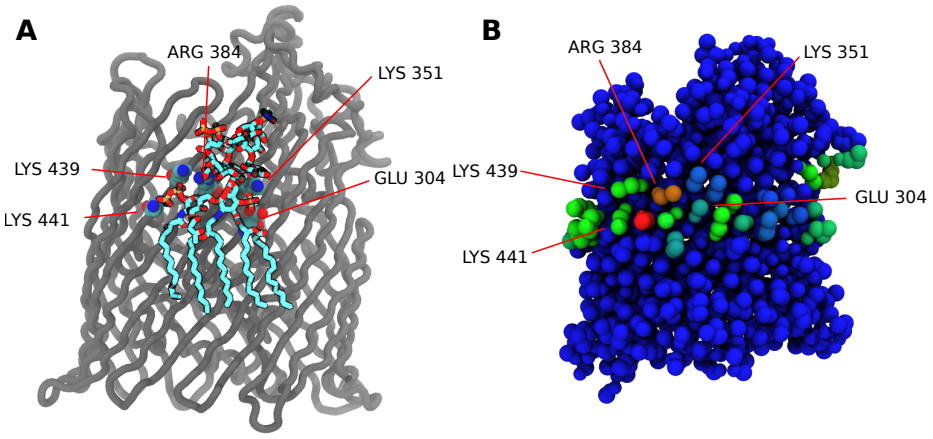

FIGURE 4.13: Image of crystal structure of FhuA (pdb code = 1QFG) which contains a bound lipopolysaccharide (LPS). The marked residues where within 0.4 nm of the Lipid A phosphate groups. B) Contact map of the coarse-grained (CG) structure of FhuA, between each FhuA residue and the phosphate beads of Lipid A in a ReLPS membrane. The contact analysis was carried out from $25 - 30$ μs using a cutoff of 0.6 nm (as is standard for the Martini model). Each residue was coloured based on their respective number of contacts from low (blue) to high (red). The residues identified in A) are marked for the sake of comparison. Reprinted with permission from Shearer et al. [172]. Copyright 2019 American Chemical Society 2019.

the contact analysis was repeated across increasing time intervals of 10 and 15 μs for contacts between EstA and ReLPS sugars (Figure 4.12). From Figure 4.12 it was clear that while the magnitudes of contact frequencies changed, the overall trends remained the same.

It is of importance to compare to experimental results when evaluating the validity of MD simulations and we have done this for OmpF and FhuA. Experimental work of OmpF in RaLPS has found that interactions between LPS and lysine residues are of importance in stabilising the OmpF trimer[171], which matches the prevalence of lysine

contacts reported here. For FhuA the crystal structure [170] used in this work as the basis of the molecular model was bound to a lipid A and so provided a perfect comparison for the evaluation of LPS binding captured via CG MD simulations. To do this a contact map of the interaction of FhuA with LPS phosphates was generated from $25-30$ μs and compared to the contacts present in the crystal structure (Figure 4.13). Overall the simulations carried out here identified similar regions of FhuA that made contact with LPS compared to the bound Lipid A in the crystal structure.

4.3.3 Membrane Thickness and Lipid Enrichment/Depletion

It is known that proteins can cause both the thinning and thickening of phosphate membrane within the annular region [44, 50]. This often is the driving force for lipid sorting or oligomerization of protein-protein complexes[55]. Here Delaunay triangulation was used for the thickness calculations, based on methods used in a previous software package APLVORO[181]. More details of how this method worked are discussed in Section 4.2. First the thickness was determined as a function of time for each repeat (Figure 4.14). In most cases thickness values changed rapidly within the first 2 μs and then subsequently converged within 15 μs. Furthermore there was agreement between the thickness values between repeats for all systems, except FhuA in OANT. There was usually around a difference of 0.1 nm between the thinnest and thickest membranes.

Then the thickness was determined as a function of distance from the protein surface to quantify local modulations in thickness. This analysis was carried out between $25-30$ μs of each simulation and the values in each bin averaged across repeats (Figure 4.15). For every protein except EstA the addition of a protein always caused membrane thinning with a local region of 2 nm. Beyond the 2 nm mark the thickness plateaued to the bulk

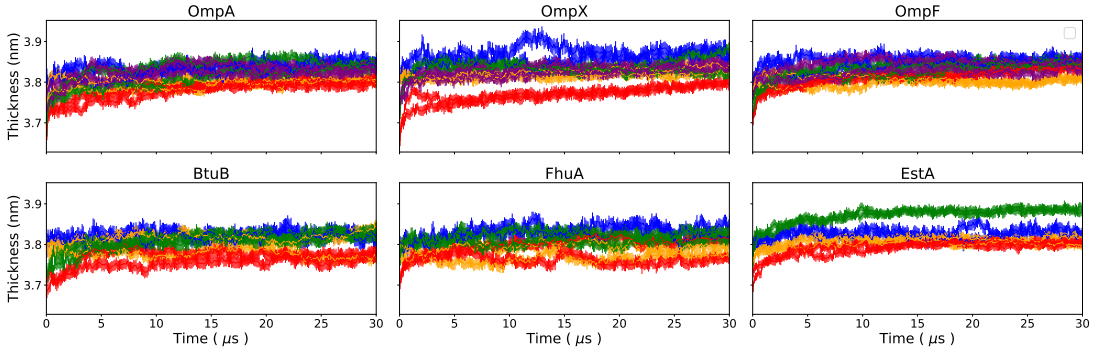

FIGURE 4.14: Thickness of each outer membrane with respect to time for the outer membrane systems ReLPS (blue), RaLPS (orange), OANT (red), OANT_PE (green) and MIXED (purple). Analysis was done over $0-30$ μs of both repeats and the values in the bins from each repeat were combined to determine the average and standard deviations. The membrane thickness was measured using the phosphate beads in each leaflet.

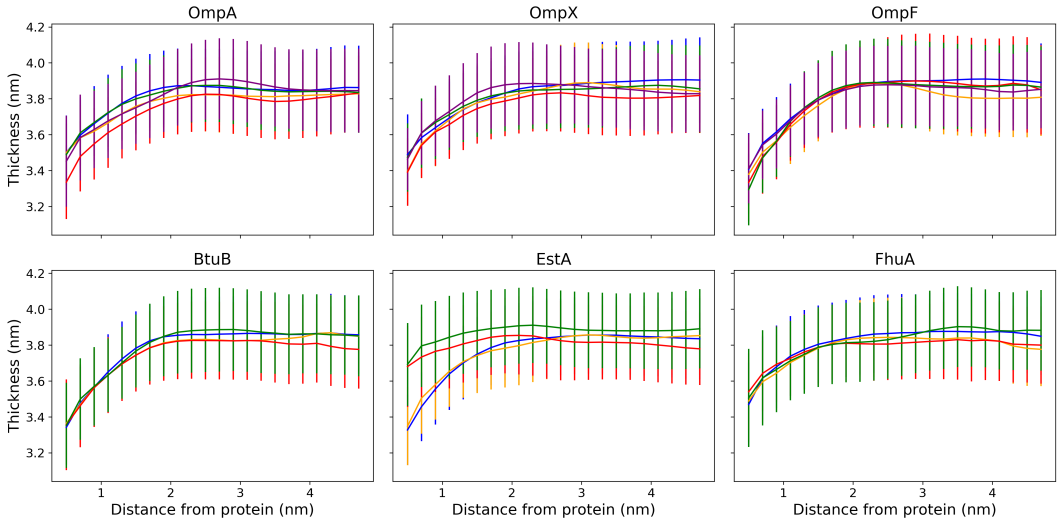

FIGURE 4.15: Thickness of each outer membrane with respect to distance from a protein's surface for the outer membrane systems ReLPS (blue), RaLPS (orange), OANT (red), OANT_PE (green) and MIXED (purple). Analysis was done over $25-30$ μs of both repeats and the values in the bins from each repeat were combined to determine the average and standard deviations. The membrane thickness was measured using the phosphate beads in each leaflet. Adapted with permission from Shearer et al. [172]. Copyright 2019 American Chemical Society 2019.

thickness of around $3.7-3.8$ nm, as observed for the average thickness with respect to time (Figure 4.14). The magnitude of thinning at the membrane surface seemed to lie between $0.3-0.4$ nm. In the case of EstA only Re and RaLPS systems showed significant thinning at the surface, whereas for OANT and OANT_PE systems a thinning of ~ 0.1 nm was observed. However, as this value is well within the estimated errors it is unclear if the observed thinning is significant. What was interesting here was the possibility that the presence of an O-Antigen chain, which lay in the extracellular region, could modulate the effect of a protein on the local membrane thickness. One explanation was that the interactions of the smooth LPS sugars with the EstA extracellular domain caused the order of LPS tails to increase such that sugar-EstA interactions were maximised. So the effect of the additional sugar interactions may outweigh the hydrophobic mismatch.

One question of importance was where does the consistent thinning effect originate from and is it a result of lipid sorting in the region of the protein? To these ends the lipid enrichment/depletion index (DE index) was determined around each protein (lipid centre of geometry within 1.4 nm) for the lipids in the inner leaflet of ReLPS systems using the method outlined by Corradi et al[160]. The 1.4 nm cutoff for enrichment and depletion was chosen such that the first and second nearest neighbours of the protein were included. Similar to the work by Corradi *et al.* for symmetric systems[160], a pattern of lipid types was observed around each protein (Figure 4.16B). Overall there was no enrichment or depletion observed for PE or PG lipids within the region around proteins, whereas the DE index observed for cardiolipin varied greatly between different proteins. Cardiolipin was either depleted from the protein or neither depleted nor enriched. It was unusual

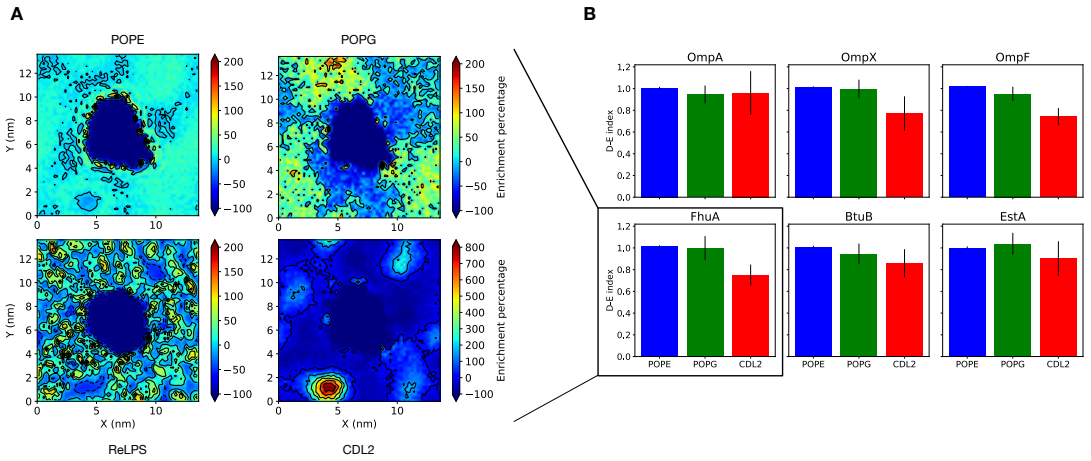

FIGURE 4.16: A) 2D lipid density analysis for the ReLPS outer membrane systems. Density maps were done for (bottom left) the entire Re lipopolysaccharide (ReLPS) lipid, (top left) 16:018:1 phosphoethanolamine (POPE), (top right) phosphatidylglycerol (POPG), and (bottom right) cardiolipin (CDL2) lipid phosphate beads and were averaged over 2530 μs. The density maps are colored by enrichment (> 0) or depletion (< 0) of each lipid type with respect to the average density of a given lipid type. B) Depletion-enrichment (D-E) indices for POPE, POPG, and CDL2 for each protein in the ReLPS membranes. The D-E index was obtained by dividing the lipid composition of the 1.4 nm shell around the protein by the bulk membrane composition; therefore, a D-E index > 1 indicates enrichment, while a D-E index < 1 indicates depletion. The D-E index was calculated from 10 to 30 μs in 5 μs blocks for both repeats to get eight values for each system; these eight values were then averaged, and the error was determined from their standard deviation. Reprinted with permission from Shearer et al. [172]. Copyright 2019 American Chemical Society 2019.

that cardiolipin displayed such different enrichment levels around each protein compared to PG.

While the DE-index allowed for a more local picture of lipid sorting, given our understanding of LPS systems from the previous chapter, the lipid sorting across the entire membrane should be considered. Thus contact maps between the protein and PG, combined with 2D enrichment maps of each lipid type were determined for each simulation and cross-referenced to find potential binding sites (Figure 4.16A and 4.17). FhuA and BtuB had a few PG binding sites. In the case of FhuA there were three binding sites that were persistent between repeats; one of these binding sites was directly below the region of Lipid A binding shown in the crystal structure (PDB code = 1QFG, see Figure 4.13). Whereas for BtuB two persistent PG binding sites were seen in the lower leaflet. For both proteins there were additional areas of PG enrichment, however these regions were not persistent between repeats.

For cardiolipin there were a lot of clusters that formed outside the 1.4 nm cutoff set for the previous D-E index analysis; this trend was repeated across all six proteins studied here. The most extreme clustering of cardiolipin, in terms of size and magnitude of enrichment, was observed for FhuA (Figure 4.16A). The areas of cardiolipin enrichment

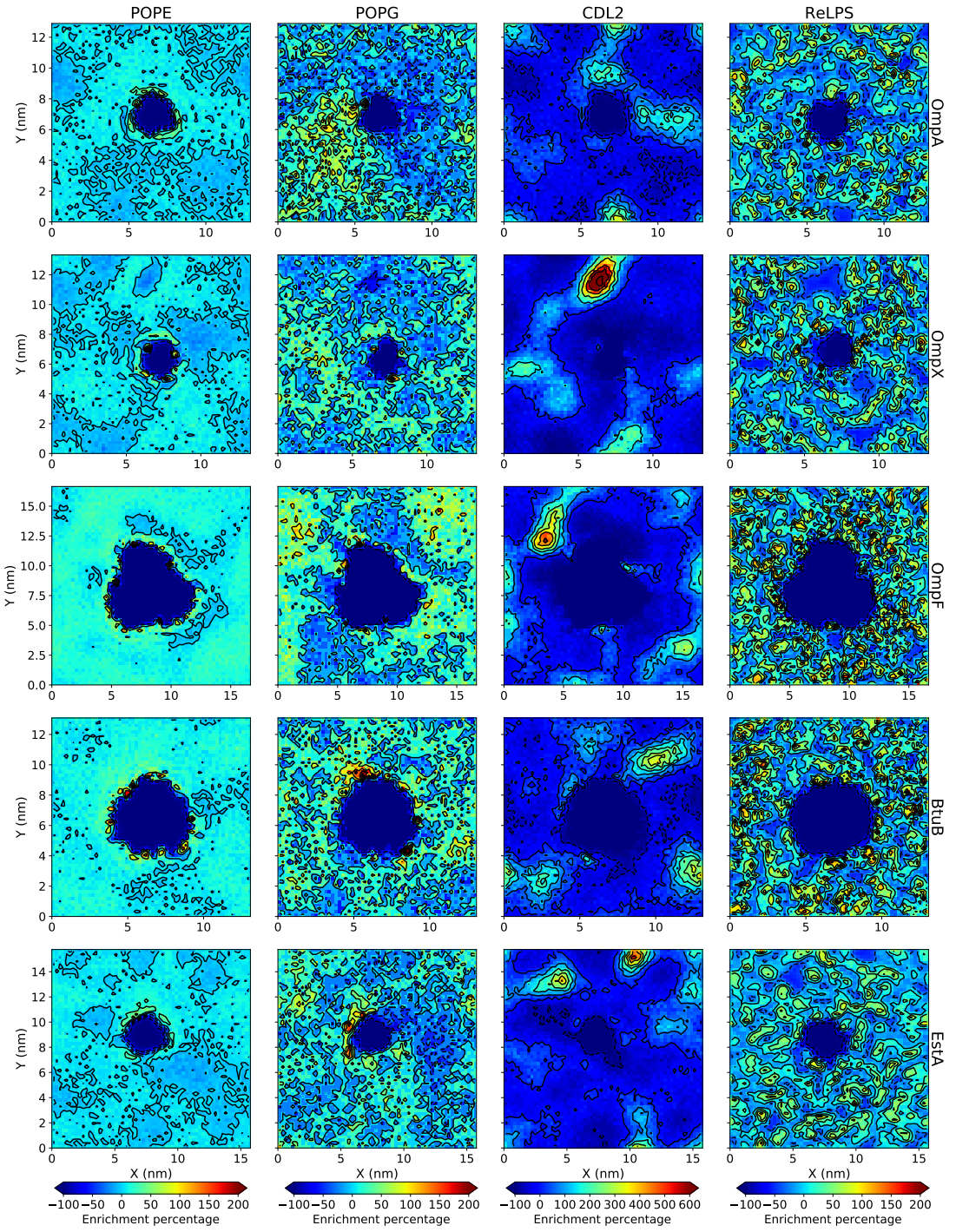

FIGURE 4.17: 2D lipid density analysis for the ReLPS outer memebrane systems. Density maps were done for the entire Re lipopolysaccharide (ReLPS) lipid, 16:0-18:1 phosphoethanolamine (POPE), phosphatidylglycerol (POPG) and cardiolipin (CDL2) lipid phosphate beads and were averaged over $25-30$ μs. The density maps are coloured by enrichment (> 0) or depletion (< 0) of each lipid type with respect to the average density of that lipid. Reprinted with permission from Shearer *et al.* [172]. Copyright 2019 American Chemical Society 2019.

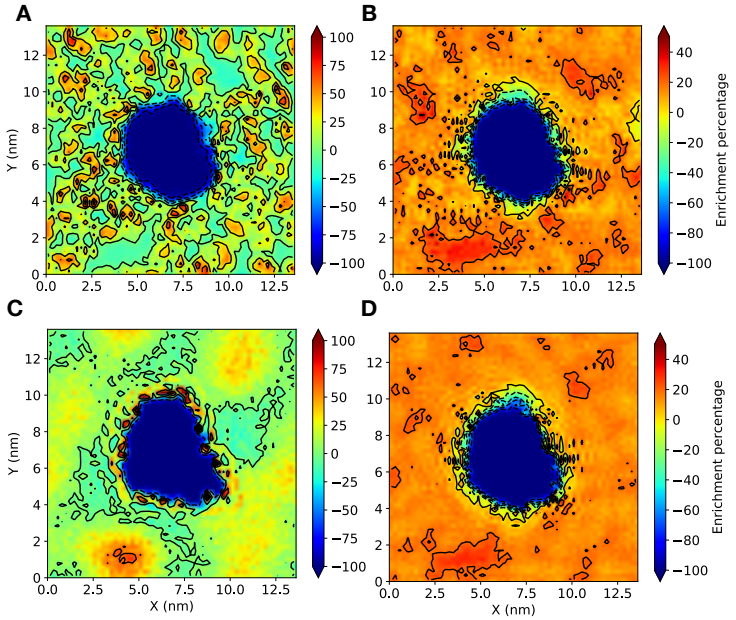

FIGURE 4.18: 2D lipid density analysis for a FhuA ReLPS system for A) the entire membrane, B) all membrane lipid tails, C) and D) phosphate beads and lipid tails in the lower leaflet of the membrane averaged over $25 - 30$ μs. The density maps are coloured by enrichment (> 0) or depletion (< 0) of each lipid type with respect to the average density of that lipid. Reprinted with permission from Shearer et al. [172]. Copyright 2019 American Chemical Society 2019.

also corresponded to regions of LPS tails depletion in the upper leaflet. This inter leaflet pattern in enrichment was also observed for all other ReLPS simulations in this chapter (Figure 4.17) and in previous work for just OmpA and OmpF in ReLPS[149]. Now that this pattern has been observed in a much broader study it is clear this is a general feature of outer membrane systems.

One important question to answer was how the depletion and enrichment of certain lipid types affected the overall density within the membrane. To ascertain the answer to this question, 2D enrichment maps were calculated for: the entire membrane, all tails beads, lower leaflet phosphates, and lower leaflet tails for the FhuA system shown in Figure 4.16 (Figure 4.18). For the entire membrane and all lipid tails, there were regions of depletion and enrichment, respectively, that coincided with cardiolipin clustering. (Figure 4.18A and B). Furthermore the lower leaflet headgroups and tail groups were both enriched at regions of cardiolipin clustering. Taking the previously noted trends into account this inferred that the LPS headgroups were depleted within the regions of cardiolipin clustering.

For the sake of comparison the 2D enrichment maps were also determined for different components of the MIXED system containing OmpA between $25 - 30$ μs (Figure 4.19). POPE was the least abundant lipid component of the upper leaflet of the MIXED system (2 : 2 : 1 smooth LPS: RaLPS : POPE in the upper leaflet) and appeared to be trapped in small domains of the membrane, with no lipid sorting occurring with the

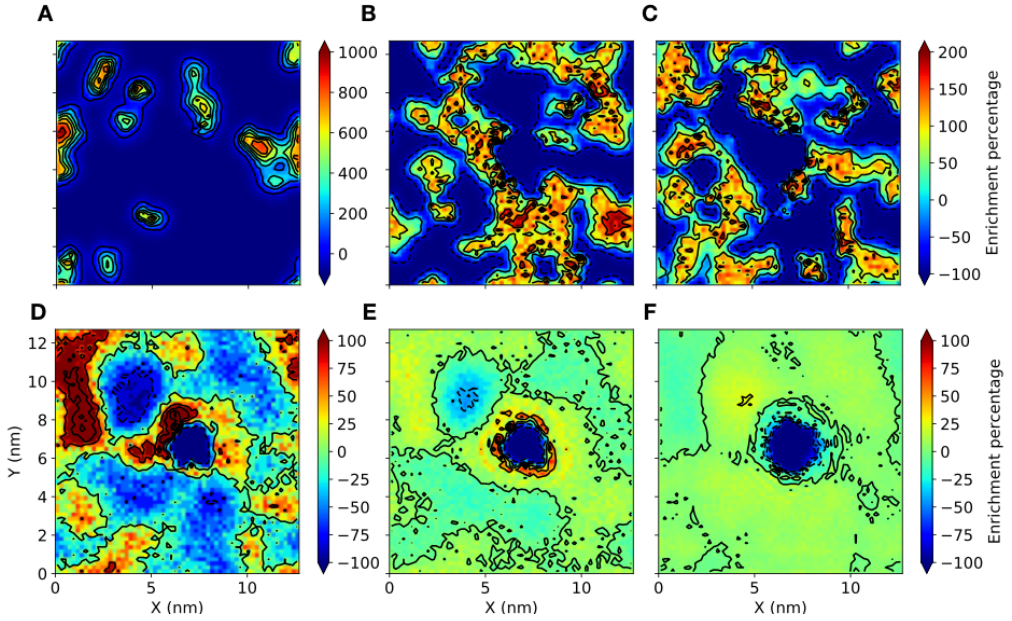

FIGURE 4.19: Enrichment maps of the mixed LPS system with an embedded OmpA for A) upper leaflet POPE tails, B) RaLPS tails, C) smooth LPS tails, D) cardiolipin phosphates, E) lower leaflet phosphates and f) upper leaflet lipid tails averaged over $25 - 30$ μs. The density maps are coloured by enrichment (> 0) or depletion (< 0) of each lipid type with respect to the average density of that lipid.

surrounding LPS (Figure 4.19A). Both RaLPS and smooth LPS formed interconnected regions (Figure 4.19B and C) that spanned large areas of the membrane (up to 8 nm in one direction). As seen in the ReLPS systems (Figure 4.16 and 4.17), large clusters of cardiolipin formed near the protein and outside the annular region (Figure 4.19D). Furthermore, regions of the most prevalent cardiolipin clustering corresponded to depletion in POPE and depletion of rough and smooth LPS tails. Overall, in the lower leaflet there was an increase in the enrichment at regions where cardiolipin clustering occurred (Figure 4.19E). The Cardiolipin clustering in these systems did not appear to be modulated by different amounts in areas containing solely smooth or rough LPS.

It has been well established in this work and within the literature that LPS diffuses at a rate of at least an order of magnitude less than typical phospholipids [23, 35, 105]. However, the rate of lipid sorting has not been discussed, but is important for sufficient sampling to occur and for understanding the macroscale phase dynamics of LPS. The rate of lipid sorting was calculated from the lifetime of a lipid at the protein surface via the lipid survival probability $P(t + \Delta t)$. The lipid survival probability, $P(t + \Delta t)$, described the probability that a lipid was still at the protein surface after time Δt has passed[190]. First the lipid survival probability was determined for $20 - 40$ μs and $40 - 60$ μs for both repeats of the RaLPS system. Then $P(t + \Delta t)$ was fitted to a sum of two exponential functions to obtain slow and fast relaxation constants for the decay of the survival probability of each lipid type. The minimum value of the sum of exponentials, C, was referred to as the decay limit (Table 4.2) and was expected to tend

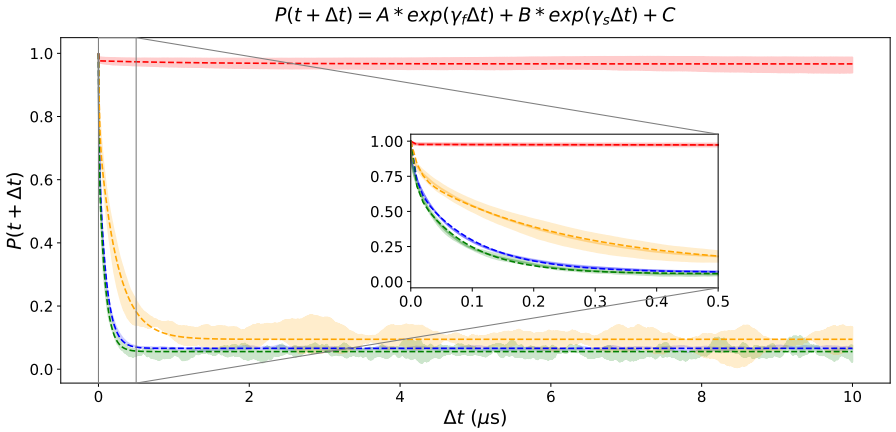

FIGURE 4.20: Lipid survival probability of RaLPS (red), POPE (blue), POPG (green) or cardiolipin (orange) being bound to OmpA at t and $t+\Delta t$ vs Δt. A lipid was defined as bound if it was within 0.6 nm of the protein surface. $P(t+\Delta t)$ was calculated from 20-40 and 40-60 μs for both repeats and the results were averaged and a double exponential fit to the resulting points (dotted lines). Note that γ_f and γ_s are the fast and slow relaxation constants of the double exponential and A, B and C are constants. The standard deviation of each set of points are shown here as a transparent area, while the averages are the transparent line. Reprinted with permission from Shearer et al. [172]. Copyright 2019 American Chemical Society 2019.

to 0. For PE and PG lipids the fast decay constants were on the order of the resolution of the trajectory (1 ns), whereas the slow decay constants (96.3 ± 2.5 and 83.5 ± 3.9 ns) were comparable to previously measured values for phospholipids in Martini systems[190, 191]. The Cardiolipin slow decay constant was an order of magnitude larger than the other phospholipids, which could be due to its comparatively large size and ability to form nanodomains of cardiolipin; which further hampers lipid sorting and diffusion. For RaLPS the decay limit was 0.96 ± 0.21 and the slow decay constant 1330.2 ± 59874.5 ns; a sign that RaLPS did not undergo lipid sorting on the timescales of these simulations.

Lipid Type	Fast Decay (ns)	Slow decay (ns)	Decay limit
RaLPS	1.8 ± 19.2	1330.2 ± 59874.5	0.96 ± 0.21
POPE	7.2 ± 0.7	96.4 ± 2.5	0.07 ± 0.00
POPG	6.3 ± 0.6	83.5 ± 3.9	0.6 ± 0.00
Cardiolipin	12.1 ± 12.0	246.0 ± 29.4	0.09 ± 0.01

TABLE 4.2: The lipid survival probabilities shown in Figure 4.20 were fit to a double exponential to obtain the fast and slow decay constants for the on off rates of each lipid type in the system. The Decay limit was the minimum value of the equation shown in Figure 4.20 i.e. the constant C. Averages and standard errors were determined from 20 μs blocks ($20-40$ and $40-60$ μs) of both repeats. Adapted with permission from Shearer et al. [172]. Copyright 2019 American Chemical Society 2019.

4.3.4 Orientation of O-Antigen Chains Within the Outer Membrane

Understanding the structure and dynamics of O-Antigen chains is important as they form a chemical and physical barrier to permeation into the cell. Previously the interactions between sugars and each protein was discussed and now the behaviour of the O-Antigen chains will be investigated. A number of methods were developed to analyse the O-Antigen tilt with respect to the z axis and neighbouring LPS lipids. First the tilt of the end-to-end vector of each O-Antigen chain was calculated with respect to the z axis and divided into "local" and "bulk" regions. The "local" region was defined by any lipid A section of smooth LPS that was within 2.5 nm of the protein surface. A radius of 2.5 nm was chosen, as this was the rough radius of a membrane protein's influence on the structure of surrounding lipids[44, 149, 160]. The pairwise tilt angle between chains was determined by calculating the angle between the end-to-end vectors of pairs of neighbouring O-Antigen chains. For both the tilt and the relative tilt the results were presented as probability distributions with respect to the tilt angles in units of $cos(\theta)$. The pairwise tilt angles took values in the interval of $[2, 0]$ if the O-Antigen chains tilted towards each other, and $[-2, 0)$ if they did not. A cosine distribution was used, as this was known to be flat in the case of random motion, and thus made meaningful trends easier to discern. The distributions for tilt and pairwise tilt were calculated from $25 - 30$ μs for all OANT systems (Figure 4.21).

For the bulk regions of O-Antigen the tilt was rarely less than 0.7 ($> 45°$), however the local regions had tilts as large as 60° (0.5). A positive correlation was observed with the size of Omps and the degree of tilting in the local region. This observation was particularly pronounced between OmpA and OmpF. For EstA large amounts of tilting in the local region was also observed, despite the transmembrane area of EstA being more similar to OmpA than OmpF. The increased tilting for EstA clearly reflected previous observations that smooth LPS formed significant interactions with the extracellular region of EstA. While both OmpA and OmpF had significant maxima in tilt near 0°, for EstA the maximum peak at $\sim$ 18° ($\sim$ 0.95) was much larger. This may reflect that O-Antigen chains near EstA tilt to maximise interactions with the curved surface of EstA. Whereas in the bulk regions the most likely tilt angle was always around 5°. The pairwise tilts were distributed mainly between $-60°$ to 60° (-1.5 to 1.5 $\cos(\theta)$). In all cases the most probable tilt angle was around $\pm 15 - 25°$. After the most probable angle the probability gradually decays to 0, with no other local maximums, which showed the highly packed nature of the O-Antigen chains (Figure 4.22C). The propensity of the chains to tilt toward or away from each other was quantified by taking the integral of each probability distribution across $[2, 0]$ for total change of tilting towards each other and integral of $(0, 2]$ for those tilting away from the each other. The integral of the region where chains pointed towards each other was 0.57 (OmpA and OMPX), 0.58 (FhuA), 0.62 (BtuB) and 0.60 (EstA and OmpF). Given that the integral of the entire probability distribution would be 1 then the O-Antigen chains preferred to tilt towards

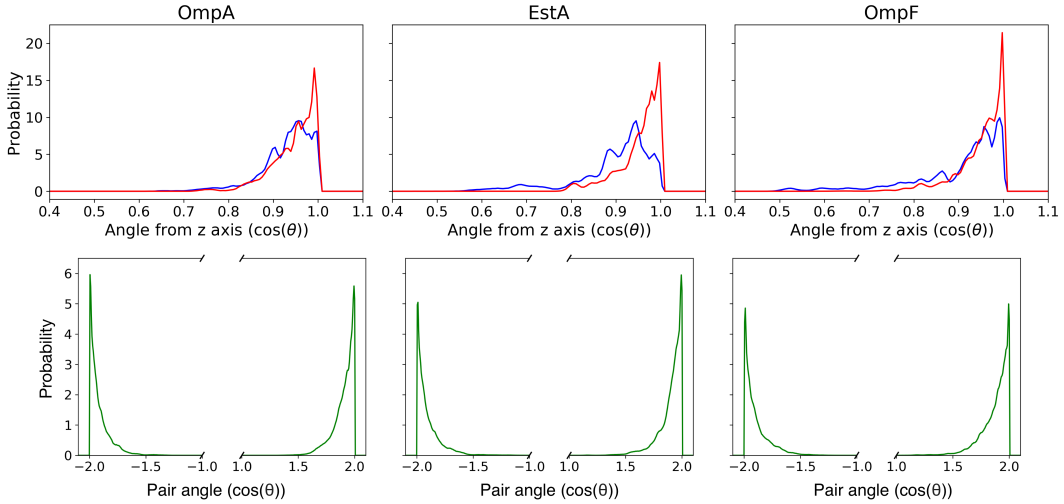

FIGURE 4.21: Probability distribution of (top) O-Antigen chain tilt with respect to the z axis and the tilt between neighbouring pairs of O-Antigen chains for $25 - 30$ μs of the OANT systems (bottom). The tilt of a single O-Antigen chain was calculated using its end to end vector. For the chain tilt with respect to the z axis, two probability distributions were generated for smooth lipopolysaccharides (LPS) closer than 2.5 nm (blue line) or further than 2.5 nm away from a given proteins surface (red line). For the pairwise O-Antigen distributions if the chains tilted towards each other the angle was positive; in all other cases the angles would be negative. Angles are presented in units of $\cos(\theta)$ where θ is an angle. For the pairwise O-Antigen relative tilt angles, if the chains tilted towards each other $\cos(\theta)$ takes the range [0, 2]; in all other cases the angles are between (-2, 0). Reprinted with permission from Shearer et al. [172]. Copyright 2019 American Chemical Society 2019.

each other. This is in line with atomistic simulation by Wonpil et al, who showed tenting of O-Antigen chains around OmpF[93].

Now the effects of increasing membrane complexity will be discussed. The tilt and relative tilt analysis was carried out, as previously done, for OANT, OANT_PE and MIXED systems for OmpA, OmpX and OmpF (Figure 4.22A). As additional components were added to the upper leaflet the maximum tilt observed increased up to 110° (around 0.35 $cos(\theta)$). Interestingly, the most probable tilt in all of the systems remained at around 10° for the bulk region, but the distribution broadened in the MIXED systems. For the smaller OmpA and OmpX proteins there was a higher chance of having a tilt less than 0.25 $cos(\theta)$, than the OmpF system. Upon visualisation of these systems it was seen that in the OmpF systems it was unlikely for the chains to tent over the protein or lie directly on the protein surface, although this did happen in one repeat (Figure 4.22D). Whereas for OmpA or OmpX proteins had a lower radius, which allowed O-antigen chains to interact with each other across the edges of the protein.

Moving onto the relative tilt trends, broadening of distributions as a function of a reduction in O-Antigen packing was observed. As the membrane complexity increased there was (Figure 4.22B-E) a reduction in the packing of O-Antigen chains, which allowed for increased chain flexibility. The thickness of the O-Antigen layer was inversely

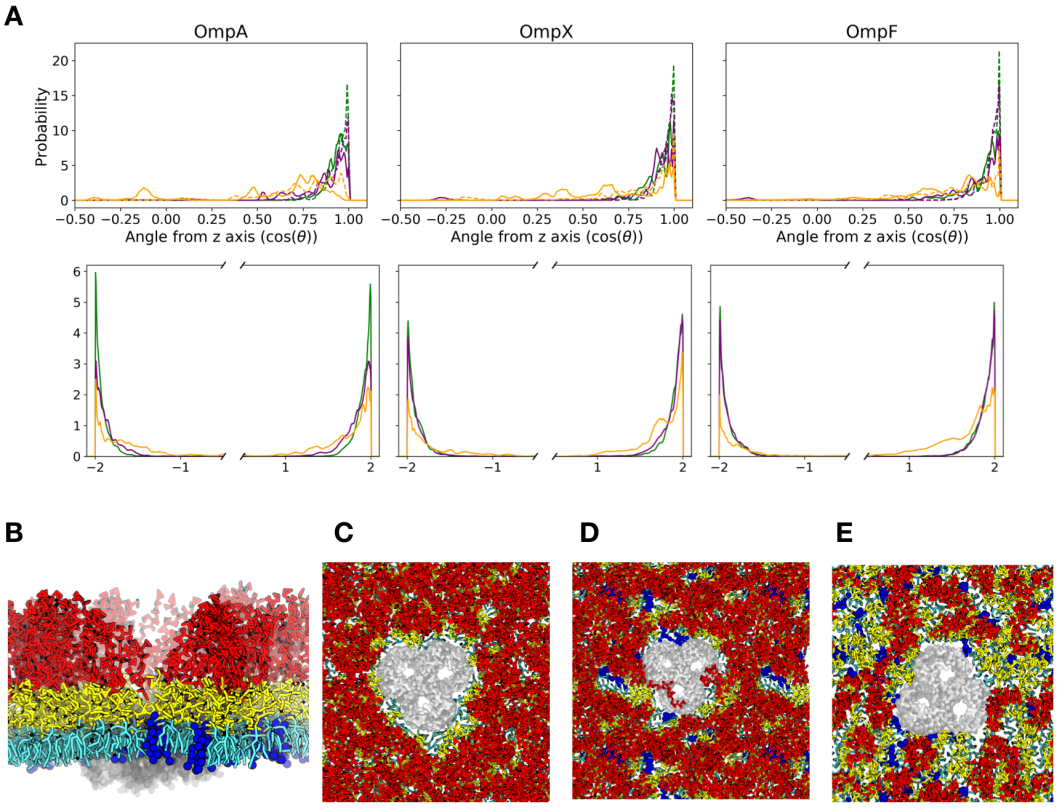

FIGURE 4.22: A) Probability distribution of (top) O-Antigen chain tilt with respect to the z axis and the tilt between neighbouring pairs of O-Antigen chains for $25-30$ μs of the OANT (green), OANT_PE (purple) and MIXED (orange) systems (bottom). Note that the dashed lines corresponded to the bulk region of the membrane 2.5 nm from the protein surface. B) Side view snapshot of OANT_PE system with a membrane OmpF. Top view snapshots of C) OANT, D) OANT_PE and E) MIXED systems. All snapshots were taken at 30 μs, with the following colour key: protein = grey, O-Antigen = red, LPS core oligosaccharides = yellow, lipid A = cyan and gold and 16:0-18:1 phosphoethanolamine (POPE) lipid in the upper leaflet = blue. Subfigures B and D were reprinted with permission from Shearer et al. [172]. Copyright 2019 American Chemical Society 2019.

proportional to overall density of the O-Antigen layer. The integral of the region of the probability distribution for chains tilting toward each other ($[0, 2]$) was calculated for MIXED systems and values of 0.59 (OmpA), 0.68 (OmpX) and 0.75 (EstA) were obtained. Thus as with the OANT system in the MIXED systems tenting of O-Antigen chains was favoured. From these observations understanding the complexity of the upper leaflet is vital if we are to further explore how the outer membrane functions as a chemical and physical barrier.

The O-Antigen did not fully block the pore of any of the ion channels in this work; only one system (Figure 4.22D) had a pore partially blocked by smooth LPS. Furthermore O-Antigen chains would often tilt away from clusters of POPE or RaLPS in favour of maximising sugar-sugar interactions with minimal chain tilting (Figure 4.22). Contacts between O-Antigen and OmpF, in the system shown in Figure 4.22D, were determined for all residues (1-340) of the OmpF trimer. As in the atomistic study by Wonpil et.al[93]

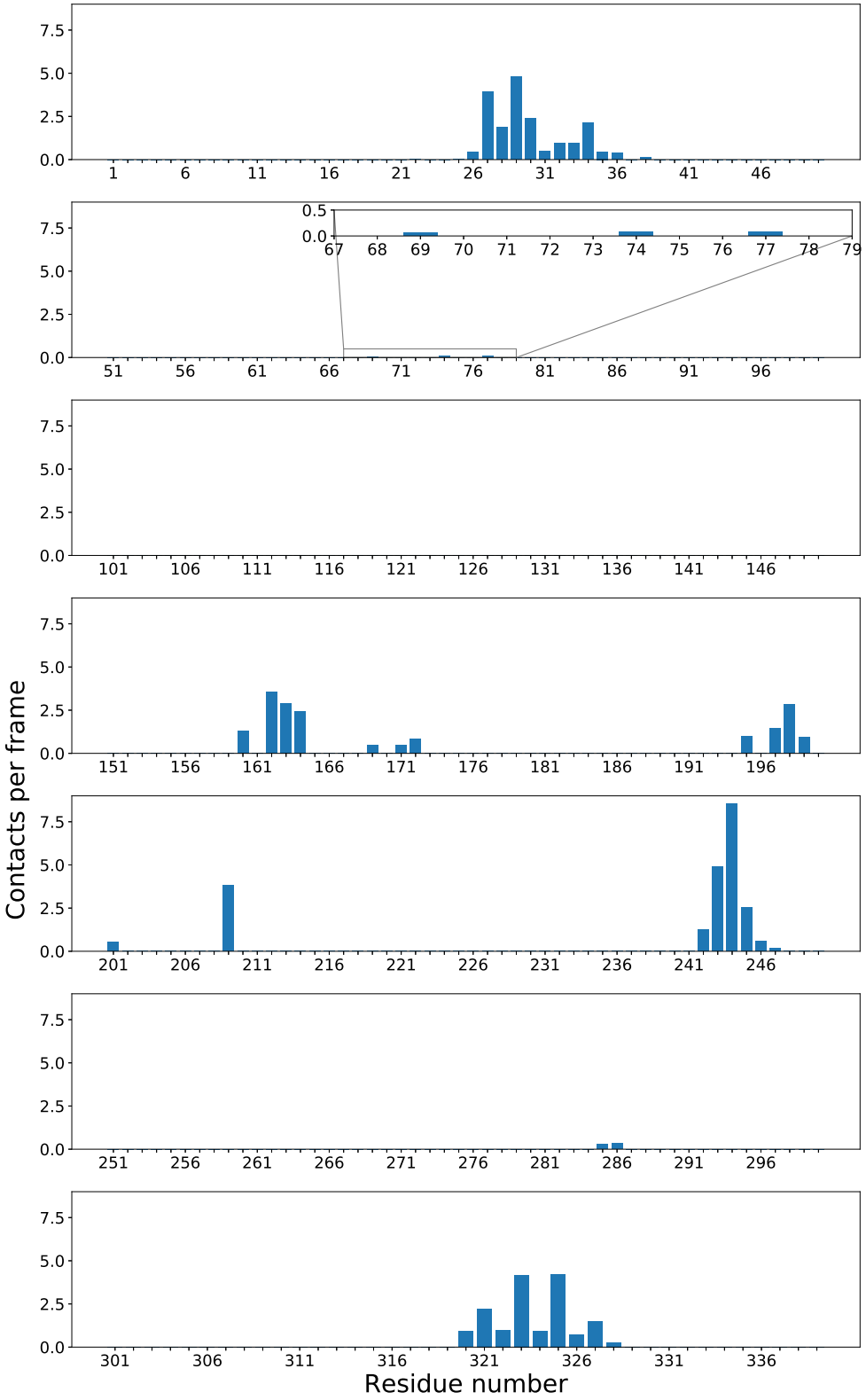

FIGURE 4.23: Average number of contacts per frame between each residue in each monomer in the OmpF timer (total of 340 residues per monomer unit) in the OANT system shown in Figure 4.22 A and D. The contact analysis was carried out between $25 - 30$ μs of the simulation. Reprinted with permission from Shearer et al. [172]. Copyright 2019 American Chemical Society 2019.

of OmpF in a smooth LPS OM model, significant contacts with parts of the loops L4 (residues $160-172$), L5 (residues $197-209$), L6 (residues $237-253$), and L8 (residues $318-330$) were observed. Compared to the atomistic study, less extreme tenting of O-antigen chains near OmpF occurred at the CG resolution. One explanation for this reduced tenting for the CG model lies with the reported stickiness of Martini sugars that can lead to over favoured clustering of sugars[192].

4.3.5 The Effect of Different Coarse-grained Protein Models

So far the trends discussed in this chapter have covered the behaviour of the proteins and membranes as a function of protein and membrane complexity. However, the effects of available model changes on these systems have yet to be discussed. The directional interactions responsible for secondary structure (e.g. hydrogen bonding) cannot be reproduced by the Martini model, as they are coarse-grained out upon dimensionality reduction. Therefore it is common to use elastic networks to maintain the secondary structure of CG proteins [120]. The ElNeDyn model assumes that the reference structure the protein is restrained to, often the crystal structure, is representative of the protein's conformations in solution, which is not always the case. Recently a new coarse-grained model was developed (the Go model[193]) and then later applied to Martini (GoMartini[173]), which utilized a LJ network to restrain protein interactions. The LJ network means that the protein secondary structure can fold and unfold, while still maintaining good agreement with atomistic models [173]. Further details of this model are discussed in the methods section (Section 4.2). Simulations using the GoMartini protein model were run for OmpA and OmpX in ReLPS for 30 μs (see Table 4.1).

To compare behaviour of the ElNeDyn model to the GoMartini model a series of protein focused analyses was carried out, the first of which was the calculation of each protein's transmembrane tilt (Figure 4.24). The protein tilts for OmpA and OmpX using the GoMartini model was comparable to the elastic network model (Figure 4.2) in terms of average magnitude and fluctuations. This was not completely unexpected as for rigid

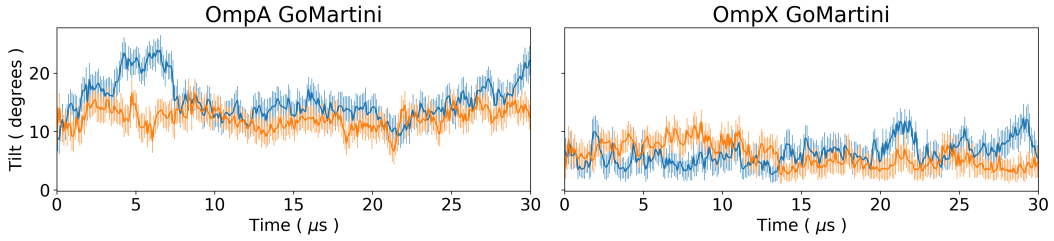

FIGURE 4.24: The protein tilt of the trans-membrane region of each protein backbone with respect to the z-axis as a function of time for each repeat. Further details of the protein tilt calculation can be found in the Methods section (Section 4.2). The errors were generated from the standard deviation of block averages taken over 100 ns intervals.

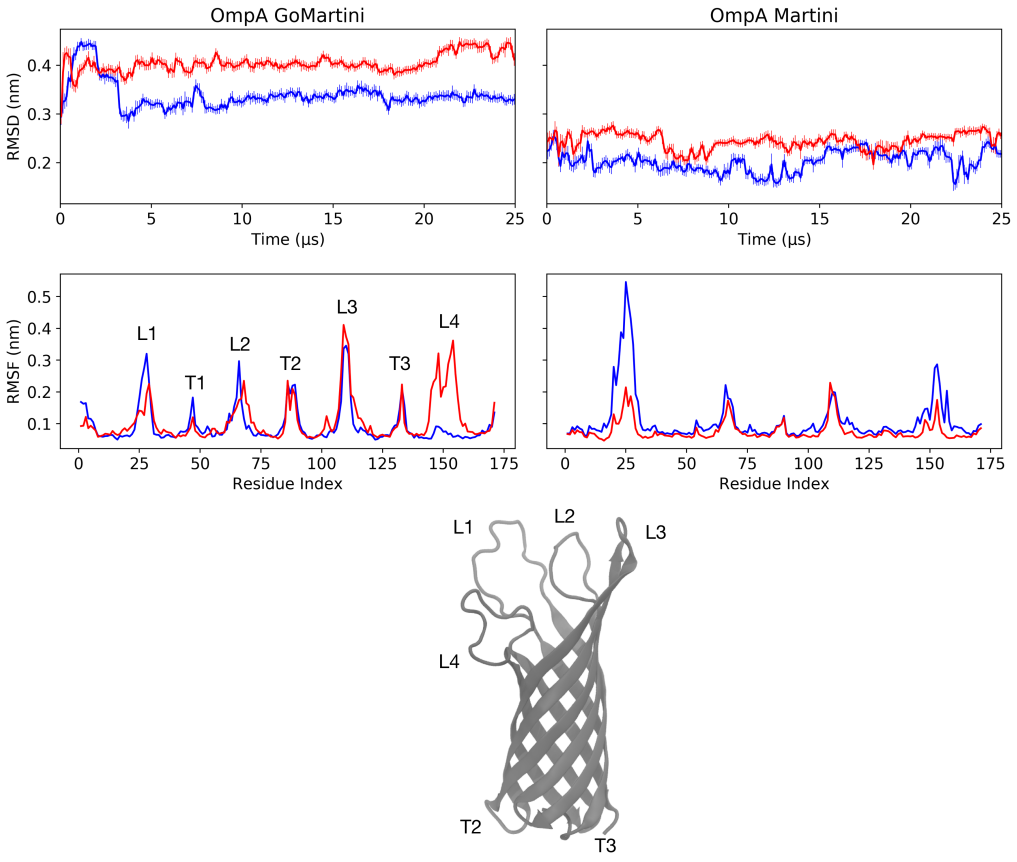

FIGURE 4.25: The root mean squared deviation (RMSD, top) and root mean squared fluctuation (RMSF, middle) of the backbone of OmpA compared to the coarse-grained (CG) crystal structure of two CG models. The error in the RMSD was determined by carrying out block averaging over 100 ns intervals. The RMSF was determined between $20-30$ μs of each trajectory. The blue and red lines signify the values for each repeat. (bottom) Atomistic model of OmpA with all loops and turns labelled.

beta barrels such as OmpX or OmpA, the replacement of an elastic network with the GoMartini model was likely to have a less noticeable effect. The only flexible parts of beta barrels are the loops or turns present in the intra or extracellular regions of the protein (Figure 4.25).

Next, the RMSD and RMSF of the protein backbone was determined between $20-30$ μs for both the ElNeDyn and GoMartini models, for the OmpA ReLPS membranes (Figure 4.25). Note that the loops regions were defined based on the crystal structure and previous atomistic simulations[53, 189]. From the RMSD it was clear that the GoMartini model differed from the crystal structure the most; this was not unexpected as the ElNeDyn model is designed to reduce deviations from the crystal structure. For the ElNeDyn model most loop regions retained their flexibility, but the flexibility of terminal strands and turns were greatly reduced or disappeared completely. For the GoMartini model there was substantial flexibility in the terminal chains and the turns, as predicted by atomistic simulations [189] and experimental work [53]. Interestingly the RMSDs, in particular for GoMartini, are quite different between repeats, but this

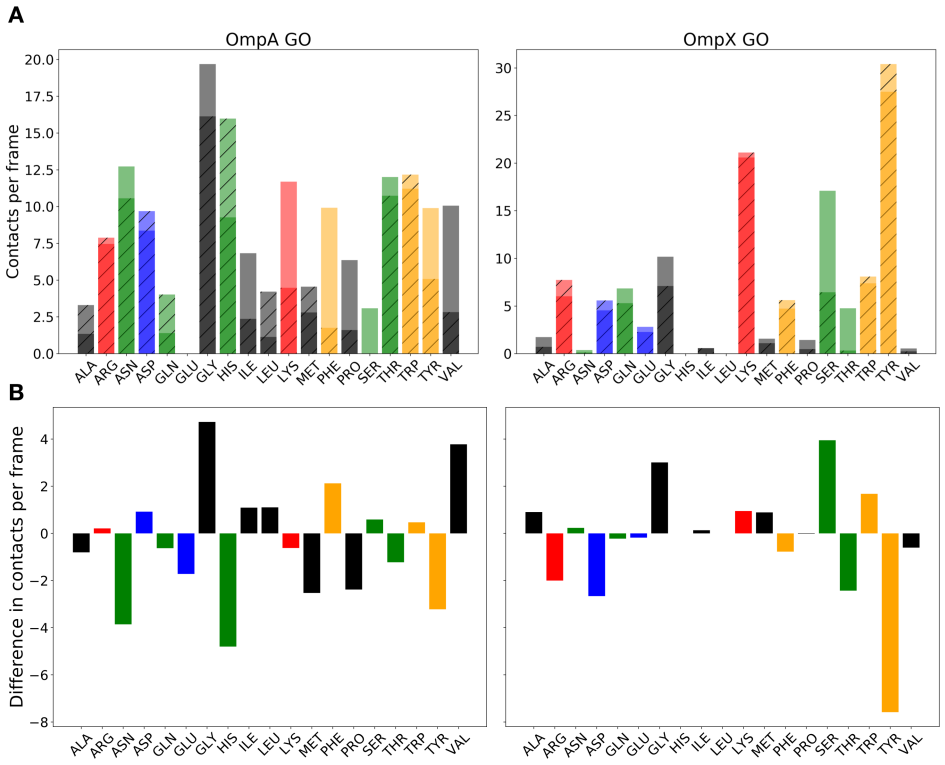

FIGURE 4.26: A) Average number of contacts per frame between each residue in a GoMartini protein model and the Lipid A headgroup for 25 – 30 μs across repeats (one repeat has hash markings). B) Difference between contacts per frame between GoMartini and Elastic Network protein models (GoMartini – ElNeDynn). Each bar was coloured with respect to the polarity of each residue: red=basic, blue=acidic, orange=aromatic, green=polar and black=non-polar.

was not reflected by the protein tilts (Figures 4.2 and 4.24), which is more proof of poor sampling in these systems.

The GoMartini model appeared to more faithfully reproduce the underlying dynamics of the protein, but it was unclear how much of an effect this had on the protein-lipid interactions. To this effect the protein contact histogram was determined for the last 5 μs of each simulation and compared to the results of the ElNeDyn model (Figure 4.8). Both OmpA and OmpX reproduced the trends previous observed with the ElNeDyn model; OmpX preferred contacts with basic and aromatic residues, while OmpA showed the same surprising affinity for primarily polar and non-polar residues. To give a more direct comparison the difference in contact frequency per residue between the GoMartini and the ElNeDynn models (GoMartini – ElNeDynn) was averaged across repeats (Figure 4.26). For OmpX there was a significant decrease in tyrosine interactions in the GoMartini system, along with a net increase in polar and non-polar interactions. Whereas for OmpA there was an decrease in polar interactions and an overall increase in non-polar interactions. In both cases there was an overall decrease in unfavourable hydrophobic interactions between the lipid head groups and the protein surface. The differences between the two models was rarely more that four contacts per frames, which

was not dissimilar to the difference between repeats. Thus Figure 4.26B may hold no significance, other than further emphasising a lack of reproducibility between repeats.

4.3.6 Let's Talk About Convergence

The message throughout this chapter has been one of "sometimes it converges, but often it does not". The term 'convergence' has been defined by whether qualitative and quantitative trends are reproduced across repeats. One common way of measuring convergence is to take a time series of an observable and deem a simulation has converged when this value oscillates around the mean. However, such methods are often not the best ways of measuring convergence and can be subjective to positive bias via human judgement. In this section a few ways to determine if sufficient sampling has been achieved will be investigated. Detailed tests of convergence will be performed on the longest 'apparently converged' trajectory simulated here, OmpA in RaLPS (2×60 μs).

The RMSD of a protein backbone is a common observable for the measurement of protein structure sampling. The RMSD measures the deviation of a protein backbone during the simulation from a reference structure (Figure 4.27); in this case the reference structure was the first frame of the simulation (for reasons that will become apparent in due course). The RMSD showed that significant structural changes can occur at the beginning of the simulation until eventually the RMSD oscillates around an average - from this it could be concluded that the protein dynamics in these simulations had converged. RMSD is a collective variable that has quite a bit of degeneracy in how many structural conformations a single RMSD value can correspond to; therefore the protein could still be undergoing significant conformational changes. So can anything better be done?

Drawing from a recent review on the assessment of errors and sampling in molecular simulations[194], further tests of convergence will now be discussed. The RMSD can be computed with respect to all other frames in the simulation to produce a frame vs frame RMSD matrix (Figure 4.27). In all systems the RMSD along the diagonal was 0, as this is the self term of the matrix. On-diagonal blocks of similar RMSDs can be interpreted as showing the number of states that the protein visits, while off-diagonal blocks indicate that the system is revisiting previous states. This revisiting of previous states is necessary for good sampling to have occurred[194]. For OmpA in DPPC on and off diagonal blocks were observed throughout the simulation. In particular, there were two main states of the protein in the simulation. The transition between the two main states occurred at 16 μs. Interestingly, these changes in state did not seem to affect the transmembrane tilt in the membrane (Figure 4.6). So while it appeared like the protein tilt had converged, the protein was still experiencing changes in conformation at the end of the simulation. Off-diagonal blocks of low RMSD were observed from $1 - 16$ μs, which suggested that the protein was revisiting previous areas of sampling. The change

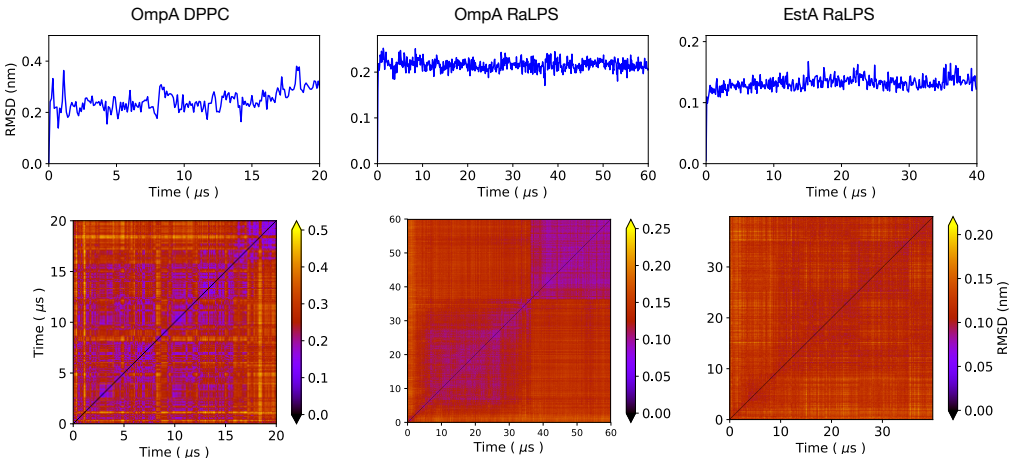

FIGURE 4.27: (top) RMSD of protein, relative to first frame of the production run. (top) Grid of the RMSD between all frames within a single independent trajectory. In both cases the RMSD was calculated every 100 ns.

of state at the end of the simulation may be a temporary transition before moving back to the state sampled from $1 - 16$ μs, but only further simulation could confirm this.

The RMSD matrix for OmpA in RaLPS showed quite different trends to the DPPC system (Figure 4.27). In the RaLPS system there were two on diagonal blocks of similar low RMSDs and no off-diagonal blocks. Therefore it was clear that OmpA was undergoing significant conformational changes, but adequate sampling could not be confirmed. The change in protein state at around 40 μs also coincided with when the protein tilt plateaued(Figure 4.2). For the RMSD matrix of EstA in RaLPS there was smaller variance in RMSD values in any given slice of the matrix. Upon closer inspection there appeared to be a large block of similar RMSDs that started at around 10 microseconds. Interestingly, this again coincided with when the protein tilt plateaued (Figure 4.2). Thus it can be tentatively assumed that the simulation of EstA in RaLPS had converged.

The RMSD matrix estimated the global sampling through the observation of a single observable during a trajectory; however, again human judgment was required to determine convergence. The next method to be discussed can quantify the relaxation times in a system and whether sampling is sufficient. This method is called block covariance analysis (BCOM)[182] and uses a combination of block averaging[195], PCA[196] and bootstrapping[197]. PCA is widely used in data science as a method to decorrelate noise in complex data or split up independent modes of motion in molecular systems[198–201]. To carry out BCOM, first PCA was carried out on subsets of the trajectory, resulting in the vectors that describe the orthogonal motions of the system and their relative importance. Following this the similarity between the PCA modes in each subset was found via computing the covariance between PCA modes. This process is then repeated over increasing subset sizes. As the size of the subsets increases the similarity between

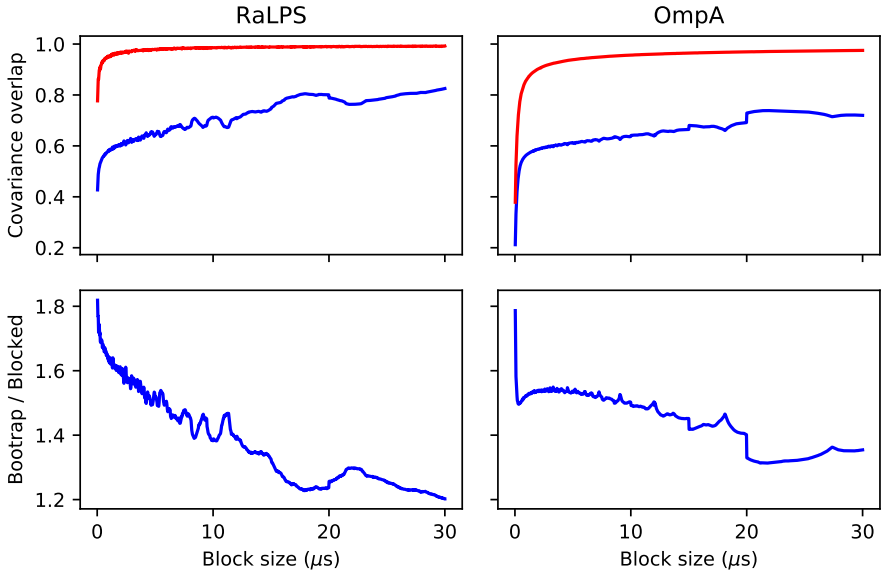

FIGURE 4.28: (top) Covariance overlap between modes of principal component analysis (PCA) across blocks of contiguous frames (blue) and blocks made via bootstrapping (red). This analysis was carried out for OmpA in RaLPS for two subsets of the system: 1) the lipid phosphates and 2) the protein backbone. A covariance overlap of 1 indicated that sufficient sampling may have occurred. (bottom) Ratio between BBCOM and BCOM. Further details can be found in the methods section (Section 4.2)

the blocks should increase (i.e. covariance between subsets should tend to 1) as is dictated by the ergodic limit. The subsets of a trajectory can be obtained through the use of contiguous blocks or via boostrapping techniques (BBCOM). The ratio between the covariance of BCOM and BBCOM as a function of block size can be used to estimate the relaxation times of sampling in a system. In both cases, the block size was increased incrementally from 0.3 to 30 μs in 0.3 μs intervals. For BBCOM the number of blocks used was always 10, whereas for contiguous blocks the number of blocks was inversely proportional to the block size.

The BCOM and BBCOM methods were carried out on two subsets of the RaLPS system containing OmpA: 1) the protein backbone and 2) the phosphates of RaLPS. These subsets were chosen to assess the sampling in important parts of the simulation separately and to reduce the computational expense of this method. In both cases the covariance overlap of the BBCOM converged to ~ 1 within 30μs. Whereas for BCOM, the covariance was lower than the BBCOM equivalent and never reached 1. At short block sizes there was likely to be a large amount of correlation within blocks, which would result in poor covariance overlap between blocks[182]. As the block size reached the same order of magnitude as the length of the simulation bootstrapping was likely to create trajectories with identical frames, resulting in erroneously high overlap values. The BCOM was normalised by the BBCOM results and the resulting ratio was fit to a double exponential, for both membrane and protein components (Figure 4.28). The phosphates in RaLPS

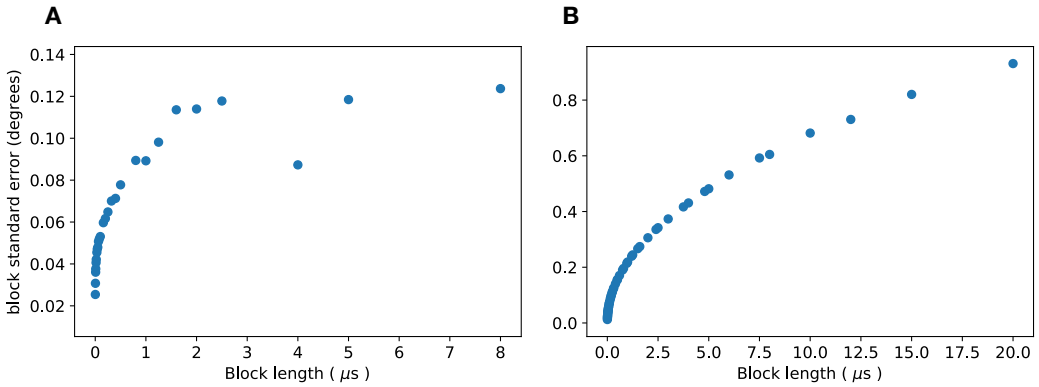

FIGURE 4.29: Standard error in the protein tilt relative to the z axis (membrane normal) as a function of block size for A) 2×20 μs of OmpA in DPPC and B) 2×60 μs of OmpA in ReLPS. Further calculation details can be found in the Section 4.2.

had decay constants of 0.16 and 12.3 μs, while the protein backbone had decay constants of 0.03 and 163 μs. In both cases the BCOM convariance overlap never reached 1 and so these simulations had not converged. Thus it was questionable whether the measured decay constants could be used to estimate the relaxation time. Overall it can be concluded that the OmpA in RaLPS system had not converged, which agreed with the previously discussed RMSD matrix.

A further convergence test was to measure the standard error in the protein tilt as a function of block size, for OmpA in DPPC and RaLPS. As the block size increases, if the system is well equilibrated the standard error will plateau [194, 195, 202]. The standard error of the DPPC system plateaued when the block size reached 2 μs to a value of $\sim 0.12°$ (Figure 4.29A). Whereas for the OmpA RaLPS system the standard error never plateaued, again suggesting that sampling was insufficient.

Observable	IACT (ns)				
	DPPC	ReLPS	RaLPS	OANT	OANT_PE
Protein tilt	3.25 ± 0.25	1120 ± 391	1452 ± 262	1525 ± 267	1934 ± 468
Membrane thickness	1.57 ± 0.00	992 ± 272	1396 ± 400	3996 ± 518	3255 ± 651
Density	1.50 ± 0.00	1.50 ± 0.00	1.50 ± 0.00	1.80 ± 0.29	1.51 ± 0.00
Energy	1.50 ± 0.00	11.9 ± 5.45	555 ± 84.7	1328 ± 158	1293 ± 212
Lipid tail orders	1.54 ± 0.01	133 ± 20.8	71.9 ± 22.8	93.7 ± 21.6	62.7 ± 20.3

TABLE 4.3: The integrated autocorrelation times (IACTs) of a range of observables averaged across all six proteins in this study. The protein tilt and membrane thickness were calculated as described in the methods section (Section 4.2). The density and total energy was calculated for the entire system. The IACT lipid tail orders were determined for each tail separately and then averaged. For outer membrane systems only the tail orders for LPS were determined. In all cases the reported error was the standard error.

It would be interesting to quantify the decorrelation for a range of observables across DPPC and OM systems. Thus the integrated correlation time (IACT) were calculated for the protein tilt, membrane thickness, density, energy and LPS tail orders for all DPPC, ReLPS, RaLPS, OANT and OANT_PE systems and then averaged across the six proteins in this chapter (Table 4.3). The IACTs for observables in DPPC systems were always below 10 ns, with very small standard errors (< 1 ns). In contrast, the IACTs of observables within LPS systems varied by multiple orders of magnitude and were much larger than their respective values for DPPC. The protein tilt and membrane thickness of OM systems took $1 - 5$ μs to decorrelate, with errors on the order of 100s of nanoseconds. The lipid tail orders tended to decorrelate quickly (within 150 ns) which suggested that the limiting factor in system relaxation was the LPS head and sugar groups. Interestingly, the IACTs of the energy, membrane thickness and protein tilt were positively correlated with increasing LPS size. It should be mentioned that these values are not guides for convergence, but simply measured the time taken for observables to decorrelate from their starting values.

4.4 Conclusions

In this chapter six outer membranes proteins OmpA, OmpX, OmpF, BtuB, FhuA and EstA were studied in a variety of outer membrane models that totalled milliseconds of simulation time. It was seen that proteins formed unique interactions across all protein sizes and LPS levels. The observed patterns were often not consistent across the same level of LPS or proteins with similar sizes or functions. The amino acids LPS preferred to form contacts with also varied in both charge and polarity across different levels of LPS. In a few cases, such as EstA, gradients in amino acid abundance as a function of extracellular height explained the observed changes in lipid - protein interactions. Transmembrane beta barrels have rings of aromatic residues at both ends of the protein, which have been commonly thought in the literature to dictate protein orientation[187]; however, here it was shown that this was an oversimplification for smaller beta barrels. Instead, the protein orientation has been shown to depend on the LPS level, especially when the protein has a significant extracellular region. For the smaller barrels the asymmetry in diffusion between leaflets can knock onto the dynamics of the protein in each leaflet; often LPS pins the protein, while the bottom half moves to the optimal orientation in the phopholipid lower leaflet.

As in the previous chapter, LPS dependant clustering of cardiolipin was observed across all proteins and multiple levels of LPS - confirming this was a property of outer membrane systems in general. For systems that contained smooth LPS, O-Antigen tilt was found to be a function of the size of the protein cross-section and extracellular domains. Furthermore, through the introduction of phospholipids or rough LPS to the upper leaflet of a smooth LPS outer membrane, the thickness of the O-Antigen layer could be modified. In all of the systems studied here the O-Antigen chains did not envelope membrane proteins or block access to transmembrane ion channels. Given that the outer membrane is a major barrier for antibacterial molecules, understanding how this barrier changes as a function of system complexity is key to future work. Here the ground work has been laid for future studies to build upon with increasingly complex membrane models.

In this work the effect of LPS level on protein orientation and interactions has been probed, but there are other important factors that have been neglected here. In particular, it is known that the outer membrane is a crowded environment and this would definitely have an effect on the behaviours of the proteins; whether from the effect of crowding on membrane properties, or the binding of protein to other proteins or the cell wall[203]. One simple study that could form the basis of such work would be to investigate OmpA crowding and its effect on protein and membrane properties. OmpA is known to be one of the most abundant outer membrane proteins[204], on top of known binding to the cell wall[203, 205].

While the work carried out here utilised state of the art simulation lengths (30−60 μs), in many cases systems were insufficiently sampled even after 60 μs. Across all simulations there was minimal lipid sorting, which would suggest the need for simulations nearing millisecond timescales for sufficient sampling to occur. Currently such timescales are not practical, even for coarse grained simulations, and so the use of enhanced sampling for outer membrane systems is likely to be key in future work.

Chapter 5

Lipid Extraction in the Gram-negative Cell Envelope

5.1 Introduction

The outer and inner membranes form important barriers to the transport of antibiotics into Gram-negative bacteria. In particular, the outer membrane has been shown to provide a large barrier to both non-polar and polar small molecules [90, 206]. Unlike phospholipid membranes, the outer membrane is thought to not exhibit passive diffusion of small molecules across the membrane; instead diffusion generally occurs via porins[102]. The impenetrability of LPS by most small molecules is a result of a combination of factors. The LPS sugar groups act as a barrier to polar and anionic groups, while the core of the membrane blocks nonpolar compounds. Further to these points, LPS is tightly packed by divalent cations that contribute to a reduction of LPS diffusion by an order of magnitude[35].

Quantifying the stability of each lipid component in the cell envelope is important for understanding mechanistic processes that involve the membrane, such as peristaltic motions of lipids or cell fusion. Lipid stability in the membrane can be quantified through the determination of the free energy of extraction of a single lipid. So far the only known study of the free energy of lipid extractions in the outer membrane was that of lipid A in a coarse-grained bilayer[207]. Furthermore, most simulation studies of lipid extraction or membrane permeation have not included the effects of integral proteins on the ease of lipid extraction[90, 208, 209]. Bacterial membranes are crowded with proteins, which should have a significant effect on lipid stability in the bilayer.

Umbrella sampling[210] (US) has been used to determine the free energy of a range of biomolecular phenomena, such as membrane permeation[90, 102, 211]. One difficulty of applying US to large and complex systems, such as membranes, is a lack of convergence due to insufficient simulation times. US can be applied to larger systems through the use of coarse-grained models, such as Martini[109]. In recent work, a combination of umbrella sampling and coarse-grained models were used to reproduce the experimentally known preference of the GRP1-PH protein for PIP_3 (a lipid) over PIP_2[212]. This work and other such studies[213, 214] have shown the validity of using coarse-grained models to study the relative free energy of protein-lipid binding.

The work in this chapter was split into two components: 1) Compare the PMFs of the extraction of different lipids in the inner and outer membranes. 2) Investigate the effects of AqpZ on lipid extraction in the inner membrane. In this chapter a cumulative total of milliseconds of coarse-grained US simulations were run. AqpZ is a water efflux pump that is found in the inner membrane of *E.coli* as a homotetramer[70]. AqpZ was chosen to study the effect of crowding on lipid extraction, as it has a preference for binding cardiolipin[71, 105, 215] over other common phospholipids.

5.2 Methods

5.2.1 Simulation Parameters

For this chapter the GROMACS[150] MD package (version 2018) and the Martini (version 2.2) force field[109–112] was used for all simulations. Simulations were run at a temperature of 323 K and a pressure of 1 bar. The temperature was controlled with the stochastic velocity rescale thermostat with a coupling constant of 1.0 ps. Equilibration steps used the Berendsen semi-isotropic barostat with a coupling constant of 4.0 ps, whereas for production runs the Parrinello-Rahman barostat with a coupling constant of 12.0 ps was used. A timestep of 10 fs was used for all US simulations or systems containing proteins; in all other cases the timestep was 20 fs. The short range cutoff for non-bonded interactions was 1.2 nm and utilised the Potential-Shift-Verlet cutoff scheme. The electrostatic interactions were determined with reaction field with short and long range dielectric constants of 15 and 0 (infinite shielding), respectively. The Verlet buffer tolerance was set to 0.005 $kJmol^{-1}ps^{-1}$. The LPS models used here were parameterised by previous members of the Khalid group[95].

5.2.2 System Setup

The outer membrane model consisted of an upper leaflet of ReLPS and a lower leaflet of 90% POPE, 5% POPG and 5%cardiolipin. The second membrane studied in this chapter was the symmetric inner membrane (75% POPE, 20% POPG and 5% cardiolipin).

The initial coordinates of the protein AqpZ (2ABM)[70] were obtained from the RCSB protein data bank. Any missing residues or broken loops were added with modeller[178] and then missing hydrogens added with PDB2PQR[179]. Then the AqbZ tetramer was generated and given a transmembrane alignment by the program MemEmbed[180].

The initial coordinates of each system were generated with the CHARMM-GUI web interface[96]. AqpZ was coarse-grained using the 'martinise.py' script[152] to the ElNeDyn model[173] and the backbone beads within a $0.9nm$ cutoff of each other restrained by a 500 $kJmol^{-1}nm^{-2}$ elastic network. The elastic network was applied between, as well as within, monomer units of AqpZ. Three systems were generated: an outer membrane model, and an inner membrane model with and without the AqpZ tetramer. The initial dimension of the system with and without a protein were $\sim 18.6 \times 18.6$ and $\sim 12.0 \times 12.0$ nm, respectively. LPS lipids were neutralised with calcium ions and then any remaining charge was balanced out with sodium ions. The system was then minimised and relaxed with a short period of equilibration (30 ns), following which additional solvent was added to give a box height of 20 nm. Once the solvated system was minimised and then equilibrated, a 10 μs or 5 μs production run was carried out for outer and inner membrane systems, respectively. Snapshots of all of the systems used in this chapter are shown in Figure C.1.

5.2.3 Choosing a Collective Variable

The first step of US is often to decide what is the reaction coordinate of interest to measure the PMF along. The reaction coordinate is also often referred to as the collective variable (CV). The choice of CV is very important for US and can determine whether free energy barrier of the process of interest is correct [216] and the simulation time required. There are a few basic guidelines for choosing a suitable CV for the enhanced sampling of any system:

1. The chosen CV should be able to distinguish the initial and final states and any intermediate configurations of interest.
2. Similar to the last point, each CV value should represent a minimal area of conformational space.

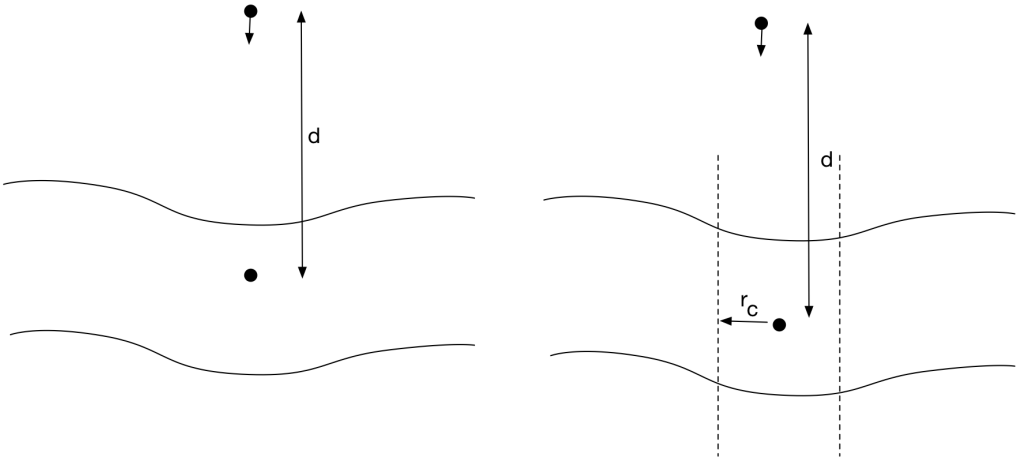

FIGURE 5.1: Figure comparing the centre of mass reference group and the cylinder reference group, with respect to a molecule of interest and the membrane. The cylinder reference group allows for the CV to be calculated within a cylinder of radius r_c of the molecule of interest. d describes the reference distance between the centre of mass of the membrane or subset of the membrane and the lipid being pulled. Note that the centre of mass of the membrane did not include the pulled lipid.

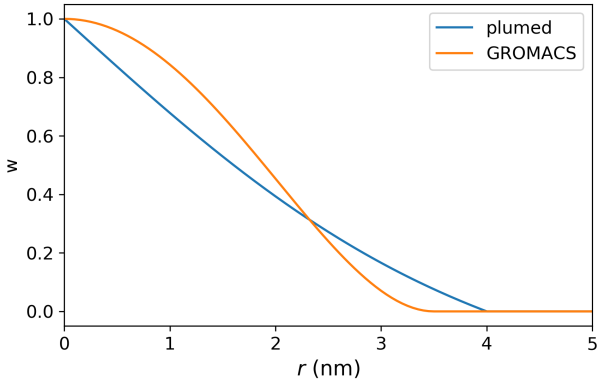

FIGURE 5.2: The weight of an atom's contribution to the CV, w, as a function of distance r from the long axis of the cylinder reference groups (see Figure 5.1) used in this chapter. Cylinder reference groups implemented in GROMACS or plumed were used. The radii of the cylinders for the GROMACs and plumed methods were 3.5 and 4.0 nm, respectively (Equations (5.1) and (5.3))

The CV for lipid extraction is usually the z component of the distance, d, between a reference group for the extracted lipid and the membrane (Figure 5.1). Thus the simplest CV would used the centre of mass of the pulled lipid and the membrane as the reference groups. For small membranes this is a reasonable CV, but as we move to larger systems ($>$ 10 nm in the xy plane) this CV gives a PMF that is dependant on the size of the membrane[217]. A more local membrane reference group is the centre of mass of the atoms within a cylindrical projection (of radius r_c) around the pulled lipid (Figure 5.1). For lipid extraction the long axis of the cylinder was in the direction of the CV path (i.e the z axis). As the atoms in the membrane can dynamically leave or enter the cylindrical projection, the contribution of atoms are weighted (Figure 5.2) to prevent large jumps

in force. For GROMACS the functional form of the weight is,

$$w(r) = \begin{cases} 1 - 2\left(\frac{r}{r_c}\right)^2 + \left(\frac{r}{r_c}\right)^4, & \text{if } r < r_c \\ 0, & \text{otherwise} \end{cases} \tag{5.1}$$

where r_c is the radius of the cylinder and r the distance of an atom from the long axis of the cylinder. The use of the cylinder reference group, for US simulations, has been shown to give PMFs of membrane permeation that are independent to membrane size[217].

To compare lipid extraction CVs in the context of the OM and IM, four different CVs were trialed. The CVs were varied based on the reference groups of the pulled lipid and that of the membrane. The reference group for the lipid was either a phosphate bead or the glycerol linker (GL0) for cardiolipin (HEAD), or the centre of mass of the entire lipid (COM). For ReLPS, the HEAD reference group was the centre of mass of both phosphate beads. The reference group of the membrane was either the center of mass of the membrane (MEMB), or the center of mass of a cylindrical projection, of radius 3.5 nm, centered on the pulled lipid (CY). There were four CVs that covered every combination of reference group:

1. COM_MEMB
2. HEAD_MEMB
3. COM_CY
4. HEAD_CY

It is important to note that the pulled lipid was not included in the reference group of the membrane.

5.2.4 Lipid extraction: Uncrowded Systems

a For each lipid type 3 different lipids were extracted and for ReLPS one lipid was extracted 3 times (total of 5 repeats for ReLPS).

TABLE 5.1: Summary of all umbrella sampling simulations carried out for uncrowded outer and inner membranes (OM and IM, respectively). For ReLPS 3 different lipids were extracted 3 times, but the extraction of one lipid had 3 repeats. In all other cases 3 different lipids were extracted. Each collective variable was defined in Section 5.2.3.

Membrane	Lipid extracted	CV	Time (μs)
OM	5×ReLPS	COM_MEMB	10
OM	5×ReLPS	HEAD_MEMB	7
OM	5×ReLPS	COM_CY	7
OM	5×ReLPS	HEAD_CY	7
OM	3×POPE	HEAD_CY	1.5
OM	3×POPG	HEAD_CY	2.0
OM	3×cardiolipin	HEAD_CY	2.0
IM	1×POPE	COM_MEMB	1.5
IM	1×POPE	HEAD_MEB	1.5
IM	1×POPE	COM_CY	1.5
IM	3×POPE	HEAD_CY	1.5
IM	3×POPG	HEAD_CY	2.0
IM	3×cardiolipin	HEAD_CY	2.0

5.2.5 Lipid Extraction: The Effect of Proteins

The IM system with and without AqpZ were used as the basis for US simulations in this section. To assess the effect of AqpZ on the ease of lipid extraction, lipid sampling was restrained to the bulk of the membrane or the region local to the protein. The local region was defined as being within 3 nm of the protein, in the xy plane, while the bulk region was anything else. The extracted lipid was restrained to a specific region with a harmonic bias, k_r, of 50 kJmol^{-1}nm^{-2} that was only applied outside the region of interest.

The lateral restraints were implemented using GROMACS (version 2018), patched with plumed (version 2.4.4)[218]. Plumed allows the simple implementation of a variety of restraints and enhanced sampling methods. Thus both the US bias and the lateral restraints were implemented using plumed. The cylindrical reference group can also be used via plumed, but the weighting of each atom's contribution to the final CV value was different,

$$w'(r) = 1 - tanh\left(\frac{r}{r_c}\right) \tag{5.2}$$

where r was the distance to the long axis of a cylinder of radius, $r_c = 4$ nm. Equation (5.2) can be modified, such that $w(r \geq r_c) = 0$, by shifting and stretching the original weighting function $w'(r)$ to give (Figure 5.2):

$$w(r) = \begin{cases} \frac{w'(r)-w'(r_c)}{w'(0)-w'(r_c)}, & \text{if } r < r_c \\ 0, & \text{otherwise} \end{cases} \tag{5.3}$$

TABLE 5.2: Summary of all umbrella sampling simulation for the study of lipid extraction in the presence of AqpZ. The region refers where the extracted lipid was restrained to in the xy plane with respect to AqpZ: local (< 3 nm from AqpZ) and bulk (> 3 nm).

Protein	Lipid extracted	Region	Time (μs)
No	1×POPE	NA	2.0
No	1×cardiolipin	NA	2.0
Yes	1×POPE	Local	2.0
Yes	1×cardiolipin	Bulk	2.0
Yes	1×POPE	Local	2.0
Yes	1×cardiolipin	Bulk	2.0

Patching GROMACs within plumed results in a reduction of the speed of any MD simulation. The speed of plumed scales based on the the number of beads involved in the biases and can be up to an order of magnitude slower than GROMACS. Thus the CV for lipid extraction was adjusted, to minimise the number of beads in each reference group, while maximising the simulation speed. The reference group for the extracted lipid was the phosphate bead or the glycerol linking bead (GL0) for cardiolipin. The reference group of the membrane included the phosphate beads of each lipid within a cylindrical projection along the z axis, with a radius of 4 nm, centred on the extracted lipid. Hence the CV was the distance between reference groups of the membrane and the extracted lipid. Again the reference group of the membrane never included any beads from the extracted lipid.

Steered MD was used to pull a lipid out of the membrane using the HEAD_CY CV, as done in Section 5.2.3. A lipid local to AqpZ or in the bulk region were restrained with a 10 kJmol^{-1}nm^{-2} harmonic restraint in the xy plane during steered MD, to prevent significant lateral diffusion. Each lipid was pulled through the membrane and out of the opposing leaflet, which gave better coverage of the expected minimum of the PMF. Then windows were generated, every 0.1 nm, from 0 to 8 nm along the CV (81 windows), where 0 was the centre of the membrane. A harmonic bias of 1000 kJmol^{-1}nm^{-2} was used for each umbrella window and a 2 μs production run generated per window. Further details of all US simulations carried out for this section are given in Table 5.2.

5.2.6 Analysis

A number of methods of calculating PMFs from US were used:

- For simulations in Section 5.2.4 - GROMACS implementation of WHAM was used[135] and the integrated autocorrelation times (IACT) for bootstrap analysis were determined with the python module 'pymbar'[136, 219]. The multistate

Bennett acceptance ratio (MBAR, described in Section 2.6.2) was used as an alternative PMF estimator and was also implemented within the 'pymbar' module. The number of bins used for PMFs calculated with MBAR was 100.

- For simulations in Section 5.2.5 - MBAR was used to calculate PMFs and their estimated uncertainties with a total of 200 bins.

All PMFs calculated with WHAM[134] used 200 bins and a convergence tolerance of 1×10^{-6}. Errors were estimated with 200 bootstraps. The value of each PMF was set to 0 in bulk water.

The free energy of lipid extraction ΔG_{PMF} was estimated by taking the difference between the minimum of the PMF and a point where the PMF had plateaued, i.e in solution. If lateral restraints (i.e k_r) were applied to restrict sampling of a lipid to a certain region in the xy plane, then the effect of the restraint must be accounted for during the calculation of the free energy of extraction. The corrected standard free energy of lipid extraction can be defined as

$$\Delta G_e^o = \Delta G_{PMF}^o - \Delta G_c \tag{5.4}$$

where ΔG_{PMF}^o and ΔG_c were the free energy change of the PMF and the correction, respectively. ΔG_{PMF}^o is a standard free energy and is found through integrating over the bound and unbound regions of the PMF[220]

$$exp(-\beta \Delta G_{PMF}^o) = \frac{\int_{bound} exp(-\beta\ PMF(z))dz}{\int_{unbound} exp(-\beta\ PMF(z))dz}. \tag{5.5}$$

The bound region started at the minimum of the PMF and ended when the PMF profile became constant. The bound region for POPE and CDL was set to end at 5.02 and 6.70 nm, respectively. Following similar work in the literature[221, 222], it is known that the correction term can be defined as

$$\Delta G_c = -RTln\left(\frac{V^o}{V_a}\right) \tag{5.6}$$

where V^o was the standard state volume (1660 $\mathring{A}$) and V_a the available volume with the lateral restraint. Thus the correction defined the free energy change from a standard solution, to the available volume after the restraint was applied. The available volume depended on the regions the lipid was restrained to 1) near the protein (local, $V_{a,local}$) or 2) far away from the protein (bulk, $V_{a,bulk}$). The local region was defined by whether the lipid reference group was within a 3 nm cutoff, in the xy plane, of AqpZ and the bulk region was anything else. $V_{a,local}$ can be approximated by taking the difference between the area (in the xy plane) within the local region $A_{l,i}$ and the area of the protein $A_{prot,i}$,

for window i, multiplied by the window spacing,

$$V_{a,local} = \sum_{i=0}^{N} (A_{l,i} - A_{prot,i}) dz, \tag{5.7}$$

where N was the total number of umbrella windows. Therefore $V_{a,bulk}$ was

$$V_{a,bulk} = \sum_{i=0}^{N} (A_{box,i} - A_{r,i}) dz, \tag{5.8}$$

where $A_{box,i}$ was the area of the simulation box. Through combining Equation (5.6) with Equation (5.7) or Equation (5.8), the bulk and local correction terms can be obtained ($\Delta G_{c,bulk}$ and $\Delta G_{c,local}$).

5.3 Results and Discussion

5.3.1 Coverage of reaction coordinate

US is usually carried out between two states of interest. To get an accurate free energy profile between these two states umbrella windows must be spaced such that the coverage of the reaction coordinate is sufficient. However, the number of windows used should not be too excessive, as this would result in an unnecessary large use of computational resources. To assess the coverage of the reaction coordinate, the percentage overlap between adjacent windows was measured. A previous study of poration through ion channels determined that a 5% overlap between adjacent windows provided sufficient coverage of the reaction coordinate[223].

The overlap between windows was measured for an extraction of ReLPS with the COM_MEMB CV(Figure 5.3). Overlap values ranged from $\sim 20-55\%$, with an average overlap of $35.0 \pm 9.9\%$. The theoretical percentage overlap between two harmonic biases, can be assumed to be [223]

$$\%overlap = 100 \times \left[1 - erf(d/\sqrt{8}\sigma)\right] \tag{5.9}$$

where d was the distance between adjacent bias centers, k the bias strength and σ was the gaussian width given by

$$\sigma = \sqrt{k_B T/k}. \tag{5.10}$$

The ideal window overlap for adjacent windows was found to be 35.6%, which was within one standard deviation of the average overlap ($35.0 \pm 9.9\%$). There are two likely contributions towards the overlaps deviating from the ideal value: 1) The steered MD path may sample areas of CV space near transitions in state poorly. 2) Windows in the region

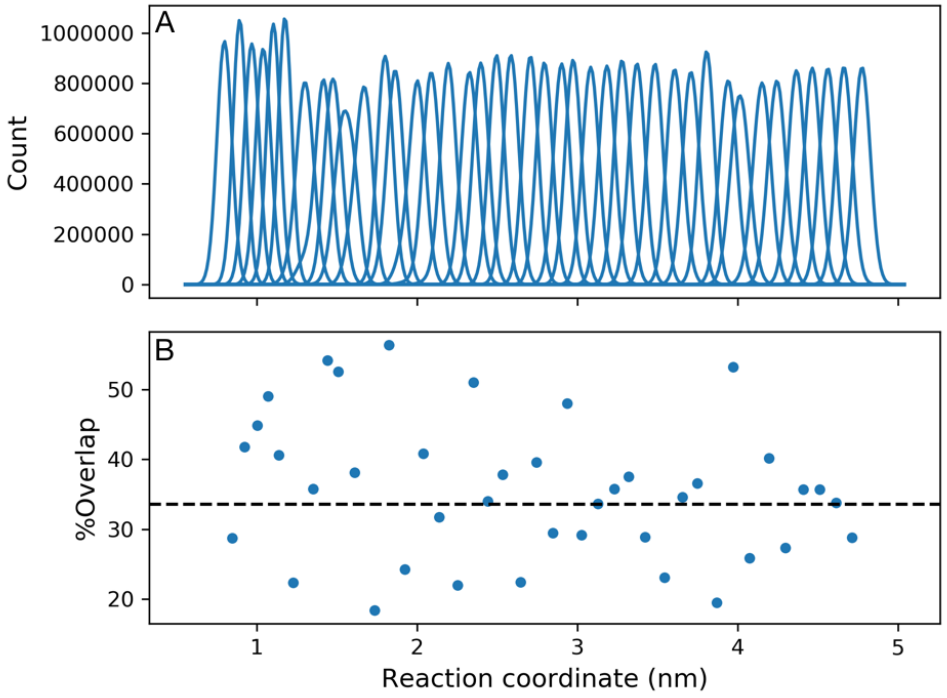

FIGURE 5.3: A) histogram of positions for 41 umbrella windows spaced every 0.1 nm. B) Percentage overlap between adjacent windows. This profile was generated for the extraction of an ReLPS lipid using the COM_MEMB CV. The dotted line was the ideal overlap between adjacent gaussians.

of transitions with large free energy barriers will have non-gaussian CV histograms.

The overlap between adjacent windows was also assessed for the other CVs trialled (Figure 5.4). For every CV trialled the overlap was always above 5%. In the bulk water region (CV $>$ 4 nm) the variation in overlap values, from the ideal value, was smaller for CVs based on the cylindrical reference group. This observation likely stemmed from the lack locality of the MEMB reference group, which would have resulted in high conformation degeneracy in each window. The main causes of high conformational degeneracy was likely local or global undulations of the membrane. While coverage of the reaction coordinate is important it is only one component of achieving sufficient sampling.

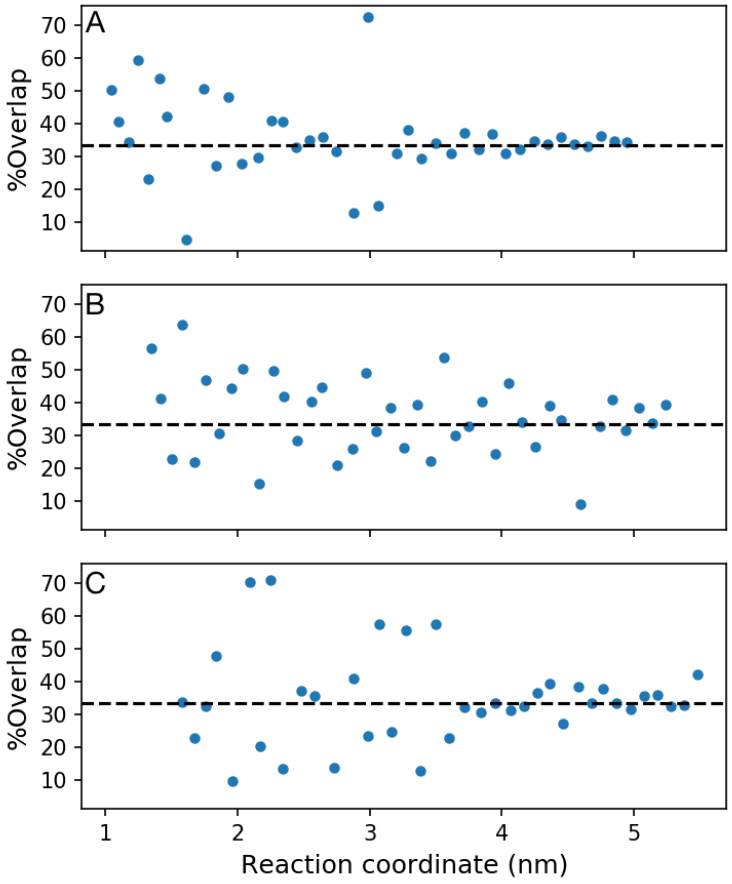

FIGURE 5.4: Percentage overlap between adjacent windows along the reaction coordinate of an ReLPS extraction for CVs A) COM_CY B) HEAD_MEMB and C) HEAD_CY. The 41 umbrella windows were spaced every $\sim$ 0.1 nm. The dotted line was the ideal overlap between evenly spaced adjacent gaussians.

5.3.2 Convergence of LPS Extraction

It is difficult to measure the performance of a CV without already knowing the solution to the problem. Thus the discussion of the performance of each CVs, for ReLPS extraction, will be quite general. First the difference in path sampling across CVs were explored. There was one big difference between the lipid extraction path between CVs that used the COM and HEAD reference groups. When the COM reference group was used, the lipid had more rotational and translational degrees of freedom for each CV value, compared to CVs that included the HEAD reference group. When a lipid was extracted using the COM group the lipid would rotate such that the LPS sugars and lipid A head group were in contact with the membrane for as long as possible (Figure 5.5). The HEAD reference group pulled the lipid out of the membrane without allowing this flip to occur.

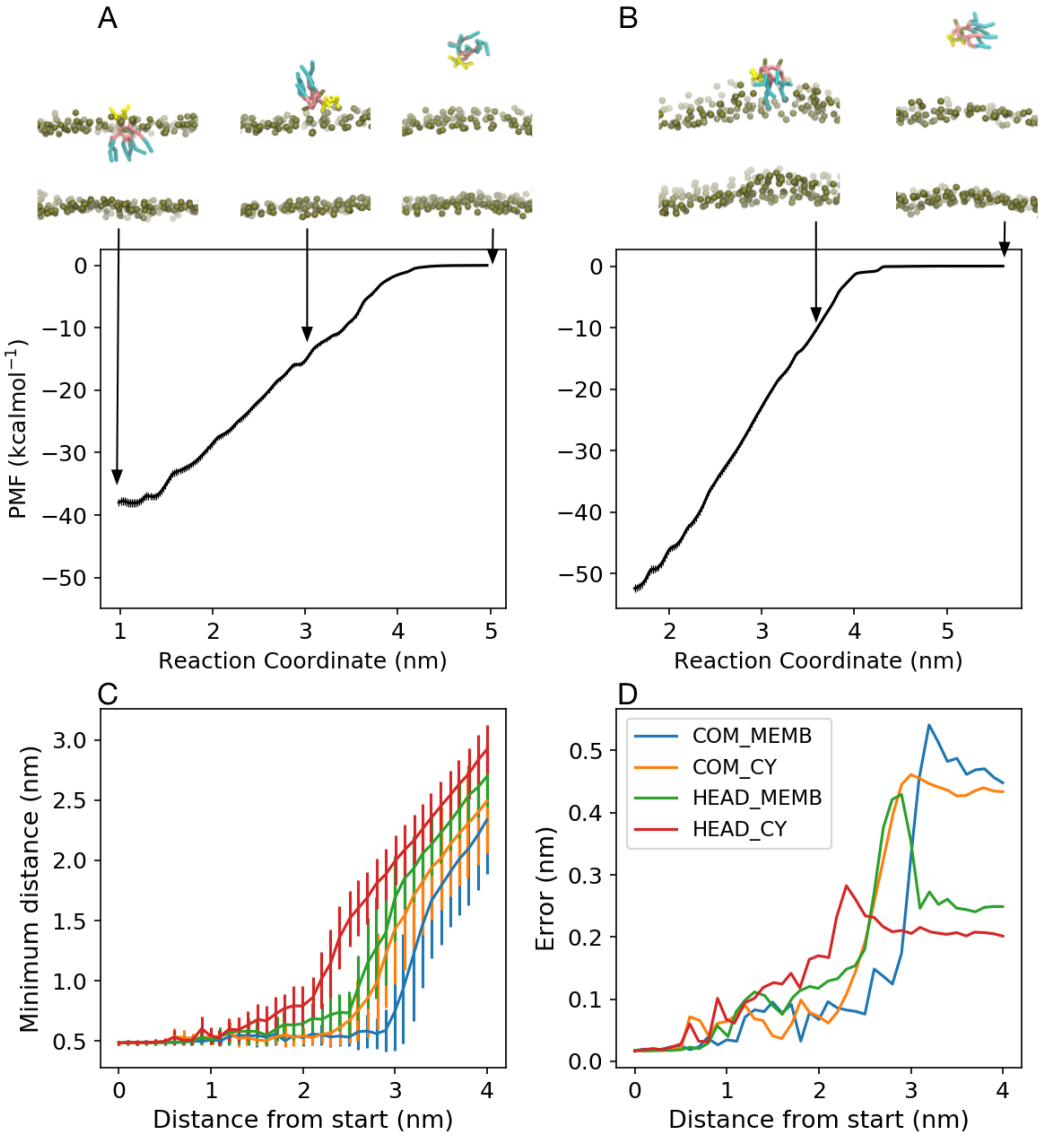

FIGURE 5.5: Snapshots of the extraction of ReLPS from the outer membrane aligned to the PMF for CVs A) COM_MEMB and B) HEAD_CY. Key for snapshots: gold=phosphates, yellow=sugars, pink=acyl groups, cyan=lipid tails. C) Minimum distance from phosphate beads in the extracted ReLPS to the outer membrane and the D) error in the minimum distance relative to the start of each CV. The CVs were defined in Section 5.2.3

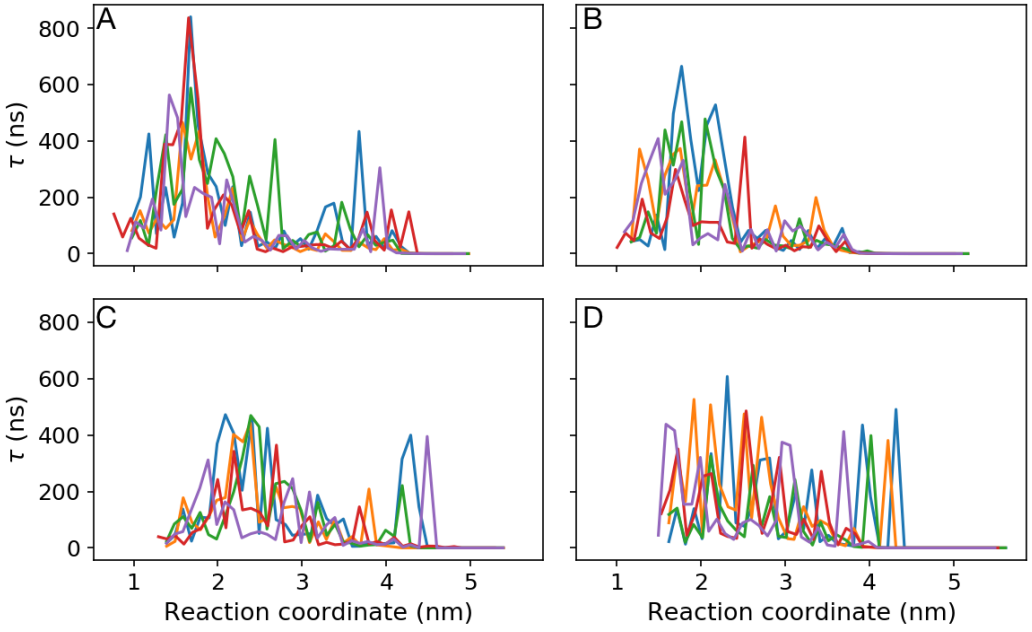

FIGURE 5.6: Integrated autocorrelation times (τ) for each umbrella window of the extraction of ReLPS from the outer membrane with CVs A) COM_MEMB, B) COM_CY, C) HEAD_MEMB and D) HEAD_CY CV. Each line represented a different repeat.

The minimum distance between the phosphate beads of the extracted LPS and the membrane was calculated to show the path the lipid headgroup took for each CV (Figure 5.5). Figure 5.5C confirmed that lipid A left the membrane surface much later in the reaction coordinate when the COM reference group was used. As the specificity of the CV increased, there was a decrease in the error of the minimum distance when ReLPS was out of the membrane Figure 5.5D. For the HEAD_CY CV there were three distinctive regions: 1) a flat plateau when lipid pulling began (< 1 nm from the pull start) 2) a gradual increase in the minimum distance as the lipid headgroup was extracted from the membrane (< 2 nm). 3) When the entire lipid was in solution (< 2.5 nm). These three regions were only observed when the lipid was pulled from the phosphate beads. What these results show is that the COM reference group gives the lipid more flexibility during the extraction process. Thus CVs that utilised the COM reference group should result in longer convergence times, but may capture the minimum free energy path of lipid extraction more accurately (this remains to be seen).

Before discussing the PMFs the autocorrelation time, τ, of CV values within each umbrella window were determined (Figure 5.6). The autocorrelation time was very inhomogeneous across the reaction coordinate, with τ ranging from a few to 100s of nanoseconds. The longest autocorrelation times occurred in the regions of the CV where the lipid was in or near the membrane. Often US simulations for atomsitic or CG simulations only report simulation lengths of < 500 ns. The autocorrelation times determined for these systems suggested that, for extraction/permeation studies involving LPS, simulation

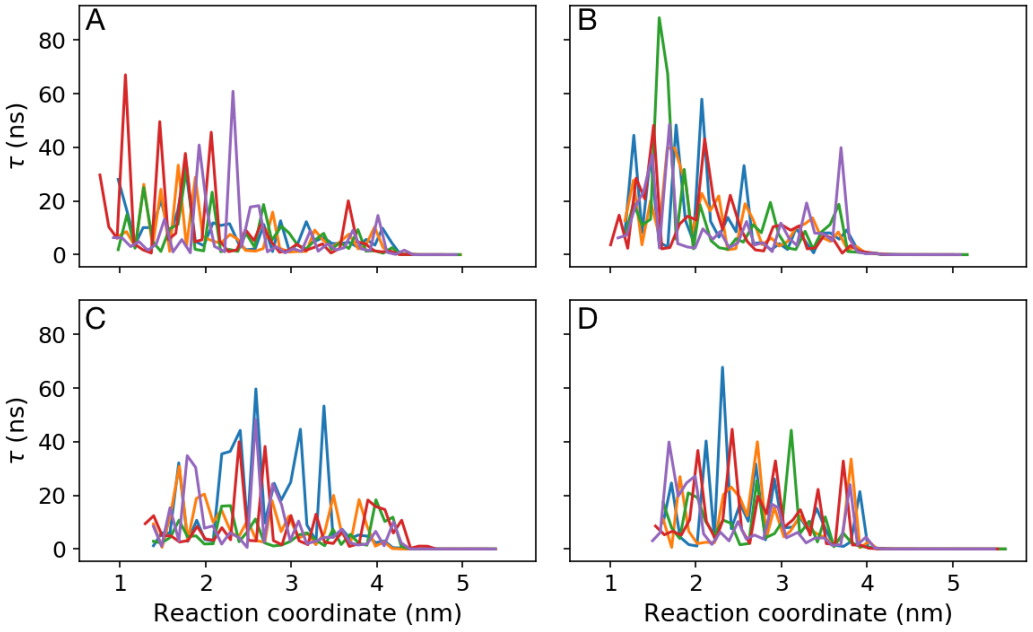

FIGURE 5.7: Integrated autocorrelation times (τ) for each umbrella window of the extraction of ReLPS from the outer membrane (from $1-2$ μs) with CVs A) COM_MEMB, B) COM_CY, C) HEAD_MEMB and D) HEAD_CY CV. Each line represented a different repeat.

times of less than 1 μs would not be advised. The autocorrelation times were also calculated for $1-2$ μs across all CVs trialled for LPS extraction (Figure 5.7). Values of τ were consistently smaller than 100 ns, but still only an order of magnitude below the analysed time period (1 μs).

For each CV, three different ReLPS lipids were extracted and one lipid was extracted three times. Thus PMF convergence could be probed for a single lipid and between different lipids. All PMFs were calculated across the last 2 μs of each umbrella window (Figure 5.8). ReLPS extraction free energies were spread across a large range of $35-55$ kcalmol^{-1}. There was little convergence between the PMFs of repeat extractions or different ReLPS lipids. The COM_MEMB CV had 10 μs of umbrella sampling run for each window, but only two out of three extractions of the same lipid were similar. The CV with least similarity between different PMFs was HEAD_MEMB. The only CV that gave the same PMF profile for all three repeats of a single lipid extraction (lipid 1) was COM_CY. Furthermore, two out of the three ReLPS lipids extracted with the COM_CY CV gave the same lipid extraction free energy.

One point of interest was whether it could be shown that individual PMF profiles had converged, without comparison to another lipid extraction. The slow kinetics of ReLPS have resulted in different environments for each LPS. Thus different LPS lipids could

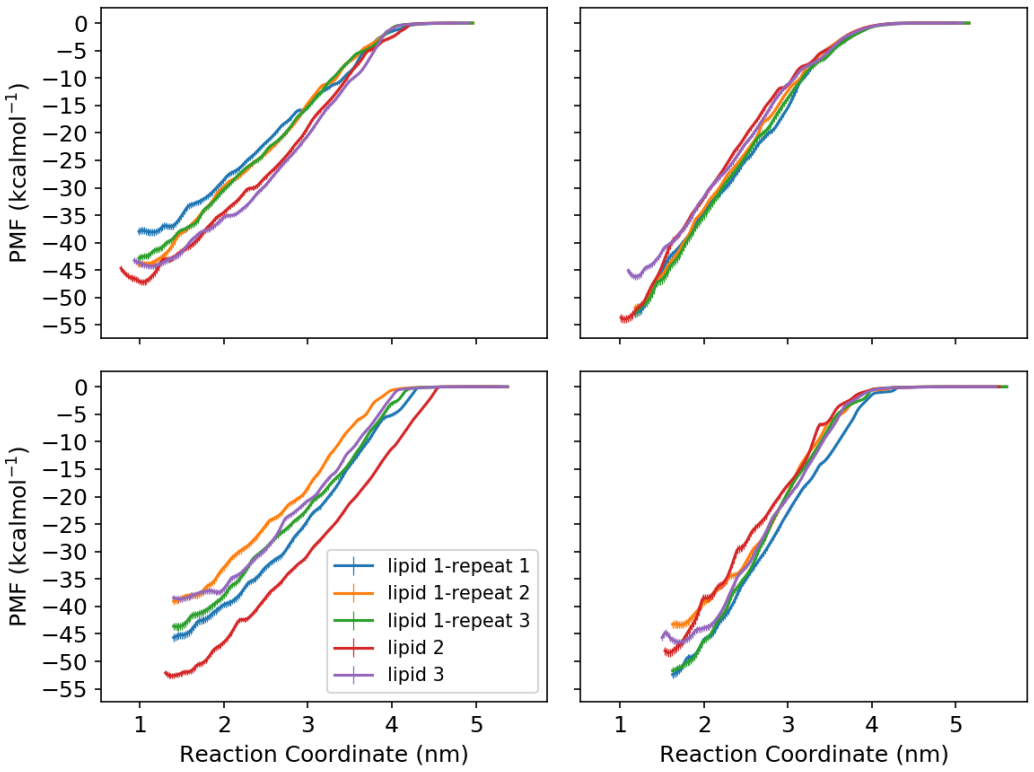

FIGURE 5.8: PMFs of ReLPS extraction from the outer membrane using the A) COM_MEMB, B) COM_CY, C) HEAD_MEMB and D) HEAD_CY CV, measured across the last 2 μs of each window. The CVs were defined in Section 5.2.3.

have converged to different extraction free energies. The convergence of a single PMF was determined by taking the PMF across a series of adjacent time intervals; in this case PMFs across 1 μs block were taken every 0.5 μs. If convergence occurred then these profiles should begin to oscillate around an average or tend to a fixed profile.

The convergence was probed for the PMFs of lipid 1 (repeats 1 and 2) and lipids 2 and 3 from Figure 5.8 (Figure 5.9). The difference in extraction free energies from the first microsecond to the last was generally around 20 kcalmol^{-1}, which was quite a significant difference. The most significant changes in the PMF occurred within the first 2 μs of each US simulation, after which any further changes were more gradual. Figure 5.9A and B showed oscillations around an average after 4.0 μs, that suggested these two profiles had converged; there was no clear convergence for the other extracted lipids. Given that the PMFs with the lowest extraction energy had not converged this suggested that each ReLPS had a different extraction free energy energy (at least on the timescales seen here).

So far the PMFs were calculated with WHAM, with the inclusion of autocorrelation times. There are alternate methods of PMF calculation that have gained popularity in the enhanced sampling community, such as MBAR[136]. One of the advantages of

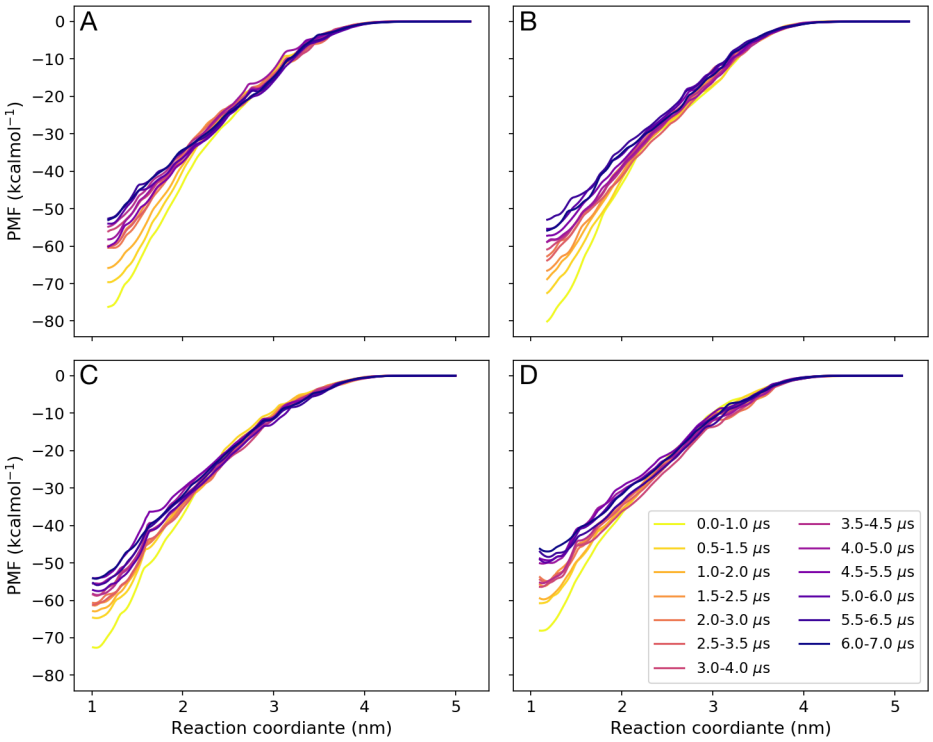

FIGURE 5.9: PMFs of ReLPS extraction of A) lipid 1-repeat 1, B) lipid 1-repeat 2, C) lipid 2 and D) lipid 3 (see Figure 5.8) using the COM_CY, measured across 1 μs blocks. The CV was defined in Section 5.2.3. Uncertainties were not included for the sake of clarity.

MBAR over WHAM is that it gives a direct method for the estimation of statistical uncertainties (Section 2.6.2). To see if the trends discussed here were consistent across calculation methods, the PMFs of the last 2 μs were repeated with: 1) WHAM with a bayesian bootstrap method (Figure C.2) 2) MBAR (Figure C.3). Overall there was little change in the observed trends when using different methods, but the estimated uncertainties were larger. Bootstrap methods that incorporate autocorrelation times can underestimate the uncertainty, especially if sampling is limited.

5.3.3 Convergence of Phospholipid Extractions

To contrast and compare the behaviour seen for ReLPS, the phospholipids in the inner leaflet of the outer membrane and the inner membrane were also extracted (Table 5.1). The PMFs of extracting different lipids of the same type usually converged within 2 μs(Figure 5.10). The difference in the free energy of extraction between the inner leaflet of the outer membrane and the inner membrane was defined as $\Delta G_t = \Delta G_{OM} - \Delta G_{IM}$, where ΔG_{IM} and ΔG_{OM} were the free energy of extraction in the outer and inner membrane, respectively. ΔG_t was -0.35, 1.24 and 1.70 kcalmol^{-1} for POPE, POPG and cardiolipin, respectively. It was interesting that only the stability of POPG and

cardiolipin were increased by the presence of ReLPS.

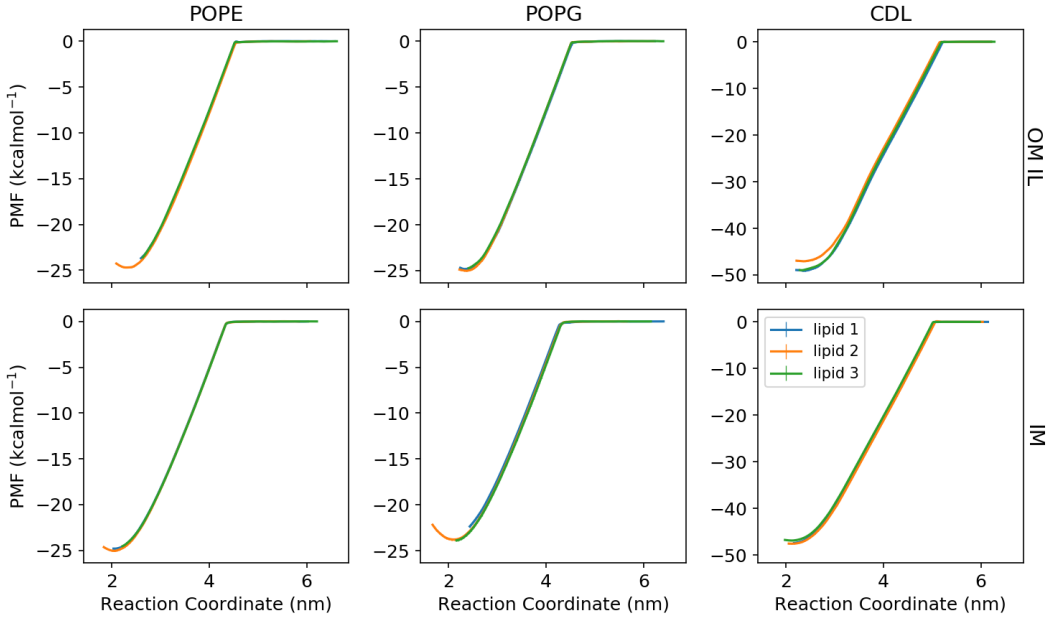

FIGURE 5.10: PMFs of the extraction of POPE, POPG or cardiolipin (CDL) from either the inner leaflet of the outer membrane (OM IL) or the inner membrane (IM). PMFs were calculated over the last 0.5 μs of each umbrella window. Three different lipid were extracted per lipid type with the HEAD_CY CV (defined in Section 5.2.3).

The speed of convergence of the extraction of POPE, using each CV, was assessed by taking PMFs across 500 ns intervals for the entire trajectory (Figure C.4). For every US simulation of POPE convergence was achieved by 1.5 μs. The CVs that converged the fastest were COM_CY and HEAD_CY. In fact, convergence was achieved within the first 500 ns, when the COM_CY CV was used.

5.3.4 Protein Crowding and Lipid Extract

PMF profiles were calculated for the extractions of POPE and cardiolipin when they were near or far away from AqpZ. These PMFs were compared to the PMFs of lipid extraction when no protein was present (Table 5.2). First the convergence of the PMF profiles was tested by taking PMFs across adjacent intervals of 500 ns during each umbrella sampling simulation, starting at 0 ns (Figure C.5). The PMFs of all lipid extractions, in this section, had converged by 1.5 μs.

To compare lipid extraction in the local and bulk regions to when no protein was present, PMFs were calculated over the last 500 ns of US simulations (Figure 5.11A and B). The standard extraction free energy, ΔG_e^o, was then determined from each PMF (Table 5.3).

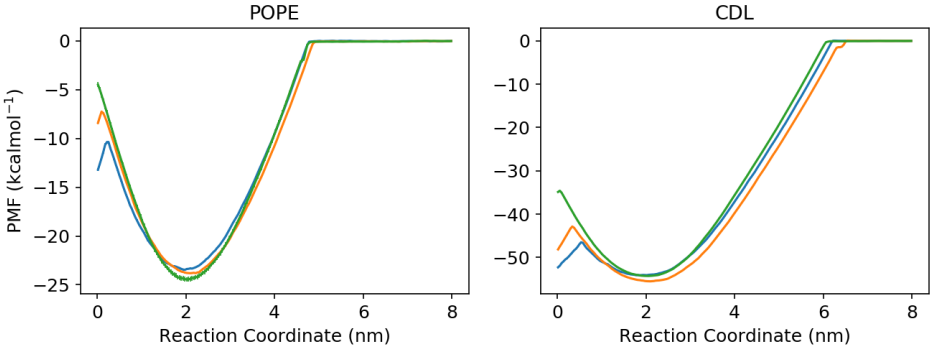

FIGURE 5.11: PMFs of the extraction of cardiolipin (CDL) or POPE from near AqpZ (blue) in the bulk of the membrane (orange) or when no protein was present (green). The PMF was calculated across the last 0.5 μs of each umbrella window.

TABLE 5.3: Table of Standard free energy of lipid extraction ΔG_e^o for POPE and cardiolipin (CDL) from the local region of AqpZ (< 3 nm), the bulk of the membrane or a system with no protein. ΔG_{PMF} was the lipid extraction free energy from the PMF, ΔG_{barr} was the barrier to the centre of the membrane and ΔG_c was the correction for effect of the lateral restraints, Equation (5.6). The reported error in ΔG_c was the standard error.

Lipid	Region	ΔG_e^o	ΔG_{barr}	ΔG_{PMF}^o	ΔG_c
CDL	Local	57.58 ± 0.03	7.61 ± 0.20	53.45	-4.13 ± 0.03
CDL	Bulk	59.02 ± 0.02	12.66 ± 0.14	54.63	-4.39 ± 0.02
CDL	No Protein	53.33	19.68 ± 0.12	53.33	NA
POPE	Local	26.43 ± 0.01	13.10 ± 0.16	22.03	-4.40 ± 0.01
POPE	Bulk	26.50 ± 0.02	16.58 ± 0.14	22.37	-4.13 ± 0.02
POPE	No Protein	22.97	19.96 ± 0.12	22.97	NA

Interestingly, it was easier to extract a lipid nearer the protein, than when the lipid was in the bulk of the membrane. Originally, it was thought that protein-lipid interactions would increase the difficulty of a lipid leaving the membrane. One possibility for thse observations was that lipids were not necessarily bound to the protein at the minimum of the PMF. The time the extracted lipid spent bound to the protein could be represented as binary heatmap with respect to time and the reaction coordinate (Figure 5.12). The extracted lipid was bound to AqpZ if a phosphate bead was within 0.6 nm of the protein. For both POPE and cardiolipin the bound state was not prevalent at the minimum of the PMF. As cardiolipin left the membrane it was rarely in the bound state after 2 nm (where the minimum was). These observations can be rationalised from the mechanism of lipid extraction (Figure 5.12). During the extraction process the membrane curved at the point where the lipid was pulled out. The membrane curvature became more extreme, until the lipid exiting the membrane was preferable to further curvature. The membrane cannot bend if the lipid is too close to the protein, and so the pulled lipid moved away from the protein during the extraction process. Still, it was not clear why it would be easier to extract a lipid near a protein, compared to in the bulk of the membrane. An enrichment map of the system across last microsecond of the

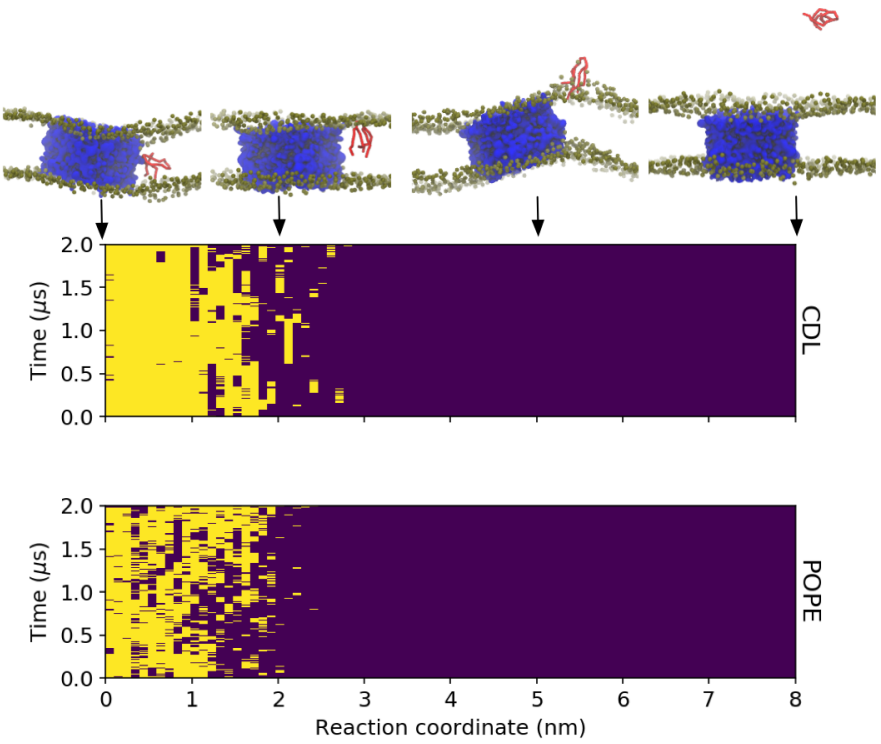

FIGURE 5.12: Heatmap of time vs reaction coordinate showing when an extracted POPE or cardiolipin (CDL) were bound to AqpZ (in yellow). A lipid was defined as bound if the phosphates were within 0.6 nm of AqpZ. The snapshots show the position of the extracted lipid at certain points of the reaction coordinate. Key: red = extracted lipid, blue = AqpZ and gold = phosphate beads.

unbiased production run was determined to quantify density gradients in the membrane (Figure C.6). In a $\sim$ 3 nm region around AqpZ there was an overall reduction in lipid density, which may explain why it was easier to extract a lipid that was near the protein.

Interestingly, the bound state was very prevalent from $0 - 1.0$ nm of the reaction coordinate; this was especially true of cardiolipin. Snapshots taken across the reaction coordinate showed that as cardiolipin translocated across the membrane it preferred to be in contact with AqpZ (Figure 5.12). The initial barrier to translocation of cardiolipin, ΔG_{barr}, was smaller than POPE, even though POPE is a much smaller lipid (Table 5.3). A comparison of the PMFs of the local and bulk lipids for POPE and CDL confirmed that the barrier for a lipid moving into the core of the bilayer was reduced near AqpZ.

One alarming difference was that it was easier to extract a lipid from anywhere in a membrane that contained AqpZ. The increase in ΔG_e^o upon the addition of AqpZ could be a result of the protein affecting the global membrane elasticity. Previous CG simulations of AqpZ in the inner membrane[105] found that the membrane bending modulus decreased upon the addition of AqpZ. A decrease in bending rigidity upon

the addition of AqpZ should have lead to a decrease in the ΔG_e^o. Thus no reasonable explanation can be given for this observation and further investigation is required. It would be of interest to see if this unexplained trend was reproduced for POPG and systems with greater protein concentrations.

5.4 Conclusions

Coarse-grained umbrella sampling (US) simulations were used to measure the free energy of extracting various lipids from the outer (ReLPS upper leaflet) and inner membranes. First, a range of lipid extraction collective variables (CVs) were used to probe the most effective CV for ReLPS extraction. Up to 10 μs of US was carried out for each trialled CV. There was little convergence of extraction free energies, even when the same lipid was extracted multiple times. There was only one CV for which three extractions of the same lipid converged to the same free energy profile. However, the best performing CV was not the most specific CV and allowed for more conformational flexibility of the lipid. Furthermore, it was found that the extraction of different ReLPS lipids could lead to different extraction free energies.

Further enhancement of umbrella sampling (US) is possible through combination with replica exchange molecular dynamics (REMD). US-REMD involves switching biases between adjacent umbrella windows and has been used to accelerate convergence of PMFs for coarse-grained and atomistic protein-protein and protein-lipid association free energies[213, 224, 225]. US-REMD has a similar computational cost to regular US and may improve the convergence of LPS extraction free energies. US-REMD would be a natural extension to the work carried out here, and would have been carried out if the time constraints had allowed it.

The convergence of the PMFs of the extraction of phospholipids from the inner leaflet of the outer membrane and the inner membrane largely occurred within only 1 μs. Interestingly, it was more difficult to remove POPG and cardiolipin from the outer membrane than the inner membrane. Previous studies of the outer membrane have reported increased clustering of cardiolipin in the presence of ReLPS[149], which would explain its increased stability in the outer membrane.

Then POPE and cardiolipin were extracted from the hydrophobic core of the inner membrane, near to and far away from the water efflux channel AqpZ. Each lipid was restrained to the local or bulk region by a lateral restraint. Lipids in the core of the membrane, in particular cardiolipin, preferred to be bound the protein. This matched previous literature on the preference of AqpZ for cardiolipin[71]. In lipid extraction was easier near the protein, due to reduced lipid densities around AqpZ. One unusual observation was that it was always easier to extract a lipid from a membrane with no protein, even if the lipid was nowhere near the protein. Previous literature found that the addition of AqpZ to a protein free inner membrane decreased the membrane bending modulus[105]; so it should have been easier to extract lipids that were far away from the protein. Further investigation could entail whether this trend could be reproduced

across other lipid types and what would happen if the protein concentration were to be increased.

Chapter 6

A Protocol For Enhanced LPS Mixing in Bacterial Membrane Models

6.1 Introduction

One of the greatest issues with the simulation of the outer membrane, in this work, has been the confined and slow nature of LPS dynamics. Inter LPS binding is so strong that lipids cannot move past each other and any dynamics is locally restricted. The local confinement of LPS has resulted in issues with convergence and extremely long auto-correlation times of observable properties (microseconds). Replica exchange (or parallel tempering)[226, 227] is a method that has been used to overcome kinetic barriers in molecular systems, such as folding proteins[228] or peptides[229]. The general principle behind replica exchange is that n replicas of a system are run in parallel at a range of increasing temperatures. Then every k steps adjacent replicas (in temperature) exchange their positions via the metropolis acceptance criterion and this allows for the molecules of interest to overcome kinetic barriers before falling back into the low temperature replica (Figure 6.1. The issue with replica exchange is that it requires a number replicas proportional to the size of the system being tempered.

Hamiltonian Replica exchange (HREX) was developed to only temper a part of the system of interest and thus minimises the number of replicas used. In this study the variant of HREX, REST2[230], will be used as this had been implemented within GROMACS[231]. In REST2 the hamilitonian of part of the system is scaled, but the temperature of each replica is the same. In an outer membrane system the bottle neck in dynamics is limited to the LPS leaflet and thus proves an ideal system for the application of HREX. In this chapter HREX was applied to the outer membrane, in order to

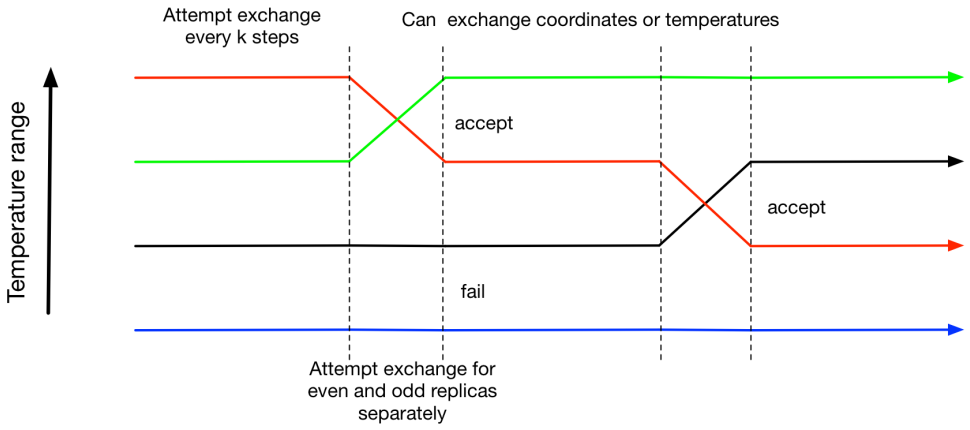

FIGURE 6.1: Diagram of the workflow of Replica Exchange enhanced sampling methods.

enhance the mixing of LPS.

While HREX has less computational cost compared to Replica exchange, the cost is still large. As discussed in the introduction, it is believed that there are some phospholipids in the LPS leaflet of the outer membrane. The investigation of protein-lipid interactions in Chapter 4 showed that quantitative values were often not reproducible across multiple repeats. It was hypothesised that if there was only a ring of LPS around a protein, and the rest of the leaflet comprised of PE, this may allow for lipid sorting of LPS around the protein and thus the convergence of LPS-protein interactions between repeats. The logic behind this hypothesis was that if the inter linking between LPS lipids did not occur across the entire membrane, individual LPS lipids would have more lateral freedom. As only two repeat simulations would be required to test this hypothesis, it could be a computationally cheaper alternative to HREX.

6.2 Methods

6.2.1 Hamiltonian Replica Exchange

In a system with coordinates $\mathbf{r}$ the potential energy is determined by $U(\mathbf{r})$. It is assumed that $U(\mathbf{r})$ is a function of a summation of few body terms and that the temperature is controlled with a thermostat (NPT or NVT). In an unbiased MD simulation the chance of sampling a configuration is $P(\mathbf{r})\ \alpha\ exp(\frac{-U(\mathbf{r})}{k_B T})$, where k_B is the Boltzmann constant. In replica exchange a series of replicas are simulation with a range of temperatures from "cold" to "hot". The hot replicas overcome the kinetic barriers obstructing sampling of the phenomena of interest, while the ground state replica is the unbiased trajectory of the system. The remaining replicas provide a smooth transition between the "cold" and

"hot" replicas (Figure 6.1)[231]. For HREX the potential energy, or Hamiltionian, of the system is varied. Thus the probability of a configuration being sampled for replica i is now

$$P(p_i)\ \alpha\ exp\left(\frac{-U_i(p_i)}{k_B T_i}\right) \tag{6.1}$$

where $U_i(p_i)$ is the hamiltonian modified from $U_0(p_0)$. Note that Equation (6.1) ignores implementation of exchanges between replicas.

As the HREX varies the Hamiltonian of the system, certain subsets of the system can be "heated". The subset of the system for which the hamiltonian is scaled is defined as the hot region $\mathcal{H}$, and the rest of the system as the cold region $\mathcal{C}$. The "effective temperature" of $\mathcal{H}$ was defined by scaling the Hamiltonian of a subset of the system, as a function of the constant λ[231]:

- Interactions in the $\mathcal{H}$ region are scaled by λ (effective temperature of T/λ).
- Interactions between the $\mathcal{H}$ and $\mathcal{C}$ regions are scaled by $\sqrt{\lambda}$.
- Interactions within the cold regions are not scaled and have an effective temperature of T

Therefore λ can take values in the range $[0, 1]$, where $\lambda = 1$ results in the Hamiltonian of the unbiased system.

The coordinates of adjacent replicas i and $i + 1$ are exchanged every k steps based on the Metropolis-Hastings acceptance probability $P_{i,i+1}$,

$$P_{i,i+1} = min[1, exp(-\Delta U_{i,i+1}/(k_B T))] \tag{6.2}$$

where

$$\Delta U_{i,i+1} = -U_i(\mathbf{r}_{i+1}) - U_{i+1}(\mathbf{r}_i) + U_i(\mathbf{r}_i) + U_{i+1}(\mathbf{r}_{i+1}). \tag{6.3}$$

If a random number generated between 0 and 1, from a uniform distribution, is greater than $P_{i,i+1}$ then the swapping of replicas is rejected; otherwise the replica swap is accepted. In the GROMACS implementation of replica exchange, even and odd pairs of replicas are exchanged in an alternating pattern, every k steps (Figure 6.1). Further details of the implementation of HREX within GROMACS can be found in the literature [231]. To allow replicas to transfer from the lowest to the highest replica in λ space and vice versa the potential energy distributions of adjacent replicas must have sufficient overlap. The degree of overlap is quantified in terms of the average acceptance probability of exchange attempts.

There are a few terms that will appear in the result section that warrant definition:

- replica trajectory - a sequence of snapshots that define the trajectory for a fixed Hamiltonian (e.g. $\lambda = 1$).
- coordinate trajectory - a trajectory that is continuous in coordinate space, but not λ space (i.e. varying Hamiltonians).
- maximum replica - the replica with the most scaled Hamiltonian or the "hottest" replica.
- minimum replica - the replica with the least scaled Hamiltonian or the "coldest" replica.
- round trip - When a coordinate trajectory traverses to the maximum and then the minimum replica.
- References to the ground state replica infer the replica when $\lambda = 1$ (i.e. the minimum replica).

6.2.2 Description of Systems

The Martini (version 2.2) force field was used for all molecular models[152]. The ReLPS model used here was parameterised at the CG levels in previous work[95]. The initial coordinates for membrane or membrane protein systems were generated with CHARMM-GUI[96]. Protein models were obtained from the the RSCB protein databank. Any missing residues or broken loops were added with modeller[178] and then missing hydrogens added with PDB2PQR[179]; subsequently the protein was given a transmembrane alignment by the program MemEmbed[180]. Each protein was then fed into CHARMM-GUI, which coarse-grained the protein to the ElNeDyn model[173] and then inserted it into a membrane. The elastic network of each protein had a cutoff of 0.9 nm and a strength of 500 $kJmol^{-1}nm^{-2}$. For all systems, ReLPS was neutralised by calcium ions and the remaining charge deficit removed through the addition of NaCl.

For the HREX study two systems were studied: a ReLPS outer membrane with 90 % POPE, 5 % POPG and 5 % cardiolipin in the inner leaflet 1) with and 2) without a transmembrane FhuA (1QFG)[170].

The enhancement of LPS sampling, through enriching the upper leaflet of the OM with phospholipids, was also studied. There were two systems of interest for this part of the chapter. In one system a POPE membrane was generated and then a cluster of 7 ReLPS lipids was inserted into the upper leaflet. The insertion was done by building a POPE membrane and a membrane with a ReLPS upper leaflet and POPE lower leaflet, separately within CHARMM-GUI[96, 98]. These two systems were then aligning and a LPS cluster from the ReLPS system inserted into the POPE membrane, with the

deletion of any overlapping POPE lipids. The second membrane had a POPE lower leaflet and a transmembrane OmpA (1QJP)[53] surrounded by 12 ReLPS lipids in the upper domain of the protein. This system was built by inserting OmpA into a membrane with ReLPS in the upper leaflet and POPE in the lower leaflet. The protein and the ring of ReLPS lipids surrounding it, were inserted into a POPE membrane and any overlapping POPE lipids were removed. Further details of the systems described here can be found in Table 6.1. Snapshots of the membrane systems used in this chapter are shown in **??**.

TABLE 6.1: Table summarising the unbiased simulations in this chapter.

System	Protein	dimensions (nm)	Time (μs)	NaCl (M)	Upper Leaflet	
					ReLPS	POPE
1	None	$8.6 \times 8.6 \times 16.8$	1×10 μs	0	47	0
2	FhuA	$10.4 \times 10.4 \times 15.8$	1×10 μs	0	54	0
3	None	$13.0 \times 13.0 \times 14.5$	2×20 μs	0.15	7	265
4	OmpA	$13.0 \times 13.0 \times 14.5$	2×30 μs	0.15	12	227

6.2.3 Simulation Protocol

The GROMACS[150] MD package (version 2018) was used for all simulations in this chapter. GROMACS was patched with plumed (version 2.4)[218] to run HREX simulations. The simulation parameters used here for minimisation, equilibration and production runs were the same as those described in Section 4.2. Production runs that had proteins in them or were HREX MD simulations used a timestep of 10 fs; in all other cases the timestep was 20 fs. All unbiased simulations that were carried out are described in Table 6.1. The initial structures used for HREX were the final snapshots of the production runs for systems 1 and 2. The convergence of the prerequisite unbiased simulations was determined from timeseries of the area per lipid (APL) and membrane thickness(Figure D.2). Further details on all of the parameters used during the optimisation of HREX for LPS systems are described in Table 6.2. Replicas were distributed exponentially across any chosen λ range.

TABLE 6.2: Summary of all Hamiltonian replica exchange simulations carried out for this chapter. The initial structure for each system was the last frame of the production runs of either system 1 or 2 from Table 6.1. Extensions to simulation times were noted in brackets.

System	Protein	temper region	λ	replicas	EAI (ps)	Time (μs)
5	None	ALL	$1 - 0.323$	30	N/A	4
6	None	HEADALL	$1 - 0.323$	30	N/A	4
7	None	HEAD	$1 - 0.323$	30	N/A	4
8	None	SUGARS	$1 - 0.323$	30	N/A	4
9	None	CHARGED	$1 - 0.323$	30	N/A	4
10	None	HEADALL	$1 - 0.646$	24	50	4
11	None	HEADALL	$1 - 0.646$	24	500	4(25)
12	FhuA	HEADALL	$1 - 0.646$	24	500	12

6.2.4 Analysis

6.2.5 General Analysis

Analysis was carried out with a combination of GROMACS tools and in-house scripts that made use of the python module 'MDAnalysis'[158]. Molecular systems were visualised with VMD[157]. The lipid survival probability $P(t + \Delta t)$, which was defined in Section 4.2.4, was also used in this chapter. $P(t + \Delta t)$ was the probability of a lipid in contact with a protein at t also being in contact with that same protein at $t + \Delta t$. $P(t + \Delta t)$ was only measured for Δt that were less than half of the length the analysed trajectory.

The 2D rotation of a protein in the xy plane was determined, by first selecting the backbone beads in the transmembrane region of the protein. The transmembrane region was then split into two sections and the vector between the centre of geometry of each section, $\mathbf{v_{2D}}$, was determined. The 2D rotation, $\Delta\theta$, was defined as the rotation of $\mathbf{v_{2D}}$ across a time interval Δt.

Protein-LPS interactions were calculated through the use of contact analysis of the LPS lipid A headgroup with each residue of the protein. The cutoff for contacts was 0.6 nm and if there were multiple contacts between a residue and a LPS headgroup then only one contact was counted.

The APL and membrane thicknesses were determined with the software package 'FATSLiM'[232]. The centres of geometry of the phosphate groups in each lipid were used as the reference points for the APL and membrane thickness calculations.

6.2.6 Replica Exchange Analysis

Some analysis was required to determine if LPS lipids were able to move past each other and thus properly mix. Two assumptions were made, the first one being that a single LPS should be neighbours with all other LPS lipids in a replica trajectory. The second assumption was that if LPS was properly mixing, then it should have an equal probability of being neighbours with any other LPS. To quantify both assumptions, nearest neighbour analysis was used and to track the six nearest neighbours of a single LPS across a trajectory. The first and second assumptions were quantified with the nearest neighbour index (NN index) and the $RMSD_{NN}$, respectively. The NN index across a trajectory for a single lipid was defined as,

$$\text{NN index} = \frac{\text{unique neighbour number} - N_{NN}}{N_{LPS} - 1 - N_{NN}} \tag{6.4}$$

where N_{LPS} was the number of LPS lipids and N_{NN} the number of nearest neighbours in frame of the trajectory (i.e 6). If the NN index was 0 then the neighbours of an LPS lipid never changed. Conversely, if the NN index was 1 then the given LPS had been neighbours with every other LPS across the entire trajectory. The NN index referred to the results section was averaged across every LPS in the membrane.

The RMSD_{NN} was defined for a single LPS as the RMSD of nearest neighbour frequencies, divided by the number of frames in a trajectory. If $\text{RMSD}_{\text{NN}} = 0$ then the LPS had an equal probability of being neighbours with every other LPS across a trajectory. The RMSD_{NN} referred to in the results section was averaged across all LPS lipids. The errors in the NN index and RMSD_{NN} were determined from the standard deviation across all LPS lipids.

To assess the mixing of replicas there were two metrics used, that were based on a previous study of replica mixing efficiency[233]. The first metric was the 'transit fraction' and was defined the fraction of replicas that achieved at least one round trip by time t in the simulation. The second metric was designed under the assumption that if replicas are sufficiently mixed then each coordinate trajectory will visit each replica an equal number of times across all M replicas. Thus the second metric was defined by the number of steps for the frequency of a replica i being in replica j after k steps, $f(k)_{i,j}$, to reach $1/M$. The criterion for whether the RMSD of the population frequency (RMSD_{pop}) across all replicas had converged was defined as[233],

$$\text{RMSD}_{\text{pop}} = \sqrt{\frac{1}{M^2}\sum_{i=0}^{M-1}\sum_{j=0}^{M-1}(\frac{1}{M} - f(k)_{i,j})^2} < 10^{-3}. \tag{6.5}$$

6.3 Results and Discussion

6.3.1 Phospholipid Enhanced LPS Sampling

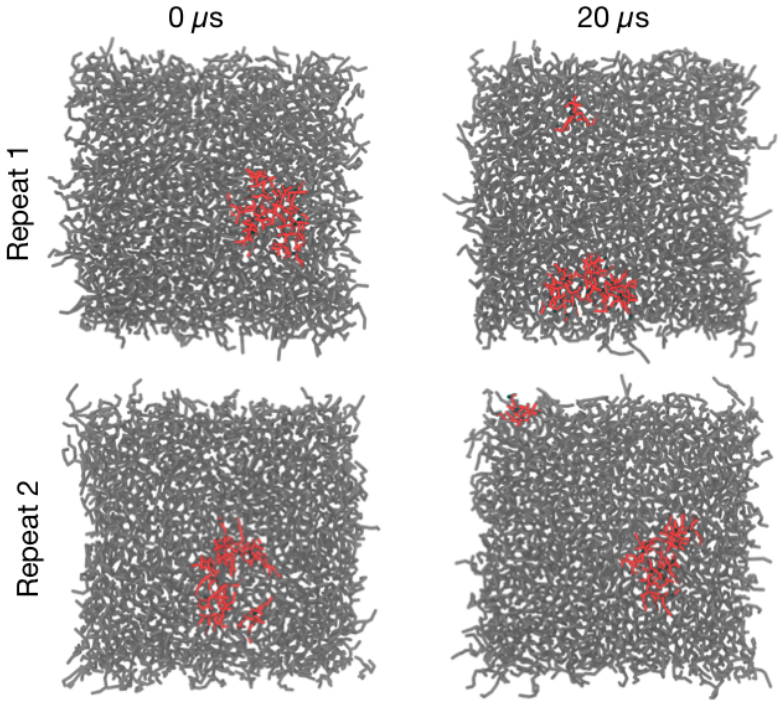

FIGURE 6.2: Top down view of POPE (gray) membrane with 7 ReLPS lipids (red) in the upper leaflet (system 3, Table 6.1). Snapshots were taken at the beginning and the end of each 20 μs production run.

It was hypothesised that the addition of a small cluster of LPS to the upper leaflet of a POPE membrane would enhance LPS sampling. A cluster of LPS was added to a membrane with or without a transmembrane OmpA (Systems 3 and 4) and the behaviour of LPS observed. Of particular interest was whether increased LPS sampling would result in the convergence of protein-LPS interactions between repeats.

First the behaviour of a LPS in system 3 (no OmpA) was investigated. The compactness of LPS lipids across repeat simulations was measured using the maximum pairwise distance between the centre of geometry of each LPS lipid, in the xy plane. Further analysis also measured the 2D radial distribution function (RDF, $g(r)$) of LPS centres in the xy plane (Figure 6.3). The initial and final structures of each repeat showed that the majority of LPS lipids were in a single cluster at the end of each simulation (Figure 6.2). The behaviour of the maximum pair-wise distances varied between repeats, but overall confirmed that LPS was not always in one cluster. The 2D RDF showed that most LPS lipids were not further than 3 nm from any other LPS in the system. At larger distances ($r > 3$ nm) $g(r) < 0.5$, which was half the value that would be expected if LPS was homogeneously distributed in the membrane. Thus in these LPS sparse systems, most

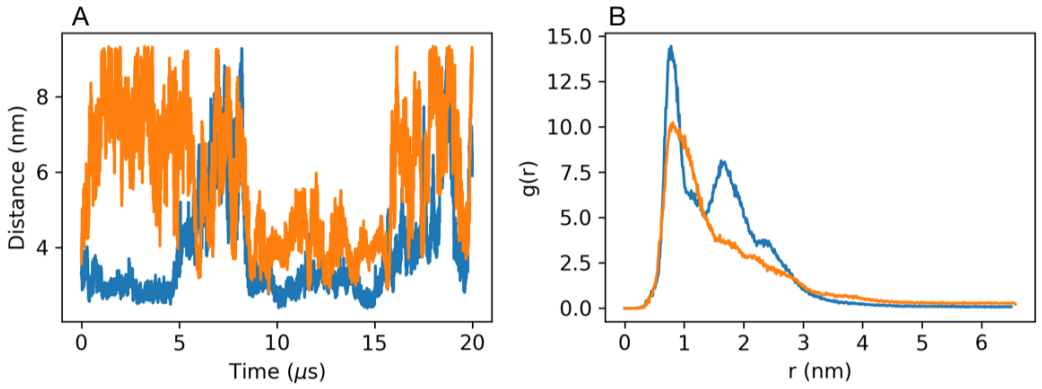

FIGURE 6.3: A) The maximum 2D pairwise distance between the center of geometries of ReLPS lipids. B) 2D RDF between the center of geometries of ReLPS lipids. The lines in each plot signify different repeats of system 4 (Table 6.1)

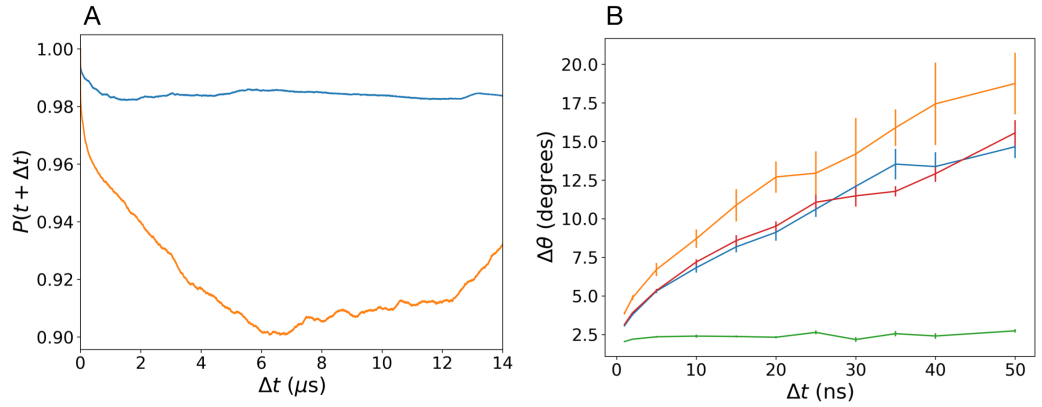

FIGURE 6.4: A) Lipid survival probability of ReLPS being bound to OmpA at t and $t + \Delta t$ vs Δt from $2 - 30$ μs for both repeats (line per repeat). A lipid was defined as bound if it was within 0.6 nm of the protein surface. B) The 2D rotation of OmpA in the xy plane, $\Delta\theta$, vs time Δt for the LPS sparse system (red and blue), the mixed phospholipid (orange) and the ReLPS outer membrane systems (OM) (green), each containing a transmmebrane OmpA. The mixed phospholipid (90% POPE, 5% POPG and 5% cardiolipin) and OM (upper leaflet ReLPS, lower leaflet 90% POPE, 5% POPG and 5% cardiolipin) systems were described in Section 3.2 (Table 3.1). $\Delta\theta$ was averaged across the last 6 μs each production run.

LPS lipids grouped into a single cluster.

The system with OmpA in POPE had a cluster of 12 LPS lipids around the extracellular domain of OmpA (system 4, Table 6.1). Of particular interest, was how tightly LPS was bound to OmpA, which can be measured from the on off rates of the LPS lipids. The on off rate refers to how frequently a lipid binding and then unbinds from a protein. The on off rates of the lipids were measured through the determination of the average survival probability $P(t + \delta t)$ LPS. The survival probability $P(t + \delta t)$, defines the probability that a lipid contacting the protein at time t was also in contact with the protein at $t+\delta t$.

$P(t+\delta t)$ was measured across the last 28 μs of each repeat simulation (Figure 6.4A). In both repeats $P(t+\delta t)$ was never less than 0.90, which signified that LPS was tightly bound to the protein. On the scale of the simulations carried out here, LPS lacked the lateral sorting expected from phospholipids.

To assess protein dynamics in the LPS sparse system (system 4), the average 2D rotation of the protein, $\Delta\theta$, was measured for different time periods Δt. The rotational dynamics of system 4 were compared to OmpA in a mixed phospholipid or ReLPS outer membrane (from chapter 3, see Table 3.1). OmpA in the ReLPS outer membrane system had reduced rotational dynamics, compared to the mixed phospholipid system (Figure 6.4B). This outlined the restrictive effect of LPS on the protein's rotation. The speed of rotation of OmpA was the same in both repeats of system 4, but was much larger than when the upper leaflet only contained ReLPS. The results of the lipid on off rates and the rotational dynamics, showed that OmpA could free rotate, but was tightly complexed to LPS.

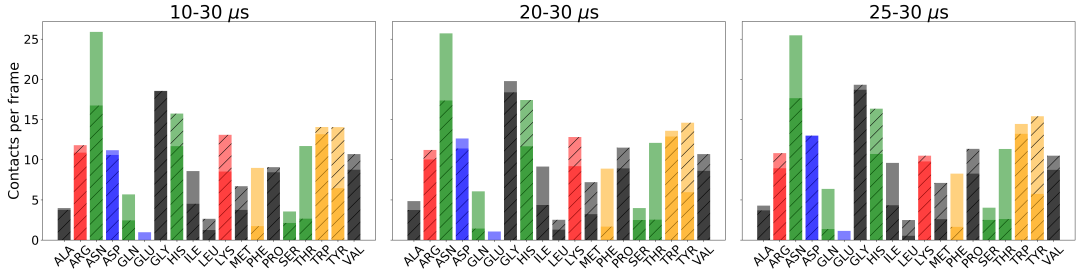

FIGURE 6.5: Average number of contacts per frame between each residue in OmpA and the ReLPS Lipid A headgroup across repeats (one repeat has hash markings) as a function of increasing analysis times. Every bar was coloured with respect to the polarity of each residue: red=basic, blue=acidic, orange=aromatic, green=polar and black=non-polar. Note that multiple contacts between a single residue and an LPS headgroup were only counted once.

One of the aims of this section, was to ascertain whether the use of sparse amounts of LPS resulted in convergence of protein-LPS interactions across repeats. Protein-LPS interactions were quantified through contact analysis between Lipid A headgroups and each amino acid type in the protein. Contacts were measured from $10-30$, $20-30$ and $25-30$ μs to determine whether contact frequencies converged within repeats (Figure 6.5). From Figure 6.5 it was seen that the contacts per frame converged within repeats, but not across repeats.

To summarise, the addition of sparse patches of LPS resulted in the localisation of most of the LPS lipids in a ring around the protein, or in clusters (if no protein was present). There was no observed convergence of protein-LPS interactions between repeats; however, the protein rotational dynamics were enhanced to values similar to phospholipid

systems. Thus it was concluded that strong LPS-protein and LPS-LPS interactions prevented the convergence of protein-LPS interactions at high and low LPS densities.

6.3.2 Replica Exchange to Enhance LPS Sampling

6.3.2.1 Optimising Tempering Region

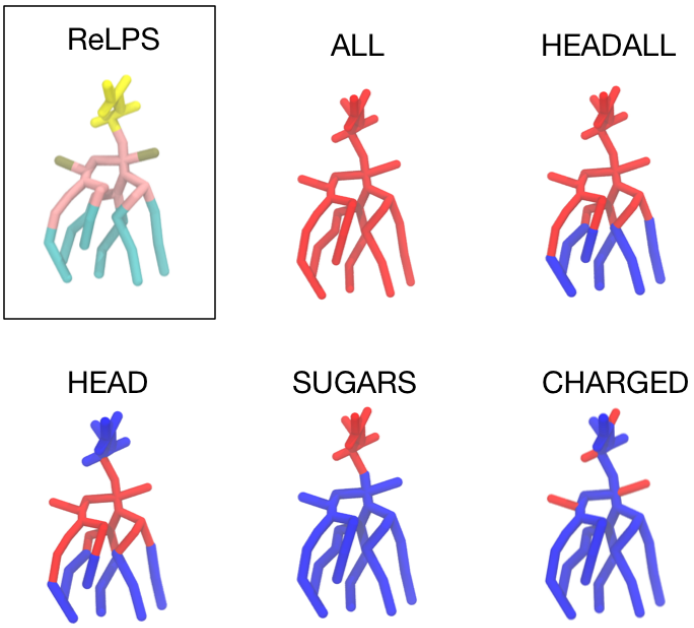

FIGURE 6.6: (Top left) coarse-grained structure of ReLPS (key: yellow = sugars, gold = phosphates, pink = lipid A sugar rings and acyl groups and cyan = lipid tails. The other structures depicted the tempered regions (in red) trialed in this study. The tempered regions were as follows: ALL = entire lipid, HEADALL = sugars + lipid A headgroup, HEAD = lipid A headgroup, SUGARS = sugars and CHARGED was any charged group on ReLPS and the calcium ions.

When designing a HREX protocol, it is important to first carefully consider what should be the tempered region (i.e. the $\mathcal{H}$ region). For replica exchange, the number of replicas required for efficient sampling of all replicas is proportional to the number of degrees of freedom in the tempered region [234]. Furthermore, number of replicas required for sufficiently large acceptance probabilities also scales with the size of the λ range. To minimise the computational cost of HREX MD, first a minimal tempering region must be identified.

The trialled $\mathcal{H}$ regions are summarised in Figure 6.6. The phospholipids were never included in the tempering region, as they were not believed to be the limiting factor of LPS mobility. The largest tempering group was the entire ReLPS lipid (ALL). The rest of the tempered regions were comprised of parts of ReLPS: the Lipid A headgroup and sugars (HEADALL), the lipid A head group (HEAD), the sugar groups (SUGARS)

and the charged molecules in LPS(CHARGED). The CHARGED tempering region also included the calcium ions. Then 30 replicas, scaled by λ values geometrically spaced between 1 and 0.323, were simulated for 4 μs for each trial tempering region (Table 6.2). No replicas were exchanged during these simulations, as the aim was to identify the ideal tempering region and range of λ values.

Nearest neighbour analysis was performed to quantify lateral sorting of LPS as a function of λ. For LPS to be well mixed two conditions were assumed: 1) An LPS must be nearest neighbours with every LPS in the membrane during the course of a trajectory. 2) An LPS must have an equal probability of being neighbours with any other LPS in the same leaflet. To quantify these two assumptions two metrics were designed, the NN index and RMSD_{NN}. The NN index was a value between 1 and 0 that quantified the first assumption. If NN index was 0 then the neighbours of a single LPS never changed. Conversely, if the NN index was 1 then the LPS had been neighbours with every other LPS in the membrane across the analysed trajectory. The RMSD_{NN} was defined as the RMSD of nearest neighbour frequencies for a single LPS, and would be 0 if the second assumption for ideal mixing was satisfied. Both metrics were averaged across all LPS lipids and errors determined from standard deviations.

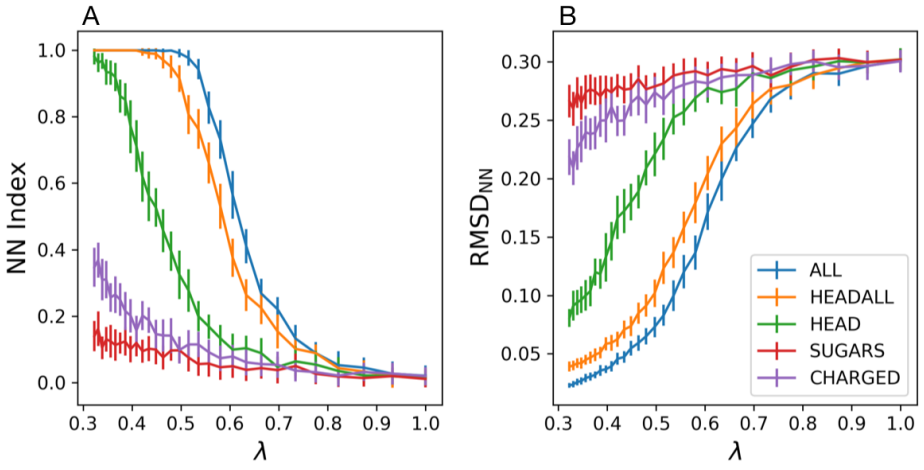

FIGURE 6.7: A) Nearest neighbour index (NN Index) and B) RMSD_{NN} vs λ for systems $5-9$ (Table 6.1). The regions that defined each labelled tempering region can be found in Figure 6.2. Further details on the analysis methods can be found in Section 6.2.6.

The NN index and RMSD_{NN} were measured across all of replicas, for each trial tempering region (Figure 6.7). Previous studies of LPS have attributed the strong binding between LPS lipids to inter lipid interactions via calcium ions [95, 105]. Therefore it was hypothesised that tempering the CHARGED region would be sufficient to accelerate LPS mixing. There was not a significant increase in the NN index at low λs, compared to the ground state. Thus the CHARGED region was a poor choice for a tempering region. Similarly the SUGARS tempering region performed very poorly at all λ, with NN indices always being less than 0.4. Scaling the interactions of the HEAD region resulted

in NN indices > 0.4 when λ was less than 0.5, which was a significant improvement on previous tempering regions. LPS lipids in the maximum replica had been neighbours with the majority of other LPS lipids, during the 4 μs trajectory.

For the ALL and the HEADALL regions, the NN index was 1 if $\lambda < 0.45$. The $\mathrm{RMSD_{NN}}$ for ALL and HEADALL was < 0.05, which compared to the ground state value of 0.30, showed that a significant improvement in lateral sorting of LPS had been made at low λ. The degree of LPS mixing was always larger for ALL, compared to HEADALL, at all λ values. However, given that the HEADALL region did not temper 38% of LPS beads, the difference was not that large. Thus it appears that the tempering of the hydrocarbon tails had a low weight contribution compared to its size. Therefore HEADALL will be used for all HREX in the following sections. Similarly, the λ range should be set to minimise the number of replicas used, while still observing LPS mixing in the maximum replica. The λ range was set to $1.00 - 0.645$, as this was large enough to allow for some LPS mixing to occur in the "hottest" replicas. Replicas exchange parameter search studies have shown that the more replicas used the longer it can take for sufficient sampling of replicas to occur[233, 235]. Thus the λ range chosen was a compromise between minimising replica numbers, while allowing for sufficient LPS mixing to occur.

6.3.2.2 Optimising Replica Exchange Parameters

There are two parameters of importance to HREX that require optimisation, the exchange probability between replicas and the exchange attempt interval (EAI). Past studies have shown that both are importance for efficient sampling to occur [235, 236]. There is no exact guide to what the average exchange probability should be, and values in previous studies range from $0.1 - 0.8$[235–238]. The ideal EAI has been a matter of debate in the literature, to which there a two schools of thought. The first school of thought is that the EAI should be larger than the autocorrelation time of the potential energy of the tempered region[233]. If the EAI is too small, this can increase the chances of a replica moving back to the last replica it was in; this has been termed 'exchange trapping'. Another study in the literature suggested that the EAI should actually be as small as computationally feasible[236]. They attributed the thinking of the first school of thought to the use of non-canonical thermostats and other flaws in the implementation of replica exchange[236, 239]. The aforementioned studies only tested simple toy models or small peptide chains in an implicit solvent and so it was uncertain whether their observations could be applied to LPS systems. The relaxation times for the potential energy of OM system have been found to be on the scale of microseconds (Section 4.3.6); hence 'exchange trapping' could be a large issue when applying HREX to LPS systems.

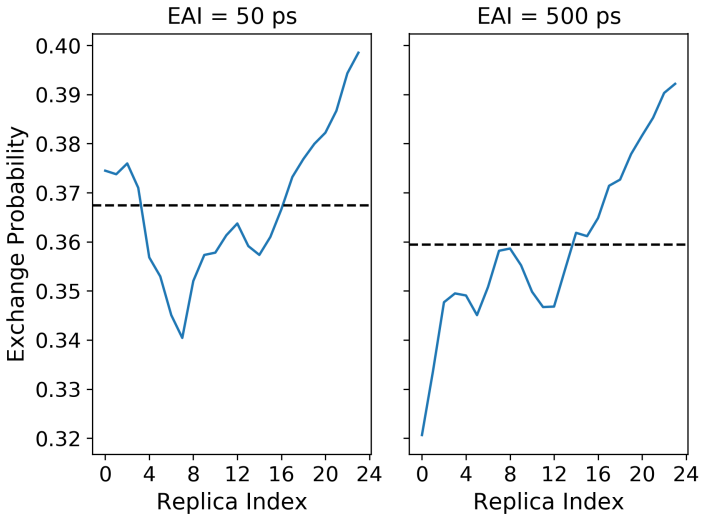

FIGURE 6.8: The exchange probability of adjacent replicas as a function of the replica index for HREX of the HEADALL region of ReLPS in an outer membrane model for exchange attempt intervals (EAI) of 50 and 500 ps. The dotted line indicates the average exchange probability.

The autocorrelation time (τ) of the potential energy of the last 1 μs of the outer membrane system (system 1) was $\sim$ 1.3 ns. The point at which an observable reaches equilibrium can be measured by maximising the number of uncorrelated samples; assuming the trajectory does reach equilibrium. The automatic equilibration detection tool written by Chodera et.al[240] found that τ was 0.3 ns from $\sim 5.2 - 10.0$ μs of the production run. It was assumed that τ lay within on the order of $0.3 - 1.3$ ns. Another estimate of τ would be to measure the τ of the potential energy of the tempered region, after the velocities of the last frame of the production run had been re-initialisation. After the re-initialisation of velocities a 2.5 μs production run was generated and τ was measured to be 900 ns. Applying an EAI on the order of microseconds would have been completely unfeasible. Instead, the effect varying EAIs on LPS mixing and replica sampling efficiency was trialled for smaller EAIs of 50 and 500 ps (systems 10 and 11, respectively). Each HREX simulation was run for a total of 4 μs per replica.

For both simulations the number of replicas used was 24, which gave an average exchange probability of around 0.36 across all replicas. The exchange probability was measured as a function of replica index for both EAIs (Figure 6.8). To prevent bottlenecks in replica space, large variances in exchange probabilities across λ space should be avoided. Bottlenecks in replica space can lead to uneven sampling of λ space and thus inefficient sampling. For both trialled EAIs, the exchange probabilities varied across a maximum range of 0.07, which was similar to previous literature[238].

The degree of exchange trapping was measured from the ratio of accepted exchanges where the new λ value was the same as two exchanges ago. The exchange trapping ratio

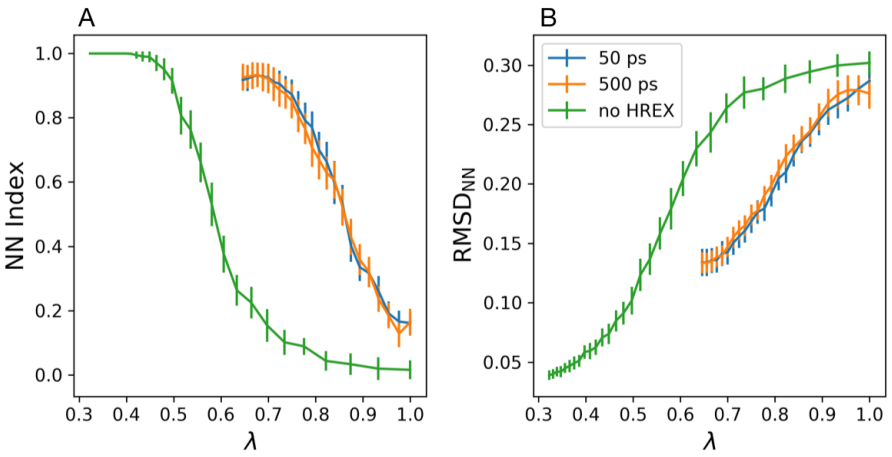

FIGURE 6.9: A) nearest neighbour index (NN Index) and B) $RMSD_{NN}$ vs λ. These analysis were done for ReLPS outer membrane systems with exchange attempt intervals (EAI) of 50 (system 9), 500 ps (system 10) and no exchanges (system 6) over the first 4 μs of each trajectory (Table 6.2). Further details on the analysis methods can be found in Section 6.2.6.

was $\sim$ 0.50 for both EAIs and so there was no reasonable difference in trapping using either EAI. To assess the effect EAI on LPS mixing the NN index and the $RMSD_{NN}$ were determined across the 4 μs HREX simulations and compared to when no replica exchanges were carried out (Figure 6.9). The mixing of LPS was identical, to within errors, for both of the trialled EAIs. It was unsurprising that the inclusion of exchanges lead to an overall increase in mixing at all values of λ. Applying exchanges adds an overhead to the simulation cost and so high EAI should be avoided if unnecessary. Thus an EAI of 500 ps was used for all subsequent HREX MD simulations (unless stated otherwise).

6.3.3 Efficiency of Sampling and Thermodynamics Properties

In the previous section a suitable number of replicas and EAI were determined. Here the efficiency of the mixing of replicas and thermodynamic convergence will be discussed. Sufficient replica mixing describes whether the replicas have exchanged enough to explore replica space evenly. While thermodynamic convergence deals with whether observable properties have converged across the state of interest (i.e. the ground state). The system with an EAI of 500 ps and 24 replicas was extended to 25 μs (system 10, Table 6.2) to observe if the mixing of replicas and/or LPS lipids improved over longer timescales. Here two metrics, one of which was used in a previous review of replica mixing efficiency, will be discussed [233].

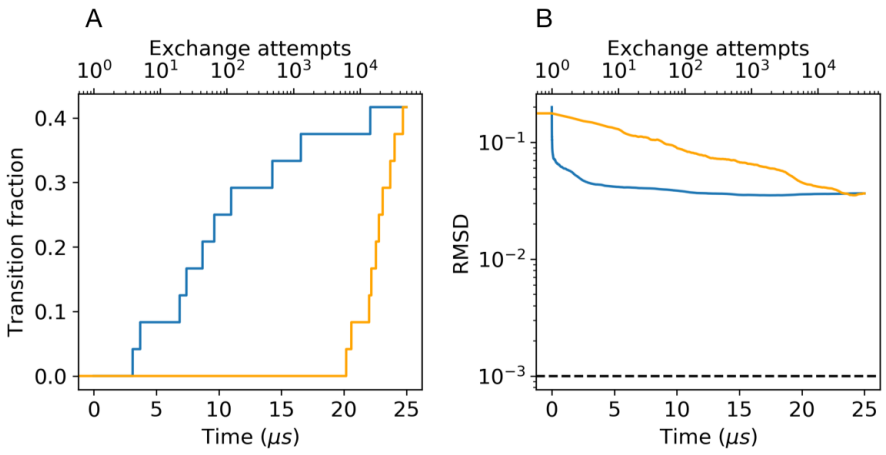

FIGURE 6.10: A) Fraction of replicas that complete at least one round trip B) RMSD of population frequency ($RMSD_{pop}$, see Equation (6.5)) vs time (blue) and number of exchange attempts (orange) for HREX of the HEADALL region of an ReLPS outer membrane (system 10, Table 6.2).

The first metric was based on the concept of 'round trips' within replica exchange, which describes when a replica travels in λ space to the maximum replica and then the minimum replica. The minimum replica was the replica of interest, while the maximum replica was the means to accelerate LPS mixing; thus it was of interest that round trips between these two states were made. The 'transit fraction' was defined as the fraction of replicas that have experienced at least one round trip. The transition fraction was plotted as a function of time and the number of exchange attempts (Figure 6.10A). The first round trip was completed within 4 μs, which was orders of magnitude larger than typical round trip times of the replica exchange of atomistic models in implicit or explicit solvents[236, 238]. As time increased, the transition fraction steadily increased until a maximum value of 0.4 was reach at 25 μs. When a 50 ps EAI was used the first round trip also occurred on the order of microseconds (Figure D.3).

The second metric was designed under the assumption that if replicas are sufficiently mixed then each coordinate trajectory will visit each replica an equal number of times across all M replicas. Thus the second metric was defined by the number of steps for the frequency of a replica i being in replica j after k steps, $f(k)_{i,j}$, to reach $1/M$. The criterion for sufficient mixing was whether the RMSD of the population frequency of all replicas, $RMSD_{pop}$, was less than 10^{-3} (see Equation (6.5)). Across the course of the simulation, the convergence criterion was never reached (Figure 6.10B). According to a previous benchmark on replica mixing [233], the simulation would need to be at least two orders of magnitude longer to achieve sufficient mixing.

In the 25 μs simulation there was a maximum of two round trips for any coordinate trajectory (Figure 6.11). There were two likely explanations for the slow round trip times:

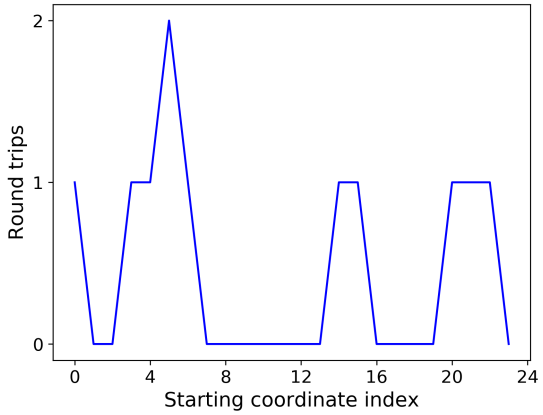

FIGURE 6.11: Number of round trips for each 25 μs coordinate trajectory of system 10 (Table 6.2) vs starting coordinate index.

1) the τ of LPS was orders of magnitude larger than for atomistic systems (nanoseconds) 2) there were bottlenecks in the replica space, resulting in poor replica mixing. The total residence time of each coordinate trajectory in λ space was determined along with the average residence time before an exchange occurred(Figure 6.12). If the sampling was efficient, it would be expected that the gradient of each line would be zero, as an equal amount of time would be spent in each replica. There was a large variance in the total residency time across replica space. Two coordinate trajectories spent over 5 μs in a few low energy replicas. Overall the total residency time was uneven across all λ space. The uneven sampling made sense, given the low number of number of round trips previously observed (Figure 6.11).

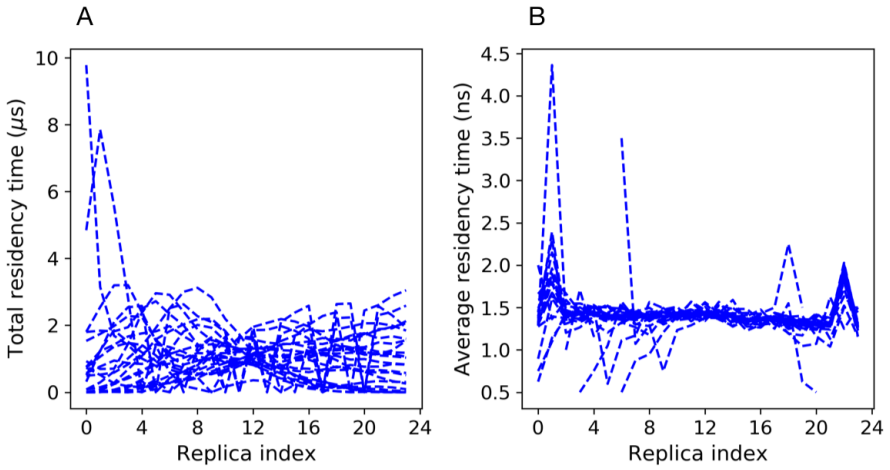

FIGURE 6.12: A) Total residency time B) Average residency time before an exchange occured for each coordinate trajectory (one coordinate trajectory per line) for every replica index in λ space. This was done for the tempering of the HEADALL region in a ReLPS outer membrane.

The average residency time before any exchange occurred was usually ~ 1.5 ns, which matched an exchange probability of ~ 0.3 (similar to previous measurements Figure 6.8). In regions of low and high λ space there were higher average residency times for a few coordinate trajectories. Whether the uneven sampling was due to insufficient simulation time, or a poor choice of HREX parameters was unclear. A more comprehensive study, of a range of HREX parameters, would be required to confirm which assertion was true.

To further assess replica mixing probability distributions of the RMSD of the HEADALL region, the membrane thickness and the area per lipid of ReLPS were determined across all coordinate trajectories (Figure 6.13). It was expected that if each coordinate set could move through space freely, then the probability distributions for each trajectory should be identical[241]. The RMSD distributions for most coordinate trajectories were largely the same, but not identical. The greatest variation in probability distributions across trajectories was observed for the membrane thickness, although the reasons for this were unclear. The probability distributions for membrane thickness all had similar ranges of non-zero values, but otherwise there were no clear similarities. Lack of overlap between probability distributions could mean that either replica mixing was poor (as previously observed) or that the replicas had not yet achieved thermodynamic convergence[194].

While replica mixing has been found to not be sufficient, this did not mean that LPS had not been sufficiently mixed. To assess LPS mixing the NN index and $RMSD_{NN}$ were measured across time intervals of increasing lengths (Figure 6.14). As the simulation progressed, the degree of mixing of LPS increased for all replicas. After 25 μs LPS lipids the ground state replica had an average NN index of ~ 0.65. Moreover when $\lambda < 0.85$, each LPS had been neighbours with every other LPS after 25 μs. The $\mathrm{RMSD_{NN}}$ showed that the homogeneity of mixing began to plateau when $\lambda < 0.7$. Given the observed trends in mixing over time, homogeneous mixing could be achieved if these simulations were extended. The increase in LPS mixing as a function of time suggested that further simulation would result in diminishing returns, and so the exact amount of additional simulation time required was unknown. While optimal mixing had not been achieved, given that LPS mixing in simulations had not been reported in the literature[149], the work carried out here is a promising start.

The structural properties of the membrane as a function of λ were calculated to probe the effects of increased LPS mixing on the membrane. The average membrane thickness and APL across each replica trajectory was determined as a function of λ (Figure 6.15) and compared to average across the last 4 μs of the unbiased system(Figure D.2). It was observed that as λ was decreased the membrane thickness decreased, while the APL of each lipid type increased. As λ decreased the lipid tails became more disordered, which resulted in an increase in the APL and thus a smaller membrane thickness. The changes

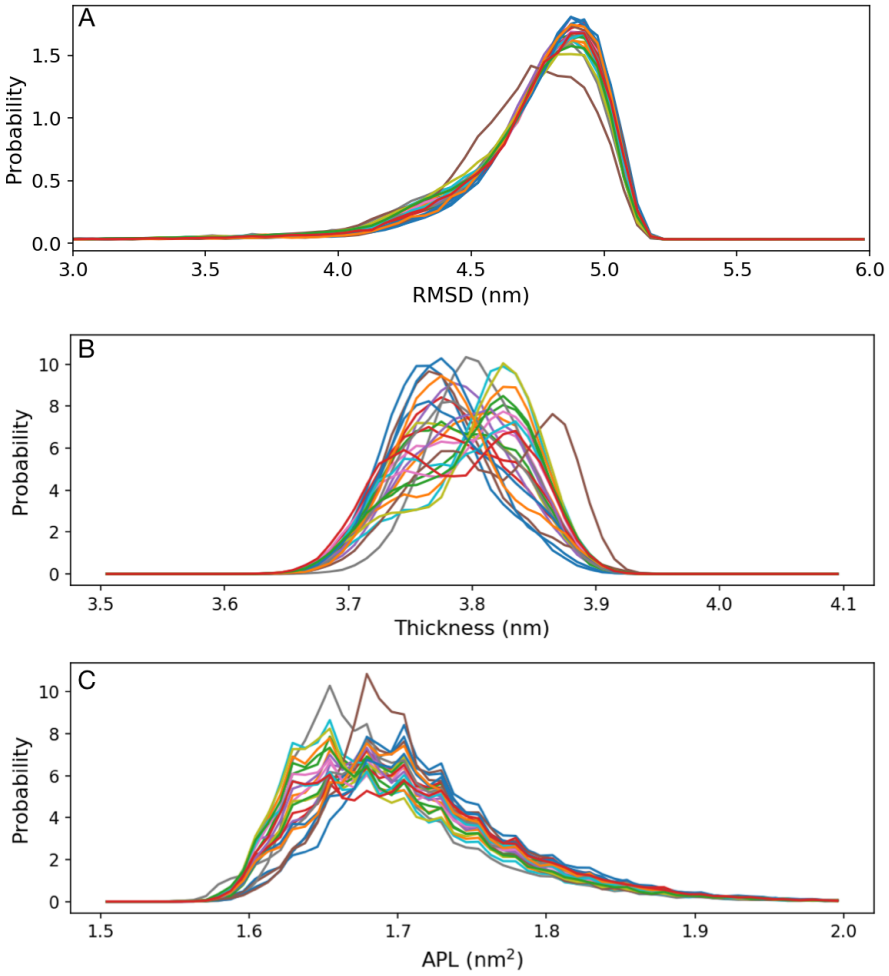

FIGURE 6.13: A) Probability distribution of the RMSD of the HEADALL region relative to the initial frame, B) the membrane thickness and C) the area per Lipid (APL) of ReLPS for each coordinate trajectory (a coordinate trajectory was represented by one line) of system 11 (Table 6.2). The APL and membrane thickness were determined using the centre of geometry of any phosphate beads in each lipid with the FATSLiM program [232].

in membrane thickness were linear as a function of λ, which suggested that no phase changes occurred. That no phase changes occurred was a meaningless observation as the Martini model was not parameterised for high temperatures ($>$ 360 K) or low *lambda*. The membrane properties of the ground state were comparable to those of the unbiased system.

To assess the behaviour of membrane properties in different regions of replica space, the area per lipid of ReLPS and the membrane thickness were measured as a function of time for the minimum and maximum replicas (Figure 6.16). The maximum replica showed highly converged membrane properties across the trajectory, but with large errors in the average value. The large errors in the membrane properties of the maximum replica were attributed to the enhanced speed of LPS mixing, compared to the minimum replica.

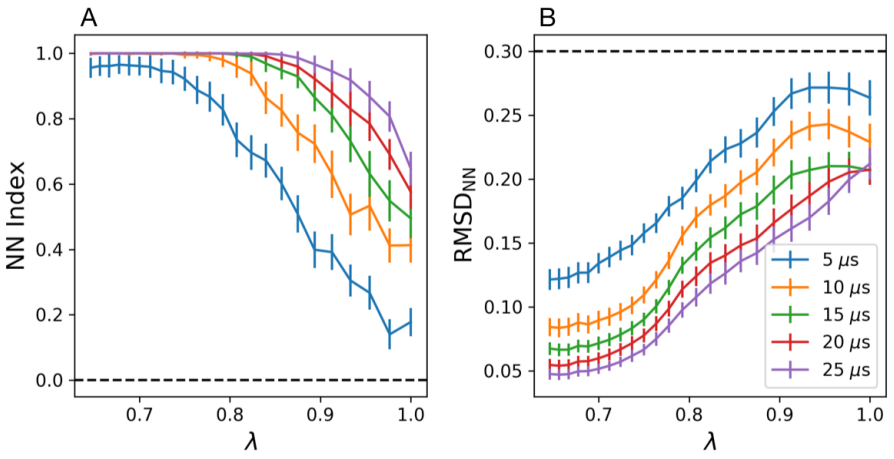

FIGURE 6.14: A) nearest neighbour index (NN Index) and B) $RMSD_{NN}$ vs λ for system 11 (Table 6.2) for different time intervals. The dotted lines represent the values obtained when no LPS mixing occurred (Figure 6.7). Further details on the methods of each analysis can be found in Section 6.2.6.

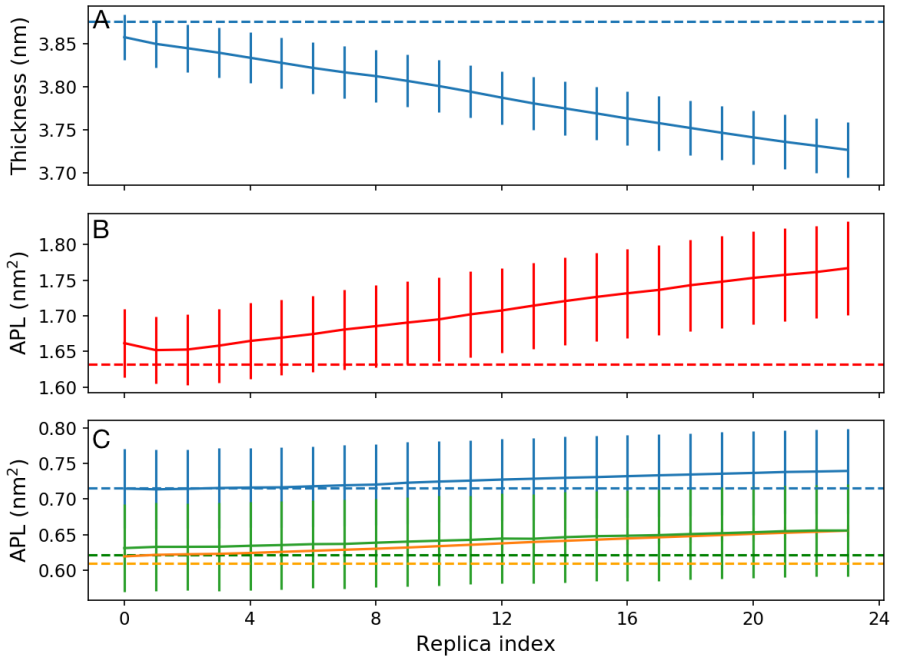

FIGURE 6.15: A) Membrane thickness B) Area per Lipid (APL) of ReLPS, C) POPE (orange), POPG (green) and cardiolipin (blue) vs replica index number for system 11 (Table 6.2). Averages and errors were generated from a taking the average and standard deviation across each trajectory. The dotted lines were the average values across the last 4 *mus* of the unbiased simulation of the outer membrane (Figure D.2). The APL and membrane thickness were determined using the centre of geometry of any phosphate beads in each lipid with the FATSLiM program [232].

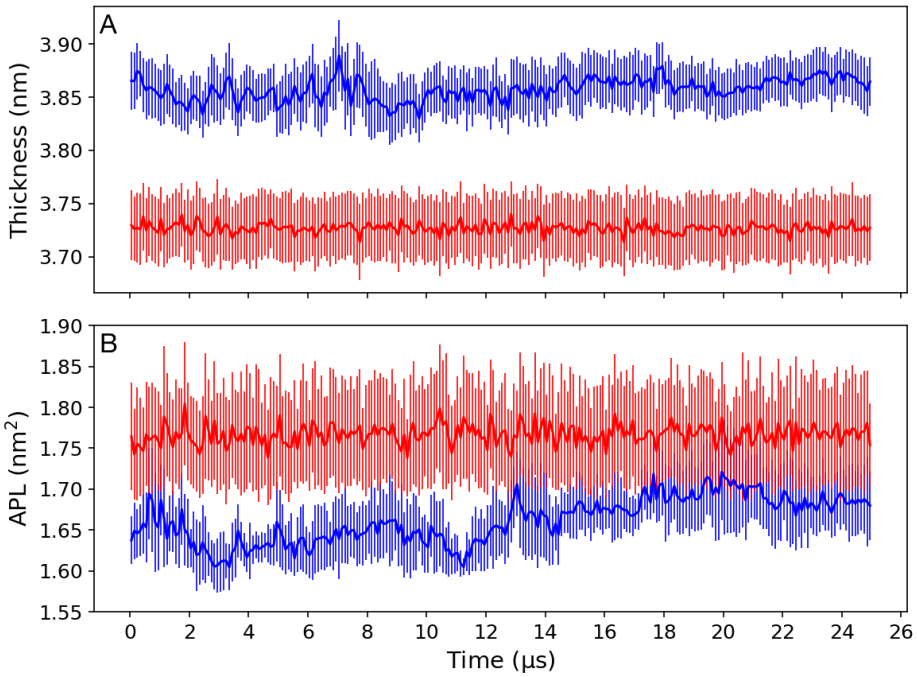

FIGURE 6.16: A) Membrane thickness B) Area per Lipid (APL) of ReLPS vs time for the maximum (red) and minimum (blue) replicas. Averages and errors determined from the block average and standard deviation, respectively, across 100 ns intervals. The APL and membrane thickness were calculated using the centre of geometry of any phosphate beads in each lipid with the FATSLiM program [232].

In the minimum replica all observable properties appeared to have converged after 14 μs.

The BCOM and BBCOM methods, described in Section 4.2.4, were used here to quantify the relaxation of the LPS phosphate beads across the last 10 μs of the ground state replica (Figure 6.17). The covariance overlap values for the ground state were $\sim$ 0.2 higher than those observed previously for an unbiased OM system (Figure 4.28). The ratio between the covariance of BCOM and BBCOM as a function of block size for the ground state was a good fit to the model of exponential decay expected from previous studies[182]; which was not the case for the unbiased OM system simulated in chapter 4. If the ratio between the BCOM and BBCOM method reached 1, then sufficient sampling had occurred. The Bootstrap/Blocked ratio did not reach 1.0 (only 1.08) within 5 μs, but was tending towards 1. The fast and slow relaxation constants from fitting the Bootstrap/Blocked ratio vs block length to a double exponential were 0.2 and 1.5 μs, respectively. The relaxation constants of the unbiased OM system (see Section 4.3.6) were 4.0 and 12.3 μs. Thus it can be confirmed that the use of HREX MD led to a large improvement of system relaxation and the lateral sorting of LPS.

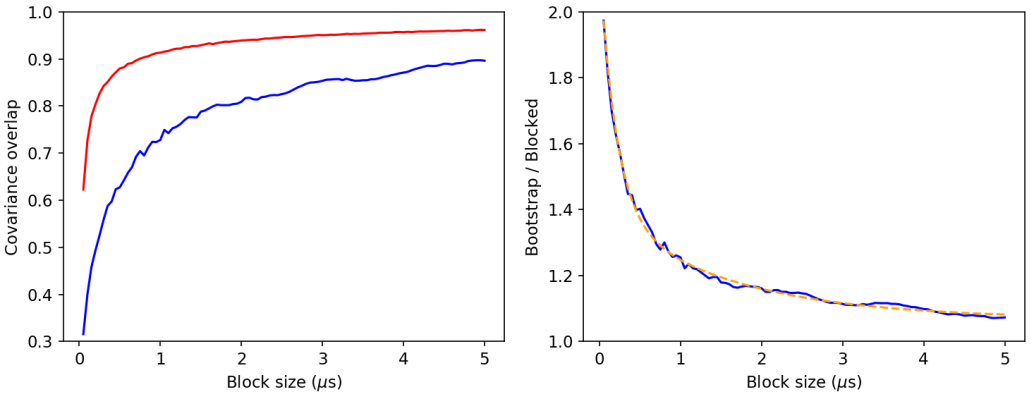

FIGURE 6.17: left) BCOM (red) and BBCOM (blue) of the phosphate beads in ReLPS across the last 10 μs of system 11 (Table 6.2). right) Ratio between BCOM and BBCOM. Further details on the method can be found in Section 4.2.4.5.

6.3.4 Application for Enhanced Protein-Lipid Interactions

One application of interest for increased LPS mixing was the convergence of protein-lipid interactions across repeats. In the previous section, it was shown that HREX can improve lateral sorting of ReLPS. Now HREX was applied to a ReLPS outer membrane with a transmembrane FhuA. The autocorrelation time after initialisation of velocities for an equilibrated system was 53 ns. It was estimated that the use of a $\sim$ 50 ns EAI would have required at least 250 μs (5×10^3 exchange attempts) per replica, for sufficient replica mixing to be achieved [233]. Instead, the parameters used in the previous section were applied (system 12, Table 6.2). If HREX showed promise for the convergence of protein-lipid interactions, then further optimisation of parameters could be carried out.

First the exchange probability and total residence time for each replica index was calculated, to assess replica mixing (Figure 6.18A and B). The average exchange probability was 0.33 and showed little variation across all replicas; whereas the total residency times indicated significant trapping in all regions, especially at the extrema of replica space. The trapping fraction was found to be 0.52, which was similar to the values reported for the membrane only systems. Only one round trip was made between the maximum and minimum replicas in the 12 μs simulation (Figure 6.18C). Similarly, the RMSD_{pop} did not converge within these simulations (Figure 6.18D). Thus the replica mixing of system 12 was even worse than what was observed for the membrane only system.

To measure LPS mixing, the NN index and RMSD_{NN} were calculated across 4 μs increments(Figure 6.19). Following the trends seen for replica mixing, it was not unexpected that after 12 μs the ground state replica was under half as mixed as the membrane only system (Figure 6.14). Thus it was likely that at least another 30 μ of simulation would be required for the membrane to to be sufficiently mixed. Improving the efficiency of

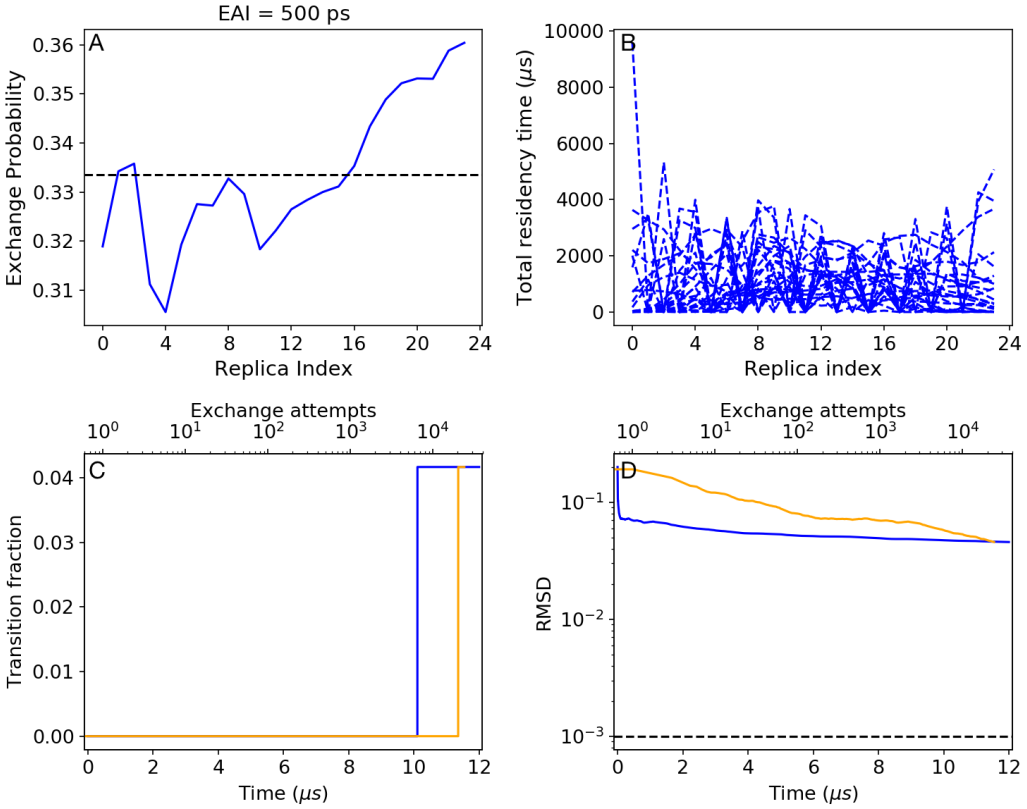

FIGURE 6.18: A) Exchange probability and B) total residency time for reach replica across the 12 μs. C) Fraction of replicas that complete at least one round trip D) RMSD of population frequency (see Equation (6.5)) vs time (blue) and number of exchange attempts (orange). These analyses were carried out on the system with FhuA in an ReLPS outer membrane (system 12, Table 6.2). The exchange attempt interval was 500 ps.

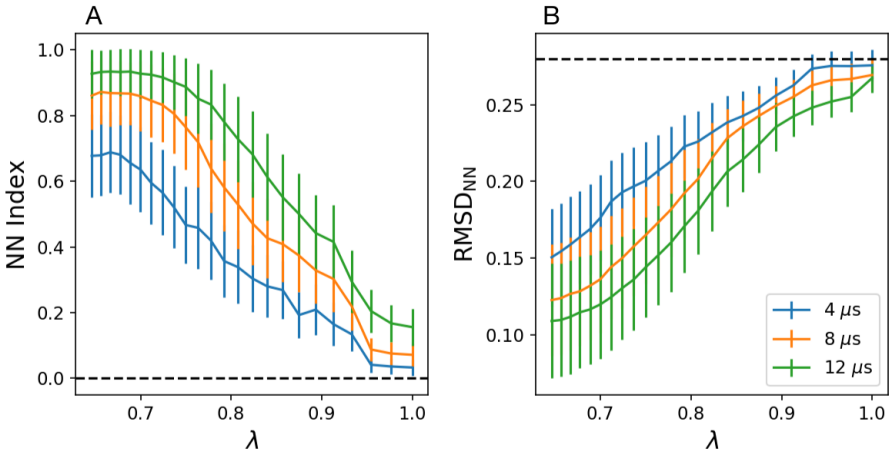

FIGURE 6.19: A) nearest neighbour index (NN Index) and B) $RMSD_{NN}$ vs λ for system 12 (Table 6.2) for different time intervals. The dotted lines represent the values obtained when no LPS mixing occurred (Figure 6.7). Further details on the analysis methods can be found in Section 6.2.6.

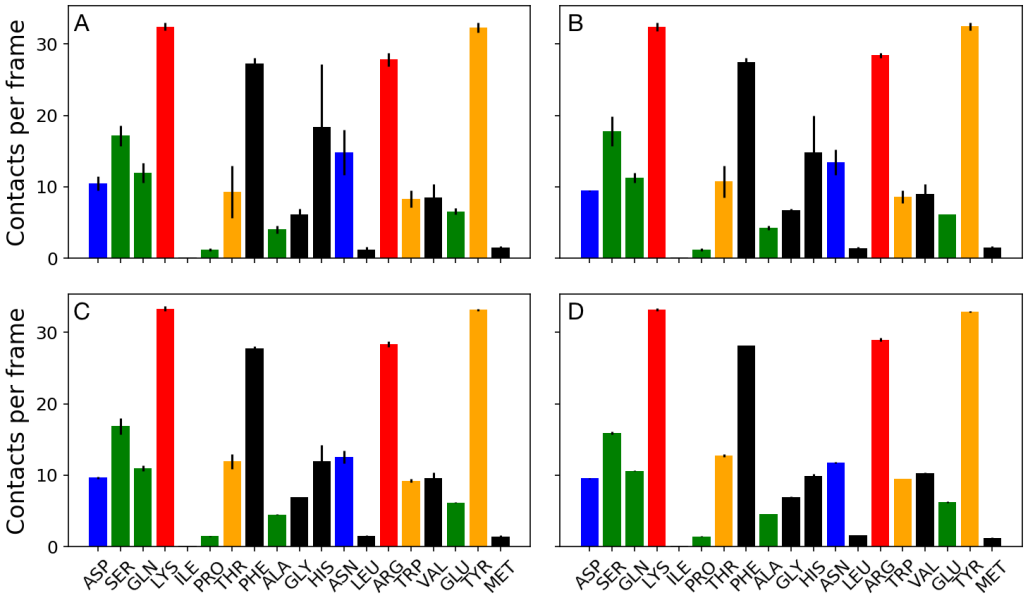

FIGURE 6.20: Average number of contacts per frame between each residue in FhuA and ReLPS Lipid A headgroup (system 12, Table 6.2) averaged across pairs of replica indices A) 0 and 23, B) 7 and 23, C) 15 and 23, D) 22 and 23. Error bars represented the standard deviation of each value. Every bar was colored with respect to the polarity of each residue: red=basic, blue=acidic, orange = aromatic, green = polar, and black = nonpolar. Note that multiple contacts between a single residue and another lipid A headgroup were only counted once.

LPS mixing could minimise the amount of simulation time required; however, the long autocorrelation times of the potential energy in OM systems make this a non-trival problem.

Contact analysis between each residue type in FhuA and the Lipid A headgroup was carried out for replica indices 0, 7, 15 and 23. Following this four plots were generated by taking the average between each replica index mentioned previously and the maximum index (Figure 6.20). Errors were calculated as the standard deviation between the two compared replicas. As the difference in λ between replica indices decreased, so did the errors between the contacts in each replica trajectory. The contacts in the two highest replicas were identical, and given the degree of LPS mixing within each replica could be considered to pseudo repeats within coordinate space. While these results are meaningless, as they are well outside of the conditions that the forcefield was parameterised for [109–112], they prove that convergence of protein-lipid properties could be achieved for the ground state replica.

Future work could include a study of the increase in mixing effectiveness as a function of EAI. Such work would require a scan of EAI values from 1 to 60 ns, for which simulations of at least 30 μs in length would be required. In Martini2 it is known that

sugar-sugar interaction are far too strong in solution[192] and this could also be a factor that contributed to the large autocorrelation times and thus poor mixing efficiency. The Martini team have begun the parameterisation of Martini3 and one of the features of this new forcefield is the improvement of polysaccharide interactions. It would be of interest to re-develop the LPS models with the new forcefield and repeat the study carried out here. Furthermore this work could be repeated with other top down coarse-grained forcefields, such as SIRAH[242, 243], however the results would not be expected to differ greatly from those seen here.

6.4 Conclusions

Here two protocols were trialled for the improvement of LPS mixing in coarse-grained MD simulations of the ReLPS outer membrane. The first protocol aimed to improve LPS mixing by adding a sparse density of LPS in the upper leaflet, thus reducing the confined nature of LPS dynamics. It was found that even for sparse densities LPS would usually form a few large clusters. If a protein was present LPS would remain locked around the protein. Reducing the fraction of LPS in the upper leaflet resulted in faster protein rotational dynamics, but protein-lipid interactions did not converge between 30 μs repeats.

The second protocol involved the use of Hamiltonian Replica exchange (HREX) to improve the mixing of ReLPS. The Hamiltonian of a number of different subsets of the LPS lipid were scaled. It was found that scaling just the charged beads or sugar regions resulted in minimal improvements to mixing. This was surprising, as LPS lipids are known to form strong inter-lipid interactions via divalent cations[105]. Scaling the Hamiltonian of just the LPS sugars and the Lipid A headgroup was found to give optimal LPS mixing, while minimising the computational resources required. Significant mixing of ReLPS was achieved over 25 μs of simulation, but the sampling of replica space was very inefficient. It was believed that slow replica mixing was due to long autocorrelation times of the potential energy in OM systems (picoseconds to microseconds). The membrane properties of the ground state replica were within errors of those calculated for an unbiased system. HREX was also applied to an outer membrane system containing FhuA. The mixing of both the replicas and the LPS lipids was much slower after the inclusion of the protein. Thus LPS mixing was not sufficient to study convergence of protein-LPS interactions in the ground state replica. Interestingly, the protein-LPS interactions did converge in "hot" replicas and so further simulation could achieve the same in the ground state. However, the amount of extra simulation required would be at least 50 μs.

These results provide a promising base to the improvement of LPS sampling in OM systems. While improved LPS mixing has been achieved, significant replica mixing only occurred over long timescales (microseconds). This may be a necessity of the physics of the systems involved, but further optimisation of HREX parameters should be investigated. The exchange attempt interval (EAI) of HREX has been noted to have a profound effect on the sampling of phase and replica space[233, 244], especially if successive exchanges are correlated. For some OM systems the EAI would have to be greater than 50 ns for exchanges to be uncorrelated, which is computationally unfeasible. Thus further optimisation of the EAI should focus on whether a compromise between frequent exchanges and minimised correlation between exchanges exists.

In Chapter 5 it was found that different LPS lipids could have different extraction free energies, and that convergence of a single PMF was slow. It is possible to combine umbrella sampling (US) and HREX to further enhance sampling of phase space[245]. US/HREX MD could enable the sampling of complex PESs, in a range of outer membrane systems. Two processes of interest would be the permeation of the membrane by antimicrobials, or defect formation in the membrane.

Chapter 7

Conclusions

7.1 Summary

Here CG MD was applied to complex bacterial membrane models to further our current understanding of the Gram-negative bacterial cell envelope. Both the behaviours of the membranes and their interactions with embedded proteins were the main focus of this work. Comparisons were also drawn to the simpler bacterial membrane models often used throughout the literature. Model membrane complexity has been shown to be essential in furthering understanding the cell envelope. However, with increasing model complexity brings with it a new set of challenges that should be the focus of future work.

In Chapter 3 CG MD simulations were performed on a series of natural and artificial nanopores that were embedded in either a symmetric phospholipid membrane or an asymmetric Gram-negative outer membrane. The aim of this chapter was to investigate the contribution of nanopore size, shape and chemistry to the properties of the surrounding membrane. The diffusion around a protein was largely impacted by protein size, whereas the asymmetry in diffusion between leaflets was impacted by protein shape and chemistry. Protein shape also played a key role in the membrane structure around each pore. The structure and the dynamics of the outer membrane was found to vary greatly from the simpler phospholipid systems. In the outer membrane the slow moving LPS layer was found to dictate protein diffusion and the structural properties of the opposing leaflet. In particular, an increase of cardiolipin clustering was caused by communication with the LPS layer. The effects of protein interactions on their local environments was found to be reduced in outer membrane models.

In Chapter 4 a more in depth study of the behaviour of a range of outer membrane proteins in different outer membrane models was carried out. The proteins had a variety of

sizes, functions and natural oligmerisation states; while each membrane contained different LPS levels. During this chapter milliseconds of CG simulations were performed. Interactions between Omps and the LPS in the outer membrane had a unique fingerprint. The observed patterns were often not consistent across the same level of LPS or proteins of similar sizes or functions. The tilt of the O-antigen component of LPS was found to depend on protein size and thus protein environment is likely to affect the thickness of the outer membrane, which acts as a barrier to antibiotics. While trends could be reproduced across repeats, quantitative values were often not reproducible. It was believed that poor convergence was the result of a lack of LPS sorting on the scale of these simulations (up to 60 μs). Observable properties often had correlation times on the order of microseconds.

In Chapter 5, umbrella sampling was used to extract lipids from outer and inner membrane models to compare and contrast the stability of each lipid in their respective membrane. The restricted dynamics of LPS meant that different LPS lipids gave different lipid extraction free energies. When the same lipid was extracted multiple times, convergence was dependant on the CV used. The highest performing CV for lipid extraction, in terms of convergence, was not the most specific one.

Chapter 6 focused on designing protocols to overcome the issues with convergence for outer membrane models described in previous chapters. It was hypothesised that the used of sparse LPS densities would lead to enhanced lipid sorting and the convergence of protein-lipid interactions between repeats. Instead, LPS remained locked around the protein and protein-lipid interactions did not converge. The second method was to apply Hamiltonian replica exchange MD (HREX MD) to LPS to enhance the lateral sorting of LPS. HREX MD was used to successfully enhance LPS mixing and speed up the relaxation of outer membrane models, compared to unbiased simulations. However, the current protocol for HREX MD was too inefficient to be applicable to large systems, and thus further optimisation should be the subject of future work.

7.2 Future Work

During the course of this thesis CG MD simulations have been used to investigate the effects of model complexity on protein-lipid interactions and membrane properties. While a number of interesting conclusions have been drawn, it is clear that there is still a lot of room for future work in this field. Studying the effects of protein crowding in complex bacterial membranes would be the next step from the single protein systems discussed here. Moreover additional complexity could be added to the current model of the cell

envelope, such as CG peptidoglycan or lipidated peptides.

However, before carrying out further studies on more complex systems there are a few areas that merit attention. One such issue is a lack of experimental data for outer membranes. This if of great concern as the accuracy of atomistic and CG models rely heavily on experimental data. In particular, there is a lack of experimental data for the diffusive behaviour of LPS. It is also uncertain whether LPS is confined to an area of the cell or homogeneously mixes. Thus it is difficult to validate the lack of LPS mixing shown in this work. Such experimental work is vital to further validate the results from simulation models. One particular weakness of the forcefield used in this work, Martini, is that sugar-sugar interactions have been overemphasised ('sticky' sugars) [192]. Sticky sugar interactions will have further reduced LPS diffusion in the CG LPS model and may be one factor in explaining the lack convergence between repeat simulations in this work. A more accurate representation of sugars is likely to be one of the goals of the next iteration of Martini.

In Chapter 6 the lateral sorting of LPS was improved through the use of HREX MD. However, LPS mixing was inefficient and only occurred over 10s of microseconds. Further optimisation of the HREX parameters could improve the speed of LPS mixing and system relaxation. Alternatively, different enhanced sampling techniques could be explored. Markov State Models (MSMs) have recently shown promise for building kinetic models that can predict properties over long timescales (milliseconds)[246]. It would be of interest to attempt to develop a MSM for the outer membrane of *E.coli* and compare its performance to HREX MD.

One issue with MD simulation as a whole is often a lack of computational power. Future increased in computational power could overcome sampling issues in bacterial membrane through longer and larger simulations, at higher model resolutions. Alternatively, initial work with machine learned forcefields have shown that is it possible to reproduce QM results at the computational cost of classical models[247]. Machine learned CG forcefields have also been developed for simple systems[248]. These forcefields offer another path to improve the speed and accuracy of simulation models of all resolutions.

Appendix A

Chapter 3 Appendix

FIGURE A.1: Copyright agreement for Table 2.1.

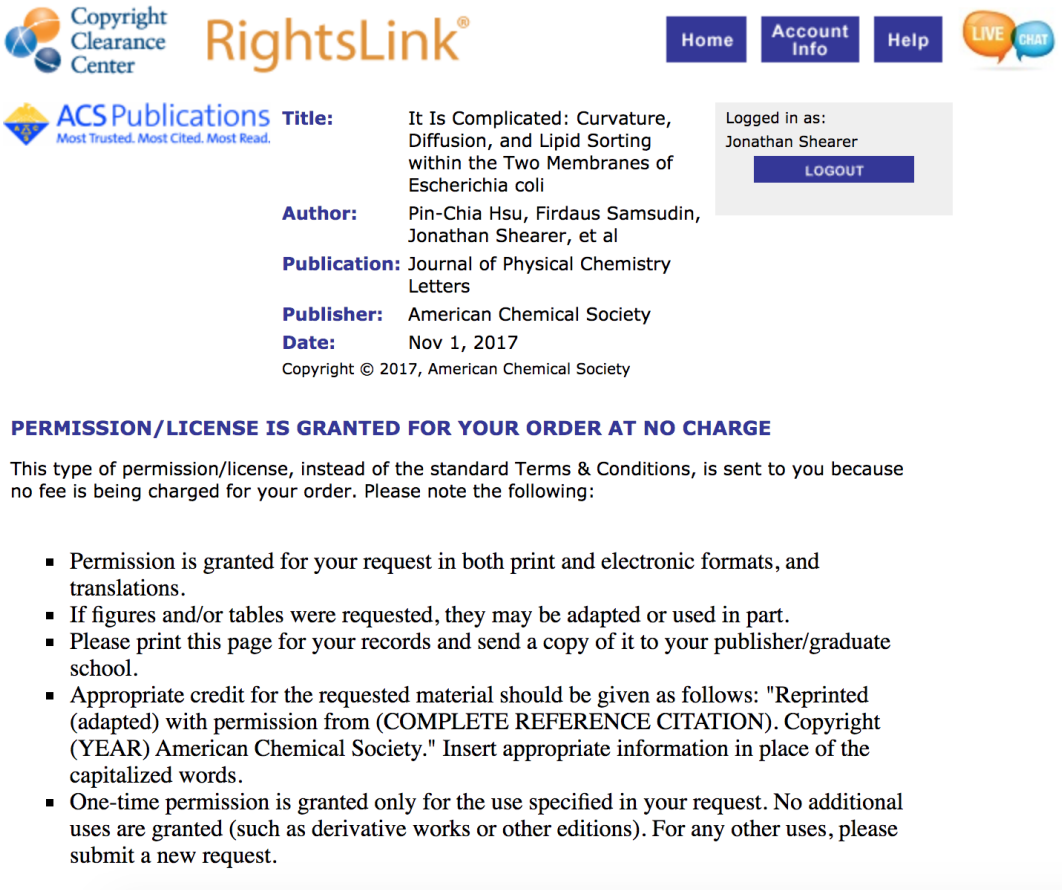

FIGURE A.2: Copyright agreement for previously published work[105].

FIGURE A.3: Copyright agreement for previously published work[149].

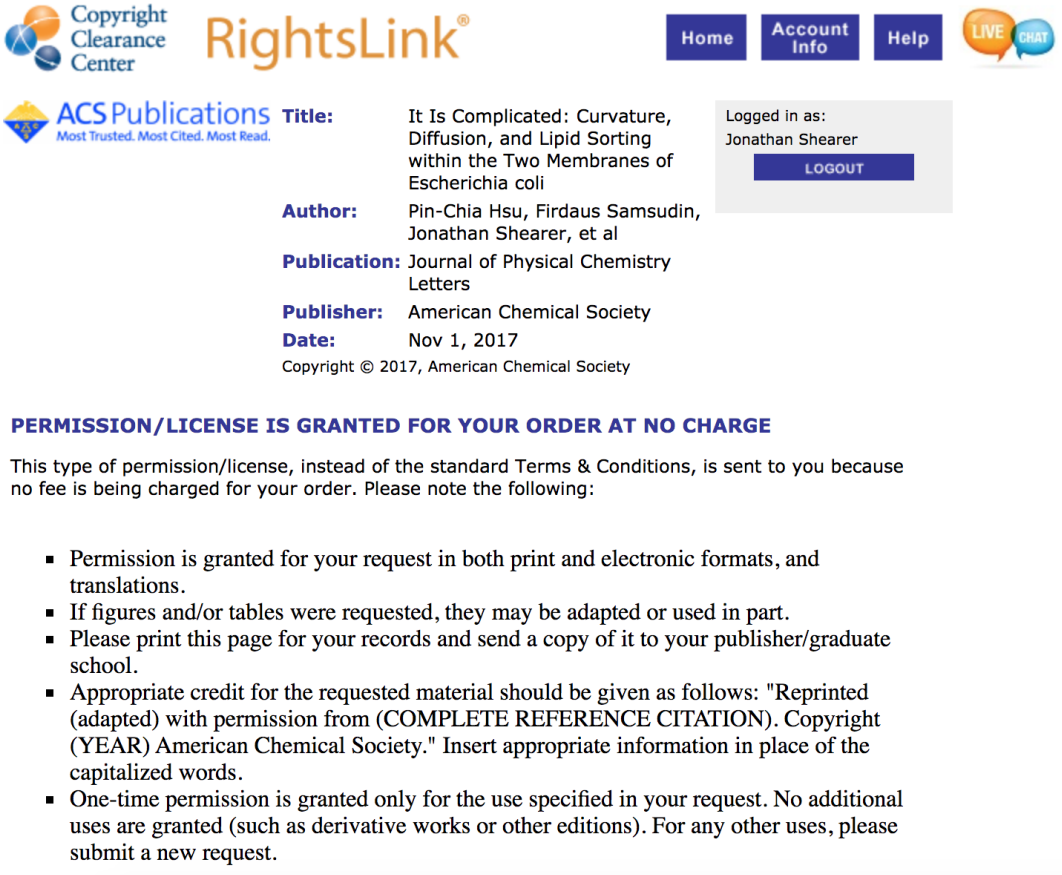

FIGURE A.4: Copyright agreement for previously published work[105].

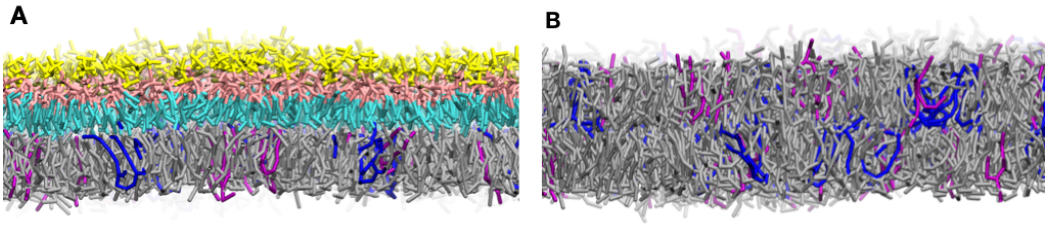

FIGURE A.5: Side on view of the A) Outer membrane and the B) mixed phospholipid systems used in this chapter. key: yellow=LPS core sugars, pink=Lipid A headgroup, cyan=LPS tails, silver=POPE, purple=POPG and blue=cardiolipin.

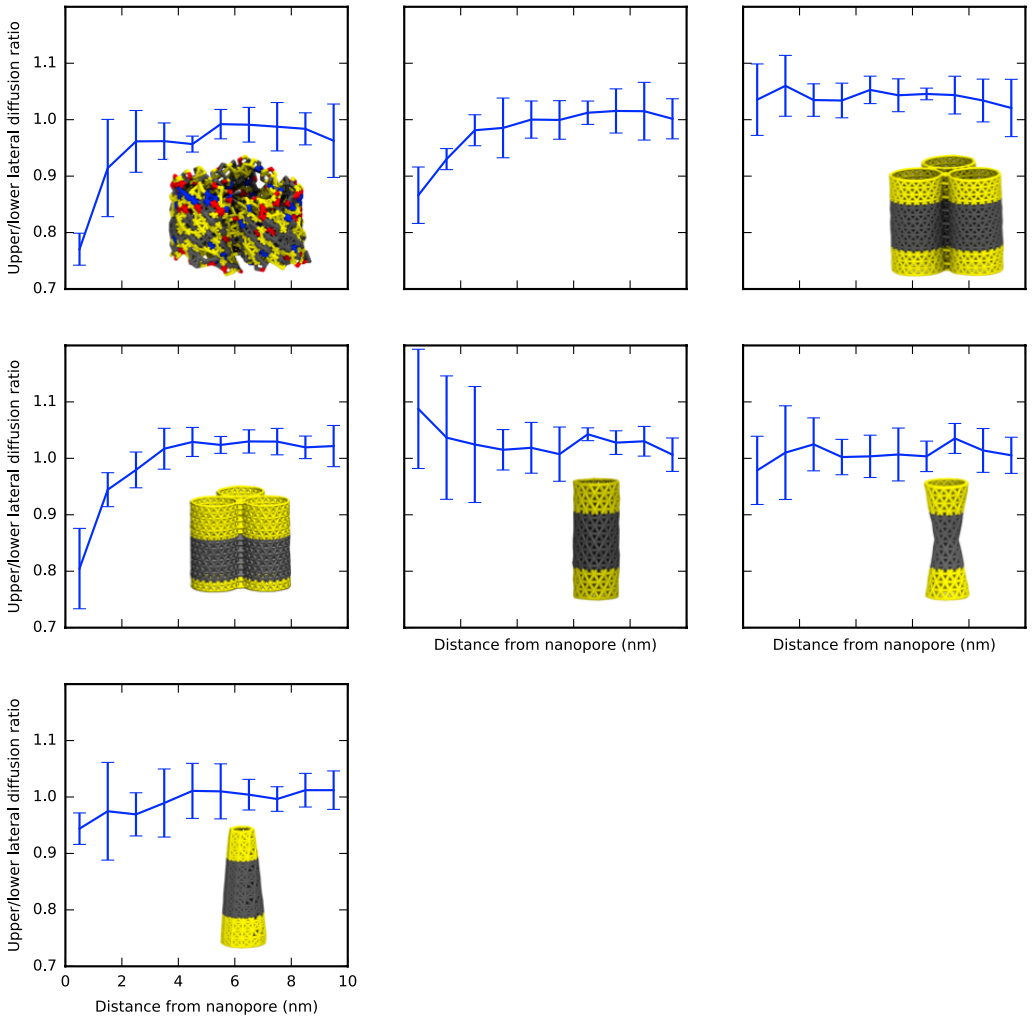

FIGURE A.6: Lateral diffusion ratio between bilayer leaflets of a mixed phospholipid bilayer (18:2:2 POPE:POPG:cardiolipin) with respect to the distance from (upper left) OmpF (upper middle) OmpF mutated (OmpF mut) with carbon nanotube (CNT) bead types (upper right) CNT trimer (middle left) CNT trimer with shifted hydrophobic region (middle) CNT (middle right) carbon nano-particle (CNP) hourglass and (lower left) CNP cone. The distances are the midpoints of each 1 nm bin.

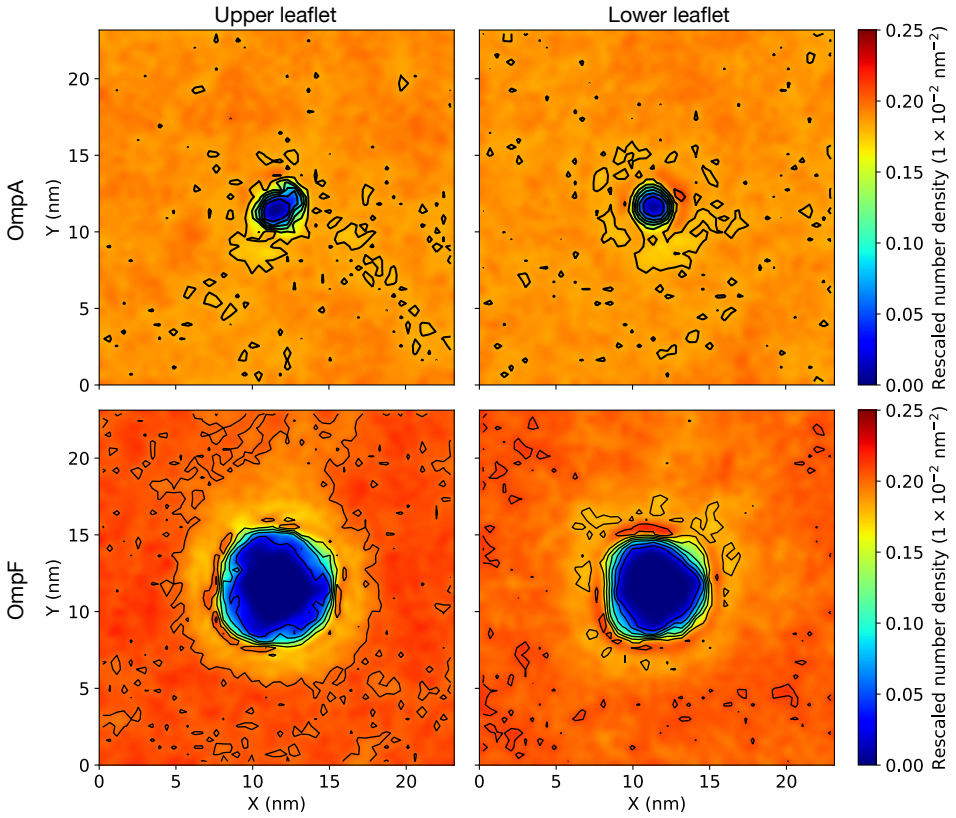

FIGURE A.7: Density maps of POPE in a) upper and b) lower leaflets of the mixed phospholipid membrane centered around a membrane Ompa. Density maps of POPE in c) upper and d) lower leaflets of the mixed phospholipid membrane centered around a membrane OmpF. The density was measured using the phosphate particle and all values normalized by the number of lipids in a given leaflet.

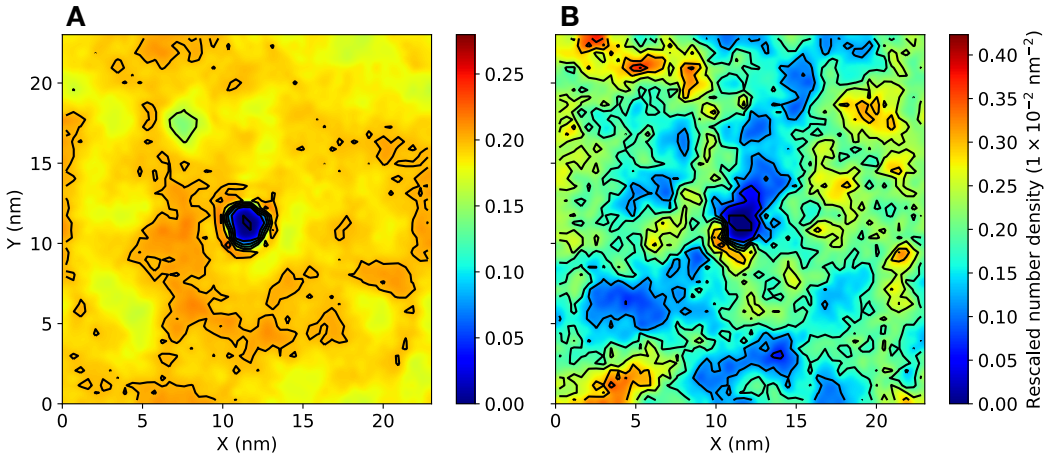

FIGURE A.8: Density maps of A) POPE and B) POPG in the outer membrane. The density was measured using one phosphate particle per lipid and all values normalized by the number of lipids. Each system was centered around a transmembrane OmpA. This is the analysis from the last 4 μs of the repeat simulation (8 μs total). Reused with permission from Shearer et al.[149]

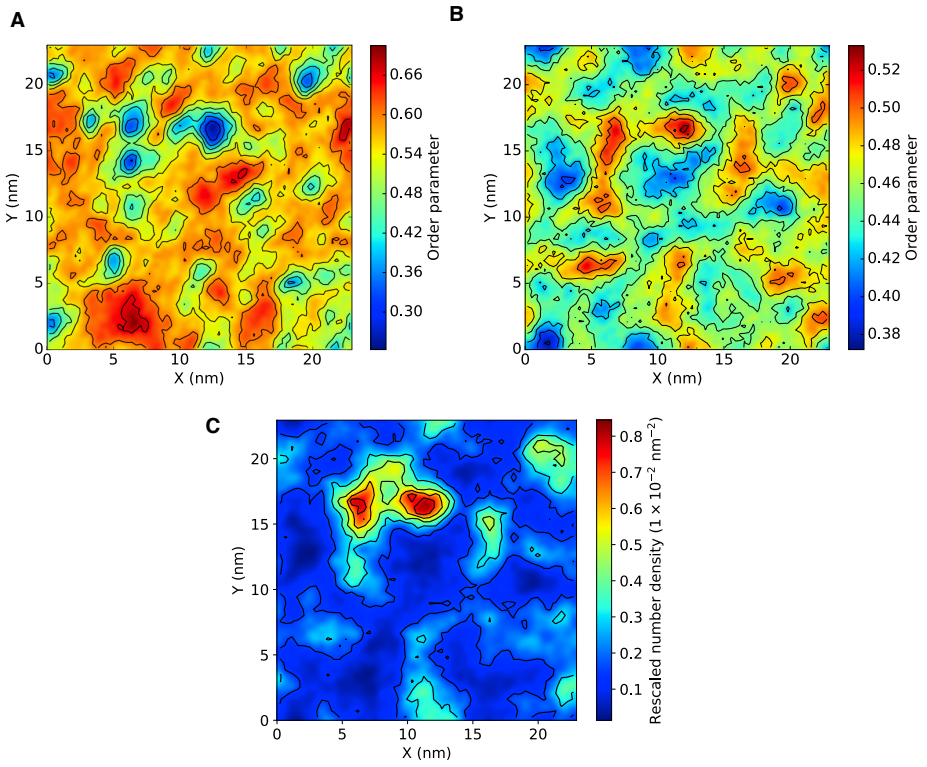

FIGURE A.9: Order analysis map of lipid tails (Equation (3.1)) of A) LPS and B) POPE in the outer membrane. C) Density maps of cardiolipin in the outer and mixed phospholipid membrane, respectively. The density was measured using one phosphate particle per lipid and all values normalized by the number of lipids in a given leaflet. Reused with permission from Shearer et al.[149]

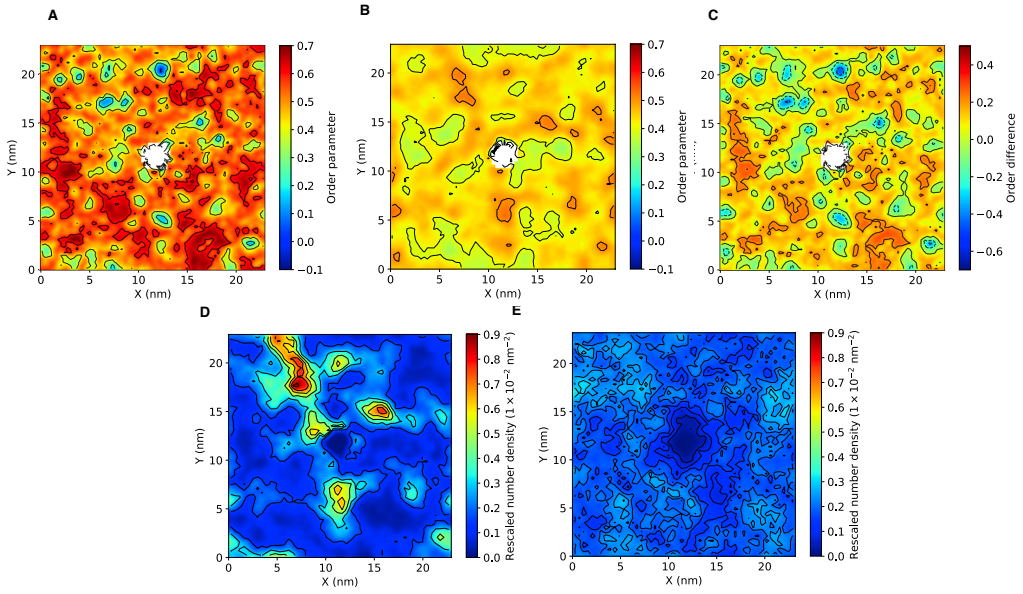

FIGURE A.10: Order analysis of the lipid tails of A) lipopolysaccharide, POPE and the C) difference between lipopolysaccharide and POPE order parameters (Equation (3.1)) in the outer membrane with a membrane OmpA (repeat). (D, E) Density maps of cardiolipin in the outer and mixed phospholipid membrane, respectively. The density was measured using one phosphate particle per lipid and all values normalized by the number of lipids. Each system was centered around a transmembrane OmpA. This is the analysis from the last 4 μs of the repeat simulation (8 μs total). Reused with permission from Shearer et al.[149]

Appendix B

Chapter 4 Appendix

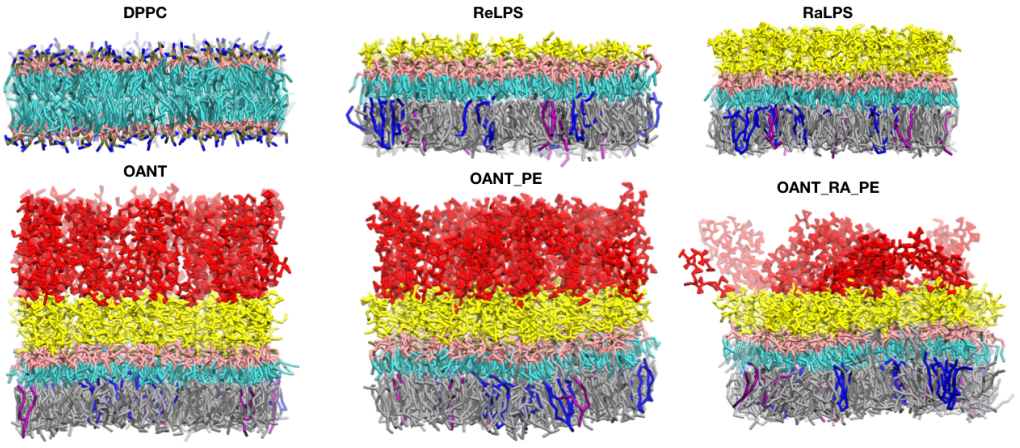

FIGURE B.1: Side on view of the systems used in this chapter (see Table 4.1 and Section 4.2). key for DPPC: green=saturated chains, purple=unsaturated chains, golden=phosphate beads and blue=amine beads. Other key: yellow=LPS core sugars, pink=Lipid A headgroup, cyan=LPS tails, silver=POPE, purple=POPG and blue=cardiolipin.

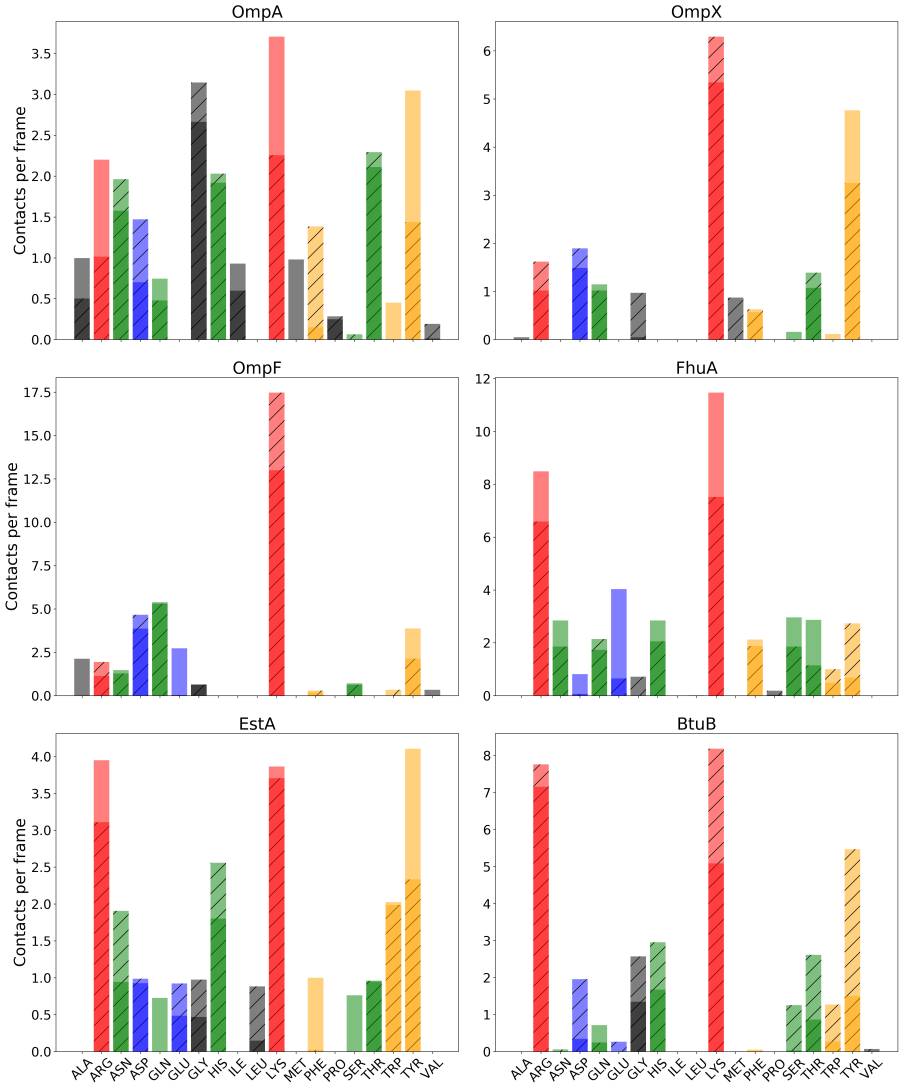

FIGURE B.2: Average number of contacts per frame between each residue in a protein and the lipid A phosphate groups for $25 - 30$ μs across repeats (one repeat has hash markings). Each bar was coloured with respect to the polarity of each residue: red=basic, blue=acidic, orange=aromatic, green=polar and black=non-polar. Note that multiple contacts between a single residue and another Lipid A headgroup were only counted once. Reprinted with permission from Shearer et al. [172]. Copyright 2019 American Chemical Society 2019.

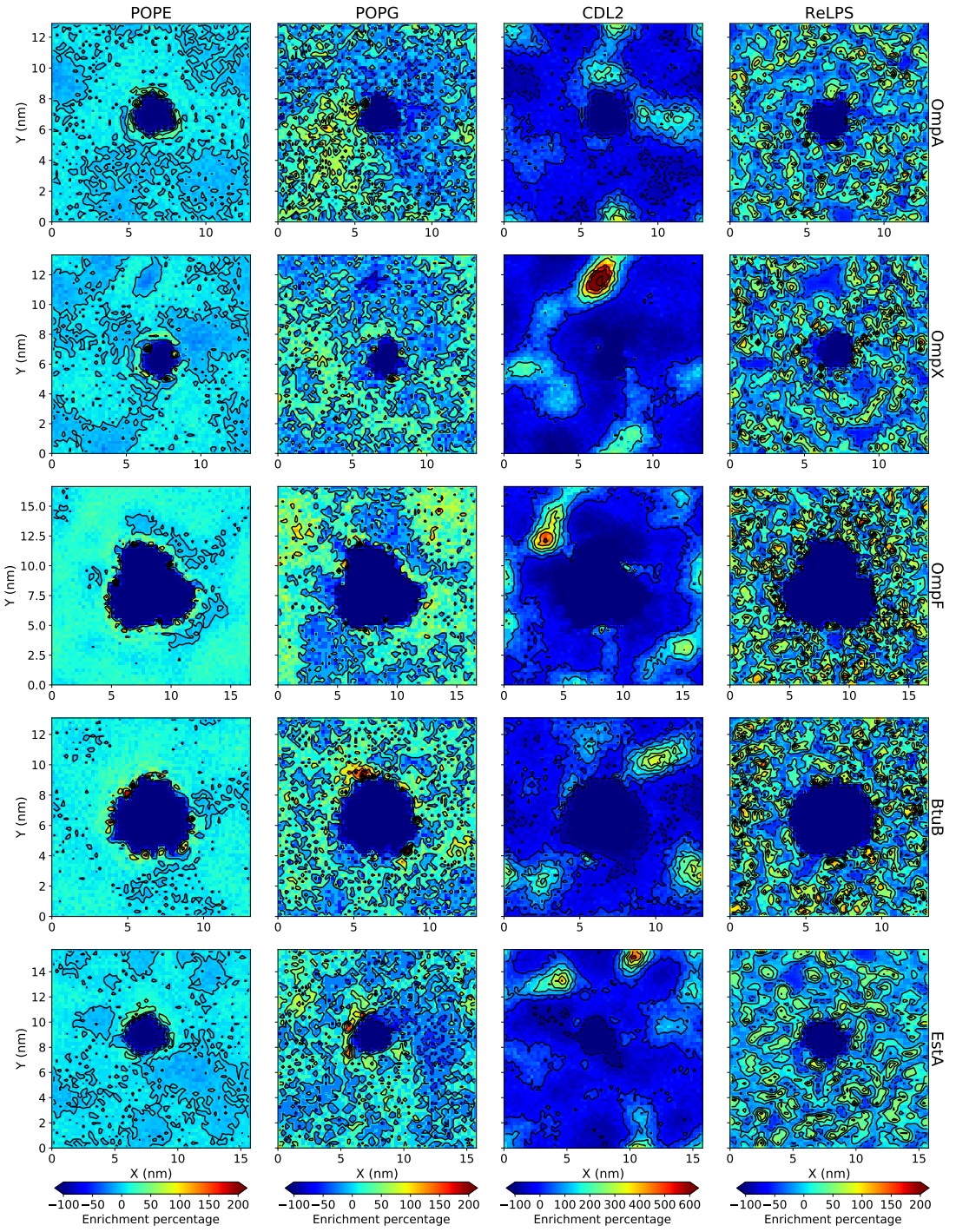

FIGURE B.3: 2D lipid density analysis for the repeats of the ReLPS outmemebrane systems. Densnity mpas were done for the entire Re lipopolysaccharide (ReLPS) lipid, 16:0-18:1 phosphoethanolamine (POPE), phosphatidylglycerol (POPG) and cardiolipin (CDL2) lipid phosphate beads and were averaged over $25 - 30$ μs. The denity mpas are coloured by enrichment (> 0) or depletion (< 0) of each lipid type with respect to the average denity of that lipid. Reprinted with permission from Shearer et al. [172]. Copyright 2019 American Chemical Society 2019.

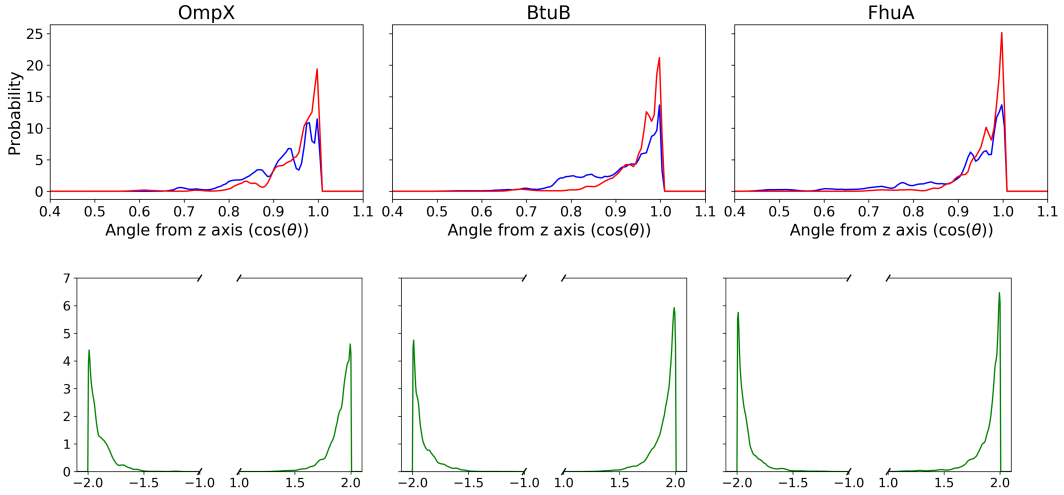

FIGURE B.4: Probability distribution of (top) O-Antigen chain tilt with respect to the z axis and the tilt between neighbouring pairs of O-Antigen chains for $25-30$ μs of the OANT systems (bottom). The tilt of a single O-Antigen chain was calculated using its end to end vector. For the chain tilt with respect to the z axis, two probability distributions were generated for smooth lipopolysaccharides (LPS) closer than 2.5 nm (blue line) or further than 2.5 nm away from a given proteins surface (red line). For the pairwise O-Antigen distributions if the chains tilted towards each other the angle was positive; in all other cases the angles would be negative. Angles are presented in units of $\cos(\theta)$ where θ is an angle. For the pairwise O-Antigen relative tilt angles, if the chains tilted towards each other $\cos(\theta)$ takes the range [0, 2]; in all other cases the angles are between (-2, 0). Reprinted with permission from Shearer et al. [172].

Appendix C

Chapter 5 Appendix

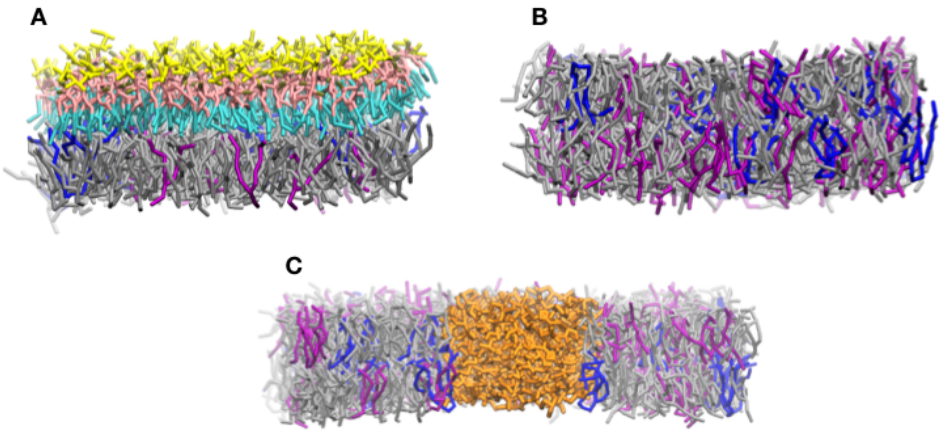

FIGURE C.1: Side on view of the A) outer and inner membrane model, B) without and C) with a membrane AqpZ. The outer membrane contained ReLPS in the upper leaflet of the membrane. key: orange=protein, yellow=LPS core sugars, pink=Lipid A headgroup, cyan=LPS tails, silver=POPE, purple=POPG and blue=cardiolipin.

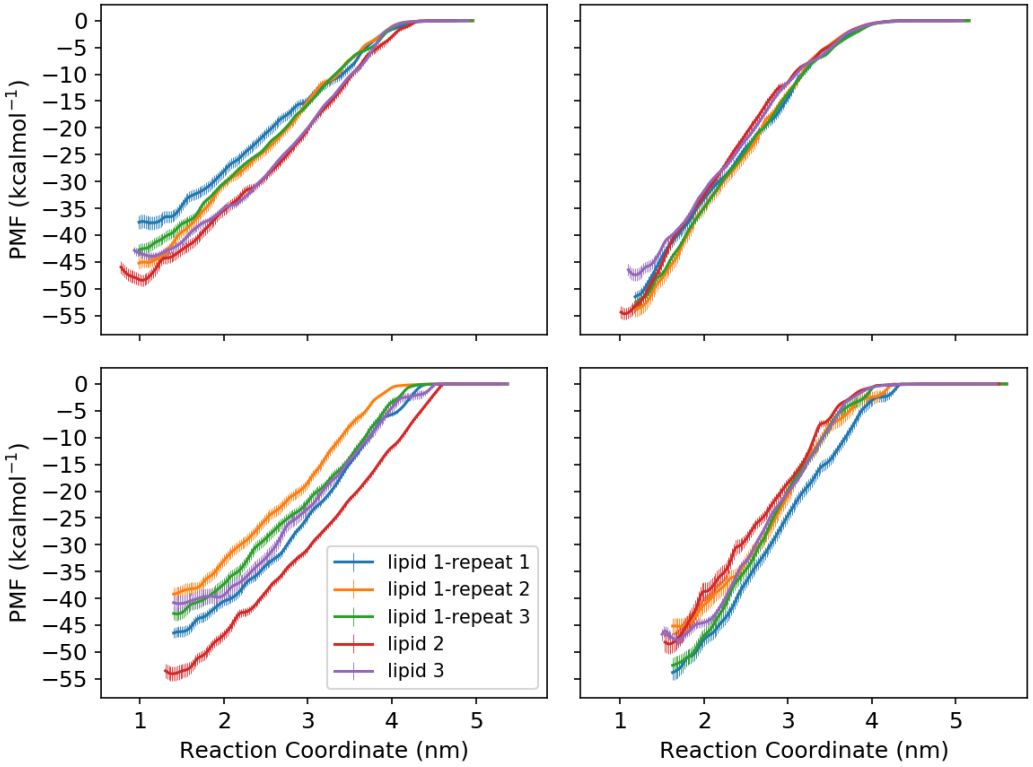

FIGURE C.2: PMFs of ReLPS extraction from the outer membrane using the A) COM_MEMB, B) COM_CY, C) HEAD_MEMB and D) HEAD_CY CV, measured across the last 2 μs of each window. The CVs were defined in Section 5.2.3. The uncertainty in each PMF was estimated with the Bayesian bootstrap method.

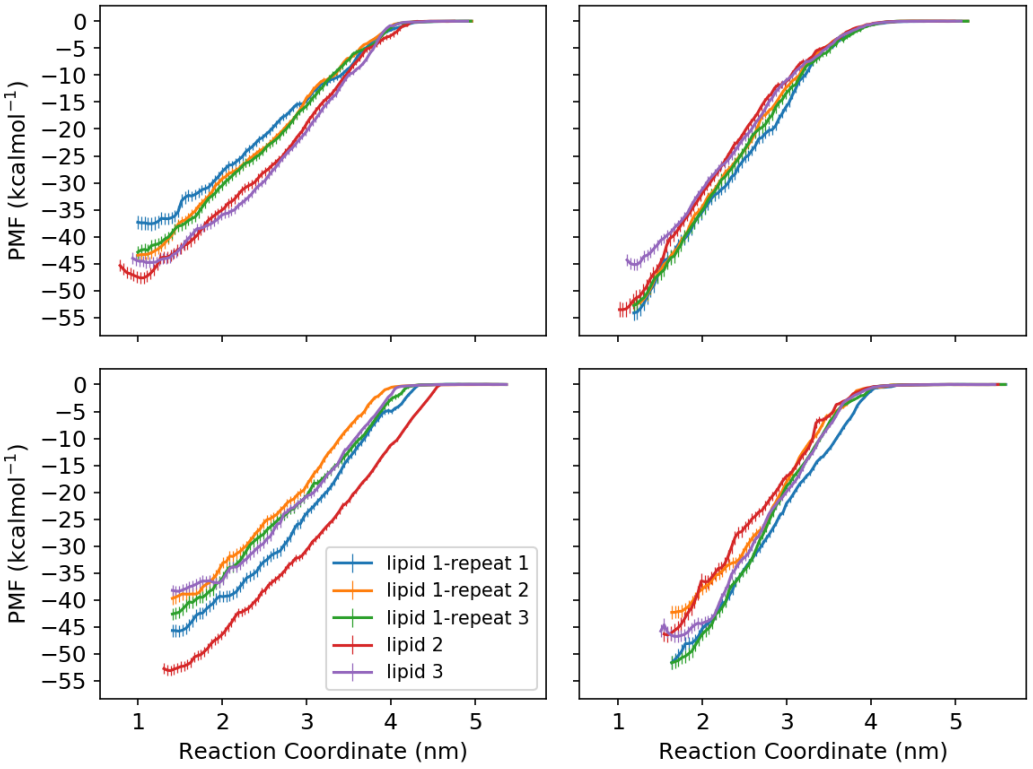

FIGURE C.3: PMFs of ReLPS extraction from the outer membrane using the A) COM_MEMB, B) COM_CY, C) HEAD_MEMB and D) HEAD_CY CVs, measured across the last 2 μs of each window. The CVs were defined in Section 5.2.3. The PMF was calculated using the MBAR free energy estimator[136].

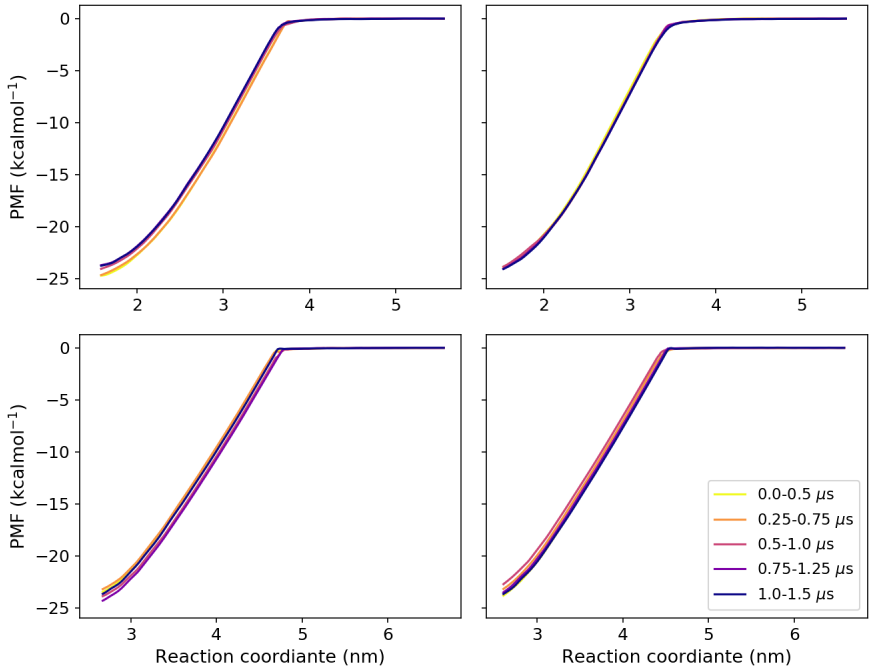

FIGURE C.4: PMFs of POPE extraction from the outer membrane using the A) COM_MEMB, B) COM_CY, C) HEAD_MEMB and D) HEAD_CY CV, measured across intervals of 0.5 μs. The CVs were defined in Section 5.2.3.

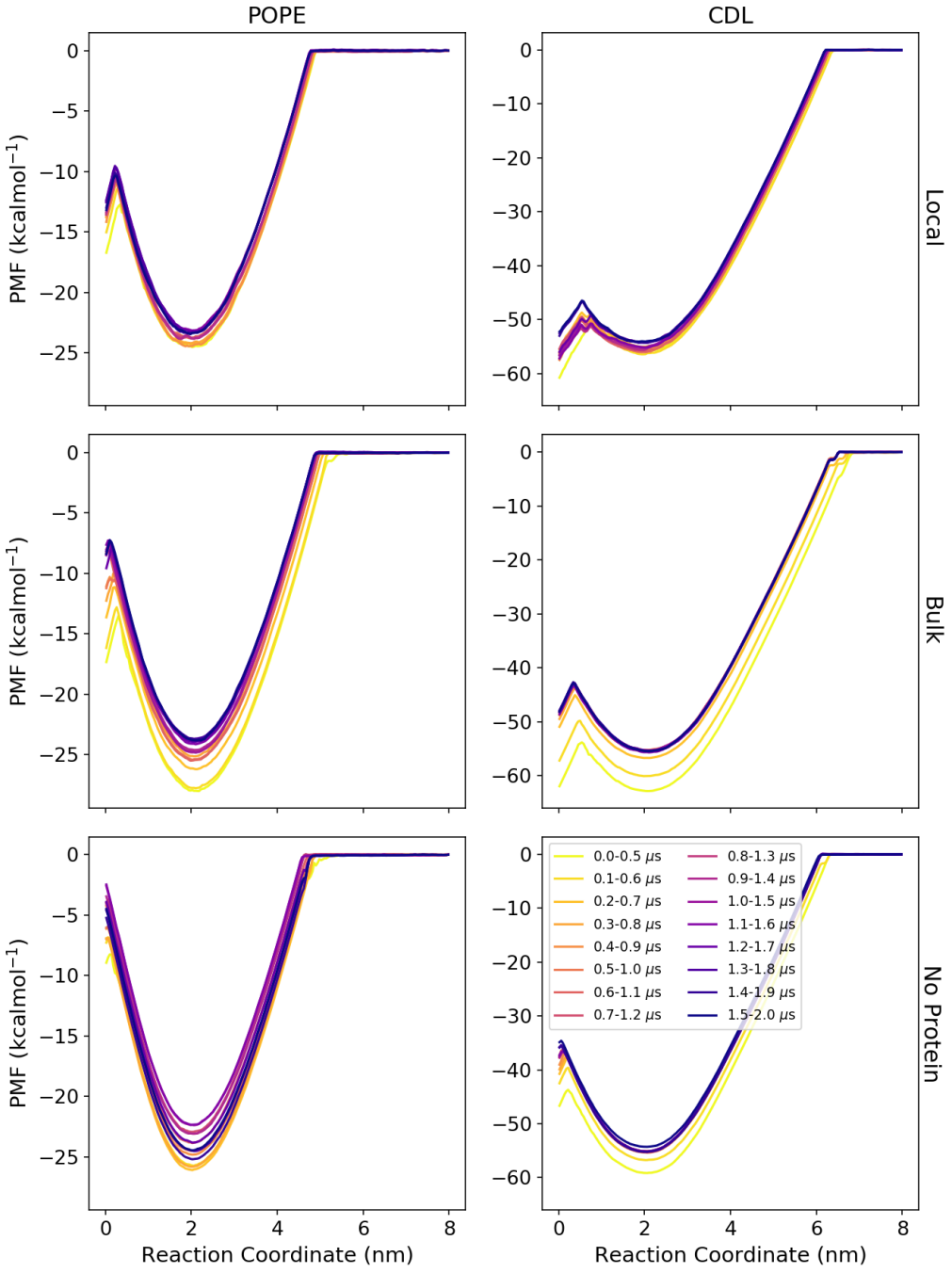

FIGURE C.5: PMFs of the extraction of a POPE or cardiolipin (CDL) lipid from near AqpZ (local), in the bulk of the inner membrane (bulk) or a membrane with no protein across intervals of 0.5 μs.

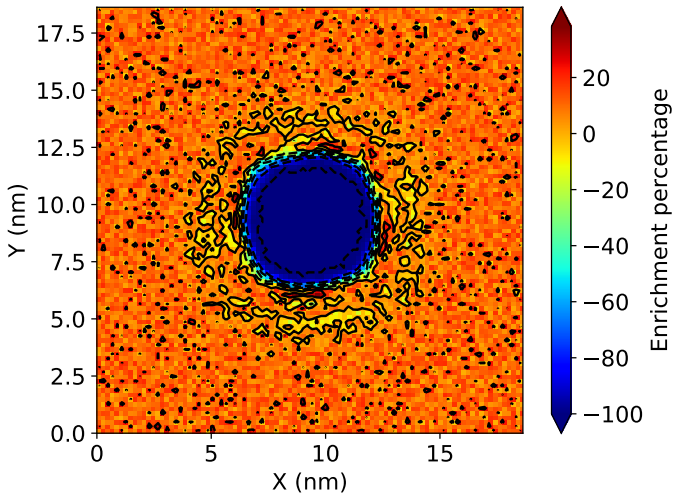

FIGURE C.6: 2D lipid density analysis for the inner membrane with a membrane AqpZ. Density maps were done for all lipid phosphate beads and were averaged over the last 1 μs of the unbiased production run. The density maps are colored by enrichment (> 0) or depletion (< 0) of each lipid type with respect to the average density of all lipids. The analysis method is described in detail in Section 4.2.4

Appendix D

Chapter 6 Appendix

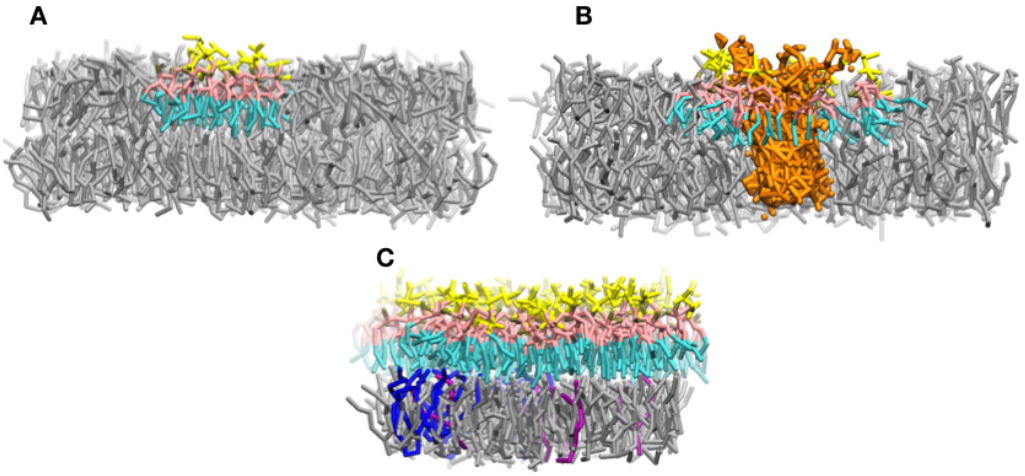

FIGURE D.1: Side on view of the A) POPE membrane with some ReLPS lipids in the upper leaflet A) without (system 3) and B) with a membrane OmpA (system 4). C) ReLPS outer membrane (LPS in the upper leaflet of the membrane, system 5). For more system details see Tables 6.1 and 6.2. key: orange=protein, yellow=LPS core sugars, pink=Lipid A headgroup, cyan=LPS tails, silver=POPE, purple=POPG and blue=cardiolipin.

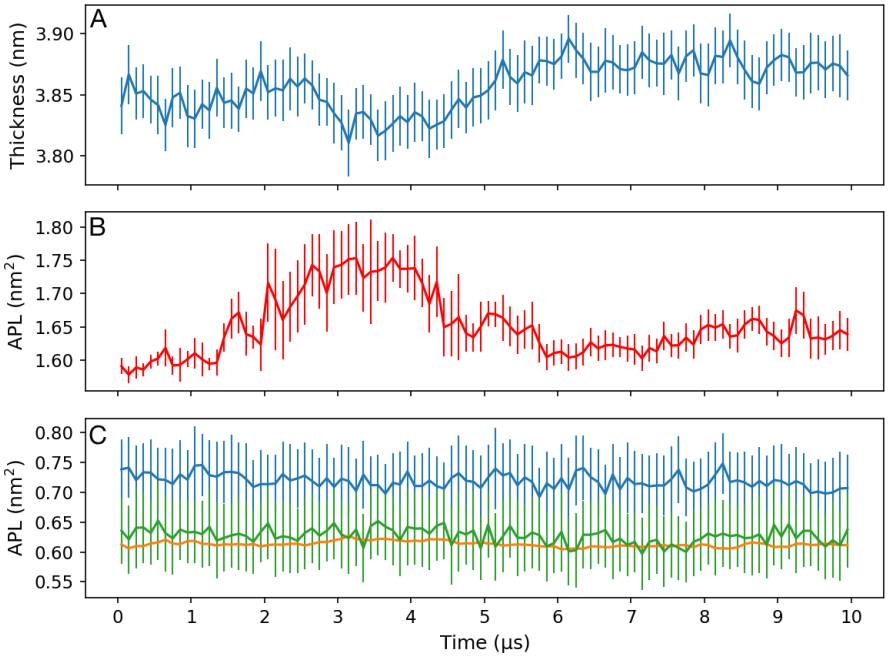

FIGURE D.2: A) Membrane thickness B) Area per Lipid (APL) of ReLPS, C) POPE (orange), POPG (green) and cardiolipin (blue) vs time. Averages and errors were generated from a taking a the block average and standard deviation, respectively, across 100 ns intervals. The APL and membrane thickness were determined using the center of geometry of any phosphate beads in each lipid with the FATSLiM program [232]

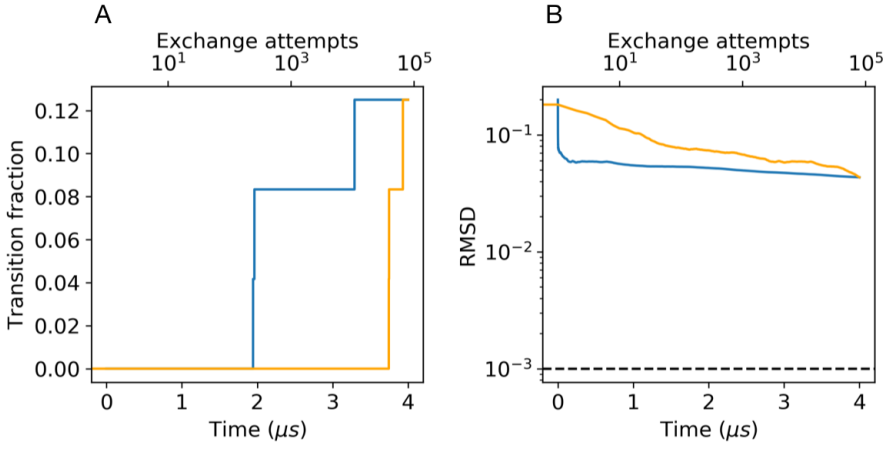

FIGURE D.3: A) Fraction of replicas that complete at least one round trip B) RMSD of population frequency (see Equation (6.5)) vs time (blue) and number of exchange attempts (orange) for HREX of the HEADALL region of an ReLPS outer membrane with an exchange attempt interval of 50 ps.

Bibliography

(1) A. G. Marr, R. J. Harvey and W. C. Trentini, *Journal of bacteriology*, 1966, **91**, 2388–9.

(2) R. A. Hull, R. E. Gill, P Hsu, B. H. Minshew and S Falkow, *Infection and immunity*, 1981, **33**, 933–8.

(3) P. M. Griffin and R. V. Tauxe, *Epidemiologic Reviews*, 1991, **13**, 60–98.

(4) K Poole, K Krebes, C McNally and S Neshat, *Journal of bacteriology*, 1993, **175**, 7363–72.

(5) J. F. Fisher, S. O. Meroueh and S. Mobashery, *Chemical Reviews*, 2005, **105**, 395–424.

(6) F. Reinthaler, J Posch, G Feierl, G Wüst, D Haas, G Ruckenbauer, F Mascher and E Marth, *Water Research*, 2003, **37**, 1685–1690.

(7) B. Lugtenberg and L. Van Alphen, *Biochimica et Biophysica Acta (BBA) - Reviews on Biomembranes*, 1983, **737**, 51–115.

(8) J. W. Costerton, J. M. Ingram and K. J. Cheng, *Bacteriological reviews*, 1974, **38**, 87–110.

(9) A. H. Delcour, *Biochimica et Biophysica Acta (BBA) - Proteins and Proteomics*, 2009, **1794**, 808–816.

(10) R. Coico, in *Current Protocols in Microbiology*, John Wiley & Sons, Inc., Hoboken, NJ, USA, 2005, vol. 00, A.3C.1–A.3C.2.

(11) I. M. López-Lara and O. Geiger, *Biochimica et Biophysica Acta (BBA) - Molecular and Cell Biology of Lipids*, 2017, **1862**, 1287–1299.

(12) J. Coley, M. Duckworth and J. Baddiley, *Journal of General Microbiology*, 1972, **73**, 587–591.

(13) W. W. Navarre and O Schneewind, *Microbiology and molecular biology reviews*, 1999, **63**, 174–229.

(14) S. Furse and D. J. Scott, *Biochemistry*, 2016, **55**, 4742–4747.

(15) M. Caroff and D. Karibian, *Carbohydrate Research*, 2003, **338**, 2431–2447.

(16) H Nikaido and M Vaara, *Microbiological reviews*, 1985, **49**, 1–32.

(17) C. R. Raetz, C. M. Reynolds, M. S. Trent and R. E. Bishop, *Annual Review of Biochemistry*, 2007, **76**, 295–329.

(18) U. Zhringer, B. Lindner and E. T. Rietschel, *Advances in Carbohydrate Chemistry and Biochemistry*, 1994, **50**, 211–276.

(19) C. Erridge, E. Bennett-Guerrero and I. R. Poxton, *Microbes and Infection*, 2002, **4**, 837–851.

(20) C. R. H. Raetz, *Annual Review of Biochemistry*, 1990, **59**, 129–170.

(21) N Qureshi, K Takayama, P Mascagni, J Honovich, R Wong and R. J. Cotter, *The Journal of Biological Chemistry*, 1988, **263**, 11971–11976.

(22) E. R. Rojas, G. Billings, P. D. Odermatt, G. K. Auer, L. Zhu, A. Miguel, F. Chang, D. B. Weibel, J. A. Theriot and K. C. Huang, *Nature*, 2018, **559**, 617–621.

(23) D. Jefferies, J. Shearer and S. Khalid, *The Journal of Physical Chemistry B*, 2019, **123**, 3567–3575.

(24) S. Snyder, D. Kim and T. J. McIntosh, *Biochemistry*, 1999, **38**, 10758–10767.

(25) N. Kucerka, E. Papp-Szabo, M.-P. Nieh, T. A. Harroun, S. R. Schooling, J. Pencer, E. A. Nicholson, T. J. Beveridge and J. Katsaras, *The Journal of Physical Chemistry B*, 2008, **112**, 8057–8062.

(26) B. Lugtenberg, H. Bronstein, N. Van Selm and R. Peters, *Biochimica et Biophysica Acta - Biomembranes*, 1977, **465**, 571–578.

(27) J. S. Park, W. C. Lee, K. J. Yeo, K.-S. Ryu, M. Kumarasiri, D. Hesek, M. Lee, S. Mobashery, J. H. Song, S. I. Kim, J. C. Lee, C. Cheong, Y. H. Jeon and H.-Y. Kim, *The FASEB Journal*, 2012, **26**, 219–228.

(28) P. M. Oger and A. Cario, *Biophysical Chemistry*, 2013, **183**, 42–56.

(29) J. Antoinette Killian, M. C. Koorengevel, J. A. Bouwstra, G. Gooris, W. Dowhan and B. de Kruijff, *Biochimica et Biophysica Acta (BBA) - Biomembranes*, 1994, **1189**, 225–232.

(30) A. DeChavigny, P. N. Heacock and W Dowhan, *The Journal of biological chemistry*, 1991, **266**, 5323–5332.

(31) B. K. Tan, M. Bogdanov, J. Zhao, W. Dowhan, C. R. H. Raetz and Z. Guan, *Proceedings of the National Academy of Sciences of the United States of America*, 2012, **109**, 16504–9.

(32) I Shibuya, C Miyazaki and A Ohta, *Journal of bacteriology*, 1985, **161**, 1086–92.

(33) S. L. Neidleman, *Biotechnology and Genetic Engineering Reviews*, 1987, **5**, 245–268.

(34) K. Amor, D. E. Heinrichs, E. Frirdich, K. Ziebell, R. P. Johnson and C. Whitfield, *Infection and Immunity*, 2000, **68**, 1116–1124.

(35) T. J. Piggot, D. A. Holdbrook and S. Khalid, *The Journal of Physical Chemistry B*, 2011, **115**, 13381–13388.

(36) N. A. Berglund, T. J. Piggot, D. Jefferies, R. B. Sessions, P. J. Bond and S. Khalid, *PLOS Computational Biology*, 2015, **11**, ed. D. van der Spoel, e1004180.

(37) S. J. Singer and G. L. Nicolson, *Science*, 1972, **175**, 720–31.

(38) A. D. Dupuy and D. M. Engelman, *Proceedings of the National Academy of Sciences of the United States of America*, 2008, **105**, 2848–52.

(39) A. Lee, *Biochimica et Biophysica Acta (BBA) - Biomembranes*, 2003, **1612**, 1–40.

(40) R. Garcia-Fandino, A. Pineiro, J. L. Trick and M. S. P. Sansom, *ACS Nano*, 2016, **10**, 3693–3701.

(41) J. Davoust and P. F. Devaux, *Journal of Magnetic Resonance*, 1982, **48**, 475–494.

(42) D. Marsh and L. I. Horváth, *Biochimica et Biophysica Acta (BBA) - Reviews on Biomembranes*, 1998, **1376**, 267–296.

(43) J. E. Goose, M. S. P. Sansom, K Schulten, O Beckstein and O Keskin, *PLoS Computational Biology*, 2013, **9**, ed. D. R. Livesay, e1003033.

(44) D. A. Holdbrook, R. G. Huber, T. J. Piggot, P. J. Bond and S. Khalid, *PLoS ONE*, 2016, **11**, DOI: `10.1371/journal.pone.0156963`.

(45) M. B. Ulmschneider and M. S. Sansom, *Biochimica et Biophysica Acta (BBA) - Biomembranes*, 2001, **1512**, 1–14.

(46) M. R. de Planque, J. A. Kruijtzer, R. M. Liskamp, D Marsh, D. V. Greathouse, R. E. Koeppe, B de Kruijff and J. A. Killian, *The Journal of biological chemistry*, 1999, **274**, 20839–46.

(47) S. W. Cowan, T. Schirmer, G. Rummel, M. Steiert, R. Ghosh, R. A. Pauptit, J. N. Jansonius and J. P. Rosenbusch, *Nature*, 1992, **358**, 727–733.

(48) J. Killian and G. von Heijne, *Trends in Biochemical Sciences*, 2000, **25**, 429–434.

(49) W. M. Yau, W. C. Wimley, K Gawrisch and S. H. White, *Biochemistry*, 1998, **37**, 14713–8.

(50) K. A. Scott, P. J. Bond, A. Ivetac, A. P. Chetwynd, S. Khalid and M. S. Sansom, *Structure*, 2008, **16**, 621–630.

(51) M. Schiffer, C.-H. Chang and F. Stevens, *"Protein Engineering, Design and Selection"*, 1992, **5**, 213–214.

(52) L. R. Forrest and M. S. Sansom, *Current Opinion in Structural Biology*, 2000, **10**, 174–181.

(53) A. Pautsch and G. E. Schulz, *Journal of Molecular Biology*, 2000, **298**, 273–282.

(54) J. A. Killian and T. K. Nyholm, *Current Opinion in Structural Biology*, 2006, **16**, 473–479.

(55) I. Casuso, P. Sens, F. Rico and S. Scheuring, *Biophysical Journal*, 2010, **99**, L47–L49.

(56) R. J. Botelho, M. Teruel, R. Dierckman, R. Anderson, A. Wells, J. D. York, T. Meyer and S. Grinstein, *The Journal of Cell Biology*, 2000, **151**, 1353–1368.

(57) J. Poveda, A. Fernández, J. Encinar and J. González-Ros, *Biochimica et Biophysica Acta (BBA) - Biomembranes*, 2008, **1778**, 1583–1590.

(58) H. Sprong, P. van der Sluijs and G. van Meer, *Nature Reviews Molecular Cell Biology*, 2001, **2**, 504–513.

(59) P.-C. Hsu, F. Samsudin, J. Shearer and S. Khalid, *The Journal of Physical Chemistry Letters*, 2017, 5513–5518.

(60) O. P. Hamill and B. Martinac.

(61) I. M. Williamson, S. J. Alvis, J. M. East and A. G. Lee, *Biophysical Journal*, 2002, **83**, 2026–2038.

(62) M. Betanzos, C.-S. Chiang, H. R. Guy and S. Sukharev, *Nature Structural Biology*, 2002, **9**, 704–710.

(63) C. Toyoshima and H. Nomura, *Nature*, 2002, **418**, 605–611.

(64) Y. Naitoh, R. Eckert, B Martinac and C Kung, *Science*, 1969, **164**, 963–965.

(65) M. Venturoli, B. Smit and M. M. Sperotto, *Biophysical Journal*, 2005, **88**, 1778–1798.

(66) K. Mitra, I. Ubarretxena-Belandia, T. Taguchi, G. Warren and D. M. Engelman, *Proceedings of the National Academy of Sciences of the United States of America*, 2004, **101**, 4083–8.

(67) T. T. Sebastian, R. D. Baldridge, P. Xu and T. R. Graham, *Biochimica et Biophysica Acta (BBA) - Molecular and Cell Biology of Lipids*, 2012, **1821**, 1068–1077.

(68) P. F. Devaux, *Annu. Rev. Biophys. Biomol. Struct*, 1992, **21**, 417–39.

(69) T. Pomorski and A. K. Menon, *Cellular and Molecular Life Sciences*, 2006, **63**, 2908–2921.

(70) J. Jiang, B. V. Daniels and D. Fu, *The Journal of biological chemistry*, 2006, **281**, 454–60.

(71) A. Laganowsky, E. Reading, T. M. Allison, M. B. Ulmschneider, M. T. Degiacomi, A. J. Baldwin and C. V. Robinson, *Nature*, 2014, **510**, 172–175.

(72) C Lange, J. H. Nett, B. L. Trumpower and C Hunte, *The EMBO journal*, 2001, **20**, 6591–600.

(73) P. L. Yeagle, J. Young and D. Rice, *Biochemistry*, 1988, **27**, 6449–6452.

(74) G. Khelashvili, A. Grossfield, S. E. Feller, M. C. Pitman and H. Weinstein, *Proteins*, 2009, **76**, 403–17.

(75) P. L. Yeagle, *Biochimica et Biophysica Acta (BBA) - Biomembranes*, 2014, **1838**, 1548–1559.

(76) P. Jordan, P. Fromme, H. T. Witt, O. Klukas, W. Saenger and N. Krauß, *Nature*, 2001, **411**, 909–917.

(77) J. Nield, P. J. Rizkallah, J. Barber and N. E. Chayen, *Journal of Structural Biology*, 2003, **141**, 149–155.

(78) K. E. McAuley, P. K. Fyfe, J. P. Ridge, N. W. Isaacs, R. J. Cogdell and M. R. Jones, *Proceedings of the National Academy of Sciences*, 1999, **96**, 14706–14711.

(79) R. Koebnik, K. P. Locher and P. Van Gelder, *Molecular Microbiology*, 2000, **37**, 239–253.

(80) H. Venter, R. Mowla, T. Ohene-Agyei and S. Ma, *Frontiers in Microbiology*, 2015, **06**, 377.

(81) B. v. d. Berg, W. M. Clemons, I. Collinson, Y. Modis, E. Hartmann, S. C. Harrison and T. A. Rapoport, *Nature*, 2004, **427**, 36–44.

(82) N. Noinaj, J. C. Gumbart and S. K. Buchanan, *Nature Reviews Microbiology*, 2017, **15**, 197–204.

(83) I Sonntag, H Schwarz, Y Hirota and U Henning, *Journal of bacteriology*, 1978, **136**, 280–5.

(84) F. Samsudin, A. Boags, T. J. Piggot and S. Khalid, *Biophysical Journal*, 2017, **113**, 1496–1504.

(85) P. J. Bond, J. D. Faraldo-Gómez and M. S. Sansom, *Biophysical Journal*, 2002, **83**, 763–775.

(86) N. Saint, E. De, S. Julien, N. Orange and G. Molle, *Biochimica et Biophysica Acta (BBA) - Biomembranes*, 1993, **1145**, 119–123.

(87) S. Khalid, P. J. Bond, T. Carpenter and M. S. Sansom, *Biochimica et Biophysica Acta (BBA) - Biomembranes*, 2008, **1778**, 1871–1880.

(88) J. Marcoux, A. Politis, D. Rinehart, D. Marshall, M. Wallace, L. Tamm and C. Robinson, *Structure*, 2014, **22**, 781–790.

(89) R. D. Lins and T. Straatsma, *Biophysical Journal*, 2001, **81**, 1037–1046.

(90) T. S. Carpenter, J. Parkin and S. Khalid, *The Journal of Physical Chemistry Letters*, 2016, **7**, 3446–3451.

(91) K. N. Kirschner, R. D. Lins, A. Maass and T. A. Soares, 2012, DOI: `10.1021/ct300534j`.

(92) E. Wu, O. Engström, S. Jo, D. Stuhlsatz, M. Yeom, J. Klauda, G. Widmalm and W. Im, *Biophysical Journal*, 2013, **105**, 1444–1455.

(93) D. Patel, S. Re, E. Wu, Y. Qi, P. Klebba, G. Widmalm, M. Yeom, Y. Sugita and W. Im, *Biophysical Journal*, 2016, **110**, 930–938.

(94) B. Van Oosten and T. A. Harroun, *Journal of Molecular Graphics and Modelling*, 2016, **63**, DOI: 10.1016/j.jmgm.2015.12.002.

(95) P.-C. Hsu, D. Jefferies and S. Khalid, *The Journal of Physical Chemistry B*, 2016, **120**, 11170–11179.

(96) P.-C. Hsu, B. M. H. Bruininks, D. Jefferies, P. Cesar Telles de Souza, J. Lee, D. S. Patel, S. J. Marrink, Y. Qi, S. Khalid and W. Im, *Journal of Computational Chemistry*, 2017, **38**, 2354–2363.

(97) E. L. Wu, X. Cheng, S. Jo, H. Rui, K. C. Song, E. M. Dávila-Contreras, Y. Qi, J. Lee, V. Monje-Galvan, R. M. Venable, J. B. Klauda and W. Im, *Journal of Computational Chemistry*, 2014, **35**, 1997–2004.

(98) S. Jo, T. Kim, V. G. Iyer and W. Im, *Journal of Computational Chemistry*, 2008, **29**, 1859–1865.

(99) S. Jo, T. Kim and W. Im, *PLoS ONE*, 2007, **2**, ed. A. Yuan, e880.

(100) A. C. Kalli, M. S. P. Sansom and R. A. F. Reithmeier, *PLoS Comput Biol*, 2015, **11**, 1004123.

(101) F. Alcock, P. J. Stansfeld, H. Basit, J. Habersetzer, M. A. B. Baker, T. Palmer, M. I. Wallace and B. C. Berks, *Assembling the Tat protein translocase*, tech. rep.

(102) F. Samsudin and S. Khalid, *The Journal of Physical Chemistry B*, 2019, **123**, 2824–2832.

(103) T. J. Piggot, D. A. Holdbrook and S. Khalid, *Biochimica et Biophysica Acta (BBA) - Biomembranes*, 2013, **1828**, 284–293.

(104) H. Yuan, C. J. Jameson and S. Murad, *Molecular Physics*, 2010, **108**, 1569–1581.

(105) P.-C. Hsu, F. Samsudin, J. Shearer and S. Khalid, *Journal of Physical Chemistry Letters*, 2017, **8**, DOI: 10.1021/acs.jpclett.7b02432.

(106) J. Parkin, M. Chavent and S. Khalid, *Biophysical Journal*, 2015, **109**, 461–468.

(107) R. Hockney, S. Goel and J. Eastwood, *Journal of Computational Physics*, 1974, **14**, 148–158.

(108) L. Verlet, *Physical Review*, 1967, **159**, 98–103.

(109) S. J. Marrink, H. J. Risselada, S. Yefimov, D. P. Tieleman and A. H. De Vries, *Journal of Physical Chemistry B*, 2007, **111**, 7812–7824.

(110) L. Monticelli, S. K. Kandasamy, X. Periole, R. G. Larson, D. P. Tieleman and S.-J. Marrink, *Journal of Chemical Theory and Computation*, 2008, **4**, 819–834.

(111) S. J. Marrink, A. H. de Vries and A. E. Mark, *The Journal of Physical Chemistry B*, 2004, **108**, 750–760.

(112) S. J. Marrink, J. Risselada and A. E. Mark, *Chemistry and Physics of Lipids*, 2005, **135**, 223–244.

(113) V. Agrawal, G. Arya and J. Oswald, *Macromolecules*, 2014, **47**, 3378–3389.

(114) M. A. Webb, J.-Y. Delannoy and J. J. de Pablo, *Journal of Chemical Theory and Computation*, 2019, **15**, 1199–1208.

(115) L. Lu, J. F. Dama and G. A. Voth, *The Journal of Chemical Physics*, 2013, **139**, 121906.

(116) P. W. Fowler, J. Hélie, A. Duncan, M. Chavent, H. Koldsø and M. S. P. Sansom, *Soft Matter*, 2016, **12**, 7792–7803.

(117) M. Javanainen, H. Martinez-Seara, R. Metzler and I. Vattulainen, *The Journal of Physical Chemistry Letters*, 2017, **8**, 4308–4313.

(118) Y. Wang, P. Gkeka, J. E. Fuchs, K. R. Liedl and Z. Cournia, *Biochimica et Biophysica Acta (BBA) - Biomembranes*, 2016, **1858**, 2846–2857.

(119) S. J. Marrink et al., *Chemical Society Reviews*, 2013, **42**, 6801.

(120) X. Periole, M. Cavalli, S.-J. Marrink and M. A. Ceruso, *Journal of Chemical Theory and Computation*, 2009, **5**, 2531–2543.

(121) U. Essmann, L. Perera, M. L. Berkowitz, T. Darden, H. Lee and L. G. Pedersen, *The Journal of Chemical Physics*, 1995, **103**, 8577–8593.

(122) T. Darden, D. York and L. Pedersen, *The Journal of Chemical Physics*, 1993, **98**, 10089.

(123) M. Orsi, J. Michel and J. W. Essex, *Journal of Physics: Condensed Matter*, 2010, **22**, 155106.

(124) I. G. Tironirené, S. E. Smithwilfred and F Van Gunsteren, *The Journal of Chemical Physics*, 1995, **102**, DOI: `10.1063/1.469273`.

(125) D. H. de Jong, S. Baoukina, H. I. Ingólfsson and S. J. Marrink, *Computer Physics Communications*, 2016, **199**, 1–7.

(126) H. J. C. Berendsen, J. P. M. Postma, W. F. van Gunsteren, A. DiNola and J. R. Haak, *The Journal of Chemical Physics*, 1984, **81**, 3684–3690.

(127) G. Bussi, D. Donadio and M. Parrinello, *The Journal of Chemical Physics*, 2007, **126**, 014101.

(128) W. G. Hoover, *Physical Review A*, 1985, **31**, 1695–1697.

(129) S. Nosé, *Molecular Physics*, 1984, **52**, 255–268.

(130) S. Nosé, *The Journal of Chemical Physics*, 1984, **81**, 511–519.

(131) G. M. Torrie and J. P. Valleau, *Chemical Physics Letters*, 1974, **28**, 578–581.

(132) G. Torrie and J. Valleau, *Journal of Computational Physics*, 1977, **23**, 187–199.

(133) M. Souaille and B. Roux, *Computer Physics Communications*, 2001, **135**, 40–57.

(134) S. Kumar, J. M. Rosenberg, D. Bouzida, R. H. Swendsen and P. A. Kollman, *Journal of Computational Chemistry*, 1992, **13**, 1011–1021.

(135) J. S. Hub, B. L. de Groot and D. van der Spoel, *Journal of Chemical Theory and Computation*, 2010, **6**, 3713–3720.

(136) M. R. Shirts and J. D. Chodera, *The Journal of Chemical Physics*, 2008, **129**, 124105.

(137) K. Kostarelos, A. Bianco and M. Prato, *Nature Nanotechnology*, 2009, **4**, 627–633.

(138) A. De la Zerda, C. Zavaleta, S. Keren, S. Vaithilingam, S. Bodapati, Z. Liu, J. Levi, B. R. Smith, T.-J. Ma, O. Oralkan, Z. Cheng, X. Chen, H. Dai, B. T. Khuri-Yakub and S. S. Gambhir, *Nature nanotechnology*, 2008, **3**, 557–62.

(139) A. Bianco, K. Kostarelos and M. Prato, *Current Opinion in Chemical Biology*, 2005, **9**, 674–679.

(140) K. T. Al-Jamal, H. Nerl, K. H. Müller, H. Ali-Boucetta, S. Li, P. D. Haynes, J. R. Jinschek, M. Prato, A. Bianco, K. Kostarelos and A. E. Porter, *Nanoscale*, 2011, **3**, 2627.

(141) M. Lelimousin and M. S. P. Sansom, *Small*, 2013, **9**, 3639–3646.

(142) S. Baoukina, L. Monticelli and D. P. Tieleman, *The Journal of Physical Chemistry B*, 2013, **117**, 12113–12123.

(143) K. Kostarelos, *Nature Biotechnology*, 2008, **26**, 774–776.

(144) J. R. Brotherus, O. H. Griffith, M. O. Brotherus, P. C. Jost, J. R. Silvius and L. E. Hokin, *Biochemistry*, 1981, **20**, 5261–5267.

(145) P. C. Jost and O. Hayes Griffith, in, 1978, pp. 369–418.

(146) M. Javanainen, H. Hammaren, L. Monticelli, J.-H. Jeon, M. S. Miettinen, H. Martinez-Seara, R. Metzler and I. Vattulainen, *Faraday Discuss.*, 2013, **161**, 397–417.

(147) A. J. de Jesus and T. W. Allen, *Biochimica et Biophysica Acta (BBA) - Biomembranes*, 2013, **1828**, 864–876.

(148) W. Im and B. Roux, *Journal of Molecular Biology*, 2002, **319**, 1177–1197.

(149) J. Shearer and S. Khalid, *Scientific Reports*, 2018, **8**, 1805.

(150) M. J. Abraham, T. Murtola, R. Schulz, S. Páll, J. C. Smith, B. Hess and E. Lindahl, *SoftwareX*, 2015, **1**, 19–25.

(151) A. Fiser and A. Šali, *Methods in Enzymology*, 2003, **374**, 461–491.

(152) D. H. de Jong, G. Singh, W. F. D. Bennett, C. Arnarez, T. A. Wassenaar, L. V. Schäfer, X. Periole, D. P. Tieleman and S. J. Marrink, *Journal of Chemical Theory and Computation*, 2013, **9**, 687–697.

(153) L. Monticelli, *Journal of Chemical Theory and Computation*, 2012, **8**, 1370–1378.

(154) I. G. Tironi, R. Sperb, P. E. Smith and W. F. van Gunsteren, *The Journal of Chemical Physics*, 1995, **102**, 5451.

(155) Y. Qi, H. I. Ingólfsson, X. Cheng, J. Lee, S. J. Marrink and W. Im, *Journal of Chemical Theory and Computation*, 2015, **11**, 4486–4494.

(156) N. Castillo, L. Monticelli, J. Barnoud and D. P. Tieleman, *Chemistry and Physics of Lipids*, 2013, **169**, 95–105.

(157) W. Humphrey, A. Dalke and K. Schulten, *Journal of Molecular Graphics*, 1996, **14**, 33–38.

(158) R. J. Gowers, M. Linke, J. Barnoud, T. J. E. Reddy, M. N. Melo, S. L. Seyler, J. Domański, D. L. Dotson, S. Buchoux, I. M. Kenney and O. Beckstein, *MDAnalysis: A Python Package for the Rapid Analysis of Molecular Dynamics Simulations*, 2016.

(159) N. Michaud-Agrawal, E. J. Denning, T. B. Woolf and O. Beckstein, *Journal of computational chemistry*, 2011, **32**, 2319–27.

(160) V. Corradi, E. Mendez-Villuendas, H. I. Ingólfsson, R. X. Gu, I. Siuda, M. N. Melo, A. Moussatova, L. J. Degagné, B. I. Sejdiu, G. Singh, T. A. Wassenaar, K. Delgado Magnero, S. J. Marrink and D. P. Tieleman, *ACS Central Science*, 2018, **4**, DOI: 10.1021/acscentsci.8b00143.

(161) F. Pedregosa, G. Varoquaux, A. Gramfort, V. Michel, B. Thirion, O. Grisel, M. Blondel, P. Prettenhofer, R. Weiss, V. Dubourg, J. Vanderplas, A. Passos, D. Cournapeau, M. Brucher, M. Perrot and. Duchesnay, *Journal of Machine Learning Research*, 2011, **12**, 2825–2830.

(162) M. Ester, H.-P. Kriegel, J. Sander and X. Xu, *A Density-Based Algorithm for Discovering Clusters in Large Spatial Databases with Noise*, tech. rep., 1996.

(163) E. Schubert, J. Sander, M. Ester, H. P. Kriegel and X. Xu, *ACM Transactions on Database Systems*, 2017, **42**, 1–21.

(164) S. Ramadurai, A. Holt, V. Krasnikov, G. van den Bogaart, J. A. Killian and B. Poolman, *Journal of the American Chemical Society*, 2009, **131**, 12650–12656.

(165) K. Brandenburg and U. Seydel, *European Biophysics Journal*, 1988, **16**, 83–94.

(166) J. Sander, M. Ester, H.-P. Kriegel and X. Xu, *Data Mining and Knowledge Discovery*, 1998, **2**, 169–194.

(167) H. Koldsø, D. Shorthouse, J. Hélie and M. S. P. Sansom, *PLoS Computational Biology*, 2014, **10**, ed. C. Fradin, e1003911.

(168) S. O. Yesylevskyy, L. V. Schäfer, D. Sengupta and S. J. Marrink, *PLoS Computational Biology*, 2010, **6**, ed. M. Levitt, 1–17.

(169) P. Stansfeld, J. Goose, M. Caffrey, E. Carpenter, J. Parker, S. Newstead and M. Sansom, *Structure*, 2015, **23**, 1350–1361.

(170) A. D. Ferguson, W Welte, E Hofmann, B Lindner, O Holst, J. W. Coulton and K Diederichs, *Structure*, 2000, **8**, 585–92.

(171) W. Arunmanee, M. Pathania, A. S. Solovyova, A. P. Le Brun, H. Ridley, A. Baslé, B. van den Berg and J. H. Lakey, *Proceedings of the National Academy of Sciences of the United States of America*, 2016, **113**, 5034–43.

(172) J. Shearer, D. Jefferies and S. Khalid, *Journal of Chemical Theory and Computation*, 2019, **15**, 2608–2619.

(173) A. B. Poma, M. Cieplak and P. E. Theodorakis, *Journal of Chemical Theory and Computation*, 2017, **13**, 1366–1374.

(174) J. Vogt and G. E. Schulz, *Structure*, 1999, **7**, 1301–1309.

(175) R. G. Efremov and L. A. Sazanov, *Journal of Structural Biology*, 2012, **178**, 311–318.

(176) D. P. Chimento, A. K. Mohanty, R. J. Kadner and M. C. Wiener, *Nature Structural & Molecular Biology*, 2003, **10**, 394–401.

(177) B. van den Berg, *Journal of Molecular Biology*, 2010, **396**, 627–633.

(178) R. Sánchez and A. Šali, in *Protein Structure Prediction*, Humana Press, New Jersey, 2000, pp. 97–129.

(179) S. Unni, Y. Huang, R. M. Hanson, M. Tobias, S. Krishnan, W. W. Li, J. E. Nielsen and N. A. Baker, *Journal of Computational Chemistry*, 2011, **32**, 1488–1491.

(180) T. Nugent and D. T. Jones, *BMC Bioinformatics*, 2013, **14**, 276.

(181) G. Lukat, J. Krüger and B. Sommer, *Journal of Chemical Information and Modeling*, 2013, **53**, 2908–2925.

(182) T. D. Romo and A. Grossfield, *Journal of Chemical Theory and Computation*, 2011, **7**, 2464–2472.

(183) M. Ramakrishnan, J. Qu, C. L. Pocanschi, J. H. Klienschmidt and D. Marsh, 2005, DOI: 10.1021/BI047603Y.

(184) F. Evanics, P. M. Hwang, C. Y. Yao, L. E. Kay and R. S. Prosser, *Journal of the American Chemical Society*, 2006, **128**, 8256–8264.

(185) G. M. Saunders, H. E. Bruce Macdonald, J. W. Essex and S. Khalid, *Biophysical Journal*, 2018, **115**, 1445–1456.

(186) M. Baaden and M. S. Sansom, *Biophysical Journal*, 2004, **87**, 2942–2953.

(187) D. P. Tieleman, L. R. Forrest, M. S. P. Sansom and H. J. C. Berendsen, 1998, DOI: 10.1021/BI981802Y.

(188) J. Døvling Kaspersen, C. Moestrup Jessen, B. Stougaard Vad, E. Skipper Sørensen, K. Kleiner Andersen, M. Glasius, C. L. Pinto Oliveira, D. E. Otzen and J. S. Pedersen, *ChemBioChem*, 2014, **15**, 2113–2124.

(189) M. Ortiz-Suarez, F. Samsudin, T. Piggot, P. Bond and S. Khalid, *Biophysical Journal*, 2016, **111**, 1692–1702.

(190) J. N. Horn, T.-C. Kao and A. Grossfield, in *G Protein-Coupled Receptors - Modeling and Simulation*, Springer, Dordrecht, 2014, pp. 75–94.

(191) J. N Horn, Ph.D. Thesis, University of Rochester, New York, 2013.

(192) P. S. Schmalhorst, F. Deluweit, R. Scherrers, C. P. Heisenberg and M. Sikora, *Journal of Chemical Theory and Computation*, 2017, DOI: 10.1021/acs.jctc.7b00374.

(193) S. Kmiecik, D. Gront, M. Kolinski, L. Wieteska, A. E. Dawid and A. Kolinski, *Chemical Reviews*, 2016, **116**, 7898–7936.

(194) A. Grossfield, P. N. Patrone, D. R. Roe, A. J. Schultz, D. Siderius and D. M. Zuckerman, *Living Journal of Computational Molecular Science*, 2019, **1**, DOI: 10.33011/livecoms.1.1.5067.

(195) H. Flyvbjerg and H. G. Petersen, *The Journal of Chemical Physics*, 1989, **91**, 461–466.

(196) B. Hess, *Physical Review E*, 2002, **65**, 031910.

(197) B. Efron and R. Tibshirani, *An introduction to the bootstrap*, Chapman & Hall, 1994, p. 436.

(198) H. Hotelling, *Journal of Educational Psychology*, 1933, **24**, 417–441.

(199) S. Wold, K. Esbensen and P. Geladi, *Chemometrics and Intelligent Laboratory Systems*, 1987, **2**, 37–52.

(200) H. Abdi and L. J. Williams, *Wiley Interdisciplinary Reviews: Computational Statistics*, 2010, **2**, 433–459.

(201) Y. Mu, P. H. Nguyen and G. Stock, *Proteins: Structure, Function, and Bioinformatics*, 2004, **58**, 45–52.

(202) A. Grossfield and D. M. Zuckerman, *Annual Reports in Computational Chemistry*, 2009, **5**, 23–48.

(203) S. Khalid, T. J. Piggot and F. Samsudin, *Accounts of Chemical Research*, 2019, **52**, 180–188.

(204) J. N. Weiser and E. C. Gotschlich, *Infection and immunity*, 1991, **59**, 2252–8.

(205) A. T. Boags, F. Samsudin and S. Khalid, *Structure*, 2019, **27**, 713–724.

(206) R. Hiruma, A. Yamaguchi and T. Sawai, *FEBS Letters*, 1984, **170**, 268–272.

(207) R. G. Huber, N. A. Berglund, V. Kargas, J. K. Marzinek, D. A. Holdbrook, S. Khalid, T. J. Piggot, A. Schmidtchen and P. J. Bond, *Structure*, 2018, **26**, 1151–1161.

(208) D. P. Tieleman and S.-J. Marrink, *Journal of the American Chemical Society*, 2006, **128**, 12462–12467.

(209) F. Stetter, L. Cwiklik, P. Jungwirth and T. Hugel, *Biophysical Journal*, 2014, **107**, 1167–1175.

(210) J. Kästner, *Wiley Interdisciplinary Reviews: Computational Molecular Science*, 2011, **1**, 932–942.

(211) C. T. Lee, J. Comer, C. Herndon, N. Leung, A. Pavlova, R. V. Swift, C. Tung, C. N. Rowley, R. E. Amaro, C. Chipot, Y. Wang and J. C. Gumbart, *Journal of Chemical Information and Modeling*, 2016, **56**, 721–733.

(212) F. B. Naughton, A. C. Kalli and M. S. P. Sansom, *The Journal of Physical Chemistry Letters*, 2016, **7**, 1219–1224.

(213) J. Domański, G. Hedger, R. B. Best, P. J. Stansfeld and M. S. P. Sansom, *The Journal of Physical Chemistry B*, 2017, **121**, 3364–3375.

(214) C. Arnarez, S. J. Marrink and X. Periole, *Scientific Reports*, 2013, **3**, 1263.

(215) V. Schmidt, M. Sidore, C. Bechara, J.-P. Duneau and J. N. Sturgis, *Biochimica et Biophysica Acta (BBA) - Biomembranes*, 2019, **1861**, 431–440.

(216) E. Rosta, H. L. Woodcock, B. R. Brooks and G. Hummer, *Journal of Computational Chemistry*, 2009, **30**, 1634–1641.

(217) N. Nitschke, K. Atkovska and J. S. Hub, *Journal of Chemical Physics*, 2016, DOI: 10.1063/1.4963192.

(218) G. A. Tribello, M. Bonomi, D. Branduardi, C. Camilloni and G. Bussi, *Computer Physics Communications*, 2014, **185**, 604–613.

(219) J. D. Chodera, W. C. Swope, J. W. Pitera, C. Seok and K. A. Dill, *Journal of Chemical Theory and Computation*, 2006, **3**, 26–41.

(220) C. Neale, W. F. D. Bennett, D. P. Tieleman and R. Pomès, *Journal of Chemical Theory and Computation*, 2011, **7**, 4175–4188.

(221) R. Capelli, P. Carloni and M. Parrinello, *The Journal of Physical Chemistry Letters*, 2019, **10**, 3495–3499.

(222) Y. Deng and B. Roux, *The Journal of Physical Chemistry B*, 2009, **113**, 2234–2246.

(223) P. C. Chen and S. Kuyucak, *Biophysical Journal*, 2011, **100**, 2466–2474.

(224) S. Côté, V. Binette, E. Salnikov, B. Bechinger and N. Mousseau, *Biophysical Journal*, 2015, **108**, 1187–1198.

(225) S. Park, T. Kim and W. Im, *Physical Review Letters*, 2012, **108**, 108102.

(226) R. H. Swendsen and J.-S. Wang, *Physical Review Letters*, 1986, **57**, 2607–2609.

(227) D. Gront, A. Kolinski and J. Skolnick, *The Journal of Chemical Physics*, 2000, **113**, 5065.

(228) Y. Sugita and Y. Okamoto, *Chemical Physics Letters*, 1999, **314**, 141–151.

(229) N. V. Buchete and G. Hummer, *Physical Review E*, 2008, **77**, 030902.

(230) L. Wang, R. A. Friesner and B. J. Berne, *The Journal of Physical Chemistry B*, 2011, **115**, 9431–9438.

(231) G. Bussi, *Molecular Physics*, 2014, **112**, 379–384.

(232) S. Buchoux, *Bioinformatics*, 2017, **33**, DOI: 10.1093/bioinformatics/btw563.

(233) M. J. Abraham and J. E. Gready, *Journal of Chemical Theory and Computation*, 2008, **4**, 1119–1128.

(234) A. Patriksson and D. van der Spoel, *Physical Chemistry Chemical Physics*, 2008, **10**, 2073.

(235) H. Fukunishi, O. Watanabe and S. Takada, *The Journal of Chemical Physics*, 2002, **116**, 9058–9067.

(236) D. J. Sindhikara, D. J. Emerson and A. E. Roitberg, *Journal of Chemical Theory and Computation*, 2010, **6**, 2804–2808.

(237) C. Predescu, M. Predescu and C. V. Ciobanu, *The Journal of Physical Chemistry B*, 2005, **109**, 4189–4196.

(238) M. K. Prakash, A. Barducci and M. Parrinello, *Journal of Chemical Theory and Computation*, 2011, **7**, 2025–2027.

(239) D. Sindhikara, Y. Meng and A. E. Roitberg, *The Journal of Chemical Physics*, 2008, **128**, 6042.

(240) J. D. Chodera, *Journal of Chemical Theory and Computation*, 2016, **12**, 1799–1805.

(241) N. M. Henriksen, D. R. Roe and T. E. Cheatham, *The Journal of Physical Chemistry B*, 2013, **117**, 4014–4027.

(242) M. R. Machado, E. E. Barrera, F. Klein, M. Sóñora, S. Silva and S. Pantano, *Journal of Chemical Theory and Computation*, 2019, **15**, 2719–2733.

(243) E. E. Barrera, M. R. Machado and S. Pantano, *bioRxiv*, 2019, 627570.

(244) X. Periole and A. E. Mark, *The Journal of Chemical Physics*, 2007, **126**, 014903.

(245) W. Jiang, Y. Luo, L. Maragliano and B. Roux, *Journal of Chemical Theory and Computation*, 2012, **8**, 4672–4680.

(246) B. E. Husic and V. S. Pande, *Journal of the American Chemical Society*, 2018, **140**, 2386–2396.

(247) J. S. Smith, O. Isayev and A. E. Roitberg, *Chemical Science*, 2017, **8**, 3192–3203.

(248) J. Wang, S. Olsson, C. Wehmeyer, A. Pérez, N. E. Charron, G. de Fabritiis, F. Noé and C. Clementi, *ACS Central Science*, 2019, acscentsci.8b00913.